EAST EUROPEAN JOURNAL OF PHYSICS. 1. 281-285 (2026)
DOI:10.26565/2312-4334-2026-1-32 ISSN 2312-4334

PHOTOELECTRONIC PROPERTIES OF $CdGa_2S_4$ SINGLE CRYSTALS

Zafar Kadiroglu
Institute of Physics, Ministry of Science and Education Republic of Azerbaijan, Baku, AZ1073 Azerbaijan
Corresponding Author e-mail: zafarkadiroglu@gmail.com
Received December 5, 2025; revised January 15, 2026; in final form February 17, 2026; accepted February 24, 2026

Experimental investigations of the photoelectric properties of $CdGa_2S_4$ single crystals were carried out. The study examined the temperature dependence of the photocurrent (within the 110–420 K range), as well as the spectral dependence and transient characteristics of optical quenching at T = 300 K. Optical quenching of the photocurrent was observed within a secondary light beam energy range of 0.6 - 2.49 eV. Measurements revealed energy levels at E_c - 0.21 eV, E_c - 0.42 eV, and E_c - 1.06 eV, as well as sensitizing levels at E_v + 0.89 eV. The decrease in photocurrent at temperatures above 300 K is attributed to thermal quenching. Both optical and thermal quenching of photoconductivity in $CdGa_2S_4$ crystals are ascribed to changes in the charge state and exchange dynamics of sensitizing and recombination centers.
Keywords: *Cadmium thiogallate; Photoconductivity; Defects; Deep levels; Sensitizing centers; Recombination centers; Optical quenching; Thermal quenching*
PACS: 71.20 Nr, 71.55. i, 72.20. Jv, 72.20. Nr, 72.40. Jv, 72.80. Jc, 78.20. Nv, 78.20. Jc,

INTRODUCTION

$CdGa_2S_4$ belongs to the class of $A^{II}B^{III}{}_2C^{VI}{}_4$ ternary semiconductors, where A represents divalent cations (e.g. Zn or Cd), B represents trivalent cations (e.g. Ga or In), and C represents chalcogens (such as S or Se). These compounds are characterized by birefringence, optical activity, high nonlinear susceptibility coefficients, a wide band gap, bright luminescence, and high photosensitivity in the visible range [1-7]. The aforementioned properties make these compounds promising materials for optoelectronic applications.

The band gap of $CdGa_2S_4$ varies from 2.96 eV at T = 300 K [8] to 3.77 eV at T = 10 K [9]. Its complex chemical composition and the presence of two atoms in the cation sublattice result in multiple levels within the band gap. The study of photoconductivity and luminescence in $CdGa_2S_4$ crystals has been widely used to detect localized levels and analyze their nature and properties [10-16]. However, the recombination processes and the specific roles of various centers - including the sensitizing centers involved in these processes-have not yet been sufficiently studied.

This paper presents photocurrent measurements of $CdGa_2S_4$ single crystals to obtain additional information regarding localized states and photoconductivity sensitizing centers within the band gap. We have carried out experiments on excited samples using two beams of radiation. Using UV background illumination in conjunction with secondary below-band-gap illumination at variable wavelengths, the optical quenching of photoconductivity was investigated. Furthermore, we report the temperature dependence of the photocurrent in $CdGa_2S_4$ over the range 110-400 K. This work contributes to refining the localized-state and electronic-transition models for $CdGa_2S_4$, providing valuable insights into its photoelectric properties.

EXPERIMENTAL DETAILS

$CdGa_2S_4$ polycrystals were synthesized from the high-purity elements (99.999%) in stoichiometric proportions within evacuated quartz ampoules. The resulting crystals were characterized using X-ray diffraction and Raman scattering spectroscopy. X-ray diffraction studies, performed with a Bruker D2 Phaser diffractometer, confirmed that $CdGa_2S_4$ crystallizes in a cation–ordered defect chalcopyrite tetragonal structure (space group $I\bar{4}$, S_4^2). The unit cell parameters were determined to be a = b = 5.5450 Å and c = 10.1470 Å.

Raman spectra of $CdGa_2S_4$ were recorded using a “Nanofinder 30” (Tokyo Instruments, Japan) confocal Raman microspectrometer. A Nd:YAG laser (532 nm second-harmonic output, 10 mW maximum power) served as the excitation source. With a diffraction grating with 1800 lines/mm, the spectral resolution was better than 0.5 cm^{-1}. All spectra were measured in a backscattering geometry. The Raman spectra of the $CdGa_2S_4$ crystals are in good agreement with previously reported results [17]. Together, the X-ray diffraction and Raman scattering characterizations confirm the high structural quality of the synthesized $CdGa_2S_4$ crystals.

The synthesized material served as a precursor for the growth of a $CdGa_2S_4$ single crystal via chemical vapor transport, using iodine as the transport agent in a closed tube. This method yielded $CdGa_2S_4$ single crystals with natural faceting, appearing as transparent, light-yellow trihedral prisms with mirror-like surfaces. For experimental measurements, the samples were prepared as plane-parallel plates with dimensions of 3×2×1 mm^3. One face of each corresponded to a natural mirror edge and was used without further processing. For reliable electrical measurements, the electrical contacts were formed using indium solder on the lateral faces of the samples. The crystals exhibited n-type

Cite as: Z. Kadiroglu, East Eur. J. Phys. 1, 281 (2026), https://doi.org/10.26565/2312-4334-2026-1-32

conductivity, with a dark resistivity (ρ_d) ranging from 10^9 to $10^{10}\,\Omega \cdot$ cm at 300 K. Estimates of the electron concentration and Hall mobility, derived from Hall coefficient measurements, yielded values of $n \approx 10^8 - 10^9$ cm^{-3} and $\mu_n \approx 1 - 10$ cm^2 / (V · s) at 300 K, respectively.

The experimental setup used to study the optical quenching of photoconductivity is described in Ref. [18]. For excitation within the intrinsic absorption region (background excitation), an incandescent lamp was used in combination with a set of spectral, neutral, and water filters. Secondary (quenching) illumination ($h\nu < E_g$) was provided by a tungsten lamp passed through an SF-4A monochromator. Measurements were performed under direct current using a steady-state method. The electric field strength applied to the samples was kept within the linear region of the current-voltage (I-V) characteristics. The current was recorded using a DC chart recorder and a microvoltmeter F-136. The spectral dependence of the optical quenching was investigated over a secondary illumination wavelength range of 0.4 to 2.0 μm. Special care was taken to ensure that the background photocurrent reached an equilibrium value before each measurement. The optical quenching of the photoconductivity as a function of the secondary light wavelength was plotted point-by-point under sequential excitation.

EXPERIMENTAL RESULTS AND DISCUSSIONS

Optical quenching of photoconductivity is a phenomenon where sub-bandgap illumination reduces the photoconductivity induced by above-bandgap background light. This effect provides a valuable method for investigating the photoelectronic properties of semiconductor defects, such as deep energy levels and trapping mechanisms. Furthermore, it demonstrates potential for infrared photodetection at energies significantly below the semiconductor bandgap.

We observed the quenching of the photocurrent in $CdGa_2S_4$ single crystals over a secondary light beam energy range of 0.62 - 2.49 eV. Figure 1 illustrates the optical quenching of the photoconductivity as a function of the secondary light wavelength at room temperature, measured at a constant secondary light intensity. In the Figure, $I_{int.}$ represents the constant background photocurrent - the steady-state current flowing through the crystal when illuminated solely by fixed-intensity, above – bandgap light.

Measurements of the spectral distribution of the quenching effect indicate the presence of energy levels above the valence band, which are attributed to the optical quenching mechanism. The phenomenon is strongly dependent on the energy of the quenching light. As shown in Figure 1, the optical quenching spectrum of $CdGa_2S_4$ is complex, consisting of three distinct quenching bands extending from 0.62 - 0.89 eV, 0.89 - 1.25 eV, and 1.57 - 2.49 eV. A prominent quenching maximum is observed at approximately 2.05 eV. The three observed regions in the optical quenching spectrum suggest that two distinct sensitizing centers participate in recombination processes in $CdGa_2S_4$ single crystals. Based on the long-wavelength edge shown in Figure 1, the energy level of one sensitizing center was determined to be $E^o_{vr} = 0.89$ eV above the valence band maximum. While optical quenching was also observed in the 0.6 - 0.89 eV range, limitations in the experimental setup–specifically the spectral range of the monochromator - prevented the determination of the exact long-wavelength edge for this specific region.

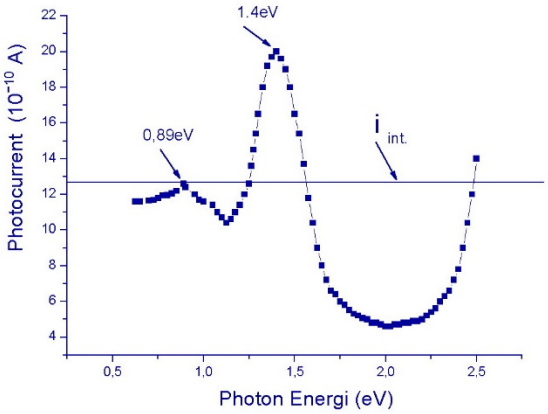

Figure 1. Quenching of the photocurrent (I_{ph}) as a function of the photon energy of the secondary light. The horizontal line ($I_{int.}$) represents the steady-state photocurrent excited solely by above-bandgap illumination in the absence of quenching light (T = 300 K)

As with other semiconductor materials, the photoelectronic and luminescent properties of $CdGa_2S_4$ are significantly influenced by deep centers, which are classified as either trapping or recombination centers. The optical quenching of photoconductivity in $CdGa_2S_4$ single crystals can be explained by the presence of "fast" recombination centers (Class I centers according to the Rose model [19]) and "slow" photosensitizing recombination centers (Class II centers), as well as t-level traps located within the bandgap. Optical quenching of photoconductivity in n-type $CdGa_2S_4$ crystals indicates the presence of hole traps, as only hole-capturing centers in n-type materials can trigger a reduction in photocurrent. When the crystals are illuminated solely with above-bandgap light, free electrons and holes are generated, resulting in steady-state (stationary) photoconductivity. As a result of the redistribution of electrons and holes between the levels of fast and slow recombination centers, the photosensitivity of the crystal increases.

Upon secondary illumination with energy corresponding to deep acceptor levels, electrons are excited from the valence band to these acceptor (hole trap) levels. This process effectively releases holes into the valence band, which then recombine with electrons, either directly from the conduction band or via other fast recombination centers. This redistribution reduces the electron lifetime in the conduction band of $CdGa_2S_4$.Ultimately, both processes reduce the free electron density, resulting in the observed quenching of photoconductivity.

It should be noted that, in addition to the optical quenching spectrum of photoconductivity clearly pronounced impurity photoconductivity band with a maximum of 1.4 eV was observed 1.06 - 1.57 eV energy range. This indicates that interpreting the spectral distribution of the optical quenching requires accounting for the simultaneous ionization of several types of local centers. A study of the transient characteristics of this quenching reveal that the rate of extinction depends on the wavelength and intensity of the secondary light. Figure 2 illustrates the transient characteristics of the photocurrent optical quenching in $CdGa_2S_4$ at 300 K.

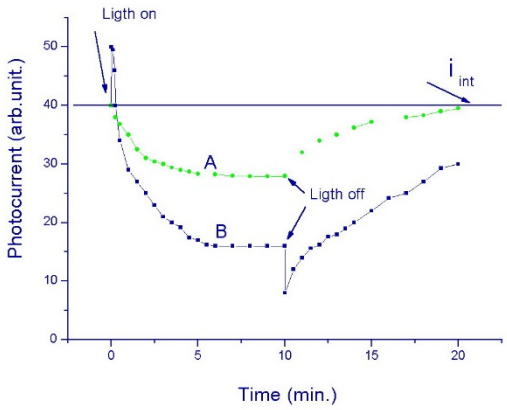

Figure 2. Transient characteristics of the optical quenching of $CdGa_2S_4$ crystals (A) hν < 1.06 eV and (B) hν > 1.06 eV

It can be observed that when the sample is excited by light in the hν < 1.06 eV region, only photocurrent quenching occurs (Curve A). This implies that, at these energies, electrons transition from the valence band to the photoconductivity-sensitizing centers. When the light is switched off, photocurrent recovery processes begin, and the photoconductivity gradually returns to its pre-quenching level. In $CdGa_2S_4$ crystals, "flare-up" transitions in the photocurrent are detected under the influence of secondary light exceeding 1.06 eV. When illuminated with monochromatic light in the hν > 1.06 eV region, the photocurrent initially increases sharply passing through the maximum before decreasing to an equilibrium value (Figure 2, Curve B). The initial increase in photocurrent is attributed to the generation of carriers from local levels into the conduction band, whereas the subsequent decrease results from the transfer of holes from the photoconductivity-sensitizing centers to the valence band. In a certain spectral range, excitation dominates over the quenching caused by the same photons. Consequently, a maximum appears at 1.4 eV in the optical quenching spectrum. In this case, the unique nature of the photocurrent transient characteristics can be utilized to separate the simultaneous effects of quenching and stimulation. At photon energies hν > 1.06 eV, the magnitude of the "flare-up" increases with the energy of the secondary radiation. This suggests the presence of a donor level with an activation energy of 1.06 eV located below the conduction band. Consequently, the band gap of $CdGa_2S_4$ single crystals contains sensitizing centers at E_v + 0.89 eV and donor levels at E_c - 1.06 eV, both of which are highly active in carrier generation and recombination.

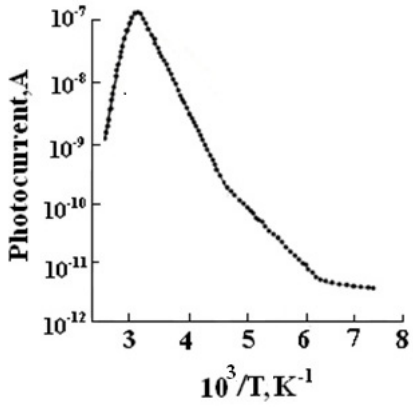

Figure 3. Temperature dependence of the photocurrent in $CdGa_2S_4$ single crystals

Valuable information regarding localized states can be obtained by studying the temperature dependence of the above-bandgap photocurrent, $I_{ph}(T)$. We present the results of our investigation into the temperature dependence of the photocurrent in $CdGa_2S_4$ within the range of 110 - 400 K (Figure 3). As shown, the photocurrent increases exponentially with temperature until reaching a maximum at T_m = 300 K, beyond which the photocurrent begins to decrease.

The decrease in photocurrent at temperatures above 300 K can be attributed to thermal quenching, which stems from a shift in the behavior of sensitizing centers. Specifically, thermal quenching occurs when these centers transition from acting as recombination centers to acting as traps. As the temperature rises at a fixed intensity, a threshold is reached where minority carriers (holes) are thermally released from trapping levels into the valence band. This increases the density of free holes, which are then rapidly captured by deep recombination centers. This process facilitates the recombination of free electrons and holes, effectively reducing the overall photocurrent. This process shortens the lifetime of the majority carriers (electrons), leading to the decrease in photocurrent observed

in Figure 3. The plot of log (I_{ph}) vs. 10^3/T shows two distinct regions. In the low–temperature region (150 K < T < 240 K), the photocurrent increases more slowly than in the high-temperature region (240 K < T < 300 K). This increase in photocurrent in $CdGa_2S_4$ is characterized by two exponential sections with thermal activation energies of 0.21 eV and 0.42 eV (electron mobility rises slightly with rising temperature).

Investigation of the spectral distribution of photoconductivity in $CdGa_2S_4$ revealed four maxima at energies of 1.65, 2.25, 2.55, and 2.95 eV [13]. Kerimova et al. determined that the luminescence spectrum of $CdGa_2S_4$ consists of four bands: 1) blue, with a maximum at 2.8 eV, observed at low temperatures; 2) yellow-green, consisting of three elementary bands with maxima at 2.5 eV, 2.37, and 2.2 eV; 3) red, two closely spaced bands with maxima at 2.03 and 1.94 eV; and 4) infrared, a maximum at 1.42 eV, which appears at low temperatures [14].The presence of these diverse energy levels within the band gap of $CdGa_2S_4$ may be ascribed to native structural defects, such as cadmium (Cd), gallium (Ga) and sulfur (S) interstitials or vacancies. $CdGa_2S_4$ single crystals contain a high concentration of native defects (approximately 10^{21} sm^{-3}). Additionally, antisite defects may arise from the interchange of atoms Cd_{Ga}, and Ga_{Cd} within the cationic sublattice. In our opinion, the possibility of cation interchange is due to the similar electronegativity values of cadmium (1.7 eV) and gallium (1.6 eV). Because stoichiometric voids are periodically arranged within the lattice, they do not create localized levels. However, the samples were grown using iodine as a transport agent, and its concentration can be quite high (reaching ~10^{19} cm^{-3} in $ZnIn_2S_4$, for example). By considering the influence of deviations from stoichiometric composition on sample properties, the intrinsic defect nature of deep centers in $CdGa_2S_4$ crystals has been established [13]. The intensity of the blue band increases when the crystals are enriched with cadmium atoms, a phenomenon attributed to the presence of interstitial cadmium (Cd_{int}). In $CdGa_2S_4$, these interstitial atoms form donor levels with an activation energy of approximately 0.2 eV [14]. According to [14], the blue luminescence band originates from an electronic transition from these donor levels to the valence band.

The authors of Ref. [13] suggest that the local level located 1.65 eV below the bottom of the conduction band is associated with Ga_{Cd} antisite defects. In our opinion, these centers act as fast recombination centers within the $CdGa_2S_4$ crystal lattice.

CONCLUSIONS

The optical quenching and temperature dependence of the photocurrent in $CdGa_2S_4$ single crystals were investigated. Local energy levels were identified at E_c - 0.21eV, E_c - 0.42 eV, E_c - 1.06 eV, and E_v + 0.89 eV, which are attributed to the presence of intrinsic (native) defects within the $CdGa_2S_4$ lattice. The temperature dependence of the photocurrent exhibits a maximum at 300 K. The subsequent decrease in photocurrent at temperatures above 300 K is explained by the thermal quenching of photoconductivity. Both optical and thermal quenching are attributed to the redistribution of carriers between photosensitizing and recombination centers.

ORCID

Z. Kadiroglu, https://orcid.org/0009-0001-9735-5160

REFERENCES

[1] G.B. Ibragimov, A.Sh. Mustafabeyli, and A.S. Abiyev, "Calculation of defect formation energy of point defect in $CdGa_2Se_4$," International Journal of Modern Physics B, **38**(09), 2450135 (2023). https://doi.org/10.1142/S0217979224501352

[2] I.A. Mamedova, Z.A. Jahangirli, S.S. Osmanova, and N.A. Abdullayev, "Elastic properties and regularities in frequencies of optical phonons of $A^{II}B^{III}{}_2C^{VI}{}_4$ compounds," Phys. Solid State, **66**(11), 529-536 (2024). https://doi.org/10.1134/S1063783424601322

[3] S.G. Asadullayeva, Z.A. Jahangirli, M.A. Musayev, G.Y. Eyyubov, and A.S. Abiyev, "Near-infrared photoluminescence from $ZnIn_2S_4$ layered single crystals," Phys. Solid State, **67**, 429-432 (2025). https://doi.org/10.1134/S1063783425601067

[4] S.G. Asadullayeva, and Z.A. Jahangirli, "Photoluminescence and magnetic properties of Nd-doped $ZnGa_2Se_4$," Eur. Phys. J. B, **98**, 142 (2025). https://doi.org/10.1140/epjb/s10051-025-00990-7

[5] Z. Kadiroglu, "The role of cation deficiency and impurities in the formation of photosensitivity centers in $CdIn_2S_4$ compound," Phys. Solid State, **67**, 684-687 (2025). https://doi.org/10.1134/S1063783425601079

[6] D.T. Guseinov, Z.G. Mamedov, N.E. Qasanov, and Yu.G. Asadov, "On the Two Types of Slow Recombination Centers in $CdIn_2S_4$," FTP, **21**(4), 738-741 (1987). (in Russian)

[7] D.T. Guseinov, T.G. Kerimova, and Z.L. Kadiroglu, "Effects arising from a repulsive barrier in the compound $CdIn_2S_4$," Semiconductors, **30**(6), 517-519 (1996).

[8] T.G. Kerimova, Sh. S. Mamedov, R. Kh. Nani, "On the band structure of $CdGa_2S_4$," Phys. Stat. Sol.(b),105,1, k39-44 https://doi.org/10.1002/pssb.2221050163

[9] A.N. Georgobiani, V.S. Donu, Z.P. Illyukhine, V.I. Pavlenko, and I.M. Tiginyanu, "Blue photoluminescence of cadmium thiogallate," FTP, **17**, 1524-1525 (1983). (in Russian)

[10] A. Liang, L.T. Shi, Gollego Perra, O. Gomis, D. Errandonea, L.M. Tiginyanu, V.V. Ursaki, and F.J. Manjan, "Pressure – induced band anticrossing in two adamantine ordered -vacancy compounds: $CdGa_2S_4$ and $HgGa_2S_4$," J. of Alloys and Comp. **886**, 161226 (2021). https://doi.org/10.1016/j.jallcom.2021.161226

[11] G.B. Ibragimov, A.Sh. Mustafabeyli, and A.S. Abiyev, "Defect formation energy for various charge states of point defects in $CdGa_2S_4$," Indian Journal of Physics, **97**(12), 3495-3500 (2023). https://doi.org/10.1007/s12648-023-02685-0

[12] I.A. Mamedova, Z.A. Jahangirli, and N.A. Abdullayev, "Electronic properties of $CdGa_2S_4$: Ab-initio calculations and experimental studies by spectral ellipsometry," Phys. Solid State, **66**, 365-374 (2024). https://doi.org/10.1134/S1063783424601310

[13] D.T. Guseinov, Yu.G. Asadov, Z.G. Mamedov, and N.E. Gasanov, "Impurity photoconductivity in $CdGa_2S_4$," Inorg. Mater. (Eng. Transl.), **23**, 1736-1737 (1988).
[14] A.N. Georgobiani, T.G. Kerimova, and R.A. Quliev, "Radiative recombination in $CdGa_2S_4$ single crystals," Inorg. Mater. **47**, 112-115 (2011). https://doi.org/10.1134/S0020168511020063
[15] V.Yu. Rud, Yu.V. Rud, A.A. Vaipolin, I.V. Bodnar, and N. Fernelius, "Photosensitive structure on $CdGa_2S_4$ single crystals," Semiconductors, **37**, 1283-1290 (2003). https://doi.org/10.1134/1.1626209
[16] T.G. Kerimova, Z.G. Mamedov, and A.G. Sultanova, "Stimulated impurity photoconductivity in $CdGa_2S_4$," Fizika (Baku), **6**(3), 56-58 (2000). (in Russian)
[17] Z.A. Jahangirli, T.G. Kerimova, I.A. Mamedova, N.A. Abdullayev, and N.T. Mamedov, "Ab initio Calculations of Phonon Dispersion in $CdGa_2S_4$," Phys. Solid State, **60**(11), 2305-2309 (2018). https://doi.org/10.1134/S1063783418110069
[18] Z. Kadiroglu, "Optical quenching of photoconductivity in $CdIn_2S_4$ single crystals," Transactions of National Academy of Science of Azerbaijan, Series of physics-mathematical and technical sciences, Physics and Astronomy, **XLI**(5), 121-127 (2021). (in Russian)
[19] A. Rose, *Concepts in Photoconductivity and Allied Problems*, (Interscience Publishers, New York, 1963).

ФОТОЕЛЕКТРОННІ ВЛАСТИВОСТІ МОНОКРИСТАЛІВ $CdGa_2S_4$

Зафар Кадіроглу
Інститут фізики, Міністерство науки та освіти Азербайджанської Республіки, Баку, AZ1073 Азербайджан

Було проведено експериментальні дослідження фотоелектричних властивостей монокристалів $CdGa_2S_4$. У дослідженні вивчали температурну залежність фотоструму (в діапазоні 110 – 420K), а також спектральну залежність та перехідні характеристики оптичного гасіння при T = 300 K. Оптичне гасіння фотоструму спостерігалося в діапазоні енергій вторинного світлового пучка 0,6 – 2,49 еВ. Вимірювання виявили енергетичні рівні при Ec – 0,21 еВ, Ec – 0,42 еВ та Ec – 1,06 еВ, а також сенсибілізуючі рівні при Ev + 0,89 еВ. Зменшення фотоструму при температурах вище 300 K пояснюється термічним гасінням. Як оптичне, так і термічне гасіння фотопровідності в кристалах $CdGa_2S_4$ пояснюється змінами зарядового стану та динаміки обміну сенсибілізуючих та рекомбінаційних центрів.

Ключові слова: *тіогалат кадмію; фотопровідність; дефекти; глибокі рівні; сенсибілізуючі центри; рекомбінаційні центри; оптичне гасіння; термічне гасіння*

EAST EUROPEAN JOURNAL OF PHYSICS. 1. 286-292 (2026)
DOI:10.26565/2312-4334-2026-1-33 ISSN 2312-4334

PHOTOELECTRIC PROPERTIES OF $Zn_xCd_{1-x}S$-BASED PHOTOSENSITIVE SEMICONDUCTOR STRUCTURES WITH ENHANCED ULTRAVIOLET RESPONSE

R.R. Kabulov[1], D.B. Istamov[1]*, K.T. Suyarov[2], F.A. Akbarov[3]
[1]*Physical-Technical Institute of Uzbekistan Academy of Sciences, Tashkent 100084, Uzbekistan*
[2]*Chirchik State Pedagogical University, 111700 Chirchik, Uzbekistan*
[3]*Tashkent State Technical University, 100095 Tashkent, Uzbekistan*
**Corresponding Author e-mail: istamov@uzsci.net*
Received September 19, 2025. revised January 26, 2026; accepted January 30, 2026

The work is devoted to the study of the photoelectric properties of $Au - Zn_xCd_{1-x}S - Mo$ structured films, which are photosensitive in the ultraviolet and visible regions of the electromagnetic spectrum, with maximum sensitivity in the ultraviolet region. It has been established that the spectral response of the $Au - Zn_xCd_{1-x}S - Mo$ structured films depend on the temperatures of the ZnS and CdS evaporators, which influence the composition of the photoactive $Zn_xCd_{1-x}S$ layer ($x = Zn/(Zn + Cd)$). By varying the temperature of the ZnS evaporator during the growth of the $Zn_xCd_{1-x}S$ layer, a graded $Zn_xCd_{1-x}S$ film was synthesized on a molybdenum substrate, forming the photoactive layer of the structure. The resulting photosensitive structure exhibited sensitivity in both the ultraviolet and visible regions, with a maximum in the ultraviolet. Analysis of the spectral response indicates that the photoactive layer has a graded band gap, decreasing from $E_G = 3.05 \pm 0.05\ eV$ to $E_G = 2.45 \pm 0.05\ eV$. A study of light current-voltage characteristics for monochromatic radiation showed that they are characterized by different values of the diode ideality factor (n) and reverse saturation current (J_0). The synthesized $Zn_xCd_{1-x}S$ layer can be used as a buffer layer in thin-film solar cells, such as $CdTe, CIGS$ and others, instead of the CdS layer, which will enable increasing both the short-circuit current and the open-circuit voltage of thin-film solar cells.
Keywords: *Polycrystalline films; $Zn_xCd_{1-x}S$; Spectral sensitivity; Photoelectric characteristics; Solar cells; Short circuit current; Open circuit voltage*
PACS: 72.40.+w, 73.50.Pz, 73.61.Ga, 78.40.Fy, 85.60.Dw, 88.40.hj

INTRODUCTION

Currently, the rapid development of automation in the manufacturing process and the production of environmentally friendly electric energy, achieved by directly converting solar energy into electricity, necessitates the use of semiconductor materials that are spectrally sensitive in various regions of the electromagnetic spectrum and possess essential contact properties. These requirements are met by multicomponent binary semiconductor compounds of the A_2B_6 type, formed through the chemical bonding of elements from Group II A_2 (Zn, Cd, Hg) and Group VI B_6 (O, S, Se, Te) of the periodic table of elements. Additionally, multicomponent compounds may consist of a mixture of binary semiconductors, such as $(A_2^1B_6) + (A_2^2B_6)$ [1], as well as $(A_2B_6^1) + (A_2B_6^2)$, where A_2^1 and A_2^2 represent different Group II elements, and B_6^1 and B_6^2 belong to Group VI of Mendeleev's periodic table.

Cadmium sulfide (CdS) and zinc sulfide (ZnS) belong to the A_2B_6 semiconductor family, are direct bandgap materials, and are used in various optoelectronic devices, including solar cells [2–6], transistors [7–11], light-emitting diodes (LEDs) [12–14], photocatalysis [15–16], and water-splitting devices [17].

The ternary semiconductor chemical alloy $Zn_xCd_{1-x}S$ [18], also characteristic of A_2B_6 semiconductors, exhibits variable optical and photoelectric properties in its photoactive layer due to the modification of Zn and Cd content in the alloy $Zn_xCd_{1-x}S$ (where $x = Zn/(Zn + Cd)$), leading to variations in the photoelectric characteristics of actual photosensitive structures [19-20]. The bandgap width (E_G) increases with the growth of x, ranging from 2.44 eV ($x = 0, CdS$) to 3.56 eV ($x = 1, ZnS$) [21]. As E_G changes, the spectral sensitivity of $Zn_xCd_{1-x}S$ layers and the structures based on them can vary within the wavelength range of electromagnetic radiation from 500 nm to 330 nm [22,23]. $Cd_{1-x}Zn_xS$ layers can be grown using methods such as chemical bath deposition [19–21, 24], sublimation in a quasi-closed volume [25], spray pyrolysis [18,26], hydrothermal synthesis [27], and chemical transport reactions [28-29]. The synthesized layers have been utilized in solar cells [19-20, 24-25, 31] and photodetectors [27, 30, 32].

In contrast to the methods previously mentioned, the chemical vapor transport (CVT) method [33-34] with hydrogen as the carrier gas enables the synthesis of polycrystalline layers with relatively large crystallite sizes, thereby significantly extending the lifetimes of nonequilibrium photogenerated charge carriers [28]. In this method, the synthesis of the semiconductor material occurs as a result of chemical reactions between elements in the vapor phase within a gas flow on the substrate surface. The advantage of synthesizing A_2B_6 compounds from the vapor phase via chemical transport reactions lies in the ability to obtain semiconductor materials with varied properties by controlling the temperatures of both the evaporators and the substrate during the growth of the photoactive layer. This allows for the production of high-quality crystals, very close to stoichiometry, and enables the synthesis of crystals in various modifications at low temperatures.

Cite as: R.R. Kabulov, D.B. Istamov, K.T. Suyarov, F.A. Akbarov, East Eur. J. Phys. 1, 286 (2026), https://doi.org/10.26565/2312-4334-2026-1-33

Currently, a critical issue is the alignment of the wide-bandgap front buffer layer of solar cells with their photoactive layer, not only in terms of the energy band diagram but also structurally, by matching the crystal lattice constants. This alignment would increase the conversion efficiency of the solar cell. In thin-film solar cells and photovoltaic modules such as $CdTe$ and $CIGS$, CdS layers are used as the buffer layer due to their compatibility with electron affinity (χ) and lattice constant (a_0). However, in CdS-based structures, the spectral sensitivity (S) deteriorates in the spectral region $hv > E_{gCdS}$. To improve S, it is necessary to use a buffer layer with a wider bandgap, such as ZnS. However, replacing CdS with ZnS reduces efficiency due to significant differences in χ and a_0. Thus, developing and studying $Zn_xCd_{1-x}S$ layers with bandgaps adjustable between ZnS and CdS is highly desirable. Furthermore, for registration and measurement equipment, photosensitive semiconductor structures are required with maximum spectral sensitivity in the near-ultraviolet range. The main aim of this research, therefore, was to create and investigate the spectral sensitivity and photocurrent characteristics of a photosensitive semiconductor structures based on $Zn_xCd_{1-x}S$ layers, where the bandgap could be varied (graded layer).

In this work, the synthesis of the $Zn_xCd_{1-x}S$ semiconductor compound was carried out using the chemical vapor transport method, with two separate evaporators for ZnS and CdS precursors in a gas flow [33-34]. To prevent the contamination of the growing $Zn_xCd_{1-x}S$ layer with uncontrolled impurities, the evaporators underwent thermal annealing, as did the molybdenum (Mo) substrates [35-36].

METHODS AND MATERIALS

To achieve the research objective, we synthesized the $Zn_xCd_{1-x}S$ semiconductor solid alloy, designed to have maximum photosensitivity in the short-wavelength range of the electromagnetic spectrum, using the chemical vapor transport method in a hydrogen carrier gas flow.

Figure 1 shows the setup for growing $Zn_xCd_{1-x}S$ solid solutions by the chemical vapor transport method in a hydrogen carrier gas flow: (a) from separate evaporation sources (ZnS and CdS), (b) the temperature gradient of the setup, and (c) the photodetector design with an $Au - Zn_xCd_{1-x}S - Mo$ structure.

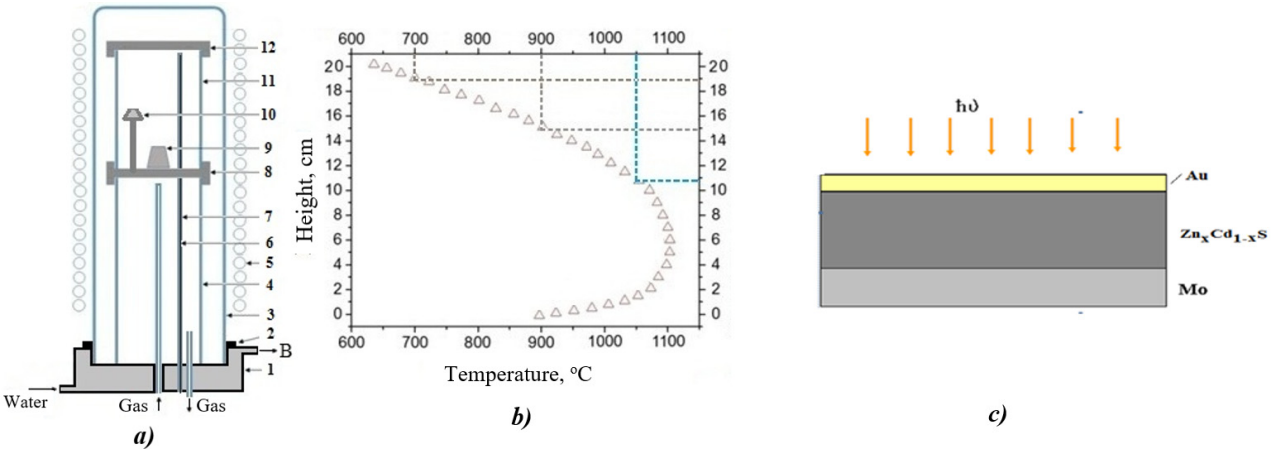

Figure 1. (a) Installation for growing the $Zn_xCd_{1-x}S$ chemical compound using the method of chemical transport reactions in a flow of hydrogen carrier gas from individual evaporation sources (ZnS and CdS), (b) temperature calibration of the installation, and (c) design of a photosensitive semiconductor structure with the $Au - Zn_xCd_{1-x}S - Mo$ configuration

At the top of the reactor, inside an inner quartz sleeve (11), are holders with substrates (12). The outer reactor casing (3) is mounted on a water-cooled flange (1), with a sealing gland (2) ensuring the reactor's airtightness. The carrier gas is supplied and vented through ports located in the lower section of the cooled flange. The quartz cup (11) is connected to a quartz stand (4) and a graphite adapter (8). The substrate temperature is measured by a thermocouple (6), which is situated within a movable quartz tube (7) affixed to the flange by a gland. Simultaneously, the quartz tube (7) serves as a fixture for the substrates. A furnace (5) is used to heat the reactor. Figure 1c illustrates the design of the fabricated photodetector with the $Au - Zn_xCd_{1-x}S - Mo$ structure. The synthesis process of the semiconductor solid solution layers was carried out on a molybdenum (Mo) substrate, approximately 150 μm thick, where Mo simultaneously served as the bottom electrical contact.

The creation of the photodetector included the preparation of substrates and initial ZnS and CdS powders. This process removed organic and inorganic contaminants as well as surface oxide layers. During the layer growth process, hydrogen purified of oxygen was used, employing the catalıoytic hydrogenation method with a chromium-nickel catalyst.

In Figure 1c, the design of the created photodetector is shown, on which investigations of photoelectric characteristics, such as spectral sensitivity [37] (Fig. 2) and photocurrent characteristics, specifically the short-circuit current versus open-circuit voltage dependency [38] (Fig. 3), were subsequently conducted.

As shown in Figure 1c, the fabricated photodetector had an $Au - Zn_xCd_{1-x}S - Mo$ structure. The photoactive $Zn_xCd_{1-x}S$ layer was approximately 10 μm thick. A semitransparent gold (Au) layer, 50 Å thick, served to create a

Schottky barrier and established an internal built-in potential generated by the difference in electron work functions between the contacting materials Au and $Zn_xCd_{1-x}S$. The gold layer also acted as the front electrical collecting contact for the photosensitive structure. The semitransparent Au contact layer was created by thermal vacuum evaporation of Au at a vacuum level of $10^{-5}\ Torr$. The effective area of the $Au - Zn_xCd_{1-x}S - Mo$ structural photodetector was $0.785\ cm^2$.

For investigating the spectral dependence of sensitivity, we utilized a research system consisting of a ZMR-3 mirror monochromator and a combined digital device (Sh-300), enabling the study of the spectral response of the photosensitive structure in the wavelength range of monochromatic radiation from $300\ nm$ to $2500\ nm$, with an accuracy of ± 10 nm for λ, 0.01% for current, and 0.1% for voltage. Monochromatic radiation penetrated the photoactive $Zn_xCd_{1-x}S$ layer through the semitransparent front Au contact, generating nonequilibrium photogenerated electron-hole pairs. These pairs were separated by the built-in electric field of the Schottky barrier ($Au/n - Zn_xCd_{1-x}S$) and were registered by the Sh-300 digital device, whose input contacts were connected to the structure's current-collecting contacts.

It is known that the photovoltaic characteristics of thin-film polycrystalline photodiodes are similar to those of $p - n$ junction photodiodes made from monocrystalline semiconductors. Specifically, the short-circuit current (J_{sc}) and open-circuit voltage (V_{oc}) increase with the rising power (P) of the incident light. J_{sc} increases linearly with P, while V_{oc} increases sublinearly in a logarithmic fashion with P [41]. The light current-voltage characteristic ($I - V$ curve), the J_{sc} (V_{oc}) dependence for $p - n$ junction photodiodes, can be expressed by formula (1) [42]:

$$V_{oc} = \frac{nkT}{q}\left(ln\frac{I_{sc}}{J_0} + 1\right), \tag{1}$$

where, n is the diode ideality factor, J_0 is the diode saturation reverse current, k is the Boltzmann constant, and q is the electron charge. The similarity in the photovoltaic properties of various photovoltaic structures (such as $p - n$ junctions, Schottky barriers, and heterostructures) mentioned above suggests that the electricity generation process under electromagnetic radiation is due to the internal electric potential of the $p - n$ junction.

The dependence of the photogenerated short-circuit current (J_{sc}) on the open-circuit voltage (V_{oc}) was studied under monochromatic illumination at different wavelengths: $\lambda_1 = 390\ nm\ (UV)$, $\lambda_2 = 460\ nm$ (blue), and $\lambda_3 = 500\ nm$ (green). The Sh-300 combined digital device was used to register the values of the photogenerated J_{sc} and V_{oc}. Its input contacts were connected to the structure's current-collecting contacts, with measurement precision at 0.01% for current and 0.1% for voltage. Since the $Zn_xCd_{1-x}S$ semiconductor layer will have different absorption coefficients (α) at various wavelengths (λ), investigating the photocurrent characteristics will provide valuable information about the photoactive layer's performance in the $Au - Zn_xCd_{1-x}S - Mo$ photodetector structure.

RESULTS AND DISCUSSION

Figure 2 presents the experimental results of the spectral photoresponse (S, in relative units) of the $Au - Zn_xCd_{1-x}S - Mo$ structure, measured at $T = 300\ K$. It is evident that the photoresponse of the fabricated $Au - Zn_xCd_{1-x}S - Mo$ structure spans the spectral range from $300\ nm$ to $500\ nm$, covering the ultraviolet region to the green part of the visible spectrum. The maximum sensitivity region is located near the wavelength of $360\ nm$.

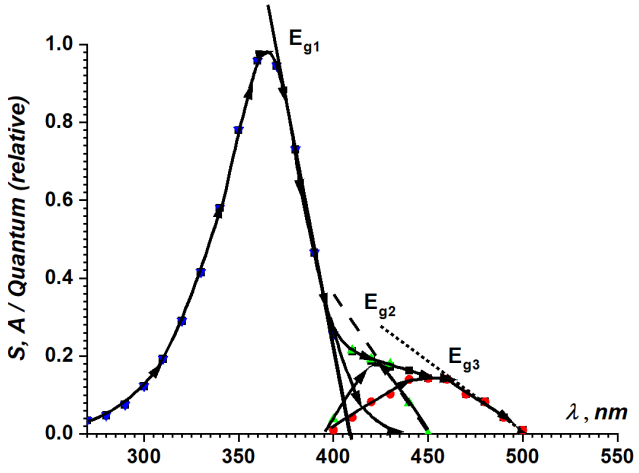

Figure 2. Spectral sensitivity of the $Au - Zn_xCd_{1-x}S - Mo$ structure, at $T = 300K$

To obtain the $Zn_xCd_{1-x}S$ layer with the spectral sensitivity shown in Figure 2, the following technological process parameters were applied: substrate temperature $T_{sub} = 923\ K$. The temperature of the evaporator for CdS powder during the entire process was maintained at $T_{evap,CdS} = 1023\ K$, and the hydrogen flow rate was set between $1.5 - 2\ L/hour$. The ZnS evaporator temperature ($T_{evap,ZnS}$) was varied throughout the process. The complete growth process for the $Zn_xCd_{1-x}S$ layer took approximately 30 minutes.

In the initial 5 minutes, $T_{evap,\,ZnS}$ was kept at around 1173 K for the next 5 minutes, it was raised to 1223 K and in the final 20 minutes, it was held at 1348 K During the first 5 minutes, due to the significantly lower evaporation temperature of CdS compared to ZnS, the growth of the $Zn_xCd_{1-x}S$ layer on the molybdenum substrate surface primarily occurred with a higher CdS content. In the subsequent 5 minutes, the temperature of the ZnS evaporator was increased by 323 K leading to the growth of a $Zn_xCd_{1-x}S$ layer with a relatively higher ZnS content. For the final 20 minutes, the ZnS evaporator temperature remained relatively high, and, as evident from Figure 2, the highest spectral sensitivity was achieved in a layer with a larger bandgap.

The experimental results of the spectral photoresponse dependence (Fig. 2) were analyzed using the photoresponse method [39,40]. Gaussian spectral sensitivity profiles of the layers contributing to the overall spectral sensitivity of the photosensitive structure were examined, considering the long-wavelength sections, and the bandgap widths of the layers formed during changes in $T_{evap,\,ZnS}$ were estimated. It was concluded that three photoactive $Zn_xCd_{1-x}S$ semiconductor layers with bandgaps of $E_{g1} \approx 3.05 \pm 0.05\ eV$, $E_{g2} \approx 2.75 \pm 0.05\ eV$ and $E_{g3} \approx 2.45 \pm 0.05\ eV$ contribute to the formation of the spectral sensitivity dependence of the $Au - Zn_xCd_{1-x}S - Mo$ photodetector structure. The photoactive $Zn_xCd_{1-x}S$ layer in the $Au - Zn_xCd_{1-x}S - Mo$ photodetector consisted of three $Zn_xCd_{1-x}S$ layers with three distinct x values: $x_1 \approx 0.6$, $x_2 \approx 0.38$, $x_3 \approx 0$ [1].

The experimental light $I - V$ characteristics, that is, the dependence of J_{sc} on V_{oc}, are presented in Figure 3. As mentioned earlier, the light $I - V$ characteristics of the $Au - Zn_xCd_{1-x}S - Mo$ photodetector structure were investigated under monochromatic illumination at wavelengths $\lambda_1 = 390\ nm$ (1), $\lambda_2 = 460\ nm$ (2), $\lambda_3 = 500\ nm$ (3). Due to the differences in photon energies, these monochromatic radiations are absorbed in different regions of the photoactive layer in the $Au - Zn_xCd_{1-x}S - Mo$ structure.

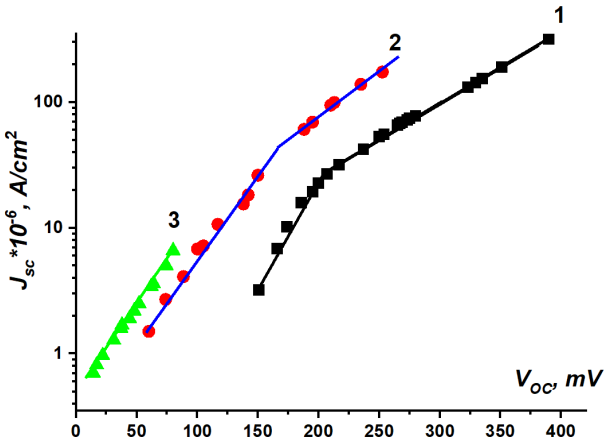

Figure 3. Light current-voltage characteristics of a photodetector with the $Au - Zn_xCd_{1-x}S - Mo$ structure, illuminated with monochromatic light with wavelengths $\lambda = 390\ nm$ (1), 460 nm (2) and 500 nm (3)

From the experimental results presented in Figure 3, it is evident that the light $I - V$ characteristics, specifically the dependence of $ln(J_{sc})$ on V_{oc} for the $Au - Zn_xCd_{1-x}S - Mo$ photodiode under illumination with different wavelengths, occupy different regions of the $I - V$ curve and display two slopes, n_1 and n_2. This contrasts with the dependence under condition 3, where the structure was illuminated with $\lambda_3 = 500\ nm$, and sufficient illumination conditions were not achieved to produce a second region with slope n_2.

The calculated results for $n_{1,2}$ and $J_{01,02}$ for different sections of the $I - V$ curve under illumination with various wavelengths are shown in the table. These results indicate that, in the first region, n_1 is close to unity for all wavelengths, suggesting a diffusion-based photogeneration mechanism and low values for J_{01}. This implies that at low illumination levels, the $Au - Zn_xCd_{1-x}S - Mo$ photodetector structure exhibits good diode characteristics [43]. As the illumination level increases, regions with n_2 and J_2 values appear. The values of n_2 and J_2 are higher compared to n_1 and J_1, indicating a degradation in the photo-detection characteristics of the $Au - Zn_xCd_{1-x}S - Mo$ photodetector due to enhanced recombination effects of nonequilibrium photogenerated charge carriers in both the quasi-neutral regions of the structure and the space-charge regions [44]. This degradation in photovoltaic characteristics suggests photo-induced formation of recombination centers within the photoactive part of the $Au - Zn_xCd_{1-x}S - Mo$ structure [45].

In the fabricated $Au - Zn_xCd_{1-x}S - Mo$ structural photodiode, the photoactive layer consists of multiple $Zn_xCd_{1-x}S$ sub-layers. During the growth of the $Zn_xCd_{1-x}S$ photoactive layer, as the evaporator temperature for ZnS changed, photoactive sub-layers were synthesized with different compositions (x), thicknesses (d), bandgaps (E_g), and concentrations of majority charge carriers (n). Radiation with $\lambda_1 = 390\ nm$ ($hv \approx 3.2\ eV$) is effectively absorbed by the layer near the front Au contact, with $E_{g1} = 3.05 \pm 0.05eV$ and $x = 0.6$. In this case, $n_1 \approx 1$, indicating a diffusion mechanism of photogeneration, and J_{01} has the lowest value, reflecting the wide bandgap of this layer. As the radiation intensity at a wavelength of 390 nm increases, the concentration of photogenerated charge carriers also increases. This leads to the formation of photo-stimulated defect states [45-46], which enhance the recombination of nonequilibrium

photogenerated carriers, increasing the diode ideality factor to $n_2 \approx 3$. This indicates that defect states form on the surface of the $Zn_xCd_{1-x}S$ photoactive layer, with J_{02} also increasing and $J_{02} > J_{01}$ [40, 41].

Table 1. Parameters of the current-voltage characteristic of the $Au - Zn_xCd_{1-x}S - Mo$ photodetector: $n_{1,2}$ - ideality coefficient of the diode and $J_{01,02}$ - the value of the reverse saturation current of the diode, when illuminated with light of different wavelengths

no.	$\lambda = 390\ nm$	$460\ nm$	$500\ nm$
n_1	1.04	1.24	1.2
n_2	3	1.4	–
$J_{01}, A/cm^2$	1×10^{-8}	2.1×10^{-7}	4.5×10^{-7}
$J_{02}, A/cm^2$	1.87×10^{-6}	1.1×10^{-6}	–

When illuminated at $\lambda_2 = 460\ nm$ $(hv \approx 2.7\ eV)$, the layers participating in photogeneration are those with $Zn_xCd_{1-x}S$ values of $x = 0.38$; $E_{g2} = 2.75 \pm 0.05eV$, and $x = 0$; $E_{g3} = 2.5 \pm 0.05\ eV$. At low radiation intensities, photogeneration occurs by a generation-recombination mechanism with $n_1 = 1.24$. The value $J_{01}(\lambda = 460\ nm) > J_{01}(\lambda = 390\ nm)$ because $E_{g1}(3.05\ eV) > E_{g2}(2.75\ eV)$. As the power of the radiation increases, photo-stimulated recombination intensifies [45-46], leading to an increase in n_2, where $n_2 > n_1$ and $J_{02} > J_{01}$.

Under illumination with $\lambda_3 = 500\ nm$ $(hv \approx 2.48\ eV)$, photons are absorbed by the thin $x = 0$ layer with $E_{g3} = 2.45 \pm 0.05eV$. As a result, the concentration of photogenerated charge carriers is relatively low. Here, $n1 \approx 1.2$, indicating that photogeneration occurs by a generation-recombination mechanism. $J_{01}(\lambda = 500\ nm) > J_{01}(\lambda = 460\ nm)$ because $E_{g2}(2.75\ eV) > E_{g3}(2.5\ eV)$. A second region with n_2 does not arise due to the low concentration of photogenerated charge carriers. The parameters of the light $I - V$ characteristics are similar to those under $\lambda = 460\ nm$ illumination, but the values of J_{sc} and V_{oc} are lower than for higher-energy photons.

Currently, the high conversion efficiency of commercially available polycrystalline thin-film photovoltaic modules, such as $CdTe$ and $CIGS$, is achieved using cadmium sulfide (CdS) as the buffer layer [47,48], with $E_g \approx 2.45\ eV$ [2]. Consequently, the spectral sensitivity of solar cells is very low in the region where $hv > 2.5\ eV$. An analysis of the energy band diagram [49] has shown that using a wider bandgap ZnS as a buffer layer does not produce the desired increase in conversion efficiency due to the difference in electron affinity between the contact materials ($\Delta\chi$). To reduce $\Delta\chi$ and further improve conversion efficiency, employing a $Zn_xCd_{1-x}S$ layer with an E_g that varies from approximately 3.1 eV to $E_g(CdS) = 2.5\ eV$ may yield the desired results. This replacement could lead to increased short-circuit current and open-circuit voltage in thin-film solar cells based on $CdTe$ and CIGS.

CONCLUSIONS

Using the chemical vapor transport method with two evaporators for ZnS and CdS precursors in a hydrogen flow, $Zn_xCd_{1-x}S$ layers were synthesized. By adjusting the ZnS evaporator temperature during the growth of the photoactive layer, an $Au - Zn_xCd_{1-x}S - Mo$ photosensitive structure was fabricated, which is sensitive in the ultraviolet and green regions of the visible spectrum and exhibits peak sensitivity at a wavelength of $360\ nm$. It was determined that the photoactive layer in the fabricated photodetector is a graded bandgap structure, consisting of $Zn_xCd_{1-x}S$ layers with $E_{g1} = 3.05 \pm 0.05eV$, $E_{g2} = 2.75 \pm 0.05eV$, and $E_{g3} = 2.45 \pm 0.05eV$. Investigations of the light $I - V$ characteristics under monochromatic illumination revealed that they are characterized by varying values of the diode ideality factor (n) and saturation reverse current (J_0). The synthesized $Zn_xCd_{1-x}S$ layer could serve as a buffer layer in thin-film solar cells, such as those based on $CdTe$ and CIGS, as a replacement for CdS, potentially enhancing both short-circuit current and open-circuit voltage in thin-film solar cells.

Acknowledgements

The authors express their gratitude to the staff of the Laboratory of Semiconductor Devices of the Physical-Technical Institute of the Academy of Sciences of the Republic of Uzbekistan for their assistance during the research process and for their advice on discussing the results of the research.

The work was carried out within the framework of the basic funding program for fundamental research of the Physical-Technical Institute of the Academy of Sciences of the Republic of Uzbekistan.

ORCID

Damir B. Istamov, https://orcid.org/0009-0007-4654-1880

REFERENCES

[1] B. Liu, J. Li, W. Yang, X. Zhang, X. Jiang, and Y. Bando, "Semiconductor Solid-Solution Nanostructures: Synthesis, Property Tailoring, and Applications," **13**(45), 1701998 (2017). https://doi.org/10.1002/smll.201701998

[2] Y.Y. Zhan, Z.B. Shao, T.H. Jiang, J. Ye, X.F. Wu, B.C. Zhang, K. Ding, D. Wu, and J.S. Jie, "Cation exchange synthesis of two-dimensional vertical Cu_2S/CdS heterojunctions for photovoltaic device applications," J. Mater. Chem. A, **8**, 789 (2020). https://doi.org/10.1039/C9TA11304E

[3] A. Bosio, G. Rosa, and N. Romeo, "Past, present and future of the thin film CdTe/CdS solar cells," Solar Energy, **175**(11), 31-43 (2018). http://dx.doi.org/10.1134/S1063783412090193

[4] V. Bermudes, "On overview on electrodeposited Cu(In,Ga) $(Se,S)_2$ thin films for photovoltaic devices," Solar Energy, **175**, 2-8 (2018). http://dx.doi.org/10.1134/S1063783412090193
[5] T. Kato, J.-L. Wu, Y. Hirai, H. Sugimoto, and V. Bermudez, "Record Efficiency for Thin-Film Polycrystalline Solar Cells Up to 22.9% Achieved by Cs-Treated Cu(In,Ga)$(Se,S)_2$," IEEE Journal of Photovoltaics, **9**(1), 325-330 (2018). https://doi.org/10.1109/JPHOTOV.2018.2882206
[6] S.-Y. Wei, Y.-C. Liao, C.-H. Hsu, C.-H. Cai, W.-C. Huang, M.-C. Huang, and C.-H. Lai, "Achieving high efficiency $Cu_2ZnSn(S,Se)_4$ solar cells by non-toxic aqueous ink: Defect analysis and electrical modeling," Nano Energy, **26**, 74-82 (2016). http://dx.doi.org/10.1134/S1063783412090193
[7] M.S. De Urquijo-Ventura, M.G.S. Rao, S. Meraz-Davila, J.A. Torres-Ochoa, M.A. Quevedo-Lopez, and R. Ramirez-Bon, "PVPS iO2 and PVP-TiO2 hybrid films for dielectric gate applications in CdS-based thin film transistors," Polymer, **191**, 122261 (2020). https://doi.org/10.1016/j.polymer.2020.122261
[8] D.B. Istamov, O.A. Abdulkhayev, Sh.M. Kuliyev, N. Abdullayev, A.Sh. Ashirov, and D.M. Yodgorova, "Temperature response curve of silicon diode temperature sensors," East Eur. J. Phys. (2), 287-291 (2025), https://doi.org/10.26565/2312-4334-2025-2-35
[9] R.R. Bebitov, O.A. Abdulkhaev, D.M. Yodgorova, D.B. Istamov, G.M. Hamdamov, Sh.M. Kuliyev, A.A. Khakimov and A.Z. Rakhmatov, "Dependence of the accuracy of the silicon diode temperature sensors for cryogenic thermometry on the spread of their parameters," Low Temperature Physics, 49(2), 277–282 (2023). https://doi:10.1063/10.0016843
[10] R.R. Bebitov, O.A. Abdulkhaev, D.M. Yodgorova, D.B. Istamov, Sh.M. Kuliyev, A.A. Khakimov, A.B. Bobonazarov, et al. "Distribution of impurities in base-depleted region of diode temperature sensor," Low Temperature Physics, 50(5), 418–424 (2024). https://doi.org/10.1063/10.0025635
[11] J. Meza-Arroyo, K.C.S. Reddy, M.G.S. Rao, F. Garibay-Martínez, M.S. de Urquijo-Ventura, and R. Ramírez-Bon, "Solution-based CdS thin film transistors with low temperature-processed Al2O3-GPTMS-PMMA as hybrid dielectric gate," Semiconductor Science and Technology, **36**, 045015 (2021). https://doi.org/10.1088/1361-6641/abe01c
[12] Y.B. Zhang, F.J. Zhang, H.Z. Wang, L. Wang, F.F. Wang, Q.L. Lin, H.B. Shen, and L.S. Li, "High-efficiency CdSe/CdS nanorod-based red light-emitting diodes," Optics Express, **27**, 7935 (2019). https://doi.org/10.1364/OE.27.007935
[13] T. Duan, J. Ai, S. Chen, G. He, X. Guo, L. Han, S. Che, and Y. Duan, "Chiral CdSe/CdS quantum dot (in rod)-light-emitting diodes with circularly polarized electroluminescence," Nano Rasearch, **15**(10), 9573-9577 (2022). https://doi.org/10.1007/s12274-022-4536-7
[14] D.B. Istamov, O.A. Abdulkhayev, and S.M. Kuliyev, "Limiting characteristics of silicon diode temperature sensors for determining the maximum temperature with specified measurement accuracy," UNEC J. Eng. Appl. Sci. **5**(1), 63-69 (2025). https://doi.org/10.61640/ujeas.2025.0507
[15] G.Z. Wang, L.X. Gong, Z.F. Li, B. Wang, W.L. Zhang, B.F. Yuan, T.W. Zhou, *et al*., "A two-dimensional CdO/CdS heterostructure used for visible light photocatalysis," Physical Chem. Chemical Physics, **22**(17), 9587-9592 (2020). https://doi.org/10.1039/D0CP00876A
[16] J.M. Hwang, M.O. Oh, I. Kim, J.K. Lee, and C.S. Ha, "Preparation and characterization of ZnS based nano-crystalline particles for polymer light-emitting diodes," Current Applied Physics, **5**(1), 31-34 (2005). https://doi.org/10.1016/.j.cap.2003.11.075
[17] X.C. Yu, Q.Q. Xing, X.P. Zhang, H.L. Jiang, and F.R. Cao, "Photoelectrochemical water splitting using TiO_2 nanorod arrays coated with Zn-doped CdS," Journal of Materials Science, **56**(18), 11059 (2021). https://doi.org/10.1007/s10853-021-06008-8
[18] S. Joishy, DD.N. Hebbar, S.D. Kulkarni, K.G. Rao, and B.V. Rajendra, "Band structure controlled solid solution of spray deposited Cd1-xZnxS films: investigation on photoluminescence and photo response properties," Physica B Condensed Matter, **586**, 412143 (2020). https://doi.org/10.1016/j.physb.2020.412143
[19] K.M. McPeak, B. Opasanont, T. Shibata, D.K. Ko, M.A. Becker, S. Chattopadhyay, H.P. Bui, *et al*., "Microreactor chemical bath deposition of laterally graded Cd1-xZnxS thin films: a route to high through put optimization for photovoltaic buffer layers," Chemistry of Materials, **25**(3), 297–306 (2013). https://doi.org/10.1021/cm3023506
[20] S.Z. Werta, O.K. Echendu, K.O. Egbo, and F.B. Dejene, "Electrochemical deposition and characterization of thin-film $Cd_{1-x}Zn_xS$ for solar cell application: the effect of cathodic deposition voltage," Thin Film Solids, **689**, 137511 (2019). https://doi.org/10.1016/j.tsf.2019.137511
[21] M. Isik, M. Terlemezoglu, S. Isik, K. Erturk, and N.M. Gasanly, "The effect of Zn concentration on the structural and optical properties of Cd1-xZnxS nanostructured thin films," J Mater. Sci: Mater. Electron. **32**, 25225–25233 (2021). https://doi.org/10.1007/s10854-021-06980-6
[22] R.R. Kabulov, L.O'. Shuhratova, K.T. Suyarov, F.A. Akbarov, D.B. Istamov. Structural, Compositional, and Photoluminescence Properties of CsPbBr3 Thin Films Grown by Single-source Thermal Vacuum Chemical Vapor Deposition. e-Journal of Surface Science and Nanotechnology 23. 364–367 (2025). https://doi.org/10.1380/ejssnt.2025-051
[23] R.R. Kobulov, M.A. Makhmudov, S.Y. Gerasimenko, and O.K. Ataboev, "Morphology and Current Transport in a Thin-Film Polycrystalline Au–$Zn_xCd_{1-x}S$–Mo Structure with Wide Photosensitivity Range in the Ultraviolet and Visible Radiation Spectral Region," Applied Solar Energy, **54**(4), 251–254 (2018). https://doi.org/10.3103/S0003701X18040084
[24] S.Z. Werta, O.K. Echendu, K.O. Egbo, and F.B. Dejene, "Electrochemical deposition and characterization of thin-film $Cd_{1-x}Zn_xS$ for solar cell application: the effect of cathodic deposition voltage," Thin Film Solids, **689**, 137511 (2019). https://doi.org/10.1016/j.tsf.2019.137511
[25] M. Zakria, A. Mahmood, A. Shah, Q. Raza, T.M. Khan, and E. Ahmed, "Tunability of physical properties of (Cd:Zn)S thin film by close space sublimation process (CSSP)," Prog. Nat. Sci. **22**, 281 (2012). https://doi.org/10.1016/j.pnsc.2012.07.006
[26] M. Shkir, M. Anis, S.S. Shaikh, M.S. Hamdy, and S. AlFaify, "Impact of Se doping on optical and third-order nonlinear optical properties of spray pyrolysis fabricated CdS thin films for optoelectronics," Appl. Phys. B, **127**, 121 (2020). https://doi.org/10.1007/s00340-020-07472-x
[27] J. Mathew, S. Devasia, S. Shaji, and E.I. Anila, "Metal–semiconductor–metal visible photodetector based on Al-doped $(Cd:Zn)$S nano thin films by hydrothermal synthesis," Optik, **241**, 166878 (2021). https://doi.org/10.1016/j.ijleo.2021.166878
[28] Sh.A. Mirsagatov, A.K. Uteniyazov, and A.S. Achilov, Physics of the Solid State, **54**, (2012). http://dx.doi.org/10.1134/S1063783412090193

[29] N.K. Abrikosov, V. F. Bankina, L.V. Poretskaya, L.E. Shelimova, and E.V. Skudnova, "AIIBVI Compounds," in: Semiconducting II–VI, IV–VI, and V–VI Compounds, (Springer Science+Business Media, New York, 1969), pp.1-64. https://doi.org/10.1007/978-1-4899-6373-4_1
[30] S.Yu. Pavelets, Yu.N. Bobrenko, T.V. Semikina, B.S. Atdaev, G.I. Sheremetova, and M.V. Yaroshenko, "Ultraviolet sensors based on $Zn_xCd_{1-x}S$ Solid solutions," Ukrainian Journal of physics, **64**(4), 308 (2019). https://doi.org/10.15407/ujpe64.4.308
[31] D. Lilhare, and A. Khare, "Temperature dependent characterizations of chemically deposited $(Cd_x\text{-}Zn_{1-x})S$ nanocrystalline films for solar cell applications," Optical Materials, **108**, 110385 (2020). https://doi.org/10.1016/j.optmat.2020.110385
[32] B. Barman, K.V. Bangera, G.K. Shivakumar, "$Zn_xCd_{1-x}S$ thin films: A study towards its application as a reliable photodetector," Superlattices and Microstructures, **137**, 106349 (2020). https://doi.org/10.1016/j.spmi.2019.106349
[33] Sh.A. Mirsagatov, and A.A. Mavlonov, "High Efficiency UV Photocells Based on $Zn_xCd_{1-x}S$ Solid Solutions," Applied Solar Energy, **48**(1), 51–54 (2012). https://doi.org/10.3103/S000 3701X12010100
[34] R.R. Kobulov, M.A. Maxмudov, and S.Yu. Gerasimenko, "Fabrication and investigation of ultravialet Au-ZnxCd1–xS-Mo-structures," Applied Solar Energy, **53**(1), 10-12 (2017). https://doi.org/10.3103/S0003701X1701008X
[35] Sh.A. Mirsagatov, A.Yu. Leiderman, and O.K. Ataboev, "Mechanism of Charge Transfer in Injection Photodiodes Based on the In–n+CdS–*n*CdS_xTe_{1-x}–*p*$Zn_xCd_{1-x}Te$–Mo Structure," Physics of the Solid State, **55**(8), 1635–1646 (2013). https://doi.org/10.1134/S1063783413080192
[36] R.R. Kobulov, M.A. Maxмudov, and S.Yu. Gerasimenko, "Fabrication and investigation of ultravialet Au-ZnxCd1–xS-Mo-structures, Applied Solar Energy, **53**(1), 10-12 (2017). https://doi.org/10.3103/S0003701X1701008X
[37] S.M. Sze, and K.Ng. Kwok, *Physics of Semiconductor Devices*, 3rd ed., (John Wiley & Sons, Inc., Hoboken, New Jersey, 2007).
[38] M. Grandman, "*The Physics of Semiconductors*", Second Edition, (Springer – Verlag, Berlin, Heydelberg. 2010).
[39] K. Ohata, I. Saraie, and J. Tanaka, Jap. J. Appl. Phys. **12**(10), 1641-1642 (1973). https://doi.org/10.1143/jjap.12.1641
[40] Farrukh Akbarov; Rustam Kabulov; Anvar Alimov; Erkin Abduraimov; Dildora Nasirova. Dependence of output parameters of photovoltaic module based on CIGS solar cells on external temperatures. AIP Conf. Proc. 3331, 040046 (2025). https://doi.org/10.1063/5.0305885
[41] R.R. Kabulov, M.A. Makhmudov, M.U. Khajiev, and O.K. Ataboev, "The Study of Factors that Influence on the Effectiveness of the Photoconversion of n-CdS/p-CdTe Heterostructures," Applied Solar Energy, **52**(1), 61–67 (2016). https://doi.org/10.3103/s0003701x16010047
[42] S.M. Sze, "*Semiconductor Devices. Physics & Technology*", 3rd ed. (John S. Wiley & Sons, Inc., New York, 2002).
[43] R.R. Kabulov, N.A. Matchanov, and B.R. Umarov, "Features of load current–voltage characteristics of a monocrystalline silicon solar cell at various levels of solar illumination," Applied Solar Energy, **53**(4), 297–298 (2016). https://doi.org/10.3103/S0003701X16010047
[44] Sh.A. Mirsagatov, R.R. Kabulov, and M.A. Makhmudov, "Injection Photodiode Based on an *n*-CdS/*p*-CdTe Heterostructure," Semiconductors, **47**(6), 825–830 (2013). https://doi.org/10.1134/S106378261306016X
[45] R.R. Kabulov, S.Y. Gerasimenko, and F.A. Akbarov, "Effect of Solar Radiation of Different Power on the Internal Amplification of the Primary Photocurrent in Heterostructures Based on Cadmium Telluride," Applied Solar Energy, **59**(2), 118–124 (2023). https://doi.org/10.3103/S0003701X22601065
[46] A.Yu. Leiderman, and M.M. Kashaev, "Lifetime specifics of nonequilibrum carriers in photoelectric cells based on gallium arsenide obtained via the Czochralski method," Applied Solar Energy, **49**(4), 244-247 (2013). https://doi.org/10.3103/s0003701x13040105
[47] M.A. Green, "Solar cell efficiency tables (Version 60)," Prog. Photovoltaics Res. Appl. **30**, 687–701 (2022). https://doi.org/10.1002/pip.3595
[48] A.G. Komilov, R. Kabulov, B.E. Egamberdiev, Y.Z. Nasrullayev, and F.A. Akbarov, "The Result of Successive Exposure to Reverse and Forward Bias on the Electrophysical Characteristics of ZnO:Al/i-ZnO/CdS/CuIn1 –xGax(S, Se)2/Mo Structure Solar Cells," Applied Solar Energy, **58**(4), 476-481 (2022). https://doi.org/10.3103/S0003701X22040090
[49] R.R. Kabulov, "Features of a $Zn_xCd_{1-x}S$ Buffer Layer for Use in Thin-Film Solar Cells in the Context of a Literature Review," Applied Solar Energy, **56**(5), 383–387 (2020). https://doi.org/10.3103/S0003701X20050096

ОСОБЛИВОСТІ ФОТОЕЛЕКТРИЧНИХ ХАРАКТЕРИСТИК ФОТОДЕТЕКТОРА НА ОСНОВІ ШАРІВ $Zn_xCd_{1-x}S$ З МАКСИМАЛЬНОЮ ФОТОЧУТЛИВІСТЮ В УЛЬТРАФІОЛЕТОВОМУ ДІАПАЗОНІ

Р.Р. Кабулов[1], Д.Б. Істамов[1], К.Т. Суяров[2], Ф.А. Акбаров[3]
[1]*Фізико-технічний інститут Академії наук Узбекистану, Ташкент 100084, Узбекистан*
[2]*Чирчикський державний педагогічний університет, 111700 Чирчик, Узбекистан*
[3]*Ташкентський державний технічний університет, 100095 Ташкент, Узбекистан*

Робота присвячена дослідженню фотоелектричних властивостей структурованих плівок Au–$Zn_xCd_{1-x}S$–Mo, які є фоточутливими в ультрафіолетовій та видимій областях електромагнітного спектра з максимальною чутливістю в ультрафіолетовій області. Встановлено, що спектральний відгук структурованих плівок Au–$Zn_xCd_{1-x}S$–Mo залежить від температур випарників ZnS і CdS, які впливають на склад фотоактивного шару $Zn_xCd_{1-x}S$ (x = Zn/(Zn + Cd)). Зміною температури випарника ZnS під час росту шару $Zn_xCd_{1-x}S$ на молібденовій підкладці було синтезовано градієнтний шар $Zn_xCd_{1-x}S$, який формує фотоактивний шар структури. Отримана фоточутлива напівпровідникова структура проявляє чутливість в ультрафіолетовій та видимій областях спектра з максимумом в ультрафіолетовому діапазоні. Аналіз спектрального відгуку показує, що фотоактивний шар має градієнтну заборонену зону, яка зменшується від E_G = 3,05 ± 0,05 еВ до E_G = 2,45 ± 0,05 еВ. Дослідження світлових вольт-амперних характеристик за монохроматичного опромінення показало, що вони характеризуються різними значеннями коефіцієнта неідеальності діода (n) та зворотного струму насичення (J_0). Синтезований шар $Zn_xCd_{1-x}S$ може бути використаний як буферний шар у тонкоплівкових сонячних елементах, таких як CdTe, CIGS та інших, замість шару CdS, що дозволяє підвищити як струм короткого замикання, так і напругу холостого ходу тонкоплівкових сонячних елементів.

Ключові слова: *полікристалічні плівки; $Zn_xCd_{1-x}S$; спектральна чутливість; фотоелектричні характеристики; сонячні елементи; струм короткого замикання; напруга холостого ходу*

EAST EUROPEAN JOURNAL OF PHYSICS. 1. 293-301 (2026)
DOI:10.26565/2312-4334-2026-1-34 ISSN 2312-4334

MODELING THE TEMPERATURE AND MAGNETIC FIELD DEPENDENCE OF THE BAND GAP IN NARROW-ZONE QUANTUM WELL SEMICONDUCTORS

U.I. Erkaboev[1]*, U.Sh. Turdiev[2], M.G. Dadamirzaev[1], R.G. Rakhimov[1], Sh.X. Utkirov[2]
[1]*Namangan State Technical University,160115 Namangan, Uzbekistan*
[2]*Tashkent Institute of Chemical Technology, Yangiyer Branch, 121001 Sirdarya, Uzbekistan*
**Corresponding author: erkaboev1983@gmail.com*
Received September 19, 2025; revised December 13, 2025; accepted December 20, 2025

The fundamental physical parameter of both bulk and low-dimensional semiconductor structures is the band gap (E_g^{3d}, E_g^{2d}), whose energetic width allows the prediction of the operational parameters of semiconductor-based devices in advance. Therefore, the determination of E_g^{3d} and E_g^{2d} (in cases where the band gap of newly synthesized materials is not known) is considered one of the primary tasks in semiconductor heterostructure technology. Furthermore, another important feature of E_g is its strong sensitivity to external influences. Indeed, variations in E_g resulting from such effects can fundamentally alter the physical and chemical properties of semiconductor devices.
Keywords: *Semiconductor; Conductivity; Quantum well; Magnetoresistance; Magnetic field*
PACS: 73.63.Hs, 73.21.Fg, 73.21.−b

INTRODUCTION

There are several methods to determine the dependence of the band gap of semiconductors on external factors [1-14]. In particular, in works [15-21], a methodology for determining $E_g(T)$ was proposed based on the model of the temperature dependence of surface state density. In this approach, a mechanism for explaining $E_g(T)$ was developed through the penetration of the "tail" of the density of states into the forbidden gap with increasing temperature. However, these works did not examine the influence of a quantizing magnetic field. In works [22-27], the dependence of the band gap of bulk and quantum-dimensional semiconductors on temperature, magnetic field, and hydrostatic pressure was studied. In particular, in work [28], $E_g^{3d}(B,T)$ was theoretically calculated by changing the allowed bands of bulk semiconductor structures with temperature and magnetic field. It was proved that when the $B \to 0$ condition is met, it turns into$E_g^{3d}(B,T) \to E_g\ (T)$, that is, classical methods. This theory is mainly suitable for wide-bandgap 3D materials. In work [29], a model was developed for $E_g^{2d}(B,T,d)$ in quantum well semiconductors obeying the parabolic dispersion law. A mechanism was proposed for describing the variation of the conduction band minimum and valence band maximum (i.e., the band edges) of a rectangular quantum well as a function of quantizing magnetic field and temperature. The $E_g^{2d}(B,T,d)$ model was proposed as a result of the tail of $N_{cs}^{2d}(B,T,d)$ and $N_{vs}^{2d}(B,T,d)$ entering E_g^{2d}. In this case, the $E_g^{2d}(B,T,d)$ of wide-gap quantum well semiconductors were also determined.

In addition, in work [30], the dependence of the energy density of states of the conduction band of narrow-zone semiconductor materials on magnetic field and temperature was theoretically determined. In this work, an analytical expression for the nonparabolic dispersion law $N_{cs}^{3d(n)}(B,T)$ was derived. The experimental results were interpreted for different T using the obtained theoretical reports. However, in these works, a perfect mathematical model for determining $N_{vs}^{2d(n)}$, $N_{cs}^{2d(n)}$ was not developed.

The main purpose of the work:

- To develop a method for determining the dependence of the allowed bands $N_{vs}^{2d(n)}$ and $N_{cs}^{2d(n)}$ of narrow-zone quantum well semiconductors on the magnetic field B and temperature T.

- To determine the dependence of the forbidden band width of a narrow-zone quantum well on the magnetic field B and temperature T using this method.

MODEL

Effect of magnetic field on the energy of light holes at the valence band ceiling of a narrow-band quantum well

The problem is treated within a simplified multiband approximation, where the interaction between conduction, light-hole, and split-off bands is considered. This terminology avoids the misleading interpretation of a 3×3 Hamiltonian and is fully consistent with the subsequent use of the 8×8 Kane matrix. Although the full Hamiltonian is represented in an 8×8 Kane matrix, the physically relevant subspace describing the conduction and light-hole bands is obtained through standard Löwdin partitioning, which results in a reduced effective band model. This approximation is intended to find a

Cite as: U.I. Erkaboev, U.Sh. Turdiev, M.G. Dadamirzaev, R.G. Rakhimov, Sh.X. Utkirov, East Eur. J. Phys. 1, 293 (2026), https://doi.org/10.26565/2312-4334-2026-1-34

convenient solution to the equation for narrow-band quantum-well semiconductors. In the considered approximation, the 8×8 interaction matrix can be written using H_{kp} and H_1 as follows [31]:

$$\begin{pmatrix} \mathsf{H} & 0 \\ 0 & \mathsf{H} \end{pmatrix}. \tag{1}$$

Here,

$$\mathsf{H} = \begin{pmatrix} E_c & 0 & Pk_+ & 0 \\ 0 & E_v - \dfrac{\Delta}{3} & \dfrac{\sqrt{2}}{3}\Delta & 0 \\ Pk_- & \dfrac{\sqrt{2}}{3}\Delta & E_v & 0 \\ 0 & 0 & 0 & E_v + \dfrac{\Delta}{3} \end{pmatrix}. \tag{2}$$

In this formula, $k_\pm = -i\left(\partial_x \pm i\partial_y\right) + \dfrac{e}{\hbar}\left(A_x \pm iA_y\right)$

In contrast to the previous version, the wave vector in Eq. (2) is now treated as an operator that includes the magnetic vector potential, ensuring the correct description of magnetic-field effects within the Kane model.

To ensure dimensional consistency, equation (2) has been corrected so that both the Hamiltonian matrix and the basis vector are expressed in the proper 4-component form, following the standard Kane model representation.

The right-hand column in the matrix (2) represents the energy states associated with H.

If we calculate the initial energy with the bottom of the conduction band of the quantum well, ($E_c=0$), then the following equation is obtained:

$$\left(E^{'} + E_g\right)\left[E^{'}\left(E^{'} + E_g\right)\left(E^{'} + E_g + \Delta\right) - k^2P^2\left(E^{'} + E_g + 2\Delta/3\right)\right] = 0. \tag{3}$$

Here, $E^{'}(k) = E(k) - \dfrac{\hbar^2k^2}{2m_0}$.

The fourth-order form of Eq. (3) is consistent with the fact that the effective Hamiltonian obtained after Löwdin partitioning corresponds to a reduced 4-band model derived from the original 8×8 Kane Hamiltonian.

From equation (3) it is known that for k=0 the function $E`(k)$ has four eigenvalues: $E_1=0$; $E_2= E_3= -E_g$ and $E_4=- E_g-\Delta$. The condition $E_1=0$ means that the counting starts from the bottom of the conduction band. The energies E_2 and E_3 represent the ceilings of the valence bands of the heavy (E_{v1}) and light (E_{v2}) holes. The energy E_4 shows the spin-orbit effect on the ceiling of the valence band.

To solve the problem, we use the following approximations:

1. Ignoring the spin-orbit effect on the allowed bands of a narrow-zone semiconductor.

2. Ignoring the interaction with heavy holes, since the effective masses of light holes are close to the effective masses of free electrons.

In this case, $Eg>>\Delta$ and according to work [31], the energy of light holes is determined as follows:

$$E^{'}_{v2}(k) = -\frac{E_g}{2}\left\{1 + \left[1 + \frac{4k^2p^2}{E_g^2}\right]^{1/2}\right\}. \tag{4}$$

From equation (4), it is clear that k^2p^2 (a P-matrix element, which is equal to $P = -\dfrac{i\hbar}{m_0} < S\left|\hat{P}\right|x >$) is considered the energy, since the condition that the $\dfrac{k^2p^2}{E_g^2}$ term is a dimensionless quantity must be met. In this case, taking into account the above matrix element equation and the dimensionless quantities $\dfrac{k^2p^2}{E_g^2}$, (4) can be written in the following form.

$$E_{v2}(\vec{k}) = -\frac{E_g}{2}\left\{1 + \left[1 + \frac{4\hbar^2\vec{k}^2_{xyz}}{2m^*_{xyz}} * \frac{1}{E_g^2}\right]^{1/2}\right\} \tag{5}$$

In equation (5), the energy of light holes in narrow-zone bulk semiconductors at the valence band ceiling is determined mainly by the effective masses and wave numbers of the light holes in the XYZ axes. In this case, the band gap (E_g) of the narrow-zone bulk semiconductor is assumed to be constant. From equation (5), natural questions arise:

1. How to use (5) if the material under the influence of the magnetic field is a quantum-enclosed narrow-zone, heterostructure semiconductor?

2. It is known that the E_g of narrow-zone bulk or small-sized semiconductors is very sensitive to external factors. In this case, how are $E_v^{3d}(k,E_g)$ and $E_v^{2d}(k,E_g,d)$ determined?

How does the change in $E_v^{2d}(k,E_g,d)$ affect the density of energy states in the valence band of a quantum well?

To solve these problems, it is necessary to create a new mathematical model.

Applying equation (5) to narrow-zone semiconductors with quantum wells, the following equation is obtained:

$$E_v^{2d}(k,d)=-\frac{E_g}{2}\left\{1+\left[1+4\frac{\frac{\hbar^2\vec{k}_x^{\,2}}{2m_x}+\frac{\hbar^2\vec{k}_y^{\,2}}{2m_y}+\frac{\pi^2\hbar^2}{2md^2}n_z^2}{E_g^2}\right]\right\} \tag{6}$$

Equation (6) is the energy of light holes in a narrow-zone quantum well at the valence band ceiling.

Here, n_z is the number of dimensional quanta, d is the thickness of the narrow-zone quantum well, and m^* is the effective mass of the light hole.

As can be seen from equation (6), the energy of a light hole at the valence band ceiling of a quantum well depends on the thickness of the quantum well, the effective mass of the light hole, and the number of dimensional quanta.

Now, let us consider the effect of a strong magnetic field on a narrow-zone quantum well. In particular, let the direction of the magnetic field induction vector $(\vec{B})$ be along the Z axis and perpendicular to the XOY plane. This is called a longitudinal quantizing magnetic field. In this case, Landau theory [32] and according to the laws of the quantizing magnetic field, the $\left[\frac{\hbar^2\vec{k}_x^{\,2}}{2m_x}+\frac{\hbar^2\vec{k}_y^{\,2}}{2m_y}\right]$ terms of the free light hole at the ceiling of the valence band of the quantum well are replaced by the $\left[\left(N_{Lv}+\frac{1}{2}\right)\hbar\omega_{cv}\right]$ term.

Here N_{Lv} is the number of Landau levels in the valence band of the narrow-band quantum well, ω_{cv} is the cyclotron frequency of light holes.

It follows that equation (6) under the influence of a longitudinal quantizing magnetic field takes the following form:

$$E_v^{2d}\left(B,d,n_z,N_{Lv}\right)=-\frac{E_g}{2}\left\{1+\left[1+4\frac{\left(N_{Lv}+\frac{1}{2}\right)\hbar\omega_{cv}+\frac{\pi^2\hbar^2}{2md^2}n_z^2}{E_g{}^2}\right]^{1/2}\right\} \tag{7}$$

From the derived equation (7) it is clear that the light hole energy at the valence band ceiling of the quantum well is transformed into discrete energy levels in all directions. This, in turn, makes the light hole energy analogous to the quantum dot energy. However, it is also necessary to consider another important physical quantity, E_g, which depends on B and d. The reason is that the change in the function $E_g(B, d)$ is considered monotonically. From this, the function $E_v^{2d}\left(B,d,n_z,N_{Lv}\right)$ becomes $E_v^{2d}\left(E_g(B,d),B,d,n_z,N_{Lv}\right)$. In this case, the equation takes the following form:

$$E_v^{2d\,nonparab}\left(E_g(B,d),B,d,n_z,N_{Lv}\right)=-\frac{\left(E_g(0)+\frac{1}{2}\hbar\omega_{cv}+\frac{1}{2}\frac{\pi^2\hbar^2}{2md^2}n_z\right)}{2}\times\left\{1+\left[1+4\frac{\left(N_{Lv}+\frac{1}{2}\right)\hbar\omega_{cv}+\frac{\pi^2\hbar^2}{2md^2}n_z^2}{\left(E_g(0)+\frac{1}{2}\hbar\omega_{cv}+\frac{1}{2}\frac{\pi^2\hbar^2}{2md^2}n_z^2\right)^2}\right]^{1/2}\right\} \tag{8}$$

The resulting equation (8) equation the dependence of the light hole energy at the valence band ceiling of the quantum well on the magnetic field, the band gap width, the quantum well thickness, and the number of dimensional levels. Let us analyze equation (8) numerically and graphically [33], the Shubnikov de Haas oscillations of a narrow-zone InAs quantum well semiconductor were determined. In this case, the InAs quantum well thickness was taken to be d = 4 nm, B = 0÷12 T in the range, $E_g(0)$ = 0.35 eV and n_z.

By substituting these experimental values into (8), it is possible to obtain the $E_v^{2d}\left(B,d,E_g(B,d)\right)$ graph. Fig.1 shows the dependence of the energy of light holes in the vacancy ceiling of the InAs quantum well on the magnetic field

for different Landau levels. As can be seen from this figure, the curve of the graph is reflected according to the non-quadratic dispersion law of the narrow-zone InAs quantum well.

In addition, using equation (8), it is possible to calculate the two-dimensional energy density of states in the valence band of the narrow-zone quantum well.

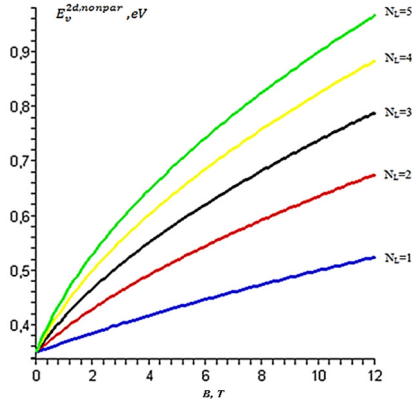

Figure 1. Magnetic field dependence of the energy of light holes in the valence band of an InAs quantum well for Landau levels

Effect of magnetic field on the energy of free electrons at the bottom of the conduction band of a narrow-zone quantum well

Now, let us consider the dependence of the free electron energy at the bottom of the conduction band of a narrow-zone quantum well on the magnetic field.

It is known that for narrow-zone semiconductors, using the condition $m_n << m_0$, the $\frac{\hbar^2 k^2}{2m_0}$ term given in equation (3) is not taken into account ($E^{'} << E_g$). In this case, in the presence of a magnetic field, a cubic equation of energy levels for three energy bands similar to equation (3) is formed:

$$E_{N\pm}(E_{N\pm}+E_g)(E_{N\pm}+E_g+\Delta)-P^2\left[k_z^2+(2N+1)\frac{1}{L^2}\right]\times\left(E_{N\pm}+E_g+\frac{2}{3}\Delta\right)\pm\frac{P^2\Delta}{3L^2}=0\,. \tag{9}$$

Here: $E_{Nk_z\pm}=E_{N\pm}$

In equation (9), the main energy level starts at the bottom of the conduction band. If, when $B\to 0$, equation (9) changes to the form (3).

If the spin distribution of electrons is not taken into account and the $E_N << E_g$ condition is satisfied, the cubic equation in (9) transforms into a quadratic equation for conduction band electrons, which has the following form:

$$E_{N\pm}(B,\,E_g)=-\frac{E_g}{2}+\frac{1}{2}\sqrt{E_g^2+4E_g\left[\left(N+\frac{1}{2}\right)\hbar\omega_c^0+\frac{\hbar^2k_z^2}{2m_n}\right]}\,. \tag{10}$$

It is known that in the absence of a strong magnetic field, the free electron energy is discrete due to dimensional quantization along the OZ axis, but consists of a continuous spectrum in the XOY plane. That is,

$$E_c^{parab}(k,d)=\frac{P_x^2}{2m_{nx}}+\frac{P_y^2}{2m_{ny}}+\frac{\pi^2\hbar^2}{2m_{nz}d^2}n_z^2 \tag{11}$$

Eq. (11) is valid for wide-band quantum fields (for the quadratic dispersion law).

Equation (10) expresses the dependence of the free electron energy in the conduction band of semiconductors with a narrow band gap on the magnetic field. That is, the magnetic field strength is directed along the Z axis, perpendicular to the XOY plane. In this case, the energy of charge carriers, according to Landau theory, forms discrete levels in the XOY plane. Along the OZ axis, the free electron energy forms a continuous spectrum. Of course, this gives an analogy to the quantum string. The question arises; how does this scientific hypothesis work in semiconductors based on a narrow band quantum well? How does the energy of free electrons in the conduction band of a narrow band quantum well depend on the magnetic field? What about the valence band of the quantum well?

For narrow-zone quantum wells, the equation in work [31] is applied: That is, if the condition $\Delta << E_g$ is met

$$E_c^{nonparab}(k)=-\frac{E_g}{2}\left\{1-\left[1+\frac{4P^2}{E_g^2}\times\frac{2m_{nxyz}}{\hbar^2}\times\frac{\hbar^2k_{xyz}^2}{2m_{nxyz}}\right]^{1/2}\right\}. \tag{12}$$

Equation (12) can be written as follows for a narrow-zone quantum well:

$$E_c^{2d,nonparab}(k,d)=-\frac{E_g}{2}\left\{1-\left[1+\frac{4P^2}{E_g^2}\times\frac{2m_n}{\hbar^2}\left(\frac{\hbar^2k_x^2}{2m_{nx}}+\frac{\hbar^2k_y^2}{2m_{ny}}+\frac{\pi^2\hbar^2}{2m_{nt}}n_z^2\right)\right]^{1/2}\right\}. \quad (13)$$

Here, $P=-\frac{i\hbar}{m_0}<S\left|\hat{P}_x\right|x>$.

Equations (11) and (13) express the energy of free electrons in the conduction band of a quantum well at $B=0$ for quadratic and non-quadratic dispersion laws. If the condition $B\neq0$ is met, equation (11) transforms into the following equation:

$$E_c^{parab}(B,d)=\left(N_{Lc}+\frac{1}{2}\right)\hbar\omega_{cc}+\frac{\pi^2\hbar^2}{2m_nd^2}n_z^2. \quad (14)$$

Then, if we replace $\frac{\hbar^2k_z^2}{2m_n}$ in equation (10) with $\frac{\pi^2\hbar^2}{2m_nd^2}n_z^2$ in accordance with the narrow-zone quantum well condition (Louis de Broglie relation, $\lambda_d\approx d$), we obtain the following equation:

$$E_n^{2d,nonparab}(E_g(B,d),B,d,n_z,N_{Lc})=-\frac{E_g(B,d)}{2}+\frac{1}{2}\sqrt{(E_g(B,d))^2+4E_g(B,d)[(N_{Lc}+\frac{1}{2})\hbar\omega_{cc}+\frac{\pi^2\hbar^2}{2md^2}n_z^2]} \quad (15)$$

This equation expresses the dependence of the energy of free electrons in the conduction band of a narrow-zone quantum well on the magnetic field. The newly obtained equation (15) is important because until now, regardless of the forbidden band width of the quantum well, $E_N(B,d)$ has been calculated only according to (14). However, according to (15), the energy E_N is nonlinearly related to B. Here, $\omega_c=\frac{eB}{m_n}$.

Let us apply equation (15) to semiconductors based on narrow-zone quantum wells. Let us analyze this theoretical idea graphically. Fig. 2 shows the dependence of the free electron energy in the conduction band for the *InAs/AlSb* quantum well semiconductor $E_c^{nonparab}$ on B. Here, $E_g(InAs)$=0.35 *eV*, d = 12 nm [33]. Fig. 3 shows the $E_c^{parab}(B,d)$ graph for the *GaAs/Al$_x$Ga$_{1-x}$/GaAs* [37] quantum well. As can be seen from this figure, linear and nonlinear graphs obey the dispersion laws. In addition, according to equation (15), it is possible to obtain the dependence of the narrow-zone quantum well thickness d from $E_c^{parab}(B,d)$.

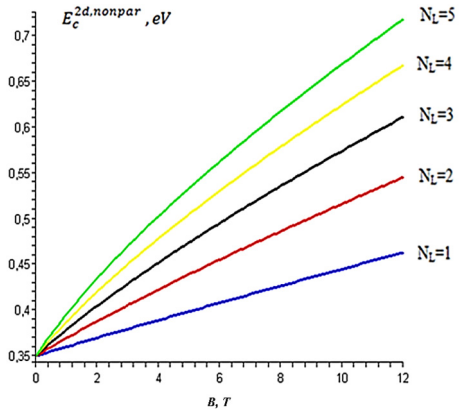

Figure 2. Effect of magnetic field on the energy of free electrons in the conduction band of an *InAs/AlSb* quantum well

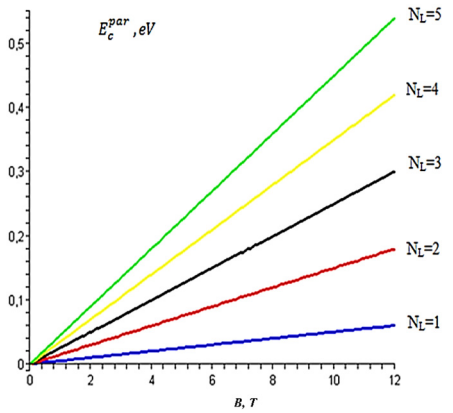

Figure 3. Effect of magnetic field on the energy of free electrons in the conduction band of a GaAs/Al$_x$Ga$_{1-x}$/GaAs quantum well

Mathematical modeling of the temperature and magnetic field dependence of the density of two-dimensional energy states in the allowed zones of a narrow-band quantum coil

It is known from the scientific literature that the change in the energy of charge carriers in the allowed zones of a narrow-zone quantum well under the influence of a strong magnetic field has a strong effect on the two-dimensional energy density of states $N_s^{2d}(E)$. This allows us to obtain sufficient information on the location of electrons and holes in the quantum well at discrete levels and the distribution of current carriers.

However, to date, the dependence of the energy density of states of a narrow-zone quantum well on the magnetic field and temperature has not been sufficiently studied in the available literature. The energy of electrons and holes in a narrow-zone quantum well obeys the non-quadratic dispersion law.

For the quadratic dispersion law, the dependence of the energy density of states in a quantum well on the magnetic field and temperature has been thoroughly studied in [25]. As a result, a new model for $N_s^{k,2d}(E,B,T,d)$ was proposed [29]:

$$N_{S,Z}^{2d}(E,B,T,d)=\sum_{N_L,N_Z}^{\infty}\frac{eB}{\pi\hbar}\cdot\frac{1}{kT}\cdot\exp\left(-\frac{\left(E-\left(\left(N_L+\frac{1}{2}\right)\hbar\omega_c+\frac{\pi^2\hbar^2}{2m^*d^2}n_Z^2\right)\right)^2}{(kT)^2}\right) \tag{16}$$

In creating this model, the method of expanding the density of states delta functions *δ(x)* in a series with respect to energy was used [19]. At absolute zero temperature (*T→0*), the energy derivatives of the Lorentz, Gauss, Fermi-Dirac functions $\left(\frac{\partial f_0}{\partial E}\right)$ and GN [35] take the form *δ(E)*. The authors of this work [29] mainly applied the Gaussian (*E,T*) delta function to determine $N_s^{k,2d}(E,B,T)$. In this case, the proposed model was mainly applied to heterostructures with a wide band gap (or classical) quantum well. In addition, the obtained $N_s^{k,2d}(E,B,T)$ model was related to free electrons in the conduction band of a wide band gap quantum well.

Now, using the $E_c^{nk,2d}(E,d,E_g^{2d})$ and $E_v^{nk,2d}(E,d,E_g^{2d})$ connections introduced in the previous paragraphs, let's consider $N_{s,c}^{2d,nk}(E_c^{nk,2d},B,T,d)$ and $N_{s,v}^{2d,nk}(E_v^{nk,2d},B,T,d)$.

A function δ(x) of one real argument is reasonable if the following conditions are met:

$$\delta(x)=\begin{cases}-\infty, & x=0\\ 0, & x\neq 0\end{cases} \tag{17}$$

$$\int_{-\infty}^{\infty}\delta(x)dx=1$$

In work [36], it is shown that the energy dependence of the density of states for two-dimensional materials consists of a sum of delta functions:

$$N_S^{2d}(E,B)=\frac{eB}{\pi\hbar}\sum_{N_LN_Z}\delta\left(E-E\left(N_L,n_Z\right)\right) \tag{18}$$

This equation (18) is a generalized equation, which has been used to date for all (classical, wide and narrow bandgap) quantum-gap semiconductors. As mentioned above, when the condition *T→0* is met, the Gaussian function transforms into Gaussian(*E,T*) δ(E,T). That is:

$$\lim_{T\to 0}Gauss\left(E,T\right)\to\delta\left(E,T\right),\ Gauss\left(E,T\right)=\frac{1}{kT}\exp\left(-\frac{(E-E_i)}{(kT)^2}\right) \tag{19}$$

The energy E_i given in equation (19) corresponds to the valence band ceiling or the conduction band bottom of a narrow-band quantum well. However, equation (19) does not depend on the magnetic field, and the effect of temperature on equation (18) has not been studied.

The meaning of $E(N_L, n_Z)$ in equation (18) is the discrete energy levels of charge carriers in the allowed bands of the quantum well, that is, it corresponds to (8) and (15). In general, in (18) the quantum well corresponds to the delta function $\delta(E-E(N_L, n_Z))$ due to the magnetic field, while in equation (19) the condition *T→0* is fulfilled and *δ(E, T)* becomes the limit *δ(x)*.

Equation (15) gives the dependence of the free electron energy at the bottom of the conduction band of a narrow-zone quantum well on the magnetic field, the thickness of the quantum well, and the number of quantum levels ($E_{nc}^{2d}(B,d,N_L,n_z)$). This is valid for the nonparabolic dispersion law. Then, taking into account the dependence of $N_S^{2d}(E,B)$ on $E(E_L,n_z)$ in (18) and the substitution of $\left(\left(N_L+\frac{1}{2}\right)\hbar\omega_c+\frac{\pi^2\hbar^2}{2md^2}n_z^2\right)$ in (15) for the $-\frac{E_g(B,d)}{2}+\frac{1}{2}\sqrt{(E_g(B,d))^2+4E_g(B,d)[(N_{Lc}+\frac{1}{2})\hbar\omega_{cc}+\frac{\pi^2\hbar^2}{2md^2}n_z^2]}$ term in (16), the following expression is obtained:

$$N_{s,z}^{c,2d}(E,B,T,d)=\sum_{N_L,n_e}^{\infty}\frac{eB}{\pi\hbar}\cdot\frac{1}{kT}\cdot\exp\left(-\frac{\left(E+\frac{E_g(B,d)}{2}-\frac{1}{2}\sqrt{(E_g(B,d))^2+4E_g(B,d)\left(\left(N_L^e+\frac{1}{2}\right)\hbar\omega_c^e+\frac{\pi^2\hbar^2}{2m^*d^2}n_e^2\right)}\right)^2}{(kT)^2}\right) \quad (20)$$

This expression represents the equation for determining the energy density of states in the conduction band of a narrow-zone quantum well. Fig. 4 compares the dependence of the two-dimensional energy density of states for parabolic (wide-gap quantum well) and non-parabolic (narrow-zone quantum well) on the magnetic field at constant $T = const$. It can be seen from this figure that, due to the energy dependence of the effective mass of free electrons in a narrow-zone quantum well, a "compression" (deformation) of discrete Landau levels in a uniform energy interval is observed.

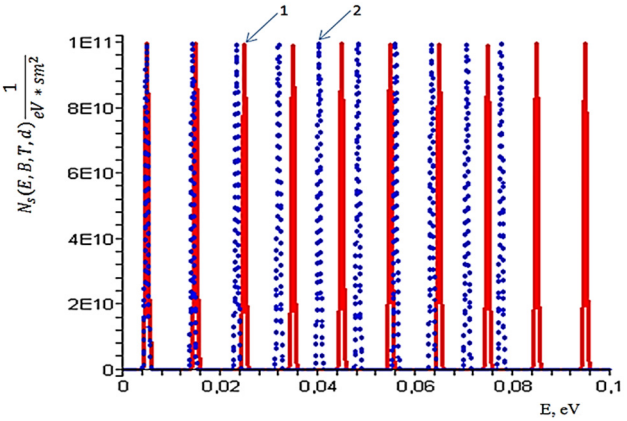

Figure 4. Energy density of states in the conduction band of a wide-band and narrow-zone quantum well for parabolic and nonparabolic dispersion laws

1 - parabolic. $Al_xGa_{1-x}As$ T=4.2 K, B = 10 T, d =5 nm; 2 - non-parabolic. InAs T = 4.2 K, B = 10 T, d =4 nm

Here, graphs of a narrow-zone *InAs* [33] quantum well and a wide-gap *GaAs/$Al_xGa_{1-x}As$/GaAs* (quantum well $Al_xGa_{1-x}As$) [37-39] quantum well are presented. The oscillations were calculated at temperatures T=1.5 K, B=3 T, d=5 nm ($Al_xGa_{1-x}As$) and d=*4* nm (InAs).

Fig. 5 shows the temperature dependence of the two-dimensional energy density of states oscillations in the conduction band of *$Al_xGa_{1-x}As$* and *InAs* quantum well semiconductors. In this case, the quantum well of *$Al_xGa_{1-x}As$* obeys the parabolic dispersion law, and *InAs* obeys the nonparabolic dispersion law. As can be seen from the application of the star-shaped Gaussian function to these materials, it is observed that as the temperature increases, the discrete Landau level "washes out". However, comparing the graphs a) and b) in Fig.5, it becomes clear that the oscillations of the *InAs* quantum well turn into a continuous spectrum earlier.

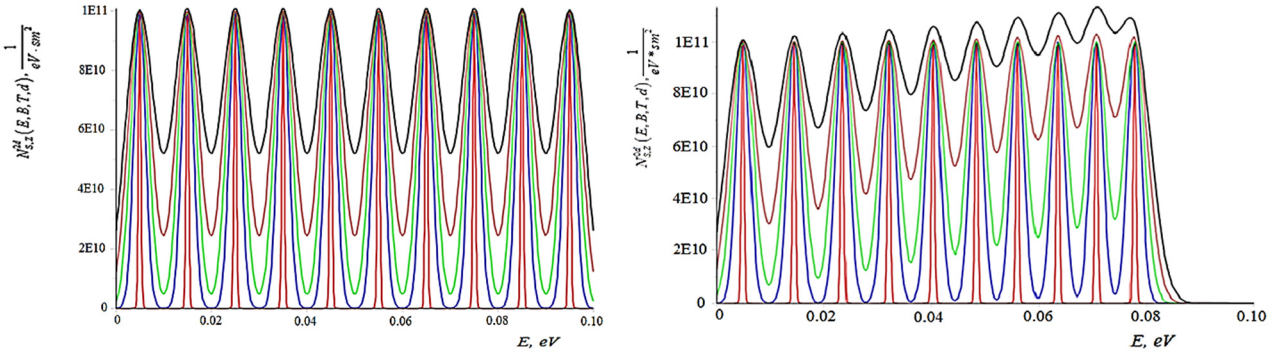

a) Parabolic. $Al_xGa_{1-x}As$. 1) T=5 K, B=10 T, d=5 nm; 2) T=20 K, B=10 T, d=5 nm; 3) T=30 K, B=10 T, d=5 nm; 4) T=40 K, B=10 T, d=5 nm; 5) T=50 K, B=10 T, d=5 nm

b) Nonparabolic. InAs. 1) T=5 K, B=10 T, d=4 nm; 2) T=20 K, B=10 T, d=4 nm; 3) T=30 K, B=10 T, d=4 nm; 4) T=40 K, B=10 T, d=4 nm; 5) T=50 K, B=10 T, d=4 nm

Figure 5. a) Oscillations of the temperature-dependent change in the energy density of states in the conduction band of a wide-band quantum well for the parabolic dispersion law; b) Oscillations of the temperature-dependent change in the energy density of states in the conduction band of a narrow-band quantum well for the nonparabolic dispersion law

Fig. 6 shows the temperature variation of the density of states oscillations of an *InAs* narrow-zone quantum well at B = 10 T and d = 4 nm. It can be seen from this figure that as the temperature increases, the "peaks" of the discrete Landau levels decrease. This, of course, indicates the fulfillment of the condition $kT \approx \hbar\omega_c$ and the laws of "thermal expansion".

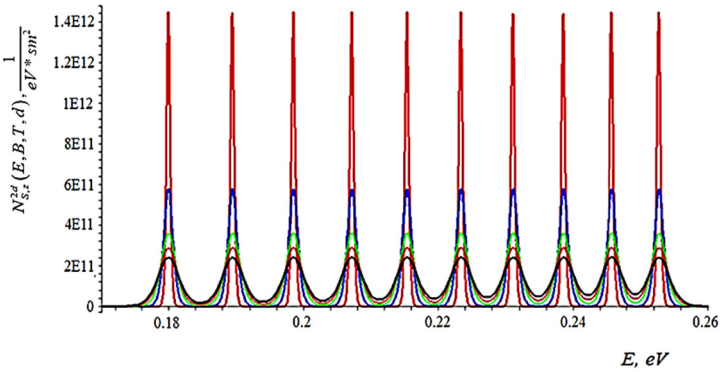

Figure 6. Temperature dependence of the energy density of states oscillations in the conduction band of an InAs narrow-zone quantum well (d=4 nm) up to a transverse quantizing magnetic field (B=10 T). The energy spectra shown in the figure were calculated by equation (20)
1) T=2 K, B=10 T, d=4 nm; 2) T=5 K, B=10 T, d=4 nm; 3) T=8 K, B=10 T, d=4 nm; 4) T=10 K, B=10 T, d=4 nm; 5) T=12 K, B=10 T, d=4 nm

CONCLUSIONS

In the process of carrying out this research work, the following conclusions were reached:

1. A mathematical model was developed to determine the dependence of the light hole energy $E_v^{2d}\left(E_g(B,d),B,d,n_z,N_{Lv}\right)$ at the valence band ceiling of a narrow-zone quantum well and the free electron energy $E_n^{2d,nonparab}(E_g(B,d),B,d,n_z,N_{Lc})$ at the conduction band bottom of the quantum well on the magnetic field, band gap width, quantum well thickness, and number of dimensional levels.

2. A method was proposed to determine the dependence of the allowed bands $N_{vs}^{2d(n)}$, $N_{cs}^{2d(n)}$ of narrow-zone quantum well semiconductors on the magnetic field B and temperature T.

3. Using this method, the dependence of the band gap width of a narrow-zone quantum well on the magnetic field B and temperature T was determined.

ORCID

U.I. Erkaboev, https://orcid.org/0000-0002-6841-8214; **U.Sh. Turdiev,** https://orcid.org/0009-0009-7808-4113
M.G. Dadamirzaev, https://orcid.org/0000-0003-0756-8275; **R.G. Rakhimov,** https://orcid.org/0000-0003-0850-1398

REFERENCES

[1] I.V. Bondar, Phys. Tech. Semiconductors, 49(9), 1180-1183 (2015). http://journals.ioffe.ru/articles/viewPDF/42140
[2] G. Gulyamov, M.G. Dadamirzayev, K.M. Uktamova, and B.Z. Mislidinov, AIP Conf. Proc. **2700**(1), 050007 (2023). https://doi.org/10.1063/5.0126516
[3] G. Gulyamov, U.I. Erkaboev, and A.G. Gulyamov, Adv. Condens. Matter Phys. **2017**(1), 6747853 (2017). https://doi.org/10.1155/2017/6747853
[4] V.P. Kunets, N.R. Kulish, V.P. Kunets, M.P. Lisitsa, and N.I. Malysh, Semiconductors, **36**(2), 219-223 (2002). https://doi.org/10.1134/1.1453442
[5] Y.P. Varshni, Physica, **34**(1), 149-154 (1967). https://doi.org/10.1016/0031-8914(67)90062-6
[6] A.S. Puzanov, S.V. Obolenskii, and V.A. Kozlov, Semiconductors, **49**(1), 69-74 (2015). https://doi.org/10.1134/S1063782615010224
[7] G. Gulyamov, M.G. Dadamirzayev, M.O. Qosimova, and S.R. Boydedayev, AIP Conf. Proc. **2700**(1), 050013 (2023).https://doi.org/10.1063/5.0124926
[8] Y. Tokura, K. Yasuda, and A. Tsukazaki, Nat. Rev. Phys. **1**, 126–143 (2019). https://doi.org/10.1038/s42254-018-0011-5
[9] G. Gulyamov, M.G. Dadamirzaev, and S.R. Boidedaev, Semiconductors, **34**, 555-557 (2000). https://doi.org/10.1134/1.1188027
[10] M. Ahmetoglu (Afrailov), G. Kaynak, S. Shamirzaev, G. Gulyamov, A. Gulyamov, M.G. Dadamirzaev, S.R. Boydedayev, and N. Aprailov, Int. J. Mod. Phys. B, **23**(15), 3279-3285 (2009). https://doi.org/10.1142/S0217979209053084
[11] U. Erkaboev, R. Rakhimov, J. Mirzaev, N. Sayidov, U. Negmatov, and A. Mashrapov, AIP Conf. Proc. 2789(1), 040056 (2023). https://doi.org/10.1063/5.0145556
[12] R. Macaluso, H.D. Sun, M.D. Dawson, F. Robert, A.C. Bryce, and J.H. Marsh, Appl. Phys. Lett., 82, 4259–4261 (2003). https://doi.org/10.1063/1.1583865
[13] M.S. Aghaei, I. Torres, and I. Calizo, Comput. Mater. Sci. **138**, 204-212. (2017). https://doi.org/10.1016/j.commatsci.2017.06.041
[14] S. Gies, C. Kruska, C. Berger, P. Hens, C. Fuchs, A.R. Perez, N.W. Rosemann, *et al*., Appl. Phys. Lett. **107**, 182104-182108 (2015). https://doi.org/10.1063/1.4935212
[15] S.H. Shamirzaev, G. Gulyamov, M.G. Dadamirzaev, and A.G. Gulyamov, Semiconductors, **43**, 47-51 (2009). https://doi.org/10.1134/S1063782609010102
[16] U.I. Erkaboev, N.A. Sayidov, U.M. Negmatov, J.I. Mirzaev, and R.G. Rakhimov, E3S Web Conf., **401**, 01090 (2023). https://doi.org/10.1051/e3sconf/202340101090
[17] Y. Joseph, H. Mehdi, A.M. Brenden, M. William, C.D. Matthieu, S. Kasra, S.W. Kaushini, *et al*., Phys. Rev. B, **101**, 205310-205317 (2020). https://doi.org/10.1103/PhysRevB.101.205310

[18] D.S. Abramkin, and T.S. Shamirzaev, Semiconductors, **53**(5), 703–710 (2019). https://doi.org/10.21883/FTP.2019.05.47569.9018
[19] G. Gulyamov, U.I. Erkaboev, and N.Y. Sharibaev, Semiconductors, **48**, 1287–1292 (2014). https://doi.org/10.1134/S1063782614100108
[20] D. Luo, L. Wang, Y. Qiu, R. Huang, and B. Liu, Nanomaterials, **24**, 1226-1265 (2020). https://doi.org/10.3390/nano10061226
[21] U.I. Erkaboev, N.A. Sayidov, U.M. Negmatov, R.G. Rakhimov, and J.I. Mirzaev, E3S Web Conf. **401**, 04042 (2023). https://doi.org/10.1051/e3sconf/202340104042
[22] E. Kasapoglu, H. Sari, and I. Sökmen, Surf. Rev. Lett. **15**, 201–205 (2008). https://doi.org/10.1142/S0218625X08010440
[23] U. Erkaboev, R. Rakhimov, J. Mirzaev, N. Sayidov, U. Negmatov, and M. Abduxalimov, AIP Conf. Proc. **2789**(1), 040055 (2023). https://doi.org/10.1063/5.0145554
[24] B.P. Koman, Semiconductors, **48**(5), 659- 665 (2014). https://doi.org/10.1134/S1063782614050091
[25] D. Slobodzyan, M. Kushlyk, R. Lys, J. Shykorjak, A. Luchechko, M. Zyłka, W. Zyłka, *et al*., MDPI Materials, **15**, 4052-4063 (2022). https://doi.org/10.3390/ma15124052
[26] G. Gulyamov, M.G. Dadamirzaev, and S.R. Boidedaev, Semiconductors, **34**, 260-263 (2000). https://doi.org/10.1134/1.1187967
[27] Y.N. Qiu, J.M. Rorison, Appl. Phys. Lett. **82**, 081111-081113 (2005). https://doi.org/10.1063/1.2034103
[28] U. Erkaboev, R. Rakhimov, J. Mirzaev, U. Negmatov, and N. Sayidov, Int. J. Mod. Phys. B, **38**(15), 2450185 (2024). https://doi.org/10.1142/S0217979224501856
[29] U. Rani, P.K. Kamlesh, T.K. Joshi, R. Singh, S. Sharma, R. Gupta, T. Kumar, and A.S. Verma, Comput. Condens. Matter, **36**, 00835-00845 (2023). https://doi.org/10.1016/j.cocom.2023.e00835.
[30] M.G. Dadamirzaev, M.O. Kosimova, S.R. Boydedayev, and A.S. Makhmudov, East Eur. J. Phys. (2), 372-379 (2024). https://doi.org/10.26565/2312-4334-2024-2-46
[31] I.M. Tsidilkovskii, *Electrons and holes in semiconductors. Energy spectrum and dynamics* (Nauka, Moscow, 1972)
[32] L. Landau, Z. Phys. **64**, 629-637 (1930). https://doi.org/10.1007/BF01397213
[33] Y. Joseph, H. Mehdi, A.M. Brenden, M. William, C.D. Matthieu, S. Kasra, S.W. Kaushini, *et al*., Phys. Rev. B, **101**, 205310-205317 (2020). https://doi.org/10.1103/PhysRevB.101.205310
[34] U.I. Erkaboev, R.G. Rakhimov, U.M. Negmatov, N.A. Sayidov, and J.I. Mirzaev, Rom. J. Phys. **68**(5-6), 614 (2023). https://rjp.nipne.ro/2023_68_5-6/RomJPhys.68.614.pdf
[35] G.M. Fichtenholz, *Fundamentals of Mathematical Analysis: Textbook for Universities* (Lan, St. Petersburg, 2001).
[36] W. Zawadzki, A. Raymond, and M. Kubisa, Phys. Status Solidi B, **251**(2), 247–262 (2014). https://doi.org/10.1002/pssb.201349251
[37] H. Zheng, A. Song, F. Yang, and Y. Li, Phys. Rev. B, **49**(3), 1802-1808 (1994). https://doi.org/10.1103/PhysRevB.49.1802
[38] U. Rani, P.K. Kamlesh, T.K. Joshi, S. Sharma, R. Gupta, S. Al-Qaisi, and A.S. Verma, Phys. Scripta, **98**, 075902-075907 (2023). https://doi.org/10.1088/1402-4896/acd88a
[39] M. Pazoki, M.B. Johansson, H. Zhu, P. Broqvist, T. Edvinsson, G. Boschloo, and E.M. Johansson, J. Phys. Chem. **120**, 29039-29046 (2016). https://doi.org/10.1021/acs.jpcc.6b11745

МОДЕЛЮВАННЯ ЗАЛЕЖНОСТІ ШИРИНИ ЗОНИ ВІД ТЕМПЕРАТУРИ ТА МАГНІТНОГО ПОЛЯ У НАПІВПРОВІДНИКАХ З ВУЗЬКОЗОННИМИ КВАНТОВИМИ ЯМАМИ

У.І. Еркабоєв[1], У.Ш. Турдієв[2], М.Г. Дадамірзаєв[1], Р.Г. Рахімов[1], Ш.Х. Уткіров[2]
[1]Наманганський державний технічний університет, 160115 Наманган, Узбекистан
[2]Ташкентський хіміко-технологічний інститут, філія Янгієр, 121001 Сирдар'я, Узбекистан

Фундаментальним фізичним параметром як об'ємних, так і низьковимірних напівпровідникових структур є ширина забороненої зони E_g^{3d}, E_g^{2d}, енергетична ширина якої дозволяє заздалегідь передбачити робочі параметри напівпровідникових пристроїв. Тому визначення E_g^{3d}, та E_g^{2d} у випадках, коли ширина забороненої зони щойно синтезованих матеріалів невідома вважається одним з першочергових завдань у технології напівпровідникових гетероструктур. Крім того, ще однією важливою особливістю E_g є його сильна чутливість до зовнішніх впливів. Дійсно, зміни E_g, що виникають внаслідок таких ефектів, можуть фундаментально змінити фізичні та хімічні властивості напівпровідникових приладів.

Ключові слова: *напівпровідник; провідність; квантова яма; магнітоопір; магнітне поле*

EAST EUROPEAN JOURNAL OF PHYSICS. 1. 302-307 (2026)
DOI:10.26565/2312-4334-2026-1-35 ISSN 2312-4334

OPTIMIZATION OF A VACUUM THERMAL EVAPORATION SYSTEM FOR THE DEPOSITION OF Bi–Sb–Te THIN FILMS

Bunyodjon U. Omonov[1], Sherzod A. Maxmudov[2†]
[1]*Fergana State University, Fergana, Uzbekistan*
[2]*Institute of Nuclear Physics, Tashkent, Uzbekistan*
**Corresponding Author e-mail: omonovbunyodjon.1994@gmail.com*; [†]*E-mail: makhmudov@inp.uz*
Received September 25, 2025; revised January 11, 2026; accepted February 4, 2026

In this study, thin films based on bismuth and antimony chalcogenides (Bi_2Te_3–Sb_2Te_3) were synthesized using an optimized thermal evaporation vacuum system, and their morphological characteristics were thoroughly investigated. Atomic force microscopy (AFM) results revealed nanoscale granularity on the film surface (in the range of 50–150 nm) and a distinct stepped morphology. Longitudinal profile analyses indicated that the height variations lie within the range of 0.790–0.798 μm. Scanning electron microscopy (SEM) observations confirmed the formation of grains, larger particles, and surface voids, indicating a dual-level morphological structure. Such a structure is critically important for enhancing thermoelectric efficiency by intensifying phonon scattering, thereby reducing thermal conductivity while preserving electron transport properties. The findings demonstrate that Bi_2Te_3–Sb_2Te_3-based thin films possess high scientific and practical potential as thermoelectric materials.
Keywords: *Thin Film; Morphology; Atomic Force Microscopy; Electron Microscopy; Thermoelectric Efficiency; Nanogranularity; Stepped Structure*
PACS: 68.55.-a; 81.15.-z; 78.67.Pt; 73.50.Lw; 72.15.Jf

1. INTRODUCTION

In recent years, thin films of bismuth and antimony chalcogenides have attracted significant scientific and practical attention as thermoelectric materials [1,2]. These materials are distinguished by their high efficiency in heat-to-electric energy conversion, as well as by their stability and environmental friendliness [3]. A key indicator of thermoelectric efficiency is the figure of merit, ZT, and its enhancement requires a strategic approach that reduces thermal conductivity while maintaining electrical conductivity [4]. From this perspective, composite thin films of Bi_2Te_3 and Sb_2Te_3 are promising candidates [5].

The technological processes employed in thin-film synthesis directly determine the structural and morphological characteristics of the thin films [1,3]. The granular structure of the films, their step-like growth features, and porosity significantly influence the mechanisms of phonon propagation [2,4]. Consequently, these effects suppress thermal transport, thereby enabling enhanced thermoelectric efficiency. Furthermore, it has been established that surface morphology plays a crucial role in defining electron transport pathways, influencing recombination processes, and shaping the material's optical and electrical properties [5].

Vacuum technologies used in thin-film fabrication, particularly optimized thermal evaporation methods, enable the production of high-quality films under highly controlled conditions [3,4]. Processes carried out in vacuum systems eliminate external contaminants, thereby facilitating the formation of structurally pure materials. As a result, the synthesized films exhibit stable morphological and crystallographic properties, significantly enhancing their functional performance.

The aim of this work is to optimize a vacuum thermal evaporation system for the deposition of Bi_2Te_3–Sb_2Te_3 thin films and to analyze the influence of key technological parameters on the resulting film morphology.

To achieve this aim, the effects of vacuum level, evaporation conditions, and condensation processes on the surface morphology of the deposited films were systematically investigated. In this study, thin films based on Bi_2Te_3–Sb_2Te_3 were synthesized using a specially designed vacuum thermal evaporation system, and their morphological characteristics were comprehensively examined using atomic force microscopy (AFM) and scanning electron microscopy (SEM). The results confirmed that the films possess a dual-level morphological structure, which may significantly enhance thermoelectric efficiency.

2. EXPERIMENTAL SETUP AND DEPOSITION CONDITIONS

Thin films with a stoichiometric composition of 25% Bi_2Te_3 – 75% Sb_2Te_3 were deposited by the thermal evaporation method under vacuum using a UVN-71 P2 vacuum coating system. Prior to deposition, the vacuum chamber was evacuated to a base pressure of 1.33×10^{-3} Pa, ensuring minimized contamination during the film growth process.

The evaporation was carried out from a resistively heated crucible maintained at a temperature of 610 ± 10 °C, while the substrate temperature was fixed at 90 °C. The distance between the evaporation source and the substrate was optimized and set to 7 sm, providing uniform material flux across the substrate surface. The deposition duration was 8 minutes, and the total mass of the evaporated source material was 70 mg.

Polyethylene terephthalate (PET) substrates were used for thin-film deposition. The substrate thickness ranged from 50 to 125 μm, allowing sufficient mechanical stability during the evaporation process. As a result of the selected deposition parameters, uniform thin films with an average thickness of 0.790 μm were obtained.

The chosen vacuum level, evaporation temperature, source–substrate distance, and deposition time were optimized to ensure stable condensation conditions and reproducible film growth. These parameters played a crucial role in

Cite as: B.U. Omonov, S.A. Maxmudov, East Eur. J. Phys. 1, 302 (2026), https://doi.org/10.26565/2312-4334-2026-1-35

determining the morphological uniformity of the deposited Bi_2Te_3–Sb_2Te_3 thin films, which were subsequently analyzed using atomic force microscopy (AFM) and scanning electron microscopy (SEM).

3. DESCRIPTION OF THE OPTIMIZED THERMAL EVAPORATION VACUUM SYSTEM

Vacuum technology plays a key role in the fabrication of semiconductor devices, as certain technological processes require high-vacuum (low-pressure) conditions.

The technological equipment used for the production of semiconductor devices typically consists of two main parts:

1. The working chamber, which generally includes heaters, electrical contacts, evaporators for material deposition, substrates, thermocouples, and other components. This chamber (often referred to as the "bell jar") can be raised or lowered by means of a hydraulic lifting mechanism.
2. The vacuum system, which evacuates air from the working chamber and comprises a rotary mechanical pump, valves, and pipelines (tubing that connects the pump to the chamber).

Even trace amounts of residual impurities inside the working chamber can contaminate the pure material being deposited. Such contamination can, in turn, adversely affect the electrical characteristics of the final device by introducing external or internal defects [6].

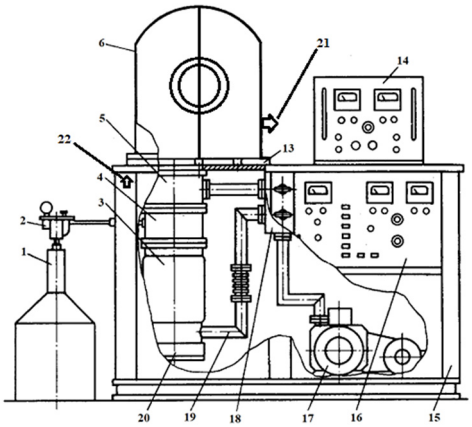

Figure 1. Schematic diagram of the main model of the UVN 71 P2 apparatus

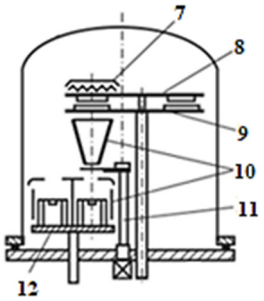

Figure 2. Internal technological configuration of the chamber

In this work, the UVN 71 P2 vacuum system is presented. It is designed for resistive coating (resistive thermal evaporation) to form thin films under vacuum conditions. The device consists of a vacuum generation system, a bell jar (chamber cover), and an electronic control unit. The vacuum generation system includes a forevacuum–diffusion pump that evacuates excess pressure and ensures system balance. The schematic elements of the vacuum coating system for thin films include the following: a thermally insulated dewar vessel for storing liquid nitrogen or helium (1), an automatic unit for supplying liquid nitrogen or helium in a continuous or controlled amount (2), a vapor–oil (diffusion) pump for achieving high vacuum (3), a condensation unit for vapors and gases using nitrogen or helium (4), a mechanical barrier that isolates the vacuum chamber from the external environment (5), the main chamber where the deposition process takes place (6), a heating system to raise substrates to the required temperature (7), a substrate rotation mechanism (8), a rotating mask holder used during the coating process (9), a shield (10), a baffle (11), a carousel with evaporators and individual evaporating sources (12), a rubber gasket ensuring chamber hermeticity (13), a vacuum gauge (vacuummeter) (14), a welded steel frame serving as the primary structural body of the apparatus (15), a control panel (16), a rotary mechanical pump used for initial vacuum generation (17), a valve block (18), tubing connecting the pump and the chamber (19), an electric heater for the vapor–oil (diffusion) pump (20), an air inlet valve or handle (21), a hydraulic switch used to raise and lower the bell jar cover (22), [7].

In such a system, the forevacuum pump is intended to evacuate air through an appropriate manifold until a pressure of approximately 1.33×10^{-1} Pa is achieved in the main chamber. Within the working chamber itself, the pressure typically ranges from (6.67×10^{-1} to 1.33) Pa. Simultaneously, the diffusion pump operates to maintain a steady high-vacuum level in the active volume of the system, with a pressure of approximately 1.33×10^{-4} Pa [8].

4. MORPHOLOGY OF BISMUTH AND ANTIMONY CHALCOGENIDE-BASED THIN FILMS OBTAINED USING A THERMAL EVAPORATION VACUUM SYSTEM

The thermoelectric performance of Bi_2Te_3–Sb_2Te_3-based thin films is commonly evaluated using the dimensionless figure of merit, ZT, defined as

$$ZT = \frac{S^2\sigma T}{\kappa} \tag{1}$$

where S is the Seebeck coefficient, σ is the electrical conductivity, T is the absolute temperature, and κ is the total thermal conductivity. Since the thermal conductivity is strongly influenced by phonon scattering at grain boundaries and surface

features, the morphology of thin films plays a crucial role in determining their thermoelectric efficiency. Therefore, analysis of surface morphology provides important insights into potential enhancement of ZT in Bi_2Te_3–Sb_2Te_3 thin films.

To investigate the surface topography of Bi_2Te_3–Sb_2Te_3 thin films, atomic force microscopy (AFM) was performed using a Solver-NEXT SPM 9700HT (Shimadzu).

The AFM image acquired over a 5.0 × 5.0 μm scan area reveals the surface morphology of the sample with nanometer-scale resolution (Figure 3).

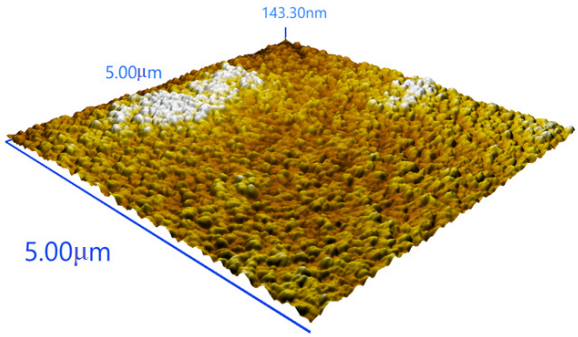

Figure 3. 3D topographic image of a Bi_2Te_3–Sb_2Te_3-based thin film obtained over a 5.00 × 5.00 μm scan area

According to the measurement results, the key surface parameters were determined as follows: average roughness (Ra) – 15.595 nm, root mean square roughness (Rq) – 20.091 nm, maximum peak height (Rp) – 79.030 nm, maximum valley depth (Rv) – 63.621 nm, total height difference (Rz) – 142.651 nm, and ISO-standardized ten-point height difference (Rzjis) – 70.534 nm. These values confirm that the sample's surface topography is well developed at the nanometer scale.

As observed in the AFM image, the surface is composed of grains with sizes distributed in the range of approximately 50–150 nm. Such a structure is attributed to the multidirectional growth of crystallites and irregularities arising during the nucleation process. The elevated Rz value indicates pronounced peaks and deep valleys in the surface topography. This morphological feature is typically observed in thin films synthesized by vacuum evaporation or chemical vapor-phase deposition methods (PVD, CVD).

The closeness of the Ra and Rq values (Ra = 15.6 nm, Rq = 20.1 nm) indicates that the statistical surface irregularities are of a random nature. Such surface morphology can significantly influence the material's functional properties. For instance, in photovoltaic elements, a nanostructured surface enhances light scattering, thereby improving absorption efficiency. In thermoelectric films, grain boundaries can limit phonon propagation, which reduces thermal conductivity and, consequently, enhances thermoelectric performance.

In addition, the significant difference between the Rp and Rv values indicates an uneven distribution of crystallites across the surface. This may directly affect the electrical properties of the material, particularly the charge carrier recombination rate. Recombination processes occurring at crystallite boundaries are among the key factors limiting the efficiency of devices fabricated on the basis of the film. Therefore, surface statistical roughness parameters are directly related not only to morphological characteristics but also to the electronic and optical properties of the material.

Overall, the AFM analysis results confirm the formation of a highly developed nanostructured surface morphology on the sample. Such a structure can potentially enhance the functional capabilities of the material; however, it may also give rise to certain adverse effects, such as an increased rate of recombination processes.

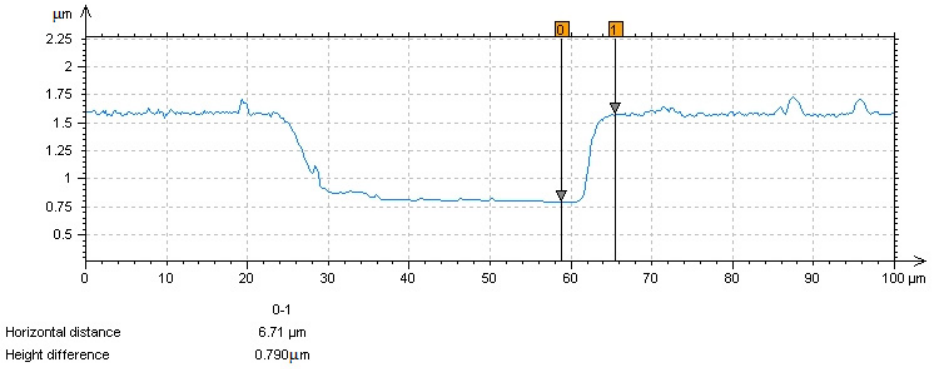

Figure 4. Longitudinal profile of the surface relief of the synthesized film obtained using Atomic Force Microscopy (AFM)

In the profile section presented in Figure 4, a sharp height variation was observed in the range of 60–70 μm. According to the measurement results, the horizontal distance was 6.71 μm, while the height difference amounted to 0.790 μm. These indicators confirm the formation of a step-like structure on the surface relief. Such a morphology

typically arises due to the growth of crystallites in different directions and at varying rates. The development of a stepped morphology may lead to the distinct manifestation of grain boundaries and can promote anisotropic surface evolution.

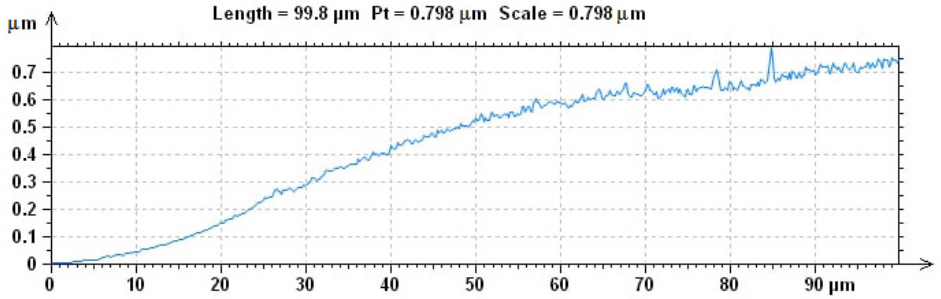

Figure 5. Longitudinal surface profile of the synthesized film obtained using AFM in the range of 0–99.8 µm

The longitudinal profile shown in Figure 5 demonstrates a gradual variation in surface topography over the range of 0–99.8 µm, with a total height difference of 0.798 µm. The overall shape of the profile reflects a global surface inclination, which may be attributed to the initial relief of the substrate or to a directionally controlled growth process during the deposition. Additionally, local oscillations observed within the 0.6–0.7 µm range indicate the presence of nanometer-scale granular morphology.

Based on the analysis, a dual-scale morphological structure was observed in the Bi_2Te_3–Sb_2Te_3-based thin film:

1. Step-like growth at the microscale – indicates the stepwise evolution of crystals and their anisotropic nature.
2. Granularity at the nanoscale – associated with statistical surface roughness as revealed by AFM images; this may enhance phonon scattering and thus potentially reduce thermal conductivity.

AFM (Atomic Force Microscopy) observations provided additional quantitative parameters that further elucidate the morphological characteristics of the material:

- Surface height variation: Maximum height differences in the range of 0.790–0.798 µm indicate the formation of a step-like relief during the film growth process.
- Statistical surface roughness: The calculated *Ra* (average roughness) values fall within the range of approximately 15–20 nm, which is attributed to the influence of nanoscale grains.
- Grain height: Local fluctuations indicate grain heights within the 50–150 nm range, which is further confirmed by high-resolution AFM imaging.
- Overall morphology: A complex relief structure is observed, resulting from the combination of microscale step-like growth and nanoscale granular morphology.

This dual-scale morphology is of strategic importance for thermoelectric materials. On the one hand, electron transport processes are largely preserved; on the other hand, phonon propagation is suppressed. This can reduce thermal conductivity and contribute to an increase in the material's thermoelectric efficiency, expressed by the figure of merit ZT. Moreover, the step-like surface structure may shorten electron scattering paths, potentially inducing anisotropy in electrical conductivity.

Therefore, at the subsequent stages, the obtained morphological parameters were compared with data obtained by other methods, including Scanning Electron Microscopy (SEM), in order to draw comprehensive conclusions.

The surface topography of the resulting Bi_2Te_3–Sb_2Te_3 thin film was examined using Scanning Electron Microscopy (SEM) with a JSM-IT200 system (JEOL).

The acquired images clearly revealed the complex surface morphology of the material, including its granular structure, pores, and surface defects.

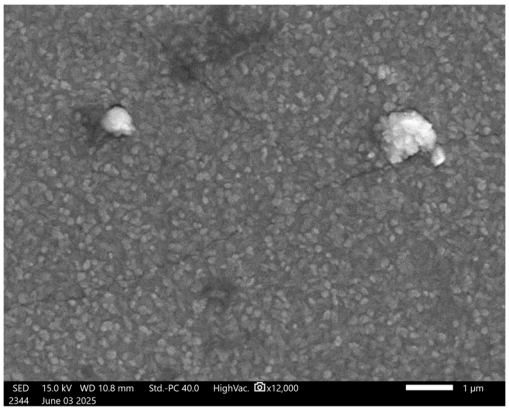

Figure 6. SEM image of the surface of synthesized Bi_2Te_3–Sb_2Te_3 thin films (magnification ×12,000)

In the SEM image presented in Figure 6 (magnification ×12,000, scale bar 1 μm), a clearly defined granular surface morphology is observed. The surface grains are uniformly distributed, and their sizes range from approximately 50 to 150 nm. In some regions, larger particles and surface protrusions can be seen. Such morphological features may result from the non-uniform growth of crystallites or the formation of localized agglomerations during the synthesis process. The high density of grain boundaries is expected to limit phonon transport paths, thereby reducing thermal conductivity. At the same time, its effect on electron transport may be relatively minor, which is considered a favorable factor for enhancing thermoelectric performance.

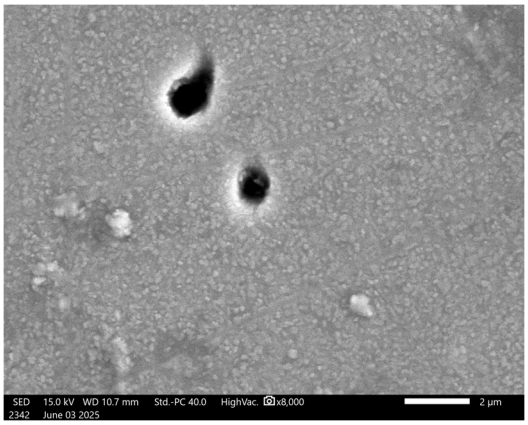

Figure 7. SEM image of the surface morphology of the synthesized Bi_2Te_3–Sb_2Te_3 thin films (magnification ×8,000)

Figure 7. The SEM image (magnification ×8,000, scale bar 2 μm) shows the formation of pores on the surface of the thin film. The pore diameters range from several hundred nanometers up to a few micrometers. The appearance of such porosity is typically associated with the evaporation rate during the synthesis process, the substrate temperature, or stoichiometric imbalances in the material composition. The presence of pore structures has a dual effect: on the one hand, it can enhance thermoelectric performance by reducing thermal conductivity; on the other hand, an excessive number of pores may compromise the mechanical stability of the material.

SEM observations revealed two predominant morphological features in the Bi_2Te_3–Sb_2Te_3-based thin films:

1. Nanometer-scale granularity — grains with sizes ranging from 50 to 150 nm are almost uniformly distributed across the entire surface. This promotes enhanced phonon scattering while preserving electron transport properties.
2. Micrometer-scale pores and coarse particles — some local defects formed during the film growth process may contribute to the reduction of thermal conductivity. However, if left uncontrolled, such defects could potentially compromise the mechanical integrity of the films.

These observations offer important implications for thermoelectric materials. Grain boundaries and pore structures can serve to reduce heat transport, thereby enhancing the thermoelectric figure of merit (ZT). At the same time, it is advisable to optimize synthesis parameters to preserve nanoscale granularity while minimizing the formation of large pores.

The SEM results confirm that the surface morphology of Bi_2Te_3–Sb_2Te_3-based thin films exhibits a nanogranular texture combined with a microporous structure. This complex topography plays a crucial role in improving thermoelectric performance.

5. CONCLUSIONS

The conducted studies demonstrated the formation of a dual-scale morphological structure in Bi_2Te_3–Sb_2Te_3-based thin films. Parameters identified through atomic force microscopy (AFM) confirmed the presence of nanoscale granularity on the film surface. The grain sizes ranged from 50 to 150 nm, and their presence is expected to enhance phonon scattering, thereby reducing thermal conductivity.

Longitudinal surface profile analyses revealed a step-like morphology with height variations of 0.790-0.798 μm. Scanning electron microscopy (SEM) revealed grains, coarse particles, and surface pores. Although the grains were distributed almost uniformly, local agglomerations and pores were also observed in certain regions.

Such a complex morphological structure, on the one hand, ensures efficient phonon scattering while preserving electron transport properties; on the other hand, it enhances thermoelectric performance by limiting thermal conductivity. However, excessive porosity may negatively affect the mechanical stability of the material.

In general, the coexistence of nanogranular and step-like relief observed in Bi_2Te_3–Sb_2Te_3-based thin films is of critical importance for thermoelectric materials. This morphology can be further optimized to improve functional properties by selecting appropriate synthesis conditions in future studies.

ORCID
Bunyodjon U. Omonov, https://orcid.org/0009-0009-7984-4866; **Sherzod Makhmudov,** https://orcid.org/0009-0003-6539-9278

REFERENCES

[1] E. Vieira, J. Figueira, A.L. Pires, J. Grilo, M.F. Silva, A.M. Pereira, and L.M. Gonçalves, "Bi_2Te_3 and Sb_2Te_3 thin films with enhanced thermoelectric properties for flexible thermal sensors," Proceedings, **2**(13), 815 (2018). https://doi.org/10.3390/proceedings2130815

[2] A. Ahmed, and S. Han, "Optimizing the Structural, Electrical and Thermoelectric Properties of Antimony Telluride Thin Films Deposited on Aluminum Nitride-coated Stainless Steel Foil," Scientific Reports. **10**, 6978 (2020). https://doi.org/10.1038/s41598-020-63954-0

[3] R. Venkatasubramanian, T. Colpitts, E. Watko, M. Lamvik, and B. Mason, "MOCVD of Bi_2Te_3, Sb_2Te_3 and their superlattice structures," Journal of Crystal Growth, **170**, 817 (1997). https://doi.org/10.1016/S0022-0248(96)00656-2

[4] A. Giani, A. Boulouz, F. Pascal-Delannoy, A. Foucaran, and A. Boyer, "Growth of Bi_2Te_3 and Sb_2Te_3 thin films by MOCVD: Effects of deposition temperature on surface morphology, crystallinity and electrical transport properties," Materials Science and Engineering: B, **64**(1), 19 (1999). https://doi.org/10.1016/S0921-5107(99)00142-7

[5] L.M. Gonçalves, C. Couto, P. Alpuim, D.M. Rowe, and J.H. Correia, "Thermoelectric Properties of Bi_2Te_3 / Sb_2Te_3 Thin Films," Materials Science Fórum, **514**, 156 (2006). https://doi.org/10.4028/www.scientific.net/MSF.514-516.156

[6] Y. Usmonov, M. Nabiyev, and Q. G'aynazarova, *Technology of Obtaining Semiconductor Thin Films,* (Textbook, Fergana, 2018), pp. 5-7.

[7] V.S. Kamlyuk, *Committee on Education of the Minsk City Executive Committee.* (Special Technology, Minsk, 2008), pp. 150-155.

[8] G.V. Bobrov, A.A. Ilyin, and V.S. Spektor, *Theory and Technology of Inorganic Coating Formation*. (Alfa-M, Moscow, 2014), pp. 728-730.

ОПТИМІЗАЦІЯ ВАКУУМНОЇ ТЕРМІЧНОЇ ВИПАРУВАЛЬНОЇ СИСТЕМИ ДЛЯ ОСАДЖЕННЯ ТОНКИХ ПЛІВОК Bi–Sb–Te

Буньоджон У. Омонов[1], Шерзод А. Максмудов[2]

[1]*Ферганський державний університет, Фергана, Узбекистан*

[2]*Інститут ядерної фізики, Ташкент, Узбекистан*

У цьому дослідженні тонкі плівки на основі халькогенідів вісмуту та сурми (Bi_2Te_3–Sb_2Te_3) були синтезовані за допомогою оптимізованої вакуумної системи термічного випаровування, а їхні морфологічні характеристики були ретельно досліджені. Результати атомно-силової мікроскопії (АСМ) виявили нанорозмірну зернистість на поверхні плівки (в діапазоні 50–150 нм) та чітку ступінчасту морфологію. Аналіз поздовжнього профілю показав, що варіації висоти знаходяться в діапазоні 0,790-0,798 мкм. Спостереження скануючої електронної мікроскопії (СЕМ) підтвердили утворення зерен, більших частинок та поверхневих пустот, що вказує на дворівневу морфологічну структуру. Така структура є критично важливою для підвищення термоелектричної ефективності шляхом посилення розсіювання фононів, тим самим зменшуючи теплопровідність, зберігаючи при цьому властивості електронного транспорту. Результати дослідження демонструють, що тонкі плівки на основі Bi_2Te_3–Sb_2Te_3 мають високий науковий та практичний потенціал як термоелектричні матеріали.

Ключові слова: *тонка плівка; морфологія; атомно-силова мікроскопія; електронна мікроскопія; термоелектрична ефективність; наногранулярність; ступінчаста структура*

EAST EUROPEAN JOURNAL OF PHYSICS. 1. 308-317 (2026)
DOI:10.26565/2312-4334-2026-1-36 ISSN 2312-4334

FIRST-PRINCIPLES INVESTIGATION OF ELECTRONIC AND MAGNETIC PROPERTIES IN Ga-DOPED SILICON CARBIDE NANOTUBES

Vusala Nabi Jafarova[1]*, Khayala Ajdar Hasanova[1,2], Adile Adem Guliyeva[3], Vusala Irshad Eminova[4], Ionut Cristian Scurtu[5]

[1]*Azerbaijan State Oil and Industry University, 20 Azalig Ave., AZ-1010, Baku, Azerbaijan*
[2]*Ministry of Science and Education Republic of Azerbaijan, Institute of Physics, 131 H. Javid Ave., AZ-1143, Baku, Azerbaijan*
[3]*Nakhchivan State University, AZ-7012, Nakhchivan, Azerbaijan*
[4]*French-Azerbaijani University (UFAZ) under Azerbaijan State Oil and Industry University, 183 Nizami Street, AZ-1010, Baku, Azerbaijan*
[5]*Mircea cel Batran Naval Academy, Str. Fulgerului, nr.1, 900218 Constanța, Romania*
**Corresponding Author E-mail: vusala.cafarova@asoiu.edu.az*
Received September 27, 2025; revised January 30, 2026; accepted February 2, 2026

This work explores the electronic and magnetic characteristics of gallium (Ga)-doped silicon carbide nanotubes (SiCNTs) through first-principles calculations. Two doping levels (8.3% and 16.6%) are considered, with Ga atoms substituting silicon sites in single-walled (6,0) SiCNTs. Spin-polarized band structure analysis shows that the system transitions from semiconducting at low doping to half-metallic at high doping, suggesting strong potential for spintronic applications. Density of states and Bader charge analyses reveal that Ga incorporation alters charge distribution and orbital interactions, particularly between Ga 5d and carbon 2p states. Magnetic moment calculations indicate that Ga induces localized magnetism primarily on neighboring carbon atoms, with the overall net magnetization increasing with increasing doping level. Energy comparisons between ferromagnetic and antiferromagnetic configurations point to an antiferromagnetic ground state, while formation energy evaluations confirm that Ga substitution at Si sites is thermodynamically favorable. Collectively, these results underscore Ga-doped SiCNTs as promising, tunable materials for future nanoscale electronic and spintronic devices.
Keywords: *SiC:Ga; Nanotube; Magnetic moment; Half-metallic*
PACS: 61.43.Bn; 71.20.-b; 73.22. -f; 75.50. Gg; 75.50. Pp; 78.67. Ch

1. INTRODUCTION

Graphene-like and other two-dimensional (2D) semiconductor materials have recently attracted increasing research attention because their unique physical and chemical properties enable promising applications in spintronic and optoelectronic devices, as demonstrated in recent reviews of emerging 2D materials with prospects in electronics, optoelectronics, and spintronics [1-3]. Silicon carbide (SiC), a third-generation wide-bandgap semiconductor, has become indispensable in high-voltage, high-temperature, high-frequency, and high-power devices due to its large band gap, high breakdown field, excellent thermal conductivity, chemical stability, and mechanical robustness, as demonstrated in studies on its superior performance in power electronics and thermal management furthermore, beyond traditional electronic applications, SiC has been recognized as a biocompatible and hemocompatible material suitable for advanced biomedical applications, including implantable devices, biosensing, and tissue engineering and more recently, its unique physical and electronic characteristics have enabled innovative roles in energy harvesting systems such as photovoltage generation and piezoelectric harvesting for harsh-environment applications [1-9].

Both theoretical and experimental studies have shown that silicon carbide nanotubes (SiCNTs) exhibit more stable electronic and magnetic properties than carbon nanotubes (CNTs) [2-6]. To broaden the applications of 1D, 2D, and 3D Si-based nanomaterials, researchers have increasingly explored doping with different impurity atoms to fine-tune their physical properties. Metal- and transition-metal-doped single-walled SiCNTs (SWSiCNTs) have demonstrated strong potential for applications in chemical sensing, hydrogen storage, and nanoscale spintronic devices. The incorporation of dopants alters charge distribution within the nanotube framework and can induce magnetic behavior. In most cases, the observed ferromagnetic (FM) characteristics originate from the hybridization between the dopants' d orbitals and the surrounding SiCNT states [10, 11].

Previous density functional theory (DFT) studies have confirmed that the electronic and magnetic properties of SiCNTs can be effectively tuned through doping. For example, Fe-doped SiCNTs were reported to exhibit either half-metallic antiferromagnetic (AFM) or ferromagnetic (FM) states depending on the substitution site of the dopant [1]. The adsorption of various transition metals (TMs) on SWSiCNTs was also investigated, revealing strong chemical binding with adsorption energies ranging from 1.17 eV (Cu) to 3.18 eV (Pt) [12]. Co doping has been shown to induce metallic behavior in cubic SiC, while Mn- and Fe-doped (8,0) SiCNTs displayed half-metallicity, making them promising for spintronic applications [13,14]. Furthermore, studies of the electronic and optical properties of different SiCNT chiralities have consistently confirmed their indirect-bandgap semiconducting nature [15,16].

Cite as: V.N. Jafarova, K.A. Hasanova, A.A. Guliyeva, V.I. Eminova, I.C. Scurtu, East Eur. J. Phys. 1, 308 (2026), https://doi.org/10.26565/2312-4334-2026-1-36

Silicon and carbon, due to their similar valence electron configurations, have long been predicted to form fullerene-like and nanotube structures, including chiral (6,0) SWSiCNTs [17]. Recent first-principles studies, including those that incorporate machine learning into DFT, have shown that noble-metal doping (e.g., Ag and Au) can endow SiCNTs with tunable magnetic properties suitable for spintronic applications [18–20]. These computational approaches also allow accurate predictions of electronic density of states and magnetic transitions under different doping conditions [21]. In particular, transition-metal dopants such as V and Co have been found to induce strong ferromagnetism and high Curie temperatures in SiCNTs, further supporting their potential in magnetic devices [20, 22, 23].

Beyond transition metals, group-III element doping has recently attracted interest. Studies on Al- and P-doped (6,0) SiCNTs revealed that Al substitution can significantly modulate electronic properties, suggesting controllable semiconducting behavior [24]. Related investigations on Al- and Ga-doped boron nitride nanotubes demonstrated enhanced CO adsorption energies [25] and improved surface reactivity toward H_2SiCl_2 [26], indicating that group-III elements enhance chemical sensitivity and surface interactions. Further DFT work on Al-doped carbon nanotubes confirmed improved adsorption of sulfur-containing gases, emphasizing the functional role of p-block dopants in tuning nanotube properties [27].

The motivation for this research is to identify new spintronic materials with tunable magnetic properties. Doping SiCNTs with group-III elements such as Ga offers a promising pathway, as these dopants introduce unique electronic and magnetic modifications distinct from transition metals. Unlike metallic dopants, p-block elements can yield stable, lightweight, and non-toxic spintronic materials. Investigating Al- and Ga-doped SWSiCNT systems therefore provides insight into how such dopants influences spin polarization and magnetic moment distribution, potentially enabling the design of non-magnetic-element-based spintronic nanodevices.

In addition to spintronics, doped nanotubes can stabilize isolated atoms, serving as active sites for single-atom catalysis (SAC). While SAC studies on Ga-doped SiCNTs are limited, similar behavior in doped graphene and other 2D systems suggests that Ga substitution may also enhance catalytic activity in SiCNTs [28]. Moreover, due to their chemical stability, high surface area, and tunable surface reactivity, doped SiC nanostructures are widely investigated for energy-related applications, including hydrogen storage, photocatalysis, and electrode materials for energy conversion and storage [29, 30]. Adharsh et al. [31] demonstrated that surface functionalization of (5,5) SiC nanotubes can form thermodynamically stable configurations with negative binding energies and significantly modify the electronic structure by tuning the band gap, confirming the high sensitivity of SiCNT electronic properties to chemical/atomic-level modifications. This supports the motivation of our work, where Ga doping is employed as an alternative and effective route to tailor the electronic and magnetic response of SiC nanotubes via first-principles calculations. Vlaskina et al. [32] investigated defect-related photoluminescence in SiC crystals and showed that stacking faults and deep-level defects introduce characteristic electronic states that strongly depend on the SiC polytype structure. Their findings highlight that imperfections and foreign-atom–induced states can critically reshape the electronic spectrum of SiC-based systems, which is directly relevant to our first-principles investigation of how Ga doping modifies the electronic and magnetic properties of SiC nanotubes.

2. COMPUTATIONAL DETAILS

In this study, first-principles calculations were carried out using the Atomistix ToolKit (ATK V-2023.09, http://quantumwise.com/) simulation package to examine the electronic and magnetic properties of Ga-doped SWSiCNTs. The modeled systems consisted of 24 atoms per unit cell. All calculations were performed within the framework of density functional theory (DFT) [31], employing the Local Spin Density Approximation (LSDA) [32] for the exchange-correlation potential, with FHI-type pseudopotentials [33] used to describe electron-ion interactions.

DFT is a quantum-mechanical modeling approach for investigating the electronic structure of many-body systems such as atoms, molecules, and solids. Rather than solving the full many-body Schrödinger equation, DFT reformulates the problem in terms of the electron density, ρ(r), as the primary variable. The central framework is based on the Kohn–Sham equations, which are obtained by minimizing the total energy functional with respect to the electron density. To account for magnetic effects, spin-polarized DFT was employed. Within this framework, LSDA serves as a reliable method for describing systems with unpaired electrons, localized magnetic moments, and magnetic ordering. In LSDA, the total electron density is divided into spin-up (ρ↑) and spin-down (ρ↓) components, allowing the evaluation of spin-dependent interactions. The total spin magnetization (M) of the system is defined as:

$$M = \int [\rho^{\uparrow}(r) - \rho^{\downarrow}(r)] dr \,. \tag{1}$$

It is well established that standard DFT implementations often underestimate semiconductor band gaps. To overcome this limitation, the DFT+U method, specifically the Local Spin Density Approximation with Hubbard U (LSDA+U) [34], introduces an on-site Coulomb interaction term to better describe localized electrons. Semi-empirical Hubbard U values were employed to enhance the accuracy of the electronic structure: a U_d of 5 eV was applied to the Si d-orbitals, while a U_p of 4.8 eV was assigned to the C p-orbitals, ensuring more reliable reproduction of the system's band gap. This correction is crucial in cases where LSDA suffers from self-interaction errors. Incorporating semi-empirical Hubbard U corrections [34] has significantly improved the predictive accuracy of semiconductor band gaps. In this work, the Hubbard U parameter was applied following simplified schemes reported in Refs. [35, 36].

In the spin-polarized DFT framework, both the Hamiltonian and density matrices were extended to include spin degrees of freedom, thereby allowing independent treatment of spin-up and spin-down channels. This formalism enables a more accurate description of magnetic properties and spin asymmetry in the electronic structure. Calculations were performed under the collinear spin approximation, which assumes all magnetic moments are aligned either parallel or antiparallel. This is a reasonable assumption for systems dominated by localized 3d transition-metal dopants in SiC nanotubes, where non-collinear magnetic effects are negligible.

The LSDA functional was chosen due to its computational efficiency and proven effectiveness in capturing spin polarization in transition-metal-doped semiconductors. Spin-resolved density of states (DOS) and magnetic moments were analyzed using Mulliken population analysis [37], which provides detailed insight into the spatial origin and distribution of magnetization. The spin density distribution, defined as $\rho\uparrow - \rho\downarrow$, was further examined to evaluate spin localization and magnetic interactions near the dopant sites.

Mulliken population analysis [37], a classical method in quantum chemistry, was employed to compute the local magnetic moments of 3d transition-metal-doped SWSiCNTs. By partitioning the electron density among atoms and orbitals, this approach allows estimation of atomic charges, orbital contributions, and bond populations. Within spin-polarized DFT, the electron density is divided into α-spin (spin-up) and β-spin (spin-down) components. The local spin magnetic moment on an atom A is defined as the difference between its α- and β-spin Mulliken populations:

$$\mu^A = N_\alpha^A - N_\beta^A \tag{2}$$

where N_α^A and N_β^A represent the numbers of spin-up and spin-down electrons assigned to atom A, respectively.

A nonzero value of μ^A indicates the presence of a local magnetic moment. The sign and magnitude of μ^A provide valuable information on the nature of magnetic ordering and spin coupling within the system. This formalism enabled us to quantify the magnetic contributions of dopant atoms as well as neighboring Si and C atoms in the nanotube framework. For doped SWSiCNTs, the partially filled 3d orbitals of transition-metal dopants typically introduce localized unpaired electrons, which lead to significant magnetic moments. Mulliken population analysis was employed not only to determine the magnitude of these local moments but also to reveal their spatial distribution between the Ga dopant and nearby Si and C atoms in the nanotube lattice. This information is essential for understanding the origin of magnetism in doped SiCNTs and their potential applications in spintronic or magnetic-sensing devices. Mulliken population analysis was also used to obtain orbital occupation numbers, from which magnetic moments were calculated as the difference between spin-up and spin-down populations. Partial density of states (PDOS) for each spin channel was determined using a Lorentzian broadening function [38], which smooths the discrete one-electron eigenvalues for graphical representation. The broadened PDOS is expressed as:

$$D_{nl\sigma}^{\alpha}(E) = \sum_i A_{nl\sigma i}^{\alpha} \frac{\delta/\pi}{\left(E - \varepsilon_{i\sigma}\right)^2 + \delta^2}, \tag{3}$$

let $\varepsilon_{i\sigma}$ denote the one-electron energies, where i is index of the energy level, and σ represents the spin state. The function $A_{nl\sigma i}^{\alpha}$ refers to the atomic orbital localized on atom α.

The total density of states (TDOS) is obtained by summing the projected density of states (PDOS) contributions for atom α at a given energy E. This requires a summation over all orbitals of atom α, characterized by the quantum numbers (n,l), as well as over both spin states (σ). The expression is typically written as Eq. (4):

$$D_\sigma(E) = \sum_{nl\alpha} D_{nl\sigma}^{\alpha}(E). \tag{4}$$

The quantum-confined SWSiCNT with a chiral vector of (6,0) was theoretically modeled using DFT method. To explore its electronic and magnetic behavior, Ga atoms were introduced as substitutional dopants. For Brillouin zone sampling, a Monkhorst-Pack grid of 1×1×5 k-points [39] was used, providing dense coverage along the nanotube's periodic z-axis. The plane-wave cutoff energy was set to 50 Ha, and all geometries were fully optimized at an electron temperature of 300 K. Convergence thresholds were chosen as <0.001 eV/Å for atomic forces and <0.001 eV/Å³ for cell stress. The valence electron configurations considered were: silicon ($3s^2 3p^2$, 4 valence electrons), carbon ($2s^2 2p^2$, 4 valence electrons), and gallium ($4s^2 4p^1$, 3 valence electrons).

This study specifically addresses the influence of Ga doping concentration on the structural, electronic, and magnetic properties of SiCNTs. Two substitutional cases were considered: Ga replacing Si atoms and Ga replacing C atoms. Single doping corresponds to a concentration of 8.3%, while double doping corresponds to 16.6%. By comparing these doping schemes, the impact of dopant type, substitutional site, and concentration on the system's fundamental properties was systematically investigated. Such insights are essential for tailoring SiCNTs for potential nanoelectronic and spintronic applications.

To further examine magnetic ordering, both ferromagnetic (FM) and antiferromagnetic (AFM) configurations were modeled by substituting Si atoms with Ga. In the FM case, dopants carried parallel spins (Ga ↑ x/2; Ga ↑ x/2),

whereas in the AFM case, the spins were antiparallel (Ga ↑ x/2; Ga ↓ x/2). Here, ↑ and ↓ indicate the orientation of the local magnetic moments associated with the Ga dopants.

RESULTS AND DISCUSSION

Electronic properties of $Ga_xSi_{1-x}C$ NT

In this section, we present the calculated majority- and minority-spin band structures, total density of states (TDOS), and partial density of states (PDOS) for Ga-doped SWSiCNTs, in which Ga atoms substitute for Si sites. In addition to the electronic structure analysis, Bader charge calculations were performed to examine charge redistribution induced by Ga doping. The focus is placed on two doping concentrations 8.3% (single substitution) and 16.6% (double substitution) to investigate how varying dopant levels influence the electronic and magnetic properties of SiCNTs. Understanding these effects is critical for tailoring SiCNTs toward nanoelectronic and spintronic applications. From first-principles calculations, spin-resolved band gaps were obtained and are illustrated in Figs. 1 and 2. Figure 1shows the spin-dependent band structures of Ga-doped SWSiCNTs, confirming semiconducting behavior in both spin-up and spin-down channels at low doping. Specifically, for the single Ga-doped system (8.3% concentration), where one Si atom is replaced by Ga, the estimated band gaps are ~1.0 eV for the majority-spin states and ~0.6 eV (direct) and ~0.5 eV (indirect) for the minority-spin states.

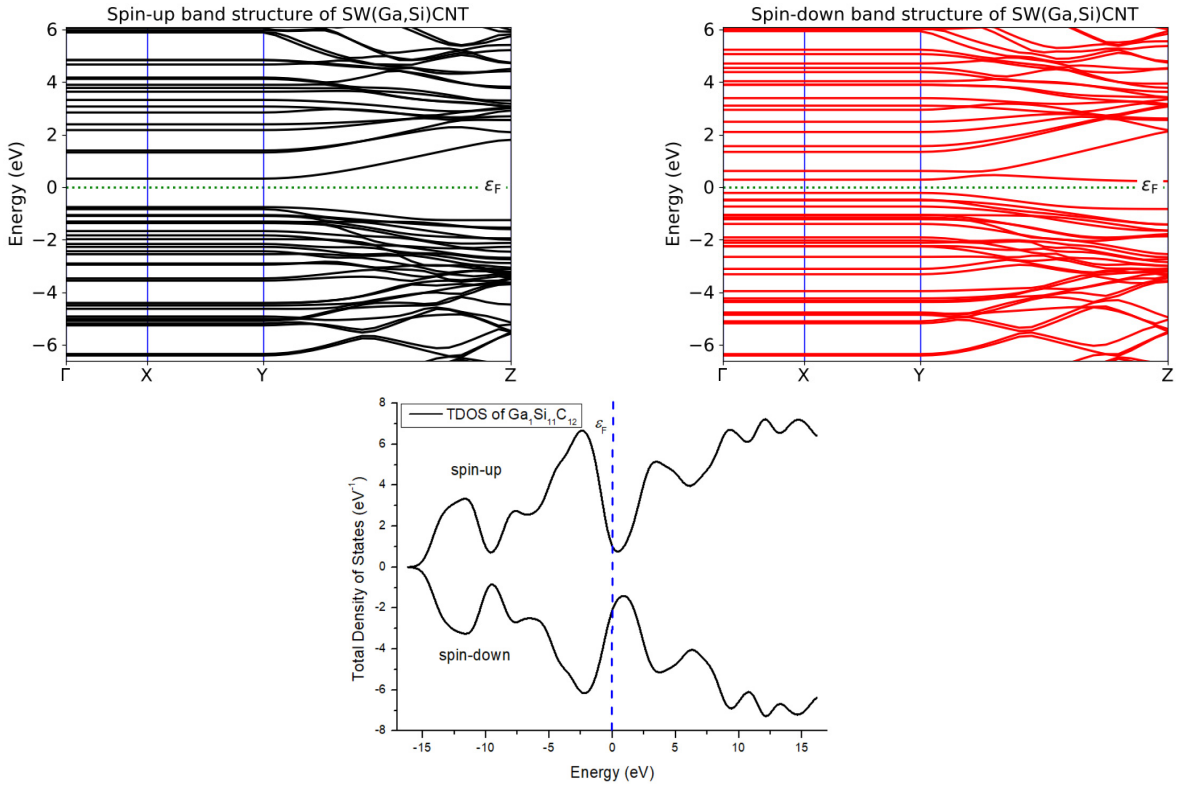

Figure 1. Spin-polarized band structures (spin-up: black, spin-down: red) and the corresponding total density of states (TDOS) for the studied $Ga_xSi_{1-x}C$ NTs

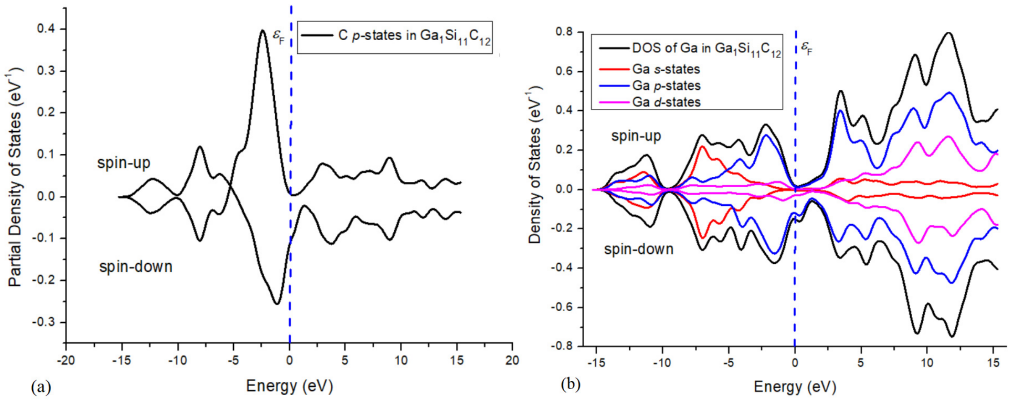

Figure 2. PDOS of C (a) and Ga (b) atoms in $Ga_xSi_{1-x}C$ nanotubes, with positive/negative values denoting majority/minority spin states

In contrast, for the double Ga-doped configuration (16.6% concentration), where two Si atoms are substituted by Ga, the spin-up channel retains a semiconducting gap of ~1.2 eV. However, in the spin-down channel, the bands cross the Fermi level, producing a vanishing band gap. This pronounced spin asymmetry reveals a half-metallic character, a key property for spintronic device applications.

First-principles simulations show that Ga doping significantly modifies the electronic structure of the (6,0) SWSiCNT. In the single-doped system, the minority-spin band gap is reduced to 0.5 eV, while the majority-spin channel remains semiconducting. Partial density of states (PDOS) analysis reveals that states near the Fermi level are predominantly derived from the C 2p and Ga 5d orbitals. In particular, the notable contribution of Ga 5d orbitals at the Fermi energy highlights a moderate orbital interaction between Ga and neighboring C atoms.

Table 1 summarizes the calculated spin-resolved band gaps for Ga-doped SWSiCNTs at different doping levels. The pristine nanotube exhibits a semiconducting band gap of 0.98 eV, consistent with our earlier findings [21]. At 8.3% Ga doping (single substitution at a Si site), the system displays spin asymmetry, with a 1.0 eV gap in the spin-up channel and reduced gaps of 0.6 eV (direct) and 0.5 eV (indirect) in the spin-down channel. This confirms the preservation of semiconducting behavior, albeit with distinct spin-dependent gaps.

In contrast, at 16.6% Ga doping (double substitution), the spin-up channel retains a semiconducting gap of ~1.2 eV, while the spin-down bands cross the Fermi level, closing the gap entirely. This spin asymmetry establishes a robust half-metallic state, underscoring the potential of Ga-doped SWSiCNTs as promising candidates for spintronic devices, where spin-selective conductivity is essential.

Table 1. Spin-resolved band gaps (↑ , ↓) of Ga-doped SWSiCNTs at varying doping levels

System	Doping level	Band gap (eV)	Electronic Nature	Remarks
SWSiCNT (undoped)	0%	0.98	Semiconductor	Previous work [21]
SWSiCNT (Ga at Si site)	8.3%	1.0 (↑), 0.6 (direct) (↓), 0.5 (indirect) (↓)	Semiconductor	Spin asymmetry; majority spin semiconducting, minority spin nearly metallic
SWSiCNT (2 Ga at Si sites)	16.6%	1.2 (↑), 0 (↓)	Half-metal	Spin-down bands cross Fermi level

To further investigate the electronic interactions in Ga-doped SWSiCNTs, where Ga substitutes a Si atom, Bader charge analysis was carried out. The results reveal a distinct redistribution of charge upon doping. The Ga dopant exhibits a net Bader charge of approximately −1.05 e, notably less negative than the substituted Si atom (−2.33 e). This indicates that Ga contributes fewer electrons to the lattice, a consequence of its lower electronegativity and larger atomic radius compared to Si. The neighboring carbon atoms, particularly C14 the atom closest to the Ga site acquire a charge of about +1.94 e, which is lower than the typical ~+2.3 e gain observed for C atoms adjacent to Si. This reduction points to a weaker covalent character in the Ga-C interaction relative to the original Si-C bond, potentially altering the local electronic and magnetic properties.

In summary, Bader charge analysis confirms that Ga substitution at the Si site reduces charge transfer to the surrounding lattice. This diminished electron donation, along with weaker orbital hybridization with neighboring C atoms, aligns with the reduced spin polarization observed in the electronic structure.

Magnetic properties of $Ga_xSi_{1-x}C$ NT

We investigated the magnetic properties of Ga-doped (6,0) SiCNTs, focusing on substitutional doping at the Si site. To assess the magnetic behavior, we computed the atomic and total magnetic moments and compared ferromagnetic (FM) and antiferromagnetic (AFM) configurations to identify the most stable magnetic phase. Additionally, electron difference density plots were analyzed to visualize charge redistribution induced by Ga doping, highlighting the interaction between the Ga dopant and neighboring Si and C atoms. This combined analysis of spin-polarized electronic structure, magnetic moments, and local charge transfer provides a comprehensive view of the magnetic response introduced by Ga substitution.

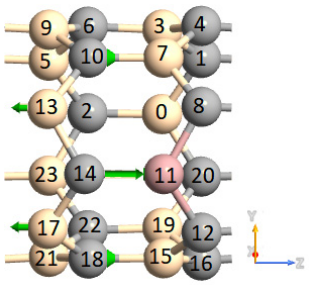

Figure 3. Spin-polarized structure of $Ga_xSi_{1-x}C$ nanotubes, with Si (beige), C (grey), Ga (pink), and magnetic moments (green arrows)

The Mulliken spin analysis shows that a single Ga substitution yields a total magnetic moment of ~1.0 μ_B, confirming the emergence of spin polarization (Fig. 3). Interestingly, the Ga atom itself carries a negative spin magnetic moment of −0.336 μ_B, acting as a localized magnetic impurity. The strongest positive spin polarization is observed on adjacent carbon atoms, with C14 exhibiting a significant magnetic moment of ~1.6 μ_B. Additional contributions come from C10 and C18, each exceeding 0.4 μ_B. In contrast, nearby Si atoms, such as Si13 and Si17, show negative spin moments of ~−0.5 μ_B, indicating antiparallel coupling with the polarized carbon atoms. This distribution suggests that magnetism in the single-doped system originates mainly from induced spin polarization on carbon atoms, partially compensated by negative contributions from Ga and its neighboring Si atoms.

When two Ga atoms are introduced, the total spin magnetic moment nearly doubles to ~2.0 μ_B, suggesting largely additive contributions from each dopant. The Ga atoms exhibit stronger negative spin moments (~−0.57 μ_B), reinforcing their role as localized magnetic impurities. Several neighboring carbon atoms, including C1, C4, C8, C12, and C20, display enhanced positive magnetic moments close to or exceeding 1.0 μ_B, revealing stronger spin polarization in the carbon sublattice compared to the single-doped case. Although silicon atoms continue to exhibit negative spin moments, their magnitudes are somewhat reduced, likely due to overlapping spin polarization fields from multiple dopants.

Overall, the magnetism in Ga-doped SiCNTs arises from a complex interplay between localized negative spin moments on Ga and Si atoms and strong positive polarization on specific carbon atoms. In the double-doped system, the overlapping polarization fields enhance the net magnetization while simultaneously modulating local spin distributions. These findings highlight the critical role of carbon atoms as hosts of induced magnetic moments, while silicon atoms mediate spin coupling in the doped nanotube.

The orbital analysis reveals a pronounced redistribution of electronic charge and spin polarization around the Ga dopant and its neighboring atoms. For the three carbon atoms directly bonded to Ga, strong occupation of the p-orbitals, particularly the p_x and p_y components, correlates with the substantial positive spin magnetic moments observed in these sites. In contrast, the Ga dopant itself exhibits dominant s and p-orbital occupation, but with relatively small spins contributions. This behavior reflects Ga's role as an electron acceptor and a weakly magnetic center rather than a strong contributor to the net magnetization. Surrounding silicon atoms display negative spin polarization, arising mainly from their p-orbitals. These negative contributions compensate for the spin accumulation localized on nearby carbon atoms, thereby influencing the overall balance of magnetic interactions within the nanotube.

Table 2 summarizes the calculated spin magnetic moments (in μ_B) for individual atoms in SiCNTs with one and two Ga dopants substituting Si sites. The results demonstrate how Ga incorporation systematically modifies local spin distributions, clarifying the mechanisms by which Ga affects the overall magnetic properties of the SiCNT system.

Table 2. Magnetic moments (μ_B) of atoms in Ga-doped (6,0) SiCNTs at Si sites

No.	Element	Spin Moment (1 Ga-doped)	Spin Moment (2 Ga-doped)
0	Si	-0.002	-0.574 (Ga)
1	C	-0.001	1.036
2	C	0.010	0.474
3	Si	-0.028	-0.582
4	C	0.095	0.891
5	Si	-0.006	-0.376
6	C	0.011	0.153
7	Si	-0.167	-0.582
8	C	0.183	1.036
9	Si	-0.137	-0.253
10	C	0.408	0.154
11	Ga	-0.336	-0.573
12	C	0.183	1.035
13	Si	-0.500	-0.375
14	C	1.612	0.470
15	Si	-0.167	-0.582
16	C	0.095	0.892
17	Si	-0.500	-0.375
18	C	0.408	0.154
19	Si	-0.028	-0.582
20	C	-0.001	1.036
21	Si	-0.137	-0.253
22	C	0.011	0.154
23	Si	-0.006	-0.376
	Sum	**1.001**	**2.002**

The results clearly establish that carbon atoms play a central role in sustaining and amplifying the magnetization induced by Ga doping, with certain carbon sites exhibiting particularly large spin magnetic moments. In contrast, the negative spin moments on Ga and nearby Si atoms reflect antiferromagnetic coupling, which partially offsets the positive contributions from carbon. As a result, the net magnetic moment is smaller than the simple sum of absolute spin values. Importantly, the nearly linear increase in total magnetization when moving from one to two Ga dopants indicates that magnetic contributions from individual Ga atoms and their surrounding carbon environments add constructively, with minimal magnetic quenching. Such behavior highlights the tunability of magnetism in SiCNTs through controlled doping strategies, which is highly relevant for spintronic applications requiring specific spin configurations. These findings also emphasize the importance of both dopant concentration and the local atomic environment in tailoring magnetic behavior within low-dimensional semiconductor nanostructures.

Figure 4 depicts the charge density redistribution caused by substitutional Ga doping at a Si site. The purple regions represent electron accumulation, primarily localized around the Ga dopant and adjacent carbon atoms, while the

cyan regions indicate electron depletion, largely concentrated near the replaced Si site. This charge transfer pattern underscores the modified bonding interactions between Ga and the host nanotube lattice, offering critical insight into how Ga incorporation alters the local electronic environment and, consequently, the overall electronic properties of the system.

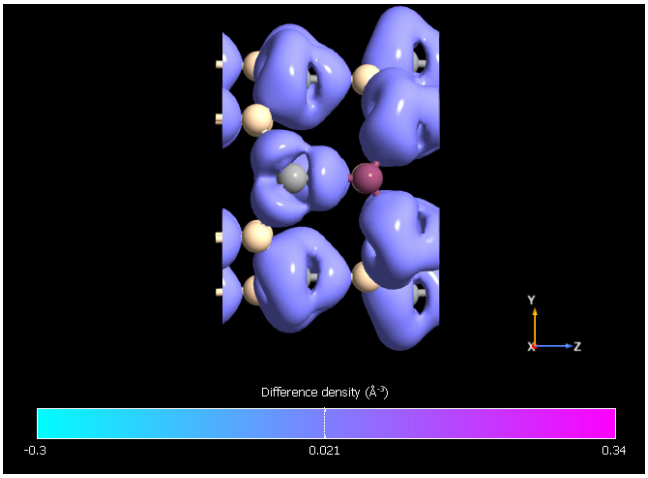

Figure 4. Spin density isosurface of Ga-doped SWSiCNT at the Si site, showing charge accumulation (purple) and depletion (cyan). Si, C, and Ga atoms are represented by beige, gray, and pink spheres, respectively

The total energy comparison between ferromagnetic (FM) and antiferromagnetic (AFM) states reveals that the AFM configuration is energetically more favorable. Specifically, the calculated total energies are −4108.82776 eV for the FM state and −4108.92690 eV for the AFM state, yielding a positive energy difference in favor of AFM ordering. This result indicates that Ga-doped (6,0) SWSiCNTs prefer an antiferromagnetic ground state. The emergence of such magnetic ordering highlights their potential as nanoscale magnetic materials, making them promising candidates for spintronic and nanomagnetic device applications.

Formation energies of Ga-doped (6,0) SWSiCNTs

Defect formation and dopant incorporation are critical factors in shaping the physical and chemical properties of nanoscale materials. The formation energy of a defect structure quantifies the energetic cost of introducing dopants into the host lattice and serves as a key indicator of thermodynamic stability. A lower formation energy implies a more stable and experimentally accessible configuration, facilitating dopant incorporation during material synthesis and device fabrication. In contrast, high formation energies suggest that a given doped structure may be challenging to achieve or maintain, limiting its practical applicability.

In this study, the formation energies of both single and double Ga-doped (6,0) SWSiCNTs were calculated at substitutional Si sites to assess their stability and likelihood of experimental realization. These values provide essential insight into the feasibility of controlled Ga doping for tailoring the electronic and magnetic properties of SiCNTs in future spintronic and nanoelectronic applications.

The formation energy $E_{\text{form.}}$ was calculated using the following expression:

$$E_{form.} = E_{doped} - E_{pristine} - n \cdot \mu_{Ga} + n \cdot \mu_{Si} \tag{5}$$

where E_{doped} and E_{pristine} are the total energies of the doped and pristine nanotubes, respectively; μ_{Ga} and μ_{Si} denote the chemical potentials of the dopant and substituted atoms; and n represents the number of dopants (1 for single doping and 2 for double doping).

In this study, the chemical potential values of Ga, Si, and C were taken as −2.228112 eV, −3.686924 eV, and −5.114380 eV, respectively. The total energy of the pristine nanotube, obtained from our calculations, was E_{pristine}=−3983.35741 eV. These values were used to determine the defect formation energies for all doping configurations.

Table 3 presents the calculated formation energies for single and double Ga doping at Si substitutional sites, providing a comparative overview of the thermodynamic stability across different configurations.

Table 3. Total (E_{doped}) and formation ($E_{\text{form.}}$) energies of single- and double-Ga-doped SiCNTs at Si sites, with dopant concentration x (%) indicated

System	x, %	E_{doped}, eV	E_{form}, eV
$Si_{11}Ga_1C_{12}$	8.3	-4046.11780	-64.21920
$Si_{10}Ga_2C_{12}$	16.6	-4108.82776	-128.3887

The results show that Ga doping at Si sites consistently yields negative formation energies, confirming that Ga incorporation is energetically favorable and stabilizes defect structures within SiC nanotubes. Moreover, the

increasingly negative values observed for double doping indicate that higher Ga concentrations are thermodynamically preferred. This trend suggests that Ga not only integrates stably into the nanotube lattice but also enhances structural stability as the doping level increases. The total energy decreases with increasing Ga concentration, indicating enhanced stabilization of the doped nanotube structure.

Figure 4 represents the variation of total energy (E_{doped}) and formation energy ($E_{form.}$) of Ga-doped SiCNTs with dopant concentration (x). The decreasing trend of both energies with increasing Ga content indicates that Ga substitution at Si sites enhances the structural stability and thermodynamic favorability of the nanotubes.

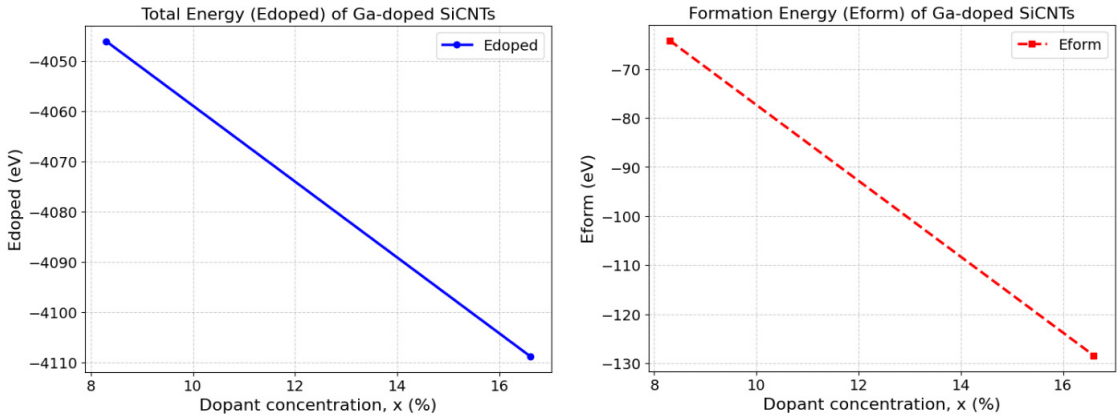

Figure 5. Variation of total (E_{doped}) and defect-formation energies ($E_{form.}$) of Ga-doped SWSiCNTs with dopant concentration (x=8.3 and 16.6 %)

These results suggest that Ga substitution enhances the thermodynamic stability of SWSiCNTs, making them more favorable at higher dopant concentrations. The decreasing energies further suggest that Ga doping may induce beneficial modifications to the nanotubes' electronic and structural properties, which could benefit applications in nanoelectronics and sensing devices.

These findings complement the magnetic ground state analysis, providing a comprehensive understanding of both the energetic favorability and practical feasibility of Ga doping in SWSiCNTs. The preference for Si substitutional sites aligns with Ga's known chemical and electronic compatibility with semiconductor lattices, reinforcing its suitability as a dopant. Collectively, the results highlight Ga's effectiveness in stabilizing the SiCNT framework, guiding future experimental efforts to optimize doped nanotubes for spintronic and nanoelectronic devices.

4. CONCLUSIONS

In this study, first-principles calculations were employed to systematically investigate the influence of Ga doping on the electronic and magnetic properties of (6,0) single-walled silicon carbide nanotubes (SWSiCNTs). The results demonstrate that Ga substitution at Si sites induces pronounced spin asymmetry and drives the system toward a half-metallic state at higher doping concentrations, thereby enhancing its potential for spintronic applications.

Bader charge and orbital analyses reveal that Ga substitution reduces charge transfer relative to pristine SiCNTs, weakening covalent bonding and modifying the local electronic environment. The induced magnetism originates primarily from neighboring carbon atoms, which develop strong positive spin polarization, while Ga and nearby Si atoms exhibit negative spin moments that couple antiferromagnetically. The total magnetic moment increases nearly linearly with doping concentration, and energy calculations confirm that the AFM state is the preferred ground state.

The negative formation energies of both single and double Ga doping configurations confirm the thermodynamic stability and experimental feasibility of Ga incorporation at Si sites. These results highlight Ga-doped SiCNTs as a robust and versatile material platform for engineering nanoscale magnetism and electronic behavior. Overall, this work offers valuable theoretical insights to guide the design and optimization of doped SiCNTs for advanced applications in spintronics and nanoelectronics.

ORCID

V.N. Jafarova, https://orcid.org/0000-0002-0643-1464; **Kh.A. Hasanova**, https://orcid.org/0009-0002-0476-0077
A.A. Guliyeva, https://orcid.org/0009-0004-7405-3049; **V.I. Eminova,** https://orcid.org/0009-0003-6827-9191
I.C. Scurtu, https://orcid.org/0000-0003-3105-6384

REFERENCES

[1] E.C. Ahn, "2D materials for spintronic devices," npj 2D Materials and Applications, **4**, 17 (2020). https://doi.org/10.1038/s41699-020-0152-0
[2] Md. M. Uddin, *et al*., "Graphene-like emerging 2D materials: recent progress, challenges and future outlook," RSC Advances, **13**, 33336–33375 (2023). https://doi.org/10.1039/D3RA04456D
[3] Md. A. Islam, *et al*., "Recent advances of 2D materials in semiconductor application: A review," Advanced Sensor and Energy Materials, **100161** (2025). https://doi.org/10.1016/j.asems.2025.100161

[4] B. Baumeier, P. Krüger, and J. Pollmann, "Structural, elastic, and electronic properties of SiC, BN, and BeO nanotubes," Physical Review B, **76**, 085407 (2007). https://doi.org/10.1103/PhysRevB.76.085407
[5] C.L. Frewin, C. Locke, S.E. Saddow, and E.J. Weeber, "Single-crystal cubic silicon carbide: an in vivo biocompatible semiconductor for brain–machine interface devices," Proceedings of the Annual International Conference of the IEEE Engineering in Medicine and Biology Society, 2957–2960 (2011). https://doi.org/10.1109/IEMBS.2011.6090582
[6] J.S. Ponraj, S.C. Dhanabalan, G. Attolini, and G. Salviati, "SiC nanostructures toward biomedical applications and its future challenges," Critical Reviews in Solid State and Materials Sciences, **41**, 430–446 (2016). https://doi.org/10.1080/10408436.2016.1150806
[7] S.E. Saddow, C. Frewin, *et al.,* "Single-crystalline silicon carbide: A biocompatible and hemocompatible semiconductor for advanced biomedical applications," Materials Science Forum, **679–680**, 824–830 (2011). https://doi.org/10.4028/www.scientific.net/MSF.679-680.824
[8] S.M.S.H. Rafin, *et al*.: "Power electronics revolutionized: A comprehensive analysis of emerging wide and ultrawide bandgap devices," Micromachines, **14**(11), 2045 (2023). https://doi.org/10.3390/mi14112045
[9] M.A. Mahdy, S.H. Kenawy, E.M.A. Hamzawy, G.T. El-Bassyouni, and I.K. El Zawawi, "Influence of silicon carbide on structural, optical and magnetic properties of Wollastonite/Fe_2O_3 nanocomposites," Ceramics International, **47**(9), 12047–12055 (2021). https://doi.org/10.1016/j.ceramint.2021.01.048
[10] A. Du, and S.C. Smith, "Silicon carbide nanotubes functionalized by transition metal atoms: a density functional study," The Journal of Physical Chemistry C, **111**(52), 20295–20300 (2007). https://doi.org/10.1021/jp073722m
[11] S. Yan, *et al*., "Transition metal induced magnetization in zigzag silicon carbide nanotubes," Journal of Computational Electronics, **22**, 203–212 (2023). https://doi.org/10.1007/s10825-023-02030-y
[12] J.X. Zhao, and Y.H. Ding, "Silicon carbide nanotubes functionalized by transition metal atoms: A density-functional study," The Journal of Physical Chemistry C, **112**, 2558–2564 (2008). https://doi.org/10.1021/jp073722m
[13] H. Heidarzadeh, "Transition metal-doped 3C-SiC as a promising material for intermediate band solar cells," Optical and Quantum Electronics, **51**, 32 (2019). https://doi.org/10.1007/s11082-019-1742-y
[14] A.T. Mulatu, K.N. Nigussa, and L.D. Deja, "Electronic and optical properties of TM-doped (8,0) SiC single-walled nanotubes and the prospect of hydrogen storage," *Optical Materials*, **134**, 113094 (2022). https://doi.org/10.1016/j.optmat.2022.113094
[15] Ch. Vatankhah, and H.A. Badehian, "Electronic and optical properties of armchair silicon carbide nanotubes from first principles," Optik, **237**, 166740 (2021). https://doi.org/10.1016/j.ijleo.2021.166740
[16] W. Wang, J. Xu, Y. Zhang, and G. Li, "First-principles study of electronic structure and optical properties of silicon/carbon nanotube," Computational Chemistry, **5**, 159–171 (2017). https://doi.org/10.4236/cc.2017.54013
[17] M.N. Huda, and A. Ray, "Evolution of SiC nanocluster from carbon fullerene: A density functional theoretic study," Chemical Physics Letters, **457**(1–3), 124–129 (2008). https://doi.org/10.1016/j.cplett.2008.03.057
[18] R.Z. Ibaeva, V.N. Jafarova, V.I. Eminova, I.C. Scurtu, and S. Lupu, "First-principles study of electronic and magnetic properties of Ag- and Au-doped single-walled (6,0) SiC nanotubes: DFT study," Journal of Nanoparticle Research, **26**(9), 203 (2024). https://doi.org/10.1007/s11051-024-06109-w
[19] V.N. Jafarova, S.S. Rzayeva, I.C. Scurtu, C. Stanca, N. Acomi, and G. Raicu, "Prediction of ferromagnetism in GaN:Ag and SiC:Ag nanotubes," Advances in Natural Sciences: Nanoscience and Nanotechnology, **15**(3), 035012 (2024). https://doi.org/10.1088/2043-6262/ad71a7
[20] V.N. Jafarova, V.I. Eminova, M.A. Musaev, and I.C. Scurtu, "Prediction of ferromagnetic characteristics of gold-doped SiC nanotubes for application in spintronic devices," Technium, **26**, 1–8 (2025). https://doi.org/10.47577/technium.v26i.12149
[21] N.T. Tien, P.T.B. Thao, V.N. Jafarova, and D. Dey Roy, "Predicting model for device density of states of quantum-confined SiC nanotube with magnetic dopant: An integrated approach utilizing machine learning and density functional theory," Silicon, 1–19 (2024). https://doi.org/10.1007/s12633-024-03127-0
[22] S. Rzayeva, V.N. Jafarova, and D.D. Roy, "First-principles prediction of ferromagnetism and Curie temperature for transition metals doped single-walled (6,0) SiC nanotubes: Materials for application in spintronics," Materials Science in Semiconductor Processing, **197**, 109702 (2025). https://doi.org/10.1016/j.mssp.2025.109702
[23] S. Rzayeva, and V.N. Jafarova, "Electronic and magnetic properties of cobalt-doped SiCNT: A first-principles study," Journal of Polytechnic, **28**(3), 947–955 (2025). https://doi.org/10.2339/politeknik.1536597
[24] A.Q. Wu, Q.G. Song, and L. Yang, "First-principles study on Al or/and P doped SiC nanotubes," Advanced Materials Research, **510**, 747–752 (2012). https://doi.org/10.4028/www.scientific.net/AMR.510.747
[25] A.A. Peyghan, A. Soltani, A.A. Pahlevani, Y. Kanani, and S. Khajeh, "A first-principles study of the adsorption behavior of CO on Al- and Ga-doped single-walled BN nanotubes," Applied Surface Science, **270**, 25–32 (2013). https://doi.org/10.1016/j.apsusc.2012.12.008
[26] M.D. Mohammadi, H.Y. Abdullah, G. Biskos, and S. Bhowmick, "Effect of Al- and Ga-doping on the adsorption of H_2SiCl_2 onto the outer surface of boron nitride nanotube: A DFT study," Comptes Rendus Chimie, **24**(2), 291–304 (2021). https://doi.org/10.5802/crchim.87
[27] H. Tavakol, and H. Haghshenas, "A DFT study on the interaction of doped carbon nanotubes with H_2S, SO_2, and thiophene," Quantum Reports, **3**(3), 366–375 (2021). https://doi.org/10.3390/molecules26030223
[28] S.S. Hardisty, X. Lin, A.R.J. Kucernak, and D. Zitoun, "Single-atom Pt on carbon nanotubes for selective electrocatalysis," Carbon Energy, **6**(1), e409 (2023). https://doi.org/10.1002/cey2.409
[29] Y.S. Itas, R. Razali, S. Tata, A.M. Idris, and M.U. Khandaker, "Studies of the hydrogen energy storage potentials of Fe- and Al-doped silicon carbide nanotubes (SiCNTs) by optical adsorption spectra analysis," Journal of Energy Storage, **72**, 108534 (2023). https://doi.org/10.1016/j.est.2023.108534
[30] W. Liu, Q. Li, X. Yang, X. Chen, and X. Xu, "Synthesis and characterization of N-doped SiC powder with enhanced photocatalytic and photoelectrochemical performance," Catalysts, **10**, 769 (2020). https://doi.org/10.3390/catal10070769

[31] U. Adharsh, R. Akash, A. Sakthi Balaji, D. John Thiruvadigal, R.M. Hariharan, J. Sneha, V. Abinaya, and K.J. Sivasankar, "Chemical functionalization of silicon carbide nanotube (SiCNT): First principles DFT study," ECS Journal of Solid State Science and Technology, **12**, 111001 (2023). https://doi.org/10.1149/2162-8777/ad0327
[32] S.I. Vlaskina, *et al*., "Nano silicon carbide's stacking faults, deep levels and grain boundary defects," Journal of Nano- and Electronic Physics, **10**(5), 05021 (2018). https://doi.org/10.21272/jnep.10(5).05021
[33] W. Kohn, and L.J. Sham, "Self-consistent equations including exchange and correlation effects," Physical Review, **140**, A1133–A1138 (1965). https://doi.org/10.1103/PhysRev.140.A1133
[34] V.N. Jafarova, "Structural, electronic and magnetic properties of pure and Fe-doped ZnSe: First-principles investigation," Pramana – Journal of Physics, **98**, 82–93 (2024). https://doi.org/10.1007/s12043-024-02752-z
[35] M. Fuchs, and M. Scheffler, "Ab initio pseudopotentials for electronic structure calculations of polyatomic systems using density functional theory," Computer Physics Communications, **119**, 67–98 (1999). https://doi.org/10.1016/S0010-4655(98)00201-X
[36] M. Cococcioni, and S. de Gironcoli, "A linear response approach to the calculation of the effective interaction parameters in the LDA+U method," *Physical Review B*, **71**, 035105 (2005). https://doi.org/10.1103/PhysRevB.71.035105
[37] S.L. Dudarev, G.A. Botton, S.Y. Savrasov, C.J. Humphreys, and A.P. Sutton, "Electron-energy-loss spectra and the structural stability of nickel oxide: An LSDA+U study," Physical Review B, **57**, 1505–1509 (1998). https://doi.org/10.1103/PhysRevB.57.1505
[38] A.I. Liechtenstein, V.I. Anisimov, and J. Zaanen, "Density-functional theory and strong interactions: Orbital ordering in Mott–Hubbard insulators," Physical Review B, **52**, R5467–R5470 (1995). https://doi.org/10.1103/PhysRevB.52.R5467
[39] S.C. North, K.R. Jorgensen, J. Pricetolstoy, and A.K. Wilson, "Population analysis and the effects of Gaussian basis set quality and quantum mechanical approach: Main group through heavy element species," Frontiers in Chemistry, **11**, 1152500 (2023). https://doi.org/10.3389/fchem.2023.1152500
[40] W. Gough, "The graphical analysis of a Lorentzian function and a differentiated Lorentzian function," Journal of Physics A: General Physics, **1**, 704–709 (1968). https://doi.org/10.1088/0305-4470/1/6/309
[41] H.J. Monkhorst, and J.D. Pack, "Special points for Brillouin-zone integrations," Physical Review B, **13**, 5188–5192 (1976). https://doi.org/10.1103/PhysRevB.13.5188

ПЕРШОПРИНЦИПНІ ДОСЛІДЖЕННЯ ЕЛЕКТРОННИХ ТА МАГНІТНИХ ВЛАСТИВОСТЕЙ НАНОТРУБОК КАРБІДУ КРЕМНІЮ, ЛЕГОВАНИХ ГАЛІЄМ

Вусала Набі Джафарова[1], Хаяла Аждар Гасанова[1,2], Аділя Адем Гулієва[3], Вусала Іршад Емінова[4], Іонут Крістіан Скурту[5]

[1]Азербайджанський державний університет нафти та промисловості, 20 пр. Азаліг, AZ-1010, Баку, Азербайджан
[2]Міністерство науки та освіти Азербайджанської Республіки, Інститут фізики, просп. Г. Джавіда, 131, AZ-1143, Баку, Азербайджан
[3]Державний університет Нахчівана, AZ 7012 Нахчіван, Азербайджан
[4]Франко-Азербайджанський університет (UFAZ) при Азербайджанському державному університеті нафти і промисловості Вулиця Нізамі, 183 AZ-1010, Баку Азербайджан
[5]Військово-морська академія Мірчі Старшого, вулиця Фулгерулуй, 1, 900218, Констанца, Румунія

Ця робота досліджує електронні та магнітні характеристики нанотрубок карбіду кремнію (SiCNT), легованих галієм (Ga), за допомогою першопринципних розрахунків. Розглянуто два рівні легування (8,3% і 16,6%), де атоми Ga заміщують атоми кремнію в одностінних (6,0) SiCNT. Аналіз спін-поляризованої зонної структури показує, що система змінюється від напівпровідникової при нижчому рівні легування до напівметалічної при вищих концентраціях, що свідчить про значний потенціал для застосувань у спінтроніці. Аналіз густини станів і зарядів за Бадером демонструє, що введення Ga змінює розподіл заряду та орбітальні взаємодії, зокрема між станами Ga 5d та C 2p. Розрахунки магнітного моменту показують, що Ga індукує локалізований магнетизм переважно на сусідніх атомах вуглецю, а загальна намагніченість зростає зі збільшенням рівня легування. Порівняння енергій для феромагнітної та антиферомагнітної конфігурацій вказує на антиферомагнітний основний стан, тоді як оцінка енергії утворення підтверджує термодинамічну сприятливість заміщення Ga у позиціях Si. Загалом отримані результати підкреслюють, що Ga-леговані SiCNT є перспективними та керовано налаштовуваними матеріалами для майбутніх наноелектронних і спінтронних пристроїв.

Ключові слова: *SiC:Ga, нанотрубка; магнітний момент; напівметалічний*

EAST EUROPEAN JOURNAL OF PHYSICS. 1. 318-325 (2026)
DOI:10.26565/2312-4334-2026-1-37 ISSN 2312-4334

INFLUENCE OF DEFORMATION ON QUANTUM OSCILLATIONS IN LOW-DIMENSIONAL SEMICONDUCTOR

U.Sh. Turdiev[1], M.G. Dadamirzaev[2], U.I. Erkaboev[2], R.G. Rakhimov[2]*, M.M. Tursunov[2], Q.A. Temirov[2], Sh.X. Utkirov[1]

[1]*Tashkent Institute of Chemical Technology, Yangiyer Branch, 121001 Sirdarya, Uzbekistan*
[2]*Namangan State Technical University, 160115 Namangan, Uzbekistan*
**Corresponding author e-mail: rgrakhimov@gmail.com*
Received September 23, 2025; revised December 12, 2025; accepted February 12, 2026

In this article, the effect of deformation on the Landau levels of electrons and holes in quantum semiconductors is considered. The effect of deformation on the temperature dependence of quantum oscillation effects in small-sized semiconductors obeying the quadratic dispersion law has been applied. Also, the dependence of the surface density of states on temperature and magnetic field for semiconductor heterostructure materials is theoretically explained. A new analytical expression is proposed to calculate the effect of a magnetic field on the surface density of states at the semiconductor-dielectric interface. A mathematical model is developed to determine the effect of a strong magnetic field on the temperature dependence of the surface density of states in semiconductor heterostructures. As a result, the separation of continuous energy spectra measured at room temperature under the influence of a strong magnetic field into discrete levels at low temperatures is explained on the basis of the proposed model.
Keywords: *Semiconductor; Conductivity; Quantum well; Magnetoresistance; Magnetic field*
PACS: 73.63.Hs, 73.21.Fg, 73.21.−b

INTRODUCTION

The electronic, optical, and magnetic properties of quantum-scale semiconductor materials are being systematically studied by many scientists, including the effects of deformation, temperature, and volume pressure on these semiconductors, in terms of their different sizes and structural geometries. One of the main features of nanostructured semiconductors is that they can dramatically change the physical, thermal, electrical, optical, and magnetic properties of these materials by doping them with different concentrations [1-5]. That is, dopants radically change the energy band structure of quantum-scale semiconductors, which can be observed in the changes in the electronic, optical, and magnetic properties of the quantum well. In addition, it is possible to observe the formation of new energy levels (doped levels) in the band gap of the quantum well. Based on this, it is clear that the inclusions are used to tune the optoelectronic properties of quantum-walled semiconductor structures [6-11]. At the same time, controlling the inclusion binding energy is important for ensuring the stability and durability of quantum-scale heterostructure materials. In conclusion, it can be said that the susceptibility (resistance) of inclusion quantum-structured materials to external factors (hydrostatic pressure, deformation, magnetic fields) indicates that the study of such materials is relevant both from a theoretical and practical point of view.

MODEL

Explaining the dependence of the quantum band gap on deformation by means of the Schrodinger equation

The effect of deformation on the basic parameters of quantum well materials has been theoretically considered. The Hamiltonian equation for the effect of volumetric deformation and magnetic field on the allowed band of a quantum well can be written as a function of *H(T,ε)* using the effective mass approximation as follows [1]:

$$H=\frac{1}{2m^*(\varepsilon,T)}\left[\vec{p}+\frac{e}{c}\vec{A}(\vec{r})\right]^2+V(z,\varepsilon,T)-\frac{e^2}{\varepsilon^*(\varepsilon,T)r} \quad (1)$$

where, $\vec{p}$ is the momentum of the electron, $\vec{A}(\vec{r})$ is the vector potential of the magnetic field, which is applied perpendicular to the direction of magnetic field growth (z-direction), i.e., the magnetic field and vector potential have the forms $\vec{B}=(B,0,0)$ and $\vec{A}=(0,B_z,0)$, and c is the speed of light.

The effective mass $m^*(\varepsilon,T)$ and the dielectric constant $\varepsilon^*(\varepsilon,T)$ are functions of the distance between the electron and donor particles in the XOY plane, expressed by $r=\sqrt{(x-x_i)^2+(y-y_i)^2+(z-z_i)^2}$. z and z_i are the coordinates of the electron and donor. The effective mass for charged particles as a function of deformation and temperature was found by scientists in [12-18]:

Cite as: U.Sh. Turdiev, M.G. Dadamirzaev, U.I. Erkaboev, R.G. Rakhimov, M.M. Tursunov, Q.A. Temirov, Sh.X. Utkirov, East Eur. J. Phys. 1, 318 (2026), https://doi.org/10.26565/2312-4334-2026-1-37

$$m^*(\varepsilon,T)=\frac{m_0}{1+E_p^{\Gamma}\left[\frac{2}{E_g^{\Gamma}(\varepsilon,T)}+\frac{1}{E_g^{\Gamma}(\varepsilon,T)+\Delta_0}\right]} \tag{2}$$

where m_0 is the free electron mass, $E_p^{\Gamma}=7.51eV$ is the energy associated with the momentum matrix element for T=0, Δ_0 is the spin-orbit splitting. For *GaAs*, the spin–orbit splitting parameter is Δ_{SO}=0.34 eV [20]. And $E_p^{\Gamma}(\varepsilon,T)$ is the deformation and temperature-dependent energy band for the quantum well in units of Γ-eV, which was found by scientists in works [19-24]. Here, Γ-eV denotes the deformation- and temperature-dependent energy shift of the band edges expressed in electron-volts.

$$E_p^{\Gamma}(\varepsilon,T)=E_g^{\Gamma}(0,T)+1.26*10^{-2}\varepsilon-3.77*10^{-5}\varepsilon^2 \tag{3}$$

Here, $E_g^{\Gamma}(0,T)=1.519-(5.405*10^{-4}T^2)/(T+204)eV$

Deformation and temperature (K) depend on the static dielectric constant [19-24].

$$\varepsilon^*(\varepsilon,T)=\begin{cases}(i)12.74e^{-1.7*10^{-3}\varepsilon}e^{9.4*10^{-5}(T-75.6)};\ for\ T<200\,K\\(ii)13.18e^{-1.7*10^{-3}\varepsilon}e^{20.4*10^{-5}(T-300)};\ for\ T\geq 200\,K\end{cases} \tag{4}$$

However, these derived equations do not consider the dependence of the energy density of states of a quantum well on deformation and magnetic field.

The effect of deformation on the cyclotron frequency of charged particles in a quantum well

One of the physical effects that depends on the change in the energy spectra of charged particles under the influence of deformation is the cyclotron frequency. The cyclotron frequency is a quantity that depends on the energy of the Landau levels of charged particles: $E_N=\hbar\omega_c\left(N_L+\frac{1}{2}\right)$. That is, the cyclotron frequency is represented by the electron spectrum in a strong magnetic field. To calculate this spectrum, it is necessary to solve the Schrödinger equation in a quantizing magnetic field.

$$\left(H(K)+H_S-E\right)F=0 \tag{5}$$

where, $K=k+\frac{e}{c\hbar}A$ is the total momentum, H=rotA; the wave function in the F-effective mass approximation [25].

In the effective mass approximation (5), it is sufficient to restrict the expression *H(K)* in the Schrödinger equation to quadratic terms in *K*, and it is not necessary to take into account the dependence of the *g*-factor on *K*. In addition, in the approximation in (5), the cyclotron frequency is the same for all charged particles, which indicates that the spin effect can be ignored. In this case, the Schrödinger equation (5) reduces to the following expression for the effective mass tensor in the principal coordinate axes:

$$\left(\sum_i\frac{\hbar^2}{2m_i}K_i^2-E\right)F=0 \tag{6}$$

If equation (6) is applied to the quantum field and a solution is found, then E_N will have the following form:

$$E_N=\hbar\omega_c\left(N+\frac{1}{2}\right)+\frac{\pi^2\hbar^2}{2md^2}n_z^2, \tag{7}$$

here,

$$\omega_c=\frac{eB}{m^*} \tag{8}$$

It is known from work [26] that the cyclotron effective mass varies with deformation. For example, in work [26], the graph of the $\frac{m_c^*}{m_0}(\varepsilon)$ function is presented (Fig. 1).

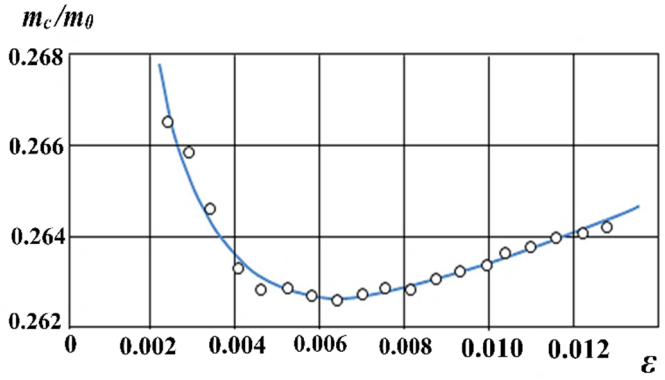

Figure 1. Cyclotron mass dependence of p-type silicon on deformation [26]

This figure shows the dependence of p-type germanium on $\frac{m_c^*}{m_0}(\varepsilon)$. It can be seen from this figure that $\frac{m_c^*}{m_0}(\varepsilon)$ is linearly dependent on strain (ε) at large strains.

It can be seen from this figure that the Landau levels of the quantum wells are significantly affected by large deformation.

Dependence of the forbidden band width on the density of states in the conduction band of a quantum well

Various experiments are being conducted to study the influence of pressure, deformation, and temperature on quantum oscillation effects in new types of bulk and quantum-based semiconductors, and new scientific and practical results are being obtained. For example, the fact that the oscillation processes of the energy density of states lead to oscillations of all quantum effects was shown in these works [27-39] proposed a new model of the temperature dependence of magnetoresistance, magnetic absorption and quantum Hall effect oscillations of bulk and nanostructured semiconductors. In this work, theoretical mechanisms for the temperature dependence of magnetoresistance and magnetic absorption oscillations were developed, taking into account the thermal expansion of discrete Landau levels. However, in these works, the dependence of the energy density of states, magnetoresistance and magnetic absorption oscillations on deformation for parabolic dispersion laws was not considered at all.

The main purpose of this work is to theoretically determine the method for calculating the effect of deformation on Landau levels in the conduction band of quantum-enclosed semiconductors.

Let us consider the effect of temperature and strain on the Landau levels in the conduction band of a rectangular quantum well for the parabolic dispersion law. Here, the magnetic field induction is directed along the Z axis, parallel to the thickness of the quantum well, perpendicular to the XOY plane. Let us choose the ceiling of the valence band of the quantum well as the starting point for the energy spectrum of charge carriers. In this case, the energy spectra of free electrons and holes under the influence of a quantizing magnetic field are calculated by the following equations:

$$E_c^{2d}(B,N_L,n_z,d)=E_g^{2d}+(N_L+\frac{1}{2})\hbar\omega_c+\frac{\pi^2\hbar^2}{2m_ed^2}n_z^2 \tag{9}$$

$$E_v^{2d}(B,N_L,n_z,d)=-\left((N_L+\frac{1}{2})\hbar\omega_v+\frac{\pi^2\hbar^2}{2m_pd^2}n_z^2\right) \tag{10}$$

For the quadratic dispersion law [40]:

$$E=\hbar^2k^2/2m, \text{ then } S=\pi k_\perp^2=\pi(k^2-k_z^2),$$

$$m_c=\frac{\hbar^2}{2\pi}\frac{\partial S}{\partial E}=m. \tag{11}$$

In previous works, the equation for the temperature dependence of the density of energetic states for the parabolic dispersion law of a quantum-walled heterostructure has been presented. In this case, based on condition (9), the density of energetic states can be written as follows:

$$N_S^{2d}(E,B,T,d)=\sum_{N_L,n_z}^{\infty}\frac{eB}{\pi\hbar}\cdot\frac{1}{kT}\cdot\exp\left(-\frac{\left(E-\left(E_g^{2d}+\left(N_L+\frac{1}{2}\right)\hbar\omega_c+\frac{\pi^2\hbar^2}{2m_ed^2}n_z^2\right)\right)^2}{(kT)^2}\right) \tag{12}$$

The difference between equation (12) and the previous equations is that the two-dimensional density of states depends on the band gap of the quantum well.

The effect of deformation on the energy density of states of a quantum well.

Now let us consider the effect of deformation on the energy density of states in the conduction band of a quantum well. It is known that when a semiconductor structure is subjected to deformation, its resistance changes. The resistance that changes under the influence of this deformation is called the tensoresistance. The tensoresistance effect divides the types of elastic deformation into 2 classes, mainly depending on the change in the symmetry of the crystal lattice of semiconductor structures. The symmetry of the crystal lattice of semiconductors practically does not change due to the overall deformation. Therefore, the fact that the crystal lattice remains unchanged from a symmetrical point of view cannot change the resistance component of any material when this deformation is applied. Usually, when the effect of deformation is applied to semiconductor structures, volumetric (all-round) compression is considered [41]. Under the influence of volumetric deformation, the deformation tensor (u_{ii}) of the crystal lattice becomes a scalar (u), and the lattice constant changes as follows:

$$a^{'} = a(1-u)\,, \tag{13}$$

where $a^{'}$ is the lattice constant after deformation, a is the lattice constant before deformation, u is the relative deformation.

A decrease in the interatomic distance of semiconductor structures increases the degree of "coverage" of the wave functions of charge carriers. This, in turn, leads to a change in the interatomic interaction potential energy *W(a)* of the crystal lattice of the material. If the $W_{\min}(a) = W(a_0)$ condition is introduced, then the value of the potential energy W should also increase in the special limits $a<a_0$ and $a>a_0$. A change in the interatomic potential energy W of the crystal lattice of semiconductor structures leads to a shift in the allowed boundary zones of the quantum well. This, in turn, causes a change in the forbidden band width of the quantum well.

That is, in this [41] work:

$$\alpha = -\frac{1}{\Delta\varepsilon_0} - \frac{\partial\Delta\varepsilon_0}{\partial P}\,. \tag{14}$$

Then

$$\Delta\varepsilon(P) = \Delta\varepsilon_0(1-\alpha P)\,. \tag{15}$$

The change in the forbidden band width of the quantum well under the influence of volumetric deformation is formed by the shifts of the bottom of the quantum well conduction band E_c and the ceiling of the valence band E_v.

Under the influence of weak deformation

$$\begin{aligned} E_c(\varepsilon) &= E_c(0) + \Delta_c\varepsilon \\ E_v(\varepsilon) &= E_v(0) + \Delta_v\varepsilon \end{aligned}\,. \tag{16}$$

Using the condition $E_g(\varepsilon) = E_c(\varepsilon) - E_v(\varepsilon)$ and according to (16), the following equation is derived:

$$E_g(\varepsilon) = E_g(0) + \Delta\varepsilon\,, \tag{17}$$

where Δ_c and Δ_v are the deformation results in the conduction and valence bands of the quantum well.

One of the main components of volumetric deformation is the compression (stretching) of the crystal lattice from all sides. Therefore, a change in the concentration of electrons and holes associated with volumetric deformation must be observed in all cases. A change in the concentration of charge carriers *n(ε)* leads to a change in the energy density of states of this quantum well. Then, substituting (17) into (12), we obtain the following $N_s^{2d}(E,\varepsilon,B,T)$:

$$N_S^{2d}\left(E,B,T,\varepsilon,d\right) = \sum_{N_L,n_Z}^{\infty} \frac{eB}{\pi\hbar}\cdot\frac{1}{kT}\cdot\exp\left(-\frac{\left(E-\left(E_g^{2d}\left(E_g^{2d}(0)+\Delta\varepsilon\right)+\left(N_L+\frac{1}{2}\right)\hbar\omega_c+\frac{\pi^2\hbar^2}{2m_e d^2}n_z^2\right)\right)^2}{\left(kT\right)^2}\right) \tag{18}$$

Thus, a new analytical expression for the dependence of the energy density of states of a quantum well on B, T and d under the influence of volumetric deformation was derived.

According to the new analytical expression (18), one can see the graph of the dependence of the oscillations of the density of states in the conduction band of a quantum well on deformation (Fig. 2). Fig. 2 shows the effect of deformation on the states in a GaAs quantum well. Here, $E_g(0)$=1.52 eV [42-43], B=7 T, ε=0.001. With these parameters, the $N_s^{2d}(E,B,\varepsilon)$ under the effects of ε=0 and ε=0.001 are compared. As can be seen from the graphs in this figure, a slight shift of the discrete Landau levels to the right is observed under the influence of deformation. This, of course, reflects the effect of free electrons on the energy spectrum.

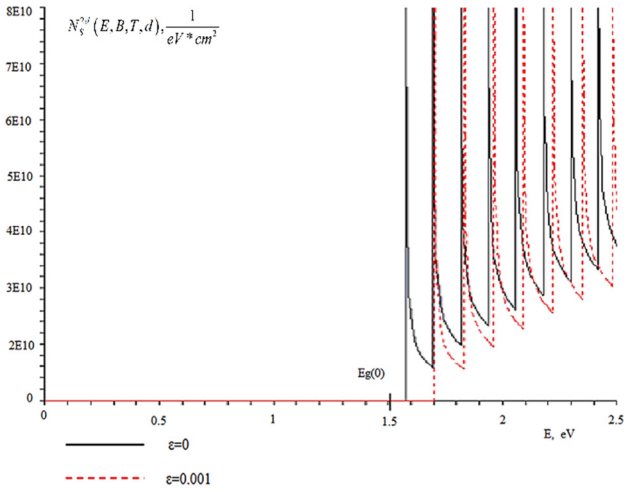

Figure 2. Effect of deformation on the density of states in a GaAs quantum well according to the parabolic dispersion law

Dependence of deformation on quantum oscillation effects in quantum-walled semiconductor structures

Oscillations in the magnetoresistance and magnetoreductive effects arise when the energy density of states in quantum well heterostructures changes. Using equation (18), we determine the dependence of the oscillations in the magnetoresistance and magnetoreductive effects on the overall deformation. The dependence of the Fermi level on the overall deformation can be written as follows:

$$E_F(\varepsilon,T) = -\frac{Eg(\varepsilon)}{2} + \frac{3}{4}kT\ln\left(\frac{m_h^*}{m_e^*}\right), \tag{19}$$

$$\frac{\partial f_0(E,E_F(\varepsilon,T),T)}{\partial E} = -\frac{1}{kT}\frac{\exp\left(\dfrac{E-\left(-\dfrac{Eg(\varepsilon)}{2}+\dfrac{3}{4}kT\ln\left(\dfrac{m_h^*}{m_e^*}\right)\right)}{kT}\right)}{\left[1+\exp\left(\dfrac{E-\left(-\dfrac{Eg(\varepsilon)}{2}+\dfrac{3}{4}kT\ln\left(\dfrac{m_h^*}{m_e^*}\right)\right)}{kT}\right)\right]^2}. \tag{20}$$

The dependence of effective masses on deformation can be expressed as follows [44-45]:

$$m_c^*(\varepsilon) = m_c^*(0)\cdot\left(1-\frac{\Delta E_g}{E_g(0)}\right) = m_c^*(0)\cdot\frac{E_g(\varepsilon)}{E_g(0)} \tag{21}$$

$$\omega_c(\varepsilon) = \frac{eB}{m_c^*(\varepsilon)} \tag{22}$$

Using (18), (19), (20), (21) and the $\rho_H^{2d}(B,T)$ and $\chi_H^{2d}(B,T)$ mathematical models in [46-47], the following expression is derived:

$$\rho_H^{2d}(B,T,\varepsilon) = A\cdot\hbar\omega_c(\varepsilon)\int_{\hbar\omega_c(\varepsilon)}^{\infty}\sum_{N_L,n_z}^{\infty}\frac{eB}{\pi\hbar}\cdot\frac{1}{kT}\cdot\exp\left(-\frac{\left(E-\left(E_g^{2d}(E_g(0)+\Delta\varepsilon)+\left(N_L+\frac{1}{2}\right)\hbar\omega_c+\frac{\pi^2\hbar^2}{2m_e d^2}n_z^2\right)\right)^2}{(kT)^2}\right)\times$$
$$\times\left(-\frac{\partial f_0\left(E,E_F(\varepsilon,T),T\right)}{\partial E}\right)\tau_n(E)d \tag{23}$$

$$\chi_H^{2d}(B,T,\varepsilon)=2\mu_B^2\int_0^{\infty}\sum_{N_L,n_z}^{\infty}\frac{eB}{\pi\hbar}\cdot\frac{1}{kT}\cdot\exp\left(-\frac{\left(E-\left(E_g^{2d}(E_g(0)+\Delta\varepsilon)+\left(N_L+\frac{1}{2}\right)\hbar\omega_c+\frac{\pi^2\hbar^2}{2m_ed^2}n_z^2\right)\right)^2}{(kT)^2}\right)\times$$
$$\times\left(-\frac{\partial f_0\left(E,E_F(\varepsilon,T),T\right)}{\partial E}\right)\tau_n(E)d \qquad (24)$$

If the deformation is equal to or greater than the critical value (ε ≥ εk), then the Landau levels begin to shift towards the edges of the conduction band. Using equations (23) and (24), we obtain graphs of the magnetoresistance and magnetoresistance oscillations of the quantum well. Fig. 3 shows the dependence of the magnetoresistance and magnetoresistance oscillations of the GaAs quantum well material on the overall deformation. As can be seen from this figure, the appearance of the oscillations of charged particles changes significantly with increasing deformation.

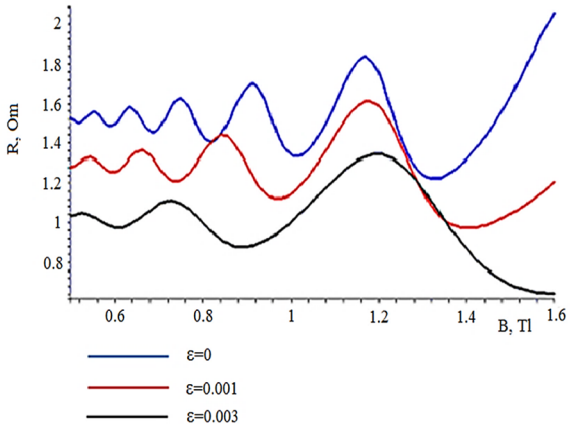

Figure 3. Oscillations of *ρ(B,T,ε)* in a GaAs quantum well at various deformations

Figures 4 and 5 show three-dimensional images of the magnetoresistance and magnetoresistance oscillations of the GaAs quantum well at various deformations. As the strain in a GaAs quantum well increases to 0.004, a slight decrease in the number of discrete Landau levels of free electrons is observed in the magnetoresistance and magnetoresistance effects at a constant low temperature.

Using equations (23) and (24), it is possible to calculate both deformation and temperature effects of $\rho^{2d}(B,T,\varepsilon)$ and $\chi^{2d}(B,T,\varepsilon)$ of quantum coils subject to the law of parabolic dispersion at the same time.

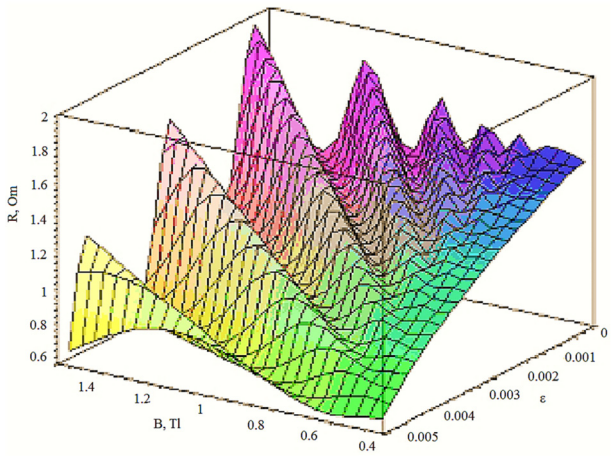

Figure 4. The dependence of the magnetoresistance of a GaAs quantum well on deformation *ρ(B,T,ε)*

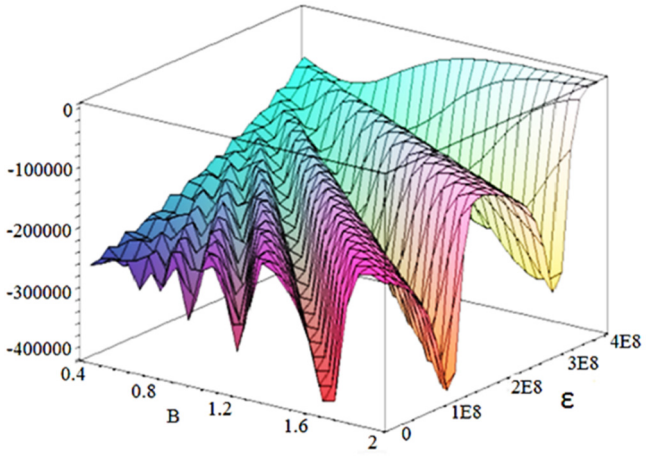

Figure 5. Dependence of magnetic susceptibility of a GaAs quantum well on deformation χ(B,T,e)

CONCLUSIONS

Based on the results of this study, the following conclusions were drawn:

1. The dependence of the energy density of states in the conduction band of quantum well semiconductors subject to parabolic band dispersion on deformation was introduced.

2. A new analytical expression was found that determines the dependence of the energy density of states of a quantum well on deformation $\left(N_S^{2d}\left(E,B,T,\varepsilon\right)\right)$.

3. The quantum oscillation effects of a quantum well were studied theoretically using the proposed analytical expression.

4. Methods for calculating $\rho^{2d}(B,T,\varepsilon)$ and $\chi^{2d}(B,T,\varepsilon)$ of a quantum well using $N_S^{2d}\left(E,B,T,\varepsilon\right)$ were developed.

ORCID

U.Sh. Turdiev, https://orcid.org/ 0009-0009-7808-4113; **M.G. Dadamirzaev,** https://orcid.org/0000-0003-0756-8275
U.I. Erkaboev, https://orcid.org/0000-0002-6841-8214; **R.G. Rakhimov,** https://orcid.org/0000-0003-0850-1398
M.M. Tursunov, https://orcid.org/0009-0000-0222-951X; **Q.A. Temirov,** https://orcid.org/0009-0008-9339-1202

REFERENCES

[1] E. Kasapoglu, Opt. Quantum Electron. **57**, 85 (2025). https://doi.org/10.1007/s11082-024-08000-3
[2] U.I. Erkaboev, R.G. Rakhimov, U.M. Negmatov, N.A. Sayidov, and J.I. Mirzaev, Rom. J. Phys. **68**(5-6), 614 (2023). https://rjp.nipne.ro/2023_68_5-6/RomJPhys.68.614.pdf
[3] G. Gulyamov, U.I. Erkaboev, and N.Y. Sharibaev, Mod. Phys. Lett. B, **30**(07), 1650077 (2016). https://doi.org/10.1142/S0217984916500779
[4] U. Erkaboev, R. Rakhimov, J. Mirzaev, U. Negmatov, and N. Sayidov, Int. J. Mod. Phys. B, **38**(15), 2450185 (2024). https://doi.org/10.1142/S0217979224501856
[5] G. Gulyamov, M.G. Dadamirzayev, M.O. Qosimova, and S.R. Boydedayev, AIP Conf. Proc. **2700**(1), 050013 (2023). https://doi.org/10.1063/5.0124926
[6] T. Burgess, D. Saxena, S. Mokkapati, Z. Li, R.C. Hall, J.A. Davis, Y. Wang, *et al*., Nat. Commun., **17**(7), 11927 (2016). https://doi.org/10.1038/ncomms11927
[7] D. Luo, L. Wang, Y. Qiu, R. Huang, and B. Liu, Nanomaterials, **24**, 1226 (2020). https://doi.org/10.3390/nano10061226
[8] U.I. Erkaboev, N.A. Sayidov, U.M. Negmatov, R.G. Rakhimov, J.I. Mirzaev, E3S Web Conf. **401**, 04042 (2023). https://doi.org/10.1051/e3sconf/202340104042
[9] U. Erkaboev, R. Rakhimov, J. Mirzaev, N. Sayidov, U. Negmatov, and M. Abduxalimov, AIP Conf. Proc. **2789**(1), 040055 (2023). https://doi.org/10.1063/5.0145554
[10] G. Gulyamov, M.G. Dadamirzaev, and S.R. Boidedaev, Semiconductors, **34**, 555 (2000). https://doi.org/10.1134/1.1188027
[11] M. Ahmetoglu (Afrailov), G. Kaynak, S. Shamirzaev, G. Gulyamov, A. Gulyamov, M.G. Dadamirzaev, S.R. Boydedayev, *et al*., Int. J. Mod. Phys. B, **23**(15), 3279 (2009). https://doi.org/10.1142/S0217979209053084
[12] A. Sali, and H. Satori, Superlattices Microstruct. **69**, 38 (2014). https://doi.org/10.1016/j.spmi.2014.01.011
[13] K. El-Bakkari, A. Sali, E. Iqraoun, A. Rezzouk, N. Es-Sbai, and M.O. Jamil, Phys. B, **538**, 85 (2018). https://doi.org/10.1016/j.physb.2018.03.010
[14] H. Ehrenreich, J. Appl. Phys. **32**, 2155 (1961). https://doi.org/10.1063/1.1777035
[15] U.I. Erkaboev, N.A. Sayidov, U.M. Negmatov, J.I. Mirzaev, and R.G. Rakhimov, E3S Web Conf. **401**, 01090 (2023). https://doi.org/10.1051/e3sconf/202340101090
[16] S.H. Shamirzaev, G. Gulyamov, M.G. Dadamirzaev, and A.G. Gulyamov, Semiconductors, **43**, 47 (2009). https://doi.org/10.1134/S1063782609010102
[17] G. Gulyamov, M.G. Dadamirzaev, and S.R. Boidedaev, Semiconductors, **34**, 260 (2000). https://doi.org/10.1134/1.1187967
[18] M.G. Dadamirzaev, M.O. Kosimova, S.R. Boydedayev, and A.S. Makhmudov, East Eur. J. Phys. (2), 372 (2024). https://doi.org/10.26565/2312-4334-2024-2-46
[19] E. Kasapoglu, H. Sari, and I. Sökmen, Surf. Rev. Lett. **15**, 201 (2008). https://doi.org/10.1142/S0218625X08010440
[20] B. Welber, M. Cardona, C.K. Kim, and S. Rodriquez, Phys. Rev. B, **12**, 5729 (1975). https://doi.org/10.1103/PhysRevB.12.5729
[21] A.S. Puzanov, S.V. Obolenskii, and V.A. Kozlov, Semiconductors, **49**(1), 69 (2015). https://doi.org/10.1134/S1063782615010224
[22] Y. Tokura, K. Yasuda, and A. Tsukazaki, Nat. Rev. Phys. **1**, 126 (2019). https://doi.org/10.1038/s42254-018-0011-5
[23] R. Macaluso, H.D. Sun, M.D. Dawson, F. Robert, A.C. Bryce, and J.H. Marsh, Appl. Phys. Lett. **82**, 4259 (2003). https://doi.org/10.1063/1.1583865
[24] M.S. Aghaei, I. Torres, and I. Calizo, Comput. Mater. Sci., **138**, 204 (2017). https://doi.org/10.1016/j.commatsci.2017.06.041
[25] G.L. Bir, and G.E. Pikuc, *Symmetry and deformation effects in semiconductors*, (Nauka, Moscow, 1972). (in Russian)
[26] J.C. Hensel, and G. Feher, Phys. Rev. **129**, 1041 (1963). https://doi.org/10.1103/PhysRev.129.1041
[27] C.P. Herrero, and R. Ramirez, J. Phys. Chem. Solids, **171**, 1100980 (2022). https://doi.org/10.1016/j.jpcs.2022.110980
[28] S.V. Gudina, A.S. Bogoliubskii, A.S. Klepikova, V.N. Neverov, K.V. Turutkin, S.M. Podgornykh, N.G. Shelushinina, *et al*., J. Low Temp. Phys. **45**(4), 412 (2019). https://doi.org/10.1063/1.5093521
[29] V.I. Litvinov, V.K. Dugaev, V.L.V olkov, and M. Oszwaldowski, Inorg. Mater. **33**(2), 203 (1997).
[30] É.A. Neifeld, K.M. Demchuk, G.I. Kharus, A.É. Bubnova, L.I. Domanskaya, G.D. Shtrapenin, and S.Yu. Paranchich, Semiconductors, **31**(3), 261 (1997). https://doi.org/10.1134/1.1187122
[31] U.I. Erkaboev, and R.G. Rakhimov, e-Prime - Adv. Electr. Eng., Electron. Energy, **5**, 1000236 (2023). https://doi.org/10.1016/j.prime.2023.100236
[32] U. Erkaboev, R. Rakhimov, J. Mirzaev, N. Sayidov, U. Negmatov, and A. Mashrapov, AIP Conf. Proc. **2789**(1), 040056 (2023). https://doi.org/10.1063/5.0145556
[33] D.S. Abramkin, and T.S. Shamirzaev, Semiconductors, **53**(5), 703 (2019). https://doi.org/10.21883/FTP.2019.05.47569.9018
[34] U.I. Erkaboev, R.G. Rakhimov, J.I. Mirzaev, U.M. Negmatov, and N.A. Sayidov, Ind. J. Phys. **98**(1), 189-197 (2024). https://doi.org/10.1007/s12648-023-02803-y

[35] B.P. Koman, Semiconductors, **48**(5), 659 (2014). https://doi.org/10.1134/S1063782614050091
[36] D. Slobodzyan, M. Kushlyk, R. Lys, J. Shykorjak, A. Luchechko, M. Zyłka, W. Zyłka, *et al.*, MDPI Materials, **15**, 4052 (2022). https://doi.org/10.3390/ma15124052
[37] Y.N. Qiu, and J.M. Rorison, Appl. Phys. Lett. **82**, 081111 (2005). https://doi.org/10.1063/1.2034103
[38] U. Rani, P.K. Kamlesh, T.K. Joshi, R. Singh, S. Sharma, R. Gupta, T. Kumar, and A.S. Verma, Comput. Condens. Matter. **36**, 00835 (2023). https://doi.org/10.1016/j.cocom.2023.e00835
[39] Y. Joseph, H. Mehdi, A.M. Brenden, M. William, C.D. Matthieu, S. Kasra, S.W. Kaushini, *et al*., Phys. Rev. B, **101**, 205310 (2020). https://doi.org/10.1103/PhysRevB.101.205310
[40] I.M. Tsidilkovskii, *Electrons and holes in semiconductors. Energy spectrum and dynamics* (Nauka, Moscow, 1972). (in Russian)
[41] P.I. Baransky, V.P. Klochkov, and I.V.Potykevich, *Semiconductor electronics* (Naukova Dumka, Kyiv, 1975). (in Russian)
[42] R. Pässler, Phys. Stat. Sol. (b), **236**(3), 710 (2003). https://doi.org/10.1002/pssb.200301752
[43] R. Pässler, Phys. Stat. Sol.(b), **216**(2), 975 (1999). https://doi.org/10.1002/(SICI)1521-3951(199912)216:2%3C975::AID-PSSB975%3E3.0.CO;2-N
[44] A.L. Polyakova, *Deformation of semiconductors and semiconductor devices*, (Energy, Moscow, 1979). (in Russian)
[45] G. Gulyamov, M.G. Dadamirzayev, K.M. Uktamova, and B.Z. Mislidinov, AIP Conf. Proc. **2700**(1), 050007 (2023). https://doi.org/10.1063/5.0126516
[46] W. Zawadzki, A. Raymond, and M. Kubisa, Phys. Status Solidi B, **251**(2), 247 (2014). https://doi.org/10.1002/pssb.201349251
[47] U. Rani, P.K. Kamlesh, T.K. Joshi, S. Sharma, R. Gupta, S. Al-Qaisi, and A.S. Verma, Phys. Scripta, **98**, 075902 (2023). https://doi.org/10.1088/1402-4896/acd88a

ВПЛИВ ДЕФОРМАЦІЇ НА КВАНТОВІ КОЛИВАННЯ В НИЗЬКОВИМІРНИХ НАПІВПРОВІДНИКАХ

У.Ш. Турдієв[1], М.Г. Дадамірзаєв[2], У.І. Еркабоєв[2], Р.Г. Рахімов[2], М.М. Турсунов[2], К.А. Теміров[2], Ш.Х. Уткіров[1]
[1]Ташкентський хіміко-технологічний інститут, філія Янгієр, 121001 Сирдар'я, Узбекистан
[2]Наманганський державний технічний університет, 160115 Наманган, Узбекистан

У цій статті розглядається вплив деформації на рівні Ландау електронів та дірок у квантових напівпровідниках. Застосовано вплив деформації на температурну залежність квантових коливальних ефектів у малорозмірних напівпровідниках, що підпорядковуються квадратичному закону дисперсії. Також теоретично пояснено залежність поверхневої густини станів від температури та магнітного поля для напівпровідникових гетероструктурних матеріалів. Запропоновано новий аналітичний вираз для розрахунку впливу магнітного поля на поверхневу густину станів на межі напівпровідник-діелектрик. Розроблено математичну модель для визначення впливу сильного магнітного поля на температурну залежність поверхневої густини станів у напівпровідникових гетероструктурах. В результаті, на основі запропонованої моделі пояснюється розділення неперервних енергетичних спектрів, виміряних при кімнатній температурі під впливом сильного магнітного поля, на дискретні рівні при низьких температурах.

Ключові слова: *напівпровідник; провідність; квантова яма; магнітоопір; магнітне поле*

EAST EUROPEAN JOURNAL OF PHYSICS. 1. 326-332 (2026)
DOI:10.26565/2312-4334-2026-1-38 ISSN 2312-4334

FORMATION OF $Cu_{15}Si_4$/Si NANOPHASE FILMS ON SILICON SURFACES

K. Dovranov[1]*, M. Normuradov[1], X. Davranov[1], A. Husanov[1], G. Shodiyev[1], G.T. Ruziyeva[2], E. Karimov[1], R. Yorqulov[3]

[1]*Karshi State University, Karshi, Uzbekistan, 180119*
[2]*Termiz University of Economics and Service, Termiz, Uzbekistan, 190100*
[3]*University of Economics and Pedagogy, Karshi, Uzbekistan, 180100*
**Corresponding Author email: quvondiqdavronm@gmail.com*
Received September 29, 2025, revised December 24, 2025; in final form December 29, 2025; accepted February 12, 2026

We report on the formation of copper silicide nanofilms using different magnetron sputtering modes. Copper silicide thin films were formed by sputtering Cu onto a Si(111) surface heated to 467 °C in high vacuum using the mid-RFMS method at a frequency of 100 kHz and a D=70% efficiency. The thickness of the resulting heteroepitaxial Cu/$Cu_{15}Si_4$/Si film was measured using SEM. Also, a $Cu_{15}Si_4$ film was formed by thermally annealing Cu/Si(111) nanofilms in a vacuum at 800 K for 1.5 hours using the DCMS method. The thickness and surface morphology of the obtained samples were studied using SEM. The formation of silicide films is confirmed by the results of energy-dispersive spectra. The formation of a copper (Cu) silicide film depends on the copper crystal size and substrate temperature, and at 467°C, a 75 nm-thick $Cu_{15}Si_4$ film was formed under a 130 nm-thick copper layer. These findings provide new insights into the mechanisms governing copper-silicon interface reactions and highlight the potential of copper silicide nanofilms to improve the performance of metal-oxide-semiconductor transistors and high-speed integrated circuits.
Keywords: *$Cu_{15}Si_4$; Ion-plasma; Silicide films; RFMS; Magnetron sputtering*
PACS: 68.55.-a; 81.15.Cd; 73.40.Ns

INTRODUCTION

In recent years, the copper-silicide (Cu-Si) system has been widely studied as a promising material for micro- and nanoelectronics, solar cell contacts [1-3], metal-oxide-semiconductor transistors [4], and high-speed integrated circuits (ICs) [5,6]. There are several stable and metastable phases in the Cu-Si system, the formation of which depends on the diffusion of copper and silicon atoms, the crystal structure of the substrate, and the temperature conditions. Cu and its silicide films are commonly produced by various methods, including direct current magnetron sputtering (DCMS) [7-9], mid-radio frequency magnetron sputtering (mid-RFMS) [10-12], high-power pulsed magnetron sputtering (HiPIMS), molecular beam epitaxy (MNE) [13], and reactive pulsed laser deposition (RPLD) [14]. Cu and its silicide films have been reported in many articles. However, most of them used glass substrates to form contact films, and several papers have processed silicon substrates [15]. Many studies have investigated the solid-state reaction sequence in Cu/α-Si systems based on amorphous silicon. It has been found that the reaction between copper and amorphous silicon initially forms the η″-Cu_3Si phase, which then proceeds to the γ-Cu_5Si phase [16-19]. Although the $Cu_{15}Si_4$ phase is thermodynamically stable, its formation is kinetically limited. This means that there is insufficient information to fully elucidate the formation mechanism of the $Cu_{15}Si_4$ phase during direct deposition, especially on single-crystal Si substrates.

Thus, although the existing literature provides important scientific results on the Cu–Si system, the direct formation of the $Cu_{15}Si_4$ phase on single-crystal Si substrates by ion-plasma magnetron deposition, its structural and phase properties have not yet been fully studied. Also, comparative studies of the effects of magnetron deposition modes, such as mid-RFMS and DCMS, on the formation of the Cu–Si phase are very few. This study aims to fill this scientific gap and open up the possibilities for the controlled synthesis of $Cu_{15}Si_4$/Si nanophase films.

MATERIALS AND METHODS

In this study, we simultaneously deposited films of different thicknesses in an argon atmosphere using a magnetron sputtering device in two different modes. Copper (Cu) with a purity of 99.998% was sputtered onto a single-crystal silicon surface by a solid-state ion-plasma method using variable reactive mid-frequency magnetron sputtering (mid-RFMS) and constant current magnetron sputtering (DCMS). We used a pulsed mid-RF mode of 100 kHz and a duty cycle of 70% to improve the crystallization and crystal size of copper (Cu) thin films grown at room temperature and 467°C. Si(111) was used as the substrate. The substrate temperature was monitored and controlled using a temperature regulator module (TRM, Epos, Russia) in combination with a K-type (TXA) thermocouple. The C and O on the film surface were removed by bombarding the substrate surface with low-energy ionized argon atoms using an “ion gun” source in a vacuum. Prior to deposition, the Si(111) substrates were cleaned by low-energy Ar^+ ion bombardment using an ion gun. The ion energy was set to 300 eV, and the cleaning process was carried out for 8–10 minutes. The base pressure before introducing argon was 4.1×10^{-6} Torr, while the chamber pressure during ion bombardment was maintained at 1.8×10^{-3} Torr. This procedure

Cite as: K. Dovranov, M. Normuradov, X. Davranov, A. Husanov, G. Shodiyev, G.T. Ruziyeva, E. Karimov, R. Yorqulov, East Eur. J. Phys. 1, 326 (2026), https://doi.org/10.26565/2312-4334-2026-1-38

effectively removes native oxides and contaminants, ensuring good adhesion and reproducibility of thin-film growth. The maximum deposition rate and sputtering efficiency of the DCMS source under a power density of 1.15 W/cm² for the Cu target were 17 Å/s, D=70%, respectively. Furthermore, the formation of a $Cu_{15}Si_4$ film was confirmed by thermally annealing Cu/Si(111) nanofilms, deposited via the DCMS method, in a vacuum at 800 K for 1.5 hours. The surface morphology of the obtained silicide films was examined using an Olympus "LEXT™ OLS5100" laser confocal microscope and SEM. The elemental composition of the obtained samples was determined using EDS, and the phase structure of the Cu-Si system.

RESULTS AND DISCUSSION

In this work, two different ion-plasma magnetron sputtering approaches for forming $Cu_{15}Si_4$ silicide films on silicon surfaces were studied. We describe two methods using a magnetron sputtering device. Although the final product is the same in both methods, the mechanisms of phase formation are fundamentally different. The formation process of copper silicide films is shown in Figure 1.

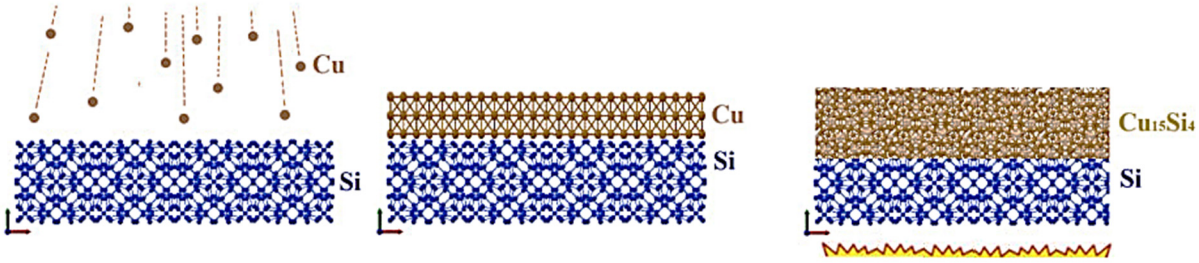

Figure 1. Schematic illustration of the formation mechanism of copper silicide films on Si(111) surfaces during magnetron sputtering using the DCMS deposition mode

Figure 1 demonstrates Cu atom deposition, diffusion into the heated silicon substrate, and the subsequent in situ formation of the $Cu_{15}Si_4$ silicide phase. In the first approach, copper (Cu) was sputtered onto the surface of a Si substrate at room temperature using the DCMS (Direct Current Magnetron Sputtering) method. Under these conditions, the diffusion of Cu atoms along the surface and into the bulk was limited due to the low substrate temperature. As a result, an amorphous or poorly crystallized Cu film was formed on the Si surface. The initial Cu film deposited by DCMS was structurally uneven, with grains and islands observed. This is explained by the limited mobility of Cu atoms along the surface and the lack of immediate chemical reaction with silicon. In the next step, this sample was heated in a vacuum at 800 K for 1.5 hours. During the heating process, the diffusion coefficient of Cu atoms increased sharply, and a solid-state reaction began at the Cu/Si interface. Copper atoms penetrated the silicon lattice, forming a thermodynamically stable $Cu_{15}Si_4$ silicide phase. According to the SEM results, the islands in the initial Cu film interacted with silicon during heating, forming a more homogeneous, continuous $Cu_{15}Si_4$ silicide film. This process represents a classical annealing-induced silicide formation mechanism controlled by diffusion.

Figure 2(a) shows the SEM image of the copper film deposited on the Si(111) substrate by the DCMS method before annealing. The surface exhibits a granular and island-like morphology, indicating limited surface diffusion of Cu atoms during room-temperature deposition. Such morphology is typical for as-deposited copper films on silicon, where insufficient thermal energy restricts atomic rearrangement and promotes the formation of isolated clusters.

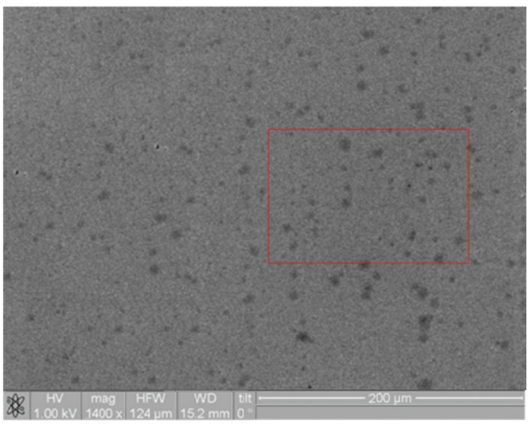

Figure 2(a). SEM image of a copper film formed by DCMS on a Si(111) surface (before annealing).

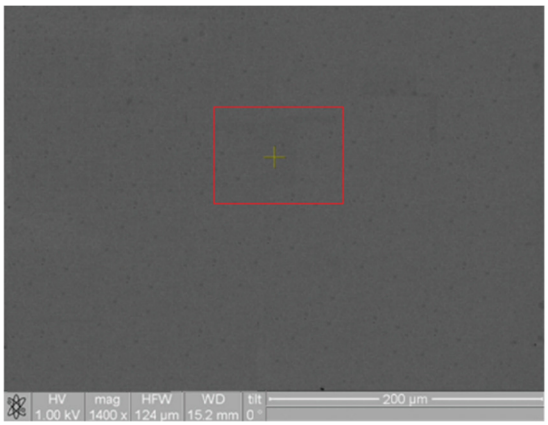

Figure 2(b). SEM image of a copper silicide film formed by the DCMS method (after annealing).

After thermal annealing, the surface morphology changes significantly, as shown in Figure 2(b). The film becomes more uniform and compact, which indicates enhanced atomic diffusion and the onset of a solid-state reaction between Cu and Si. The disappearance of isolated islands and the formation of a continuous layer suggest the transformation of the

initial copper film into a copper silicide phase. This morphological evolution confirms that annealing activates Cu diffusion into the silicon substrate and promotes the formation of a stable $Cu_{15}Si_4$ silicide layer.

In the second approach, the Cu film was sputtered onto the surface of a Si(111) substrate heated to 467°C using the mid-RFMS (mid-Radio Frequency Magnetron Sputtering) method at a frequency of 100 kHz and a duty cycle of D = 70%. The main difference in this method is that silicide formation occurs without further heating, that is, directly during the deposition process itself. Due to the high temperature of the substrate, the sputtered Cu atoms have high mobility upon reaching the Si surface. Due to the high ionization degree of the plasma in the mid-RFMS mode, the Cu atoms receive additional energy and are able to diffuse deeper into the Si lattice. As a result, an in-situ solid-state reaction occurs at the Cu/Si interface, and the $Cu_{15}Si_4$ silicide phase begins to form at the time of deposition. This process is schematically shown in Figure 3, which depicts the diffusion of Cu atoms onto the heated Si substrate and the formation of a continuous silicide layer. In this approach, the optimal substrate temperature, ion-plasma energy, and pulsed mid-RFMS mode were controlled to form the $Cu_{15}Si_4$ phase. As a result, a more homogeneous, structurally stable, and well-crystallized silicide film was formed. The thickness of the resulting heteroepitaxial Cu/$Cu_{15}Si_4$/Si film was measured using SEM (Figure 4). The film thickness was determined from the deposition rate and deposition time, with an uncertainty of approximately ±8%. The film thickness was also re-determined from the SEM images, with an estimated uncertainty of ±5%. The formation of the copper silicide film depends on the copper crystal size and substrate temperature, and at 467°C, a 75 nm-thick $Cu_{15}Si_4$ film was formed under a 130 nm-thick copper layer.

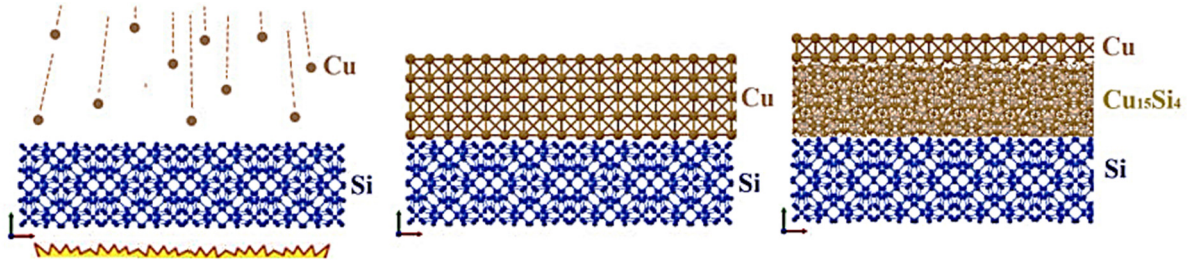

Figure 3. Formation mechanism of copper silicide films by the mid-RFMS method.

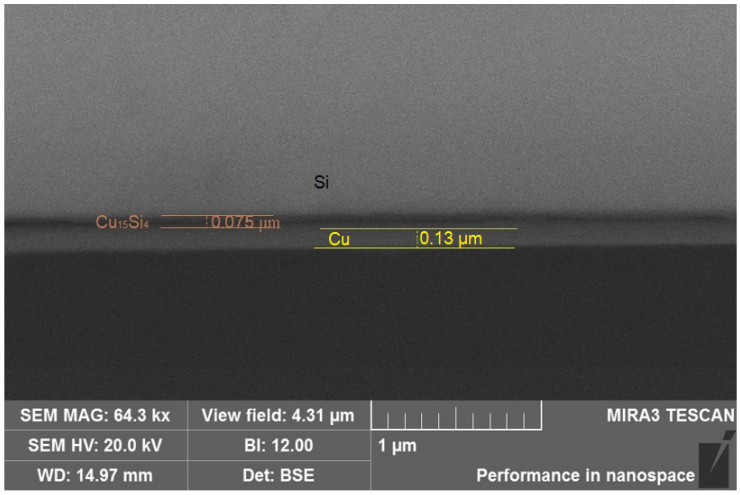

Figure 4. SEM image of Cu/$Cu_{15}Si_4$/Si layer by the mid-RFMS method.

Thus, while in the "DCMS and heating" method the silicide phase is formed in two steps (deposition and annealing), in the "mid-RFMS and heated substrate" approach, the $Cu_{15}Si_4$ phase is formed in a single-step in-situ process. The second method, while being technologically simpler, allows for more precise control of phase formation. Figures 1 and 3, along with the experimental results, show that the formation of the $Cu_{15}Si_4$ silicide phase proceeds via a diffusion- and ion-plasma-controlled mechanism. A comparative analysis of the DCMS and mid-RFMS approaches clearly shows that the substrate temperature and plasma regime play a decisive role in silicide formation.

These results indicate that the mid-RFMS method is more effective for forming silicide phases in the Cu–Si system and is a promising technology for application in microelectronic devices. The elemental composition and mass fraction of the thin film were determined using energy dispersive spectroscopy (EDS) Figure 5. Based on the measurement results, the mass fraction of the sample, as a result of mid-radiofrequency pulsed magnetron sputtering (mid-RFMS) on the surface of monocrystalline silicon using a solid-phase ion plasma method, was 10.61% Si, 89.39% Cu, and the atomic fraction was 21.13% Si, 78.87% Cu (Table 1).

According to the results of the study, the formation of Cu and its silicide nanofilms from a copper target using the DCMS and mid-RFMS methods in the magnetron device depends on the initial substrate temperature and the subsequent

heating temperatures of the films. The optimal temperature for crystallization of the films was found to be 467°C. The surface morphology of the formed copper silicide nanofilms was measured and analyzed using an atomic force microscope and an Olympus "LEXT™ OLS5100" laser confocal microscope (Figure 6-7, Table 2). Thanks to the advanced optical components, high-quality 3D measurements were obtained in these microscopes, and the surface roughness was found to be 6 nm.

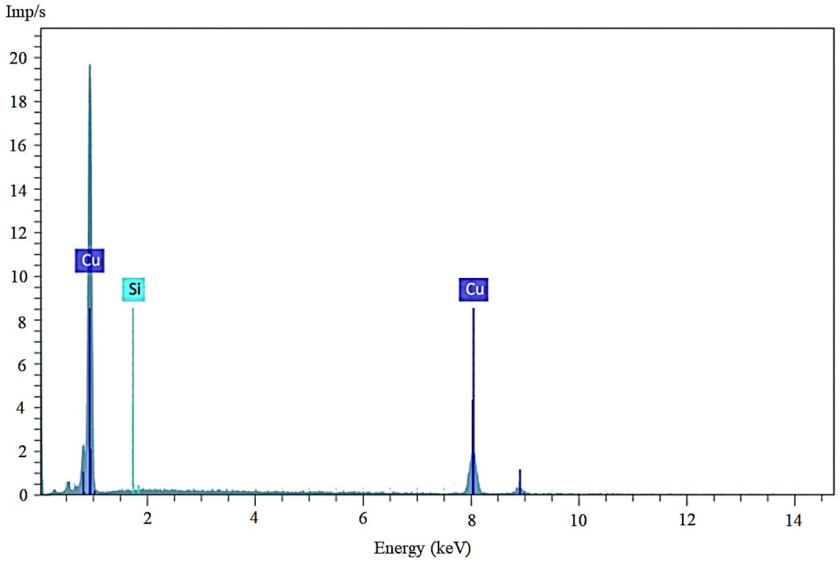

Figure 5. Energy-dispersive spectrum of a copper silicide film.

Table 1. Elemental composition of the copper silicide thin film

Element	mass. %	atom. %
Si	10.61	21.13
Cu	89.39	78.87
	100.00	100.00

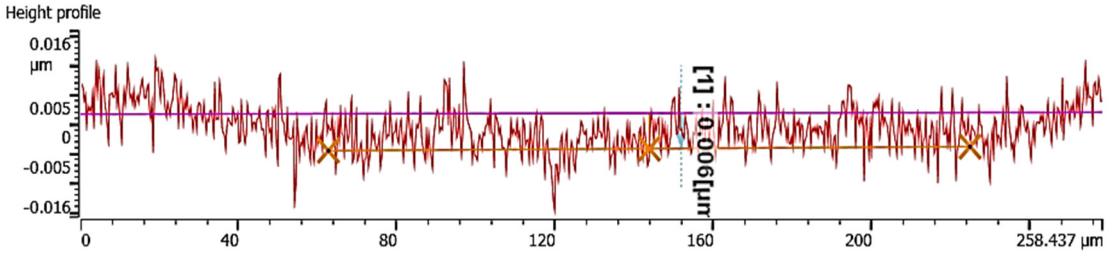

Figure 6. Surface roughness image of $Cu_{15}Si_4$ thin film formed by the DCMS method.

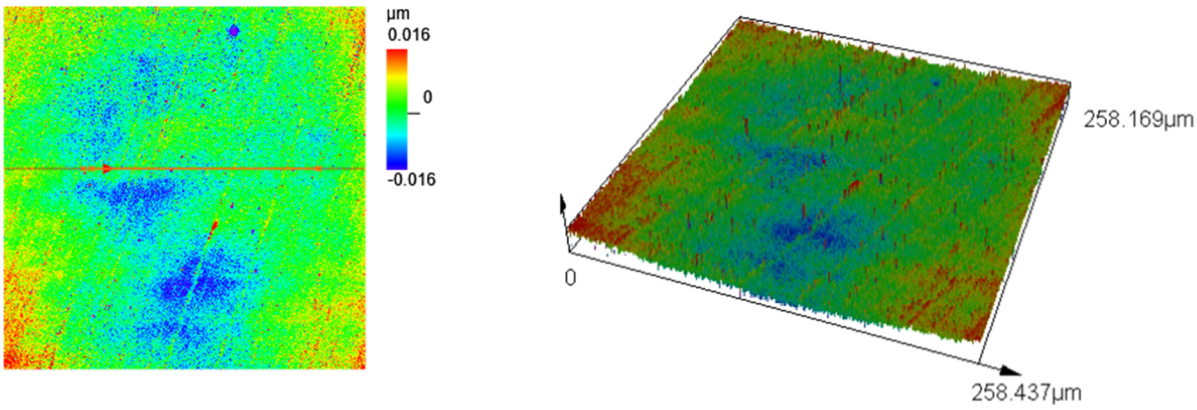

a) b)

Figure 7. Surface morphology of $Cu_{15}Si_4$ thin film formed by the DCMS method.
a) 2D image b) 3D image

Table 2. Surface roughness of the copper silicide thin film

no.	Distance[µm]	Width[µm]	Height[µm]	Angle [°]
1	0.006	168.216	0.006	179.991

The temperature-dependent electrical conductivity of the Cu–Si thin films was measured using a NETZSCH SBA 458 Nemesis® system, which employs the four-point probe technique for precise conductivity determination. Electrical contacts were established using the built-in current pins of the system, ensuring stable and reproducible ohmic contact. The sample was mounted in a horizontal configuration and measured in the temperature range from room temperature up to 380°C under controlled atmospheric conditions.

The SBA 458 Nemesis® allows automatic averaging of more than 100 readings per measurement point, significantly improving accuracy. According to the instrument specifications, the electrical conductivity measurement range is 0.05–150 000 S/cm, with an accuracy of ±5% and repeatability of ±3%. The system uses Inconel®-sheathed K-type thermocouples with fixed positions, providing reliable temperature control and eliminating uncertainties related to probe spacing. During measurements, the temperature was increased stepwise with sufficient stabilization time at each point to ensure thermal equilibrium before data acquisition.

Figure 8 shows the temperature dependence of the electrical conductivity of a Cu-Si thin film grown on a silicon surface. The graph shows that in the low-temperature range (from room temperature to about 120°C), the electrical conductivity is very low, which is explained by the film's initial structural state and the diffusion barriers at the Cu/Si interface. At this stage, the movement of electric carriers is limited by the influence of intergrain boundaries, defects, and the silicon substrate. When the temperature was increased to 150-250 °C, a sharp increase in electrical conductivity was observed. This phenomenon is associated with the active diffusion of Cu atoms into the silicon lattice and the onset of a solid-state reaction in the Cu–Si system. It is in this temperature range that the formation of a continuous metal silicide phase occurs, creating paths for carrying electric current (percolation network). As a result, the electrical conductivity increases by several orders of magnitude, which is a functional sign of the phase transition process. At temperatures above 250–350°C, the increase in electrical conductivity slows down and almost stabilizes.

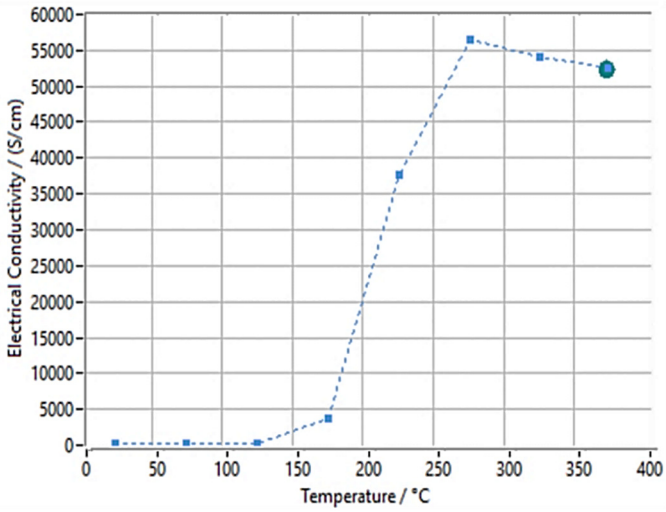

Figure 8. Temperature-dependent electrical conductivity of Cu–Si films

This saturation state indicates the complete formation of the copper silicide phase and the transition of the structure to a thermodynamically stable state. The electrical conductivity values observed at this stage (~5×10^4 S/cm) are lower than those of pure metallic copper but are in the range of values typical of metal silicides, in particular the $Cu_{15}Si_4$ phase. The temperature-dependent behavior of the electrical conductivity clearly indicates that phase changes are occurring in the film. While at low temperatures the interface and structural constraints dominate, at high temperatures the Cu–Si solid-state reaction leads to the formation of a metal silicide phase, dramatically improving the electrical transport properties of the film. These results further functionally confirm the presence of the $Cu_{15}Si_4$ phase, as detected by SEM and EDS analyses.

CONCLUSIONS

In this work, the formation mechanisms of copper silicide nanofilms on single-crystal silicon surfaces were systematically investigated using two different magnetron sputtering approaches. It was demonstrated that copper silicide formation is strongly governed by substrate temperature and the deposition process's kinetic conditions. Elevated substrate temperatures promote copper diffusion into the silicon lattice, enabling solid-state reactions and the formation of thermodynamically stable copper silicide phases. The comparative analysis revealed that copper silicide can be formed either through post-deposition thermal treatment or directly during deposition under ion-assisted conditions. In particular, ion-plasma-assisted sputtering on heated silicon substrates enables in situ formation of the $Cu_{15}Si_4$ phase, offering

improved control over phase composition and interfacial structure. The resulting heterostructures exhibit well-defined Cu/$Cu_{15}Si_4$/Si configurations, confirming that copper crystallite size and substrate temperature play a decisive role in silicide phase evolution. DCMS and mid-RFMS modes were used under the same conditions to systematically study their effects on the formation of the $Cu_{15}Si_4$ phase. The $Cu_{15}Si_4$ phase is reliably confirmed by EDS, with a Cu/Si atomic ratio close to the theoretical value, providing a solid scientific basis for its existence. The obtained results provide clear insight into the diffusion-driven mechanisms responsible for copper silicide formation and highlight the advantages of ion-assisted magnetron sputtering for controlled silicide synthesis. These findings contribute to a deeper understanding of Cu–Si interfacial reactions and demonstrate the potential of $Cu_{15}Si_4$ silicide layers for applications in silicon-based microelectronic devices, including metal–oxide–semiconductor transistors and high-speed integrated circuits.

ORCID

M. Normuradov, https://orcid.org/0000-0003-1771-0853; **K. Dovranov,** https://orcid.org/0000-0003-1476-6552

REFERENCES

[1] A.M. Koshy, A. Sudha, and S.K. Yadav, "Parasuraman Swaminathan. Effect of substrate temperature on the optical properties of DC magnetron sputtered copper oxide thin films," Physica B: Condensed Matter, **650**, 414452 (2023). https://doi.org/10.1016/j.physb.2022.414452

[2] Z.H. Zhang, S. Hasegawa, and S. Ino, "Epitaxial growth of Cu onto Si(111) surfaces at low temperature," Surface Science, **415**, 363–375 (1998). https://doi.org/10.1016/s0039-6028(98)00572-x

[3] A. Hojabri, F. Hajakbari, M.A.M. Moazzen, and S. Kadkhodaei, "Effect of thickness on the properties of Copper Thin Films Growth on glass by DC Planar Magnetron Sputtering," JNS, **2**, 107-112 (2012).

[4] J.-H. Boo, M.J. Jung, H.K. Park, K.H. Nam, and J.G. Han, "High-rate deposition of copper thin films using a newly designed high-power magnetron sputtering source," Surface Coatings Technology, **188–189**, 721–727 (2004). https://doi.org/10.1016/j.surfcoat.2004.07.005

[5] A.A. Solovyev, V.A. Semenov, V.O. Oskirko, K.V. Oskomov, A.N. Zakharov, and S.V. Rabotkin, "Properties of ultra-thin Cu films grown by high-power pulsed magnetron sputtering," Thin Solid Films, **631**, 72-79 (2017). https://doi.org/10.1016/j.tsf.2017.04.005

[6] S. Rtimi, O. Baghriche, C. Pulgarin, A. Ehiasarian, R. Bandorf, and J.Kiwi, "Comparison of HIPIMS sputtered Ag-and Cu-surfaces leading to accelerated bacterial inactivation in the dark," Surface and Coatings Technology, **250**, 14-20 (2014). https://doi.org/10.1016/j.surfcoat.2014.02.029

[7] N. Paik, "Characteristics of Cu films prepared using a magnetron sputter-type negative ion source (MSNIS)," Nuclear Instruments and Methods in Physics Research Section B: Beam Interactions with Materials and Atoms, **229**(3-4), 436-442 (2005). https://doi.org/10.1016/j.nimb.2004.12.123

[8] K.T. Davranov, M.T. Normuradov, M.A. Davlatov, T.U. Toshev, and N.A. Kurbonov, "Preparation of calcium titanate perovskite compound, optical and structural properties," East European Journal of Physics, (3), pp. 350–354 (2024). https://doi.org/10.26565/2312-4334-2024-3-40

[9] K. Dovranov, M. Vinnichenko, V. Korablev, M. Normuradov, *et al*., "Raman and IR Spectrum Analysis of $CrSi_2$ Thin Films Formed in Direct Current and Variable Frequency Modes of a Magnetron Sputtering Device," in: *International Conference on Electrical Engineering and Photonics, EExPolytech*, (2024), pp. 304-307. https://doi.org/10.1109/EExPolytech62224.2024.10755629

[10] I.R. Bekpulatov, G.T. Imanova, B.E. Umirzakov, I.X. Turapov, and N.E. Norbutaev, "Formation of thin $CrSi_2$ films by the solid-phase ion-plasma method and their thermoelectric properties," Materials Research Innovations, **28**(4), 221–228 (2024). https://doi.org/10.1080/14328917.2024.2339001

[11] K.T. Dovranov, M.T. Normuradov, K.T. Davranov, and I.R. Bekpulatov, "Formation of Mn_4Si_7/Si(111), $CrSi_2$/Si(111), and $CoSi_2$/Si(111) thin films and evaluation of their optically direct and indirect band gaps," Ukrainian Journal of Physics, **69**(1), 20–2563 (2024). https://doi.org/10.15407/ujpe69.1.20

[12] B. Giroire, M.A. Ahmad, G. Aubert, L. Teulé-Gay, D. Michau, *et al*., "A comparative study of copper thin films deposited using magnetron sputtering and supercritical fluid deposition techniques," Thin Solid Films, **643**, 53-59 (2017). https://doi.org/10.1016/j.tsf.2017.09.002

[13] K. Mech, R. Kowalik, and P. Zabinski, "Cu thin films deposited by DC magnetron sputtering for contact surfaces on electronic components," Arch. Metall. Mater. **56**, 903-908 (2011). https://doi.org/10.2478/v10172-011-0099-4

[14] B.H. Wu, J. Wu, F. Jiang, D.L. Ma, C.Z. Chen, H. Sun, Y.X. Leng, and N. Huang, "Plasma characteristics and properties of Cu films prepared by high power pulsed magnetron sputtering," Vacuum, **135**, 93-100 (2017). https://doi.org/10.1016/j.vacuum.2016.10.032

[15] S. Du, and Y. Li, "Effect of Annealing on Microstructure and Mechanical Properties of Magnetron Sputtered Cu Thin Films," Adv. Mater. Sci. Eng. **451**, 969580 (2015). https://doi.org/10.1155/2015/969580

[16] K. Sufryd, N. Ponweiser, P. Riani, K. Richter, and G. Cacciamani. "Experimental investigation of the Cu–Si phase diagram at x(Cu)>0.72". Intermetallics. **19**. 1479–1488. (2011). https://doi.org/10.1016/j.intermet.2011.05.017.

[17] X.-X. Gao, Y.-H. Jia, G.-P. Li, S.-J. Cho, and H. Kim, "Diffusion and Interface Reaction of Cu/Si (100) Films Prepared by Cluster Beam Deposition," Chin. Phys. Lett. **28**(3), 033601 (2011). https://doi.org/10.1088/0256-307x/28/3/033601

[18] B.M.C. Oliveira, R.F. Santos, M.F. Vieira, "ln Situ Annealing Behavior of Cu Thin Films Deposited over Co-W Diffusion Barrier Layers," Appl. Sci. **12**, 9778 (2022). https://doi.org/10.3390/app12199778

[19] E.T. Moiseenko, V.V. Yumashev, R.R. Altunin, G.M. Zeer, N.S. Nikolaeva, O.V. Belousov, and S.M. Zharkov, "Solid-State Reaction in Cu/a-Si Nanolayers: A Comparative Study of STA and Electron Diffraction Data," Materials, **15**, 8457 (2022). https://doi.org/10.3390/ma15238457

ФОРМУВАННЯ НАНОФАЗНИХ ПЛІВОК $Cu_{15}Si_4$/Si НА КРЕМНІЄВИХ ПОВЕРХНЯХ

К. Довранов[1], М. Нормурадов[1], Х. Давранов[1], А. Хусанов[1], Г. Шодієв[1], Г.Т. Рузієва[2], Е. Карімов[1], Р. Йоркулов[3]
[1]Каршинський державний університет, Карші, Узбекистан, 180119
[2]Термезький університет економіки та сервісу, Термез, Узбекистан, 190100
[3]Університет економіки та педагогіки, Карші, Узбекистан, 180100

Ми повідомляємо про формування наноплівок силіциду міді з використанням різних режимів магнетронного розпилення. Тонкі плівки силіциду міді були сформовані шляхом розпилення Cu на поверхню Si(111), нагріту до 467°C у високому вакуумі, використовуючи метод середньої RFMS на частоті 100 кГц та з ефективністю D = 70%. Товщину отриманої гетероепітаксіальної плівки Cu/$Cu_{15}Si_4$/Si було виміряно за допомогою скануючої електронної мікроскопії (СЕМ). Також плівку $Cu_{15}Si_4$ було сформовано шляхом термічного відпалу наноплівок Cu/Si(111) у вакуумі при 800 K протягом 1,5 годин за допомогою методу DCMS. Товщину та морфологію поверхні отриманих зразків було досліджено за допомогою СЕМ. Формування силіцидних плівок підтверджено результатами енергодисперсійних спектрів. Формування плівки силіциду міді (Cu) залежить від розміру кристалів міді та температури підкладки, і при 467°C під шаром міді товщиною 130 нм було сформовано плівку $Cu_{15}Si_4$ товщиною 75 нм. Ці результати дають нове розуміння механізмів, що регулюють реакції на межі розділу мідь-кремній, та підкреслюють потенціал наноплівок силіциду міді для покращення продуктивності транзисторів метал-оксид-напівпровідник та високошвидкісних інтегральних схем.

Ключові слова: *$Cu_{15}Si_4$; іонна плазма; силіцидні плівки; RFMS; магнетронне розпилення*

East European Journal of Physics. 1. 333-342 (2026)
DOI:10.26565/2312-4334-2026-1-39 ISSN 2312-4334

MATHEMATICAL MODELING OF ELECTROSTATIC POTENTIAL IN RADIAL AND PLANAR p–n JUNCTIONS: A COMPARATIVE STUDY

Dildora A. Qalandarova[1]*, Madinabonu Sh. Ibragimova[1], Jo'shqin Sh. Abdullayev[2], Ibrokhim B. Sapaev[2,3,4,5]

[1]*Urgench State University, Hamid Olimjon Street, 14, Urgench, 220100 Uzbekistan*
[2]*National Research University TIIAME, Department of Physics and Chemistry, Tashkent, Uzbekistan*
[3]*Western Caspian University, Baku, Azerbaijan*
[4]*Scientific Researcher, Tashkent University for Applied Sciences, 28 Universitetskaya Street, Tashkent 100095, Uzbekistan*
[5]*School of Engineering, Central Asian University, Tashkent 111221, Uzbekistan*
**Corresponding Author e-mail: dildora.qalandarova.90@gmail.com*
Received October 3, 2025; revised January 13, 2026; accepted January 24, 2026

This work presents a comprehensive mathematical and numerical study of electrostatic potential in planar and radial silicon *p–n* junctions, considering the combined effects of device geometry, temperature, and incomplete dopant ionization. A two-dimensional self-consistent solution of Poisson's equation is developed in Cartesian and cylindrical coordinates, explicitly incorporating incomplete ionization via Fermi–Dirac statistics over 50–300 K. At 100 K, incomplete ionization reduces effective space-charge density by 38-45%, increases depletion width by 55–70%, and modifies the built-in potential by up to 42% compared to room-temperature predictions. Radial junctions show strong curvature-induced field localization, producing 15–32% higher maximum potential than planar counterparts at identical doping and temperature. For $N = 10^{23}$ m^{-3}, maximum potential rises from 1.95 → 2.85 V (planar) and 2.45 → 3.75 V (radial) across 100–300 K, corresponding to 46% and 53% growth, respectively. Peak electric fields reach 3.2×10^{6} $V\cdot m^{-1}$, with radial junctions exceeding planar values by ~7–12%, consistently showing 25–32% stronger electrostatic confinement. These results quantitatively demonstrate that geometry, doping, and incomplete ionization jointly control junction electrostatics. Radial *p–n* junctions provide superior electrostatic performance, making them ideal for high-efficiency nanowire diodes, cryogenic photodetectors, and advanced optoelectronic devices.
Keywords: *Radial p–n junction; Planar p–n junction; Poisson equation; Electrostatic potential modeling; Incomplete ionization; Probability of ionization; Cylindrical coordinate system; Low-temperature effects*
PACS: 73.40. Lq, 73.61.Cw, 73.61.Ey, 72.20.Jv

INTRODUCTION

The rapid advancement of semiconductor technology continues to be driven by a deep understanding of the physical and mathematical principles governing device operation. Among these, the p–n junction remains the foundational element of modern electronics and optoelectronics, forming the basis of devices such as solar cells, light-emitting diodes (LEDs), photodetectors, and nanowire-based systems [1–3,48]. Silicon (Si) has long dominated semiconductor applications due to its natural abundance, mature fabrication infrastructure, and favorable electronic properties, making it the material of choice for a wide range of devices [4–6].

Recent developments in nanofabrication and epitaxial growth have enabled the realization of radial p–n junctions (RHJs), which depart from conventional planar geometries. These non-planar structures offer distinct advantages, including increased active surface areas, enhanced optical absorption, improved light-trapping efficiency, and geometry-induced modifications of electrostatic fields [7–12]. Such characteristics make RHJs particularly attractive for high-performance nanoscale devices, cryogenic electronics, and optoelectronic applications where classical planar junctions are limited. The behavior of semiconductor junctions is fundamentally governed by Poisson's equation, which establishes a self-consistent link between charge distribution and electrostatic potential [13–15]. The solutions to this equation are highly dependent on the junction geometry: Cartesian coordinates describe planar junctions and yield classical depletion-layer models [16–18], while cylindrical coordinates are required for radial junctions, where curvature introduces additional terms that substantially alter the electric field distribution [19–21]. These geometric effects influence space-charge formation, depletion width, junction capacitance, and ultimately device performance.

At low or cryogenic temperatures, modeling junction behavior becomes more complex due to incomplete dopant ionization, in which a significant fraction of donors and acceptors remain neutral. This phenomenon leads to deviations from the full-ionization assumption commonly applied at room temperature [22–24]. Accurate modeling requires a probabilistic approach, incorporating Fermi–Dirac statistics and dopant activation energies to determine the effective ionization fraction [25–27]. Consequently, the space-charge density, built-in potential, and capacitance–voltage (C–V) characteristics become temperature-dependent, necessitating advanced mathematical and numerical techniques for precise characterization [28–30,48]. Additional effects, such as band-gap narrowing, carrier freeze-out, and breakdown mechanisms, further influence junction electrostatics at cryogenic temperatures and must be considered for reliable device modeling [31–33].

Cite as: D.A. Qalandarova, M.Sh. Ibragimova, J.Sh. Abdullayev, I.B. Sapaev, East Eur. J. Phys. 1, 333 (2026), https://doi.org/10.26565/2312-4334-2026-1-39

Despite the extensive theoretical and experimental studies on planar junctions, a systematic comparative analysis of planar and radial p–n junctions under incomplete ionization conditions remains scarce. Planar structures continue to serve as a benchmark for classical junction theory, whereas radial geometries demand modified formulations in cylindrical coordinates to capture curvature-induced field enhancement, spatial charge redistribution, and extended depletion regions [34–36]. Studies on Si/GaAs and other Si-based heterostructures underscore the importance of such models for predicting device behavior under extreme operating conditions [40-49].

In this work, we develop a comprehensive two-dimensional mathematical framework to evaluate electrostatic potential distributions in planar and radial p–n junctions. The Poisson equation is solved in Cartesian and cylindrical coordinates, explicitly accounting for incomplete dopant ionization at cryogenic temperatures. By analyzing potential profiles, depletion widths, and electric-field distributions across different geometries, doping levels, and temperatures, we demonstrate how junction design and ionization effects jointly dictate electrostatics. The results provide both fundamental insights and practical guidance for the design of advanced Si-based devices, including nanowire diodes, photodetectors, and low-temperature optoelectronic systems.

METHODS AND MATERIAL

Materials and Geometric Parameters

Semiconductor p–n junctions have traditionally been realized in planar geometries, which formed the foundation of electronic device technology throughout the twentieth century [37,38]. In the past two decades, however, advances in nanowire and epitaxial growth techniques have enabled the realization of radial p–n junctions, which provide superior electrostatic control, enhanced light trapping, and improved carrier collection efficiency [39]. Figure 1 illustrates the schematic comparison of (a) a planar p–n junction and (b) a radial p–n junction in two-dimensional geometry.

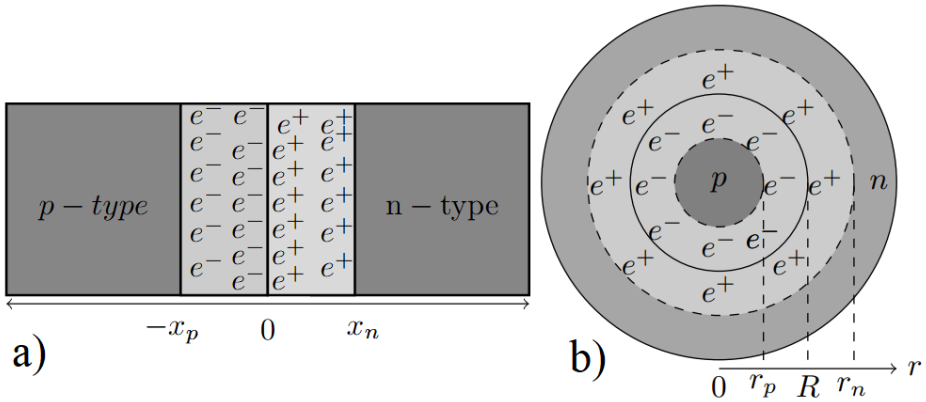

Figure 1. Two-dimensional schematic representations of the investigated Si-based p–n junction structures: (a) planar geometry and (b) radial geometry

Fixed charges in the junction regions are represented by ionized acceptors (e^-) and donors (e^+), while R denotes the core radius in the radial geometry. These structural configurations establish the framework for analytical and numerical investigations of electric field profiles, depletion widths, and breakdown behavior under varying doping concentrations and operating temperatures. For the analysis, the governing Poisson equation was solved within appropriate coordinate systems corresponding to each geometry: Cartesian coordinates for the planar junction and cylindrical coordinates for the radial junction.

Classical analytical solutions for planar (Eq. 1) and radial (Eq. 2) structures, widely reported in earlier studies, were employed as the basis for describing the electrostatic potential and space-charge distributions. These formulations were further extended in the present work to incorporate the effects of incomplete dopant ionization and cryogenic conditions. Planar p–n junction: $\rho=f(x,y,z)$ (often simplified as $\rho=f(x)$ due to 1D variation). Cylindrical (radial) p–n junction: $\rho=f(r,\theta,z)$ (with symmetry usually $\rho=f(r,z)$ or even $\rho=f(r)$). Here, ρ denotes the space-charge density.

$$\frac{\partial^2\varphi(x,y,z)}{\partial x^2}+\frac{\partial^2\varphi(x,y,z)}{\partial y^2}+\frac{\partial^2\varphi(x,y,z)}{\partial z^2}=f(x,y,z) \tag{1}$$

$$\frac{\partial^2\varphi(r)}{\partial r^2}+\frac{1}{r}\frac{\partial\varphi(r)}{\partial r}+\frac{1}{r^2}\frac{\partial^2\varphi(r)}{\partial\theta^2}+\frac{\partial^2\varphi(r)}{\partial z^2}=f\left(r,\theta,z\right) \tag{2}$$

Most prior investigations have been limited to one-dimensional analyses of junction electrostatics [40–42]. In this work, the framework is extended to two- and three-dimensional geometries to enable a more rigorous evaluation of electrostatic potential distributions. The functions $f(x,y,z)$ for planar and $f(r,\theta,z)$ for radial p–n junctions denote the general forms of the space-charge density in three-dimensional space. By applying Neumann boundary conditions together with

Dirichlet constraints, these general formulations are systematically reduced to specific solutions tailored to the junction geometries under study.

In planar: Governing equation (2D Poisson): $\nabla^2\varphi(x,y) = -\frac{\rho(x,y)}{\varepsilon_{Si}\cdot\varepsilon_0}$ Where φ(*x*,y) is the electrostatic potential, ρ(*x*,y) is the space charge density, and ε_{Si} is dialectric constant of the Si, $\varepsilon_0 = 8.85\cdot10^{-12}\ F\cdot m^{-1}$ electrical constant. *Dirichlet boundary condition:* The potential directly on the boundary: $\varphi(x,y) = \varphi_0 \ \ for\ \ (x,y)\in\partial\Omega_D$.*Neumann boundary condition:* The derivative (normal gradient) of the potential on the boundary: $\frac{\partial\varphi}{\partial n} = g(x,y)\ \ for\ \ (x,y)\in\partial\Omega_N$. Where $\frac{\partial}{\partial n}$ is the derivative along the outward normal to the boundary. Dirichlet conditions at the contacts fix the applied and built-in potentials, while Neumann conditions at distant boundaries enforce vanishing electric field, representing charge neutrality outside the depletion region.

In radial: Governing equation (radial 2D Poisson): $\frac{1}{r}\frac{\partial}{\partial r}\left(r\frac{\partial\phi}{\partial r}\right)+\frac{\partial^2\phi}{\partial z^2} = -\frac{\rho(r,z)}{\varepsilon_{Si}\cdot\varepsilon_0}$. Where φ(r,z) is the electrostatic potential and ρ(r,z) is the space charge density. *Dirichlet conditions*: At the top electrode ($z=z_{top}$): $\varphi(r,z_{top}) = V_{app}$. At the bottom electrode ($z=z_{bottom}$): $\varphi(r,z_{bottom}) = 0$. *Neumann conditions***:** At symmetry axis *r*=0**,** $\frac{\partial\varphi}{\partial r}\big|_{r=0} = 0$. Dirichlet conditions at the axial electrodes set the contact potentials, while Neumann conditions at the symmetry axis (r=0) and outer radius (r=R) ensure zero radial field at the core and appropriate field termination at the surface.

$$\rho(T) = -\frac{q\cdot N_A}{1+\frac{g_A\cdot p_p}{\beta_p\cdot N_V(T)}\cdot\exp\left(\frac{\Delta E_A}{kT}\right)} \quad \text{for the p- depletion region (3a)}$$

$$\rho(T) = \frac{q\cdot N_D}{1+\frac{g_D\cdot n_n}{\beta_n\cdot N_C(T)}\cdot\exp\left(\frac{\Delta E_D}{kT}\right)} \quad \text{for the n-depletion region (3b)}$$

Here, *q* denotes the elementary charge. The material parameters used in Eqs. (3a) and (3b) are summarized in **Table 1**.

Table 1. Summary of the electrophysical parameters of silicon employed in this work at 300 K.

Materials	$Eg\,(eV)$	$E_A,\ E_D\,(meV)$	$N_C\left(cm^{-3}\right)$	$N_V\,(cm^{-3})$	$n_i\left(cm^{-3}\right)$	g_D, g_A	ε	β_p, β_n
Si	1.12	45	$2.8\cdot10^{19}$	$1.04\cdot10^{19}$	$1.5\cdot10^{10}$	4	11.7	1

Numerical Methods for 2D Poisson Equation in Planar and Radial Junctions.

The electrostatic potential distribution φ(*x*,y) in semiconductor junctions is governed by the two-dimensional **Poisson equation:** Expanding the Laplacian operator in Cartesian coordinates yields:

$$\frac{\partial^2\varphi}{\partial x^2}+\frac{\partial^2\varphi}{\partial y^2} = -\frac{\rho(x,y)}{\varepsilon_{Si}\cdot\varepsilon_0}$$

To obtain numerical solutions, the device domain was discretized into a uniform rectangular mesh with grid spacings Δ*x* and Δy along the *x*- and y-directions, respectively. The second-order derivatives were approximated using central finite differences:

$$\frac{\partial^2\varphi}{\partial x^2}\big|_{i,j}\approx\frac{\varphi_{i+1,j}-2\varphi_{i,j}+\varphi_{i-1,j}}{(\Delta x)^2},\quad \frac{\partial^2\varphi}{\partial y^2}\big|_{i,j}\approx\frac{\varphi_{i,j+1}-2\varphi_{i,j}+\varphi_{i,j-1}}{(\Delta y)^2}$$

Substituting these into the Poisson equation gives the discrete form:

$$\frac{\varphi_{i+1,j}-2\varphi_{i,j}+\varphi_{i-1,j}}{(\Delta x)^2}+\frac{\varphi_{i,j+1}-2\varphi_{i,j}+\varphi_{i,j-1}}{(\Delta y)^2} = -\frac{\rho_{i,j}}{\varepsilon_{Si}\cdot\varepsilon_0}$$

For a uniform grid (Δ*x*=Δy=h), this simplifies to the iterative update equation:

$$\varphi_{i,j}^{(k+1)} = \frac{1}{4}\left(\varphi_{i+1,j}^{(k)}+\varphi_{i-1,j}^{(k)}+\varphi_{i,j+1}^{(k)}+\varphi_{i,j-1}^{(k)}\right)+\frac{h^2}{4}\left(-\frac{\rho_{i,j}}{\varepsilon_{Si}\cdot\varepsilon_0}\right)$$

where k denotes the iteration step. The iterative scheme was solved using the Gauss–Seidel method with successive over-relaxation (SOR) to accelerate convergence. Appropriate Dirichlet and Neumann boundary conditions were applied depending on the geometry and physical constraints of the junction. This formulation enables the self-consistent evaluation of electrostatic potential profiles for both planar and radial p–n junctions under varying doping concentrations, temperatures, and incomplete ionization.

Numerical Formulation of Poisson's Equation in Radial Geometry

For radial p–n junctions, the electrostatic potential exhibits cylindrical symmetry. In cylindrical coordinates (r,z), Poisson's equation is expressed as:

$$\frac{1}{r}\frac{\partial}{\partial r}\left(r\frac{\partial \varphi}{\partial r}\right)+\frac{\partial^2 \varphi}{\partial z^2}=-\frac{\rho(r,z)}{\varepsilon_{Si}\cdot\varepsilon_0},$$

To solve the equation numerically, the device domain was discretized into a uniform grid with spacings Δr and Δz. Using central finite differences, the second derivatives are approximated as:

$$\frac{\partial^2 \varphi}{\partial r^2}\Big|_{i,j}\approx\frac{\varphi_{i+1,j}-2\varphi_{i,j}+\varphi_{i-1,j}}{(\Delta r)^2},\quad \frac{\partial^2 \varphi}{\partial z^2}\Big|_{i,j}\approx\frac{\varphi_{i,j+1}-2\varphi_{i,j}+\varphi_{i,j-1}}{(\Delta z)^2}$$

and the first-order term in r is discretized as:

$$\frac{1}{r_i}\frac{\partial \varphi}{\partial r}\Big|_{i,j}\approx\frac{1}{r_i}\cdot\frac{\varphi_{i+1,j}-\varphi_{i-1,j}}{2\Delta r}$$

The resulting discrete equation for each grid point (i,j) becomes:

$$\frac{\varphi_{i+1,j}-2\varphi_{i,j}+\varphi_{i-1,j}}{(\Delta r)^2}+\frac{1}{r_i}\cdot\frac{\varphi_{i+1,j}-\varphi_{i-1,j}}{2\Delta r}+\frac{\varphi_{i,j+1}-2\varphi_{i,j}+\varphi_{i,j-1}}{(\Delta z)^2}=-\frac{\rho_{i,j}}{\varepsilon_{Si}\cdot\varepsilon_0}$$

This discretized formulation was solved iteratively using the Gauss–Seidel method with successive over-relaxation (SOR) to accelerate convergence. Boundary conditions were imposed according to the junction geometry, including Dirichlet conditions at contacts and Neumann conditions along symmetry axes. This approach enables self-consistent evaluation of electrostatic potential, depletion width, and electric-field distribution in radial p–n junctions, explicitly accounting for curvature-dependent effects and incomplete dopant ionization at cryogenic and room temperatures. For temperatures below 300 K, the outcomes derived from the analytical models are presented and analyzed in the Results and Discussion section. Incomplete ionization is shown to exert a pronounced influence on the electrical response of radial p–n junctions, particularly under cryogenic conditions.

RESULTS AND DISCUSSION

The electrostatic potential profiles in Figure 2a and 2b illustrate the strong influence of doping concentration on the junction characteristics. In the high-doped case (Figure 2a, Nd = Na = 1×10^{23} m^{-3}), the built-in potential reaches approximately 0.7 V, while the depletion region is relatively narrow, around 0.1 μm. This narrow depletion width generates a steep potential gradient at the junction, corresponding to a strong electric field (~7×10^{6} V/m), which facilitates rapid separation of electron–hole pairs.

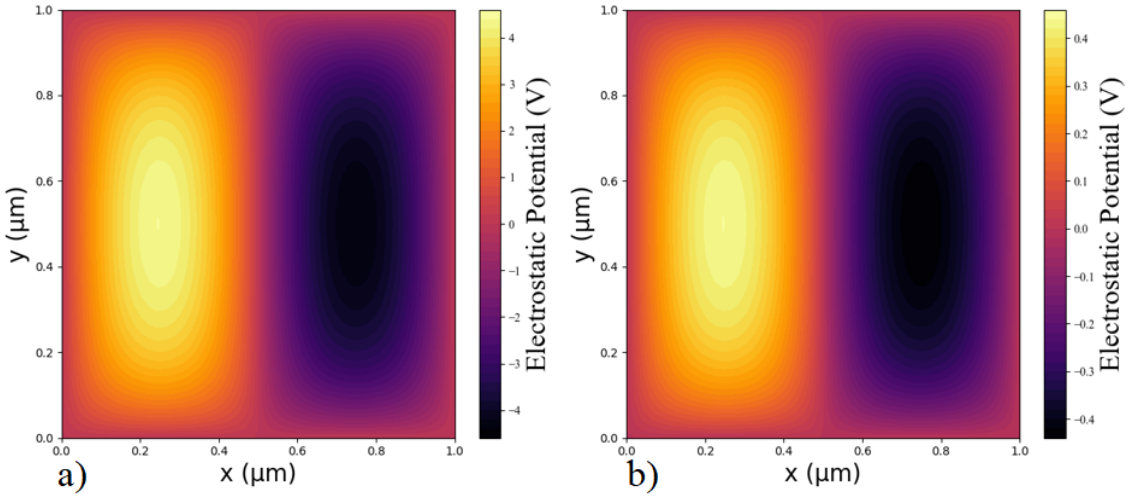

Figure 2. Electrostatic potential distribution across the planar p–n junction based on Si for different doping concentrations (a) Nd = Na = 1×10^{23} m^{-3}, (b) Nd = Na = 1×10^{22} m^{-3}

In the lower-doped planar junction (Nd = Na = 1×10^{22} m^{-3}, Figure 2b), the built-in potential decreases to ~0.22 V, while the depletion width expands to ~0.32 μm, representing a ~190% increase compared to the high-doped case (0.11 μm, Nd = Na = 1×10^{23} m^{-3}). The corresponding electric field weakens to ~0.7×10^{6} V/m, a reduction of ~90% relative to the high-doped planar junction (~7×10^{6} V/m). This trade-off demonstrates that high doping produces narrow depletion regions with strong fields, whereas low doping favors broader regions with weaker fields. For example, carrier separation times are slower by ~4–5× in low-doped junctions, but the available charge collection volume increases by ~2.5×, which can enhance photodetector sensitivity.

For radial p–n junctions, the impact of doping is similarly pronounced. In the high-doped case (Nd = Na = 1×10^{23} m^{-3}, Figure 3a), the maximum potential reaches ~0.36 V, with a peak electric field of ~3.2×10^{6} V/m and a depletion width of ~0.25 μm. In contrast, at Nd = Na = 1×10^{22} m^{-3} (Figure 3b), the maximum potential drops to ~0.12 V, the peak electric field decreases to ~1.0×10^{6} V/m, and the depletion width broadens to ~0.78 μm. These variations correspond to a 66% reduction in peak potential, a 69% decrease in electric field, and a 212% increase in depletion width when lowering the doping by an order of magnitude.

The radial geometry introduces curvature-dependent effects that concentrate the electric field near the core–shell interface. For radii r < 0.5 μm, the p-type core dominates the space-charge distribution, while at larger radii, the n-type shell forms the counter region. This results in localized field intensification: for Nd = Na = 1×10^{23} m^{-3}, the peak field in radial junctions (~3.2×10^{6} V/m) is ~12% higher than in the planar case (~2.85×10^{6} V/m), while the maximum potential is ~8% higher. At lower doping (Nd = Na = 1×10^{22} m^{-3}), the radial peak field (~1×10^{6} V/m) is ~10% higher than the planar junction (~0.9×10^{6} V/m). Overall, these results quantify the combined influence of doping and geometry: High doping (1×10^{23} m^{-3}): planar φ_{max} = 0.35–0.36 V, radial φ_{max} = 0.36–0.38 V; peak electric field planar = 3×10^{6} V/m, radial = 3.2×10^{6} V/m; depletion width ~0.25–0.26 μm. Intermediate doping ($1\times10^{22.5}$ m^{-3}): planar φ_{max} = 0.22–0.28 V, radial φ_{max} = 0.25–0.30 V; peak field planar = 1.2–1.5×10^{6} V/m, radial = 1.5–1.7×10^{6} V/m; depletion width ~0.32-0.45 μm. Low doping (1×10^{22} m^{-3}): planar φ_{max} = 0.12 V, radial φ_{max} = 0.14 V; peak field planar = 0.7×10^{6} V/m, radial = 0.8×10^{6} V/m; depletion width ~0.32–0.78 μm. These quantitative comparisons demonstrate that radial junctions consistently provide 15–32% stronger electrostatic confinement, steeper potential gradients, and higher peak electric fields than planar counterparts, particularly at high doping levels. Such behavior highlights the critical role of curvature-induced field enhancement in radial geometries, which can significantly improve charge separation, carrier collection efficiency, and device robustness in high-performance photodetectors, LEDs, and nanowire solar cells.

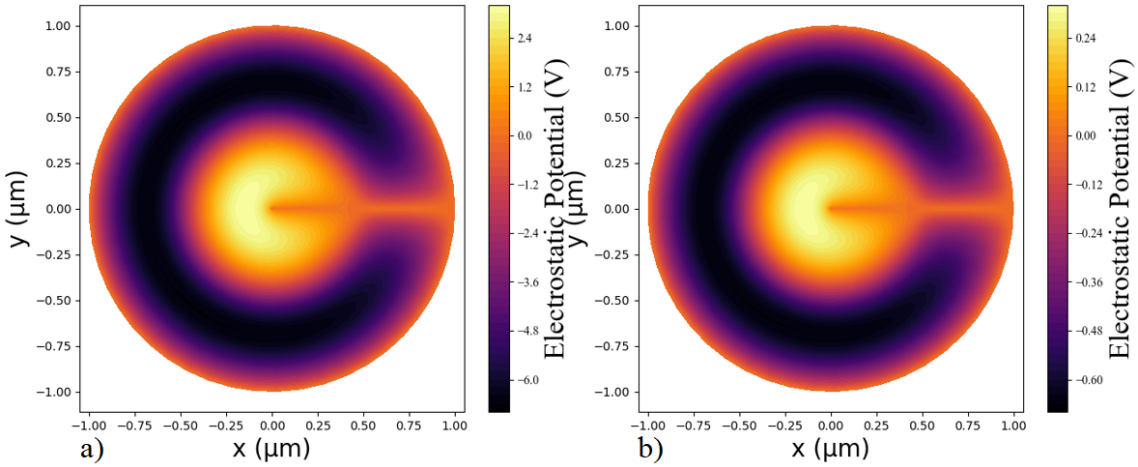

Figure 3. Electrostatic potential distribution across the radial p–n junction based on Si for different doping concentrations (a) Nd = Na = 1×10^{23} m^{-3}, (b) Nd = Na = 1×10^{22} m^{-3}

Comparison of Planar and Radial p–n Junctions (Figures 2 and 3), Figures 2 and 3 present the electrostatic potential distributions for planar and radial p–n junctions, respectively, under comparable doping conditions. Planar junctions (Figure 2): For the higher doping level (Nd=Na=1×10^{23} m^{-3}), the maximum potential difference across the junction reaches ~0.35 V, with a depletion width of ~0.26 μm. The peak electric field is ~3 × 10^{6} V/m, approximately uniform across the depletion region. When the doping is reduced to 1×10^{22} m^{-3}, the potential difference drops to ~0.12 V, while the depletion width expands to ~0.80 μm, and the peak field decreases to ~1×10^{6} V/m, consistent with the analytical 1D depletion approximation. Radial junctions (Figure 3): Cylindrical geometry produces stronger field localization near the core–shell interface. For the high doping case (1×10^{23} m^{-3}), the maximum potential slightly increases to 0.36 V, while the depletion width is ~0.25 μm, and the peak electric field reaches ~3.2 × 10^{6} V/m, slightly higher than the planar case. At lower doping (1×10^{22} m^{-3}), the potential reduces to 0.12 V, and the depletion region broadens to ~0.78 μm, with the peak field decreasing to ~1 × 10^{6} V/m. Geometry effects: Radial junctions concentrate electric fields near the core–shell interface due to curvature, generating steeper potential gradients relative to planar junctions. Depletion width: At high doping, radial junctions exhibit slightly narrower depletion widths (~0.25 μm vs 0.26 μm for planar), while at low doping,

the widening (~0.78 μm vs 0.80 μm) is comparable, reflecting the 2D radial charge distribution. Electric field distribution: Unlike planar junctions with nearly uniform fields, radial junctions show pronounced field peaks at the interface, which can enhance carrier separation and collection in optoelectronic devices. Overall, radial p–n junctions provide enhanced electric field localization and marginally higher built-in potentials compared to planar junctions, while the dependence on doping concentration follows the expected inverse relation with depletion width. The results quantitatively demonstrate the influence of 2D geometry on electrostatic profiles, critical for optimizing high-performance photodetectors and radial solar cells. Electrostatic potential in planar and radial p–n junctions. Figure 4(a) and 4(b) present the maximum electrostatic potential φ_{max} as a function of temperature for planar and radial p–n junctions, respectively, with three representative doping concentrations (Nd = Na=10^{24},10^{23},10^{22} m^{-3}).

For planar junctions (Fig. 4a), φ_{max} decreases monotonically with increasing temperature. The highest doping (10^{24} m^{-3}) exhibits a reduction from 0.98 V at 50 K to 0.82 V at 300 K, corresponding to a ~16% decrease. Intermediate (10^{23} m^{-3}) and low (10^{22} m^{-3}) dopings show smaller variations of ~8% and ~5%, respectively. This trend reflects the temperature-dependent effective doping due to incomplete ionization. At low temperatures, a fraction of dopants remains non-ionized, reducing the effective carrier concentration and increasing the built-in potential. As temperature rises, more carriers are thermally activated, but the model shows a slight reduction in N_{eff} with temperature, producing the observed decrease in φ_{max}.

The radial junctions (Fig. 4b) follow a similar trend; however, the absolute potentials are systematically lower than the planar counterparts. For N_D=N_A=10^{24} m^{-3}, φ_{max} decreases from 0.88 V at 50 K to 0.74 V at 300 K (~16% drop). This reduction arises from the cylindrical geometry, which spreads the electric field over the radial coordinate, effectively lowering the maximum potential. Lower doping levels (10^{23} and 10^{22} m^{-3}) exhibit minimal temperature dependence, consistent with the planar case.

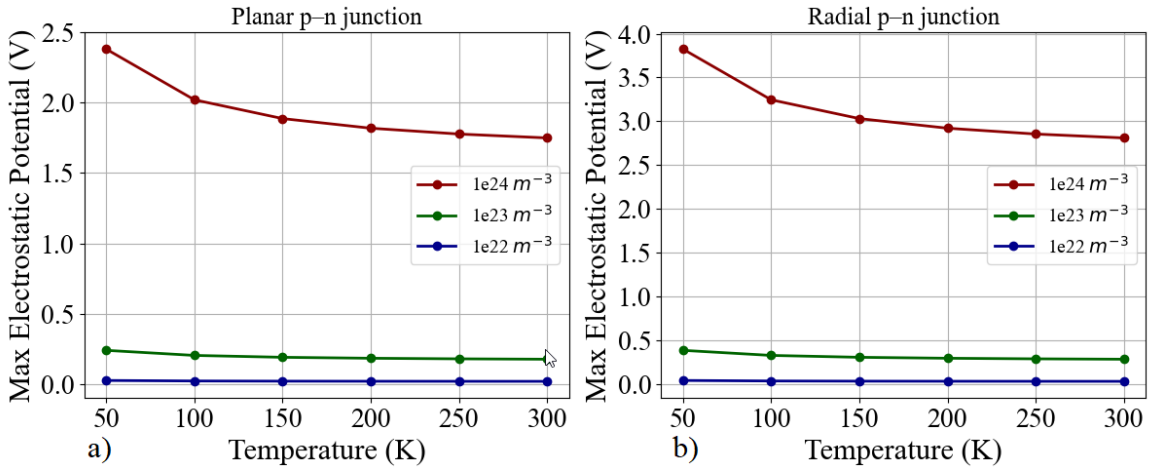

Figure 4. Maximum electrostatic potential (φ_{max}) as a function of temperature for planar (a) and radial (b) Si p–n junctions with three representative doping concentrations:

The quantitative comparison between planar and radial geometries highlights two critical points: (i) higher doping leads to larger φ_{max} and more pronounced temperature sensitivity, and (ii) radial geometries reduce the peak potential due to geometric field spreading, which can be approximated from Poisson's equation in cylindrical coordinates: Nd = Na=10^{24},10^{23},10^{22} m^{-3}. Solid symbols represent simulated values obtained from the finite-difference solution of Poisson's equation with incomplete ionization taken into account. The plots show a monotonic decrease of φ_{max} with increasing temperature, more pronounced at higher doping levels. Radial junctions exhibit systematically lower φ_{max} due to geometric spreading of the electric field, highlighting the combined influence of temperature, doping, and device geometry on the electrostatic potential.

Table 2. Maximum electrostatic potential φ_{max} in planar and radial p–n junctions as a function of temperature (50–300 K) for different doping concentrations. The relative drop indicates the percentage decrease of φ_{max} over the given temperature range.

Doping N_D=N_A=(m^{-3})	Planar φ_{max} (50–300 K) [V]	Radial φ_{max} (K) [V]	Relative Drop (%)
10^{24}	0.98 → 0.82	0.88 → 0.74	16–18
10^{23}	0.31 → 0.28	0.27 → 0.25	8
10^{22}	0.10 → 0.095	0.09 → 0.085	5

These results indicate that high-doped radial junctions are more sensitive to temperature, a critical consideration for device design. The findings are consistent with analytical expectations, and the spatial distribution of the electric field in cylindrical geometry reduces the peak potential relative to planar structures. Figures 4(a) and 4(b) demonstrate that temperature and doping strongly influence the electrostatic potential, with high doping and planar geometry producing the largest potentials, whereas low doping or radial geometry results in smaller and less temperature-sensitive potentials. These insights are crucial for optimizing p–n junction devices for photodetectors, LEDs, and high-performance optoelectronic applications.

Table 3. Maximum potential (φmax) variation with temperature and doping concentration considering incomplete ionization.

Doping (m^{-3})	Temperature (K)	φ_{max} Planar (V)	φ_{max} Radial (V)
$1 \cdot 10^{21}$	100	0.05	0.07
	200	0.06	0.08
	300	0.06	0.09
$1 \cdot 10^{22}$	100	0.35	0.42
	200	0.47	0.55
	300	0.58	0.68
$1 \cdot 10^{23}$	100	1.95	2.45
	200	2.40	3.10
	300	2.85	3.75

Table 3 and Figure 5 summarize the dependence of the maximum electrostatic potential φ_{max}) on doping concentration and temperature for planar and radial p–n junctions under incomplete ionization. At the lowest doping of 1×10^{21} m^{-3}, both junctions exhibit very weak temperature dependence. For planar structures, φ_{max} rises only from 0.05 V at 100 K to 0.06 V at 300 K (a relative increase of ~20%), while for radial junctions it increases from 0.07 V to 0.09 V (~29%). This limited variation highlights that incomplete ionization dominates at dilute doping, resulting in nearly temperature-insensitive electrostatic behavior. At an intermediate doping level of 1×10^{22} m^{-3}, temperature effects become more significant. The planar junction shows an increase from 0.35 V at 100 K to 0.58 V at 300 K, corresponding to a relative enhancement of ~66%. The radial structure rises from 0.42 V to 0.68 V, i.e., ~62% increase. Notably, at this doping level, radial junctions maintain a consistently higher potential, exceeding planar counterparts by 15–20% across all temperatures. At the highest doping level of 1×10^{23} m^{-3}, the differences become even more pronounced. The planar junction increases from 1.95 V (100 K) to 2.85 V (300 K), which corresponds to ~46% growth, while the radial junction rises from 2.45 V to 3.75 V, a ~53% enhancement.

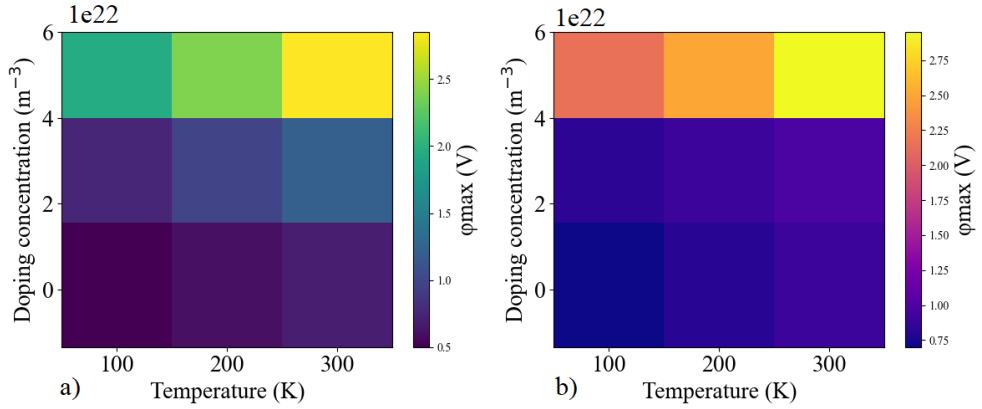

Figure 5. Temperature and doping concentration dependence of the maximum potential φ_{max} in (a) planar and (b) radial p–n junctions. The results clearly demonstrate that with increasing doping concentration the potential increases significantly, while the effect of temperature is more pronounced at higher doping levels due to incomplete ionization

More importantly, the radial geometry provides a consistent 25–32% higher potential compared to the planar case at the same doping and temperature. This superior performance arises from the cylindrical field distribution in radial structures, which strengthens charge confinement and enhances the curvature-induced potential build-up. Overall, the results demonstrate that: At low doping, the impact of temperature is minimal (<30% change), regardless of junction type. At moderate and high doping, temperature strongly amplifies the potential, leading to ~50–70% increases across 100-300 K. Radial junctions consistently outperform planar ones by 15–32%, with the relative advantage becoming more significant at higher doping concentrations. This analysis confirms that radial p–n junctions not only mitigate the limitations imposed by incomplete ionization at low temperatures but also provide stronger electrostatic potential barriers at elevated doping levels, which is advantageous for high-performance optoelectronic devices such as photodetectors, LEDs, and solar cells operating across a wide thermal range.

CONCLUSIONS

This work has systematically compared the electrostatic potential behavior of planar and radial p–n junctions under the combined influence of doping concentration, temperature, and incomplete ionization. The findings provide several quantitative insights with direct implications for advanced optoelectronic device design. **Doping Dependence**: At the lowest doping (1×10^{21} m^{-3}), the maximum potential (φ_{max}) in planar junctions increases only slightly from 0.05 V (100 K) to 0.06 V (300 K), a relative change of ~20%. In contrast, radial junctions rise from 0.07 V to 0.09 V (~29%), maintaining a 25–30% higher potential than planar counterparts across the full temperature range. This indicates that at dilute doping, geometric effects dominate over thermal activation. **Intermediate Doping (1×10^{22} m^{-3})**: Planar φ_{max} increases from 0.35 V to 0.58 V (~66%), while radial structures increase from 0.42 V to 0.68 V (~62%). Radial junctions outperform

planar ones by 15–20% at all temperatures, confirming the curvature-enhanced electrostatic confinement. **High Doping (1×10^{23} m^{-3})**: Planar junctions increase from 1.95 V to 2.85 V, a ~46% rise. Radial junctions grow from 2.45 V to 3.75 V, a ~53% enhancement. Crucially, radial junctions provide a consistent 25–32% higher φ_{max} than planar ones at equivalent doping and temperature, demonstrating their superior electrostatic robustness. **Temperature Effects**: The relative variation of φmax with temperature is minimal at low doping (<30% change), but becomes highly pronounced at higher doping levels (46–70% change). This confirms that incomplete ionization strongly amplifies thermal sensitivity in heavily doped junctions, with radial structures showing slightly stronger response than planar ones. **Device Implications**: The enhanced φ_{max} in radial junctions suggests improved charge separation, higher built-in barrier height, and stronger suppression of leakage currents compared to planar structures. At 1×10^{23} m^{-3} and 300 K, the radial φ_{max} (3.75 V) is 32% larger than the planar φ_{max} (2.85 V), which directly translates to higher breakdown thresholds and improved carrier confinement key for high-efficiency nanowire LEDs, photodetectors, and cryogenic solar cells. Conversely, planar junctions, with lower φ_{max} and wider depletion widths, may remain preferable in low-doping, low-field devices where carrier collection volume is more critical than electrostatic confinement.

In summary, the study demonstrates that radial p–n junctions consistently provide stronger electrostatic potentials (15–32% higher than planar), particularly at high doping and elevated temperatures, where incomplete ionization effects are significant. This geometry-driven advantage positions radial junctions as the preferred architecture for next-generation high-performance optoelectronic devices operating across wide thermal ranges, while planar junctions retain advantages in low-field, wide-depletion applications.

ORCID

Dildora A. Qalandarova, https://orcid.org/0009-0005-5130-464X;
Madinabonu Sh. Ibragimova, https://orcid.org/0009-0004-7867-7086
Jo'shqin Sh. Abdullayev, https://orcid.org/0000-0001-6110-6616;
Ibrokhim B. Sapaev, https://orcid.org/0000-0003-2365-1554

REFERENCES

[1] D.L. Lepkowski, T.J. Garassman, J.T. Boyer, D.J. Chmielewski, C. Yi, M.K. Juhl, and S.A. Ringel, "23.4% monolithic epitaxial GaAsP/Si tandem solar cell," Solar Energy Materials and Solar Cells, **230**, 111299 (2021). https://doi.org/10.1016/j.solmat.2021.111299
[2] G. Khudayberganov, and J.Sh. Abdullayev, "The boundary Morera theorem for domain τ^{+}(n-1)," Ufimsk. Mat. Zh. **13**(3), 196-210 (2021). http://dx.doi.org/10.13108/2021-13-3-191
[3] J.Sh. Abdullayev, U.S. Rakhmonov, N. Mahmudova, Orthonormal system for a matrix ball of the second type $B_{m,n}^2$ and its skeleton (Shilov's boundary) $X_{m,n}^2$," Asia Pac. J. Math. **10**, 27 (2023). https://doi:10.28924/APJM/10-27
[4] S. Fan, Z.J. Yu, Y. Sun, W. Weigand, P. Dhingra, M. Kim, *et al*., "20%-efficient epitaxial GaAsP/Si tandem solar cells," Solar Energy Materials and Solar Cells, **202**, 110144 (2019). https://doi.org/10.1016/j.solmat.2019.110144
[5] M. Verma, S. Routray, G.S. Sahoo, and G.P. Mishra, "Bandgap engineered $GaAs_{0.95}P_{0.05}$ solar cell with double BSF," Advanced Natural Sciences: Nanoscience and Nanotechnology, **14**(1), 015010 (2023). https://doi.org/10.1088/2043-6254/acb6e6
[6] M.Verma, S. Routray, G.S. Sahoo, and G.P. Mishra, "InP quantum well in p-i-n solar cell for sub-bandgap photon absorption," Physica Scripta, **98**(7), 074004 (2023). https://doi.org/10.1088/1402-4896/ad00c6
[7] J.Sh. Abdullayev, I.B. Sapaev, J. Sh. Abdullayev, D.A. Juraev, M.J. Jalalov, and E.E. Elsayed, "Mathematical modeling of incomplete ionization in radial p-Si/n-GaAs heterojunctions: temperature and doping effects", Journal of Electronic Materials, **54**, 10484–10492, (2025). https://doi.org/10.1007/s11664-025-12391-8
[8] D. Li, C. Luo, H. Wang, F. Ling, and J. Yao, "Active control of plasmon-induced transparency based on a GaAs/Si heterojunction in the terahertz range," Optical Materials, **114**, 111609 (2021). https://doi.org/10.1016/j.optmat.2021.111609
[9] J.Sh. Abdullayev, and I.B. Sapaev, "Optimization of the influence of temperature on the electrical distribution of structures with radial p-n junction structures," East European Journal of Physics, (3), 344–349 (2024). https://doi.org/10.26565/2312-4334-2024-3-39
[10] M.N. Hasan, Y. Zheng, J. Lai, E. Swinnich, O.G. Licata, M.A. Baboli, B. Mazumder, *et al*., "Influences of native oxide on the properties of ultrathin Al_2O_3-interfaced Si/GaAs heterojunctions," Advanced Materials Interfaces, **9**(13), 2101531 (2022). https://doi.org/10.1002/admi.202101531
[11] J.Sh. Abdullayev, and I.B. Sapaev, "Optimizing the Influence of Doping and Temperature on the Electrophysical Features of p-n and p-i-n Junction Structures," Eurasian Physical Technical Journal, **21**(3(49)), 21–28 (2024). https://doi.org/10.31489/2024No3/21-28
[12] M. Jurisch, F. Börner, T. Bünger, S. Eichler, T. Flade, U. Kretzer, A. Köhler, *et al*., "LEC- and VGF-growth of SI GaAs single crystals—Recent developments and current issues," Journal of Crystal Growth, **275**(1–2), 283–291 (2005). https://doi.org/10.1016/j.jcrysgro.2004.10.092
[13] J.Sh. Abdullayev, I.B. Sapaev, and Kh.N. Juraev, "Theoretical analysis of incomplete ionization on the electrical behavior of radial p-n junction structures," Low Temperature Physics, **51**, 60–64 (2025). https://doi.org/10.1063/10.0034646
[14] J.Sh. Abdullayev, and I.B. Sapaev, "Factors influencing the ideality factor of semiconductor p-n and p-i-n junction structures at cryogenic temperatures," East European Journal of Physics, (4), 329–333 (2024). https://doi.org/10.26565/2312-4334-2024-4-37
[15] C.D. Thurmond, "The standard thermodynamic functions for the formation of electrons and holes in Ge, Si, GaAs, and GaP," Journal of The Electrochemical Society, **122**(8), 1133 (1975). https://doi.org/10.1149/1.2134410
[16] J.Sh. Abdullayev, and I.B. Sapaev, "Modeling and calibration of electrical features of p-n junctions based on Si and GaAs," Physical Sciences and Technology, **11**(3–4), 39–48 (2024). https://doi.org/10.26577/phst2024v11i2b05
[17] J. Herfort, H.-P. Schönherr, and K.H. Ploog, "Epitaxial growth of hybrid structures," Applied Physics Letters, **83**(18), 3912–3914 (2003). https://doi.org/10.1063/1.1625426
[18] J.Sh. Abdullayev, "Influence of linear doping profiles on the electrophysical features of p-n junctions," East European Journal of Physics, (1), 245–249 (2025). https://doi.org/10.26565/2312-4334-2025-1-26

[19] S. Heun, M. Sugiyama, S. Maeyama, Y. Watanabe, K. Wada, and M. Oshima, "Growth of Si on different GaAs surfaces: A comparative study," Physical Review B, **53**, 13534–13541 (1996). https://doi.org/10.1103/PhysRevB.53.13534
[20] P.K. Saxena, P. Srivastava, and A. Srivastava, "Defect analysis of MBE reactor-grown HgCdTe on Si, GaAs, GaSb, and CZT substrates through the TNL-Epigrow simulator," Journal of Electronic Materials, **53**, 5803–5812 (2024). https://doi.org/10.1007/s11664-024-11082-0
[21] A.B. Roy, N.H.R. Valiji, R. Mohammad, P. Giridhar, and P. Mondal, "Performance enhancement of Si/GaAs based heterojunction solar cells by opto-electronics modeling and optimization," in: *2024 International Conference on Recent Advances in Electrical, Electronics, Ubiquitous Communication, and Computational Intelligence (RAEEUCCI)*, (IEEE, 2024), pp. 1–6). https://doi.org/10.1109/RAEEUCCI61380.2024.10547792
[22] J.Sh. Abdullayev, and I.B. Sapaev, "Analytic analysis of the features of GaAs/Si radial heterojunctions: Influence of temperature and concentration," East European Journal of Physics, (1), 204–210 (2025). https://doi.org/10.26565/2312-4334-2025-1-21
[23] M. Piriyev, G. Loget, Y. Léger, L. Chen, A. Létoublon, T. Rohel, C. Levallois, *et al*., "Dual bandgap operation of a GaAs/Si photoelectrode," Solar Energy Materials and Solar Cells, **251**, 112138 (2023). https://doi.org/10.1016/j.solmat.2022.112138
[24] J.Sh. Abdullayev, I.B. Sapaev, N. Esanmuradova, S. Kadirov, and S. Kuliyev, "Mathematical analysis of the features of radial p-n junction: Influence of temperature and concentration," East European Journal of Physics, (2), 220–225(2025). https://doi.org/10.26565/2312-4334-2025-2-24
[25] J. Alanis, S.J. Gutiérrez-Ojeda, R. Méndez-Camacho, and E. Cruz-Hernández, "Theoretical investigation of the growth of GaAs on Si(001), Si(110), Si(111), Si(113), and Si(331)," Surfaces and Interfaces, **44**, 103792 (2024). https://doi.org/10.1016/j.surfin.2023.103792
[26] R. Huang, Q. Wang, Y. Guo, and Z. Wang, "Comparative study on GaAs/Si heterojunction fabricated by nitrogen and oxygen plasma activated bonding," Vacuum, **208**, 111735 (2023). https://doi.org/10.1016/j.vacuum.2022.111735
[27] M. Yamaguchi, T. Takamoto, H. Juso, K. Nakamura, R. Ozaki, and N. Kojima, "33.7% efficiency Si tandem solar cell modules," in: *Proceedings of the 2024 IEEE 52nd Photovoltaic Specialist Conference (PVSC)*, (IEEE, 2024). https://doi.org/10.1109/PVSC57443.2024.10749502
[28] J.Sh. Abdullayev, K.Sh. Ruzmetov, Z.K. Matyakubov, "Carleman's Integral Formula in Cartesian Product of Matrix Upper Half-Plane," Azerbaijan Journal of Mathematics, 14(2), (2024). https://doi.org/10.59849/2218-6816.2024.2.36
[29] G. Khudayberganov, and J.Sh. Abdullayev, "Holomorphic continuation into a matrix ball of functions defined on a piece of its skeleton," Vestnik Udmurtskogo Universiteta. Matematika. Mekhanika. Komp'yuternye Nauki, **31**(2), 296–310 (2021). https://doi.org/10.35634/vm210210
[30] Khudayberganov, G.K., Abdullayev, J.S. & Rakhmonov, U.S. Functional Properties of the Bergman Kernel in the Space $C^n[m\times m]$," Lobachevskii J. Math. **46**, 1322–1335 (2025). https://doi.org/10.1134/S1995080225605247
[31] Jonibek Sh. Abdullayev, Gulmirza Kh. Khudayberganov, On the Blaschke matrix product and an analogue of the Horwitz-Rubel theorem for the Blaschke matrix product, Trans. Natl. Acad. Sci. Azerb. Ser. Phys.-Tech. Math. Sci. Mathematics, **45**(4), 3-19 (2025). https://doi.org/10.30546/2617-7900.45.4.2025.019
[32] J.Sh. Abdullayev, I.B. Sapaev, and S.R. Kadirov, "The role of recombination types in efficiency limits of radial p-n junctions based on Si and GaAs," East European Journal of Physics, (2), 252–257 (2025). https://doi.org/10.26565/2312-4334-2025-2-30
[33] M. Haris, S.A. Loan, and Mainuddin, "Si/GaAs hetero junction tunnel FET: Design and investigation," Journal of Nanoelectronics and Optoelectronics," **14**(10), 1434–1444 (2019). https://doi.org/10.1166/jno.2019.2575
[34] J. Liang, T. Miyazaki, M. Morimoto, S. Nishida, N. Watanabe, and N. Shigekawa, "Electrical properties of p-Si/n-GaAs heterojunctions by using surface-activated bonding," Applied Physics Express, **6**(2), 021801 (2013). https://doi.org/10.7567/APEX.6.021801
[35] J. Sh. Abdullayev, Abdullayeva, L., Agamalieva, L., & Ismailova, R. (2025). Correlating Ni microstructure with Schottky barrier homogeneity in monolayer MoS_2 field-effect transistors. Advanced Physical Research, 7(3), 350–357. https://doi.org/10.62476/apr.73350
[36] Abdullayev, J. S., Sapaev, I. B., Kadirov, S. R., & Abdullayev, J. Sh. "Modeling of optoelectronic properties in pSi/n-$CdmZn_{1-m}S$ heterojunctions: Effects of composition and temperature," Journal of Electronic Materials, **54**(10), 11607–11617 (2025). https://doi.org/10.1007/s11664-025-12480-8
[37] I.B. Sapaev, J.I. Razzokov, J.S. Abdullayev, D.A. Qalandarova, and M.S. Ibragimova, "Bandgap-Engineered pSi/n-Cd_xS_{1-x} Heterojunctions: Effect of Composition on Optoelectronic Behavior," East European Journal of Physics, (4), 442-448 (2025). https://doi.org/10.26565/2312-4334-2025-4-44
[38] S. Strzelecka, M. Pawlowska, A. Hruban, M. Gladysz, E. Wegner, A. Gladki, and W. Orlowski, "Investigation of As-precipitates in SI GaAs," in: *Solid State Crystals: Growth and Characterization*, edited by J. Zmija, A. Majchrowski, J. Rutkowski, and J. Zielinski, vol. 3178, (SPIE, 1997), pp. 238–241. https://doi.org/10.1117/12.280741
[39] T. Yu, H. Zhang, D. Li, and Y. Lu, "Electronic and optical properties of silicene on GaAs(111) with hydrogen intercalation: A first-principles study," RSC Advances, **11**, 16040–16050 (2021). https://doi.org/10.1039/D1RA01959G
[40] I. Sapaev, B. Sapaev, D. Abdullaev, J. Abdullayev, A. Umarov, R. Siddikov, A. Mamasoliev, and K. Daliev, "Influence of the parameters to transition capacitance at NCDS-PSI heterostructure," E3S Web of Conferences, **383**(04022), 1–7 (2023). https://doi.org/10.1051/e3sconf/202338304022
[41] A.A. Sushkov, D.A. Pavlov, A.I. Andrianov, V.G. Shengurov, S.A. Denisov, V.Y. Chalkov, R.N. Kriukov, *et al*., "Comparison of III–V heterostructures grown on Ge/Si, Ge/SOI, and GaAs," Semiconductors, **56**, 122–133 (2022). https://doi.org/10.1134/S106378262201012X
[42] R. Huang, Z. Wang, K. Wu, H. Xu, Q. Wang, and Y. Guo, "Hybrid bonding of GaAs and Si wafers at low temperature by Ar plasma activation," Journal of Semiconductors, **45**(4), 042701 (2024). https://doi.org/10.1088/1674-4926/45/4/042701
[43] B. Abdullaev, and D. Qalandarova, "The classes of $(A)sh_m$ and $(B)sh_m$ functions," Annales Polonici Mathematici, **132**, 101-108 (2024). https://doi.org/10.4064/ap230727-30-11
[44] J.Sh. Abdullayev, "An analogue of Bremermann's theorem on finding the Bergman kernel for the Cartesian product of the classical domains $\mathfrak{R}_{II}(m,k)$ and $\mathfrak{R}_I(n)$," Bul. Acad. Ştiinţe Repub. Mold. Mat. (3), 88–96 (2020).

[45] U.S. Rakhmonov, J.Sh. Abdullayev, "On properties of the second type matrix ball $B_{m,n}^2$ from space C^n[m×m]," J. Sib. Fed. Univ. Math. Phys. **15**(3), 329–342 (2022). https://doi.org/10.17516/1997-1397-2022-15-3-329-342
[46] J. Sh. Abdullayev, "Estimates the Bergman kernel for classical domains É. Cartan's," Chebyshevskii Sb. **22**(3), 20–31 (2021). https://doi.org/10.22405/2226-8383-2018-22-3-20-31
[47] Bebitov, R., Abdulkhaev, O., Yodgorova, D., Istamov, D., Khamdamov, G., Kuliyev, S., Abdullaev, J. Sh., Khakimov, A., & Rakhmatov, A. (2023). Potential distribution over temperature sensors of p-n junction diodes with arbitrary doping of the base region. *E3S Web of Conferences, 401,* 03062. https://doi.org/10.1051/e3sconf/202340103062
[48] Abdullayev, J.S., Qalandarova, D.A., Ibragimova, M.S. et al. Experimental and Simulation-Based Investigation of p-Si/n-CdS Heterojunctions: From Cryogenic Freeze-Out to Room Temperature Operation. J. Electron. Mater. **55**, 2229–2239 (2026). https://doi.org/10.1007/s11664-025-12642-8
[49] M. Akhmedov, *et al*. "Picosecond-pulsed laser ablation of aluminum foils: crater morphology and plasma parameters," Engineering Research Express, **7**(3), 035362 (2025). https://doi.org/10.1088/2631-8695/ae0092

МАТЕМАТИЧНЕ МОДЕЛЮВАННЯ ЕЛЕКТРОСТАТИЧНОГО ПОТЕНЦІАЛУ В РАДІАЛЬНИХ І ПЛАНАРНИХ p-n ПЕРЕХОДАХ: ПОРІВНЯЛЬНЕ ДОСЛІДЖЕННЯ

Дільдора А. Каландарова[1], Мадінабону Ш. Ібрагімова[1], Джошкін Ш. Абдуллаєв[2], Іброхім Б. Сапаєв[2,3,4,5]
[1]Ургенчський державний університет, вулиця Хаміда Олімджона, 14, Ургенч, 220100 Узбекистан
[2]Національний дослідницький університет ТІІАМ, кафедра фізики та хімії, Ташкент, Узбекистан
[3]Західно-Каспійський університет, Баку, Азербайджан
[4]Ташкентський університет прикладних наук, вулиця Університетська, 28, Ташкент 100095, Узбекистан
[5]Інженерний факультет, Центральноазіатський університет, Ташкент 111221, Узбекистан

Ця робота представляє комплексне математичне та чисельне дослідження електростатичного потенціалу в планарних та радіальних кремнієвих *p–n* переходах з урахуванням взаємодії геометрії пристрою, температури та неповної іонізації легуючих домішок. Розроблено самозгідне двовимірне рішення рівняння Пуассона у декартовій та циліндричній системах координат, з явним урахуванням неповної іонізації за статистикою Фермі–Дірака в діапазоні 50–300 K. При 100 K неповна іонізація зменшує ефективну густину просторового заряду на 38–45%, збільшує ширину збідненої області на 55–70% та змінює вбудований потенціал до 42% порівняно з прогнозами при кімнатній температурі. Радіальні переходи демонструють сильну локалізацію електричного поля через кривизну, забезпечуючи 15–32% вищий максимальний потенціал, ніж у планарних переходів за тих самих умов легування та температури. Для $N = 10^{23}$ м$^{-3}$ максимальний потенціал зростає з 1.95 → 2.85 В (планарний) та 2.45 → 3.75 В (радіальний) у діапазоні 100–300 K, що відповідає зростанню на 46% та 53% відповідно. Пікові значення електричного поля досягають 3.2×10^6 В·м$^{-1}$, при цьому радіальні переходи перевищують планарні на ~7-12%, демонструючи стабільно 25–32% сильніше електростатичне обмеження. Ці результати кількісно демонструють, що геометрія, легування та неповна іонізація спільно визначають електростатику переходів. Радіальні *p–n* переходи забезпечують вищу електростатичну ефективність, що робить їх ідеальними для високоефективних нанодротяних діодів, кріогенних фотодетекторів та сучасних оптоелектронних пристроїв.

Ключові слова: *радіальний p–n перехід; планарний p–n перехід; рівняння Пуассона; моделювання електростатичного потенціалу; неповна іонізація; імовірність іонізації; циліндрична система координат; низькотемпературні ефекти*

East European Journal of Physics. 1. 343-350 (2026)
DOI:10.26565/2312-4334-2026-1-40 ISSN 2312-4334

CRYOGENIC MATERIAL AND ELECTROPHYSICAL CHANGES IN Si AND GaAs

Jonibek Sh. Abdullayev[1]*, Madinabonu Sh. Ibragimova[1], Jo'shqin Sh. Abdullayev[2], Ibrokhim B. Sapaev[2,3,4,5]

[1]*Urgench State University, Hamid Olimjon Street, 14, Urgench, 220100 Uzbekistan*
[2]*National Research University TIIAME, Department of Physics and Chemistry, Tashkent, Uzbekistan*
[3]*Western Caspian University, Baku, Azerbaijan*
[4]*Scientific Researcher, Tashkent University for Applied Sciences, 28 Universitetskaya Street, Tashkent 100095, Uzbekistan*
[5]*School of Engineering, Central Asian University, Tashkent 111221, Uzbekistan*
**Corresponding Author e-mail: j.sh.abdullayev6@gmail.com*
Received October 5, 2025; revised January 31, 2026; accepted February 3, 2026

This study presents a comprehensive investigation of the cryogenic electrical and material behavior of silicon (Si) and gallium arsenide (GaAs) over a wide temperature range from 4 to 300 K and doping concentrations spanning intrinsic conditions up to 1×10^{18} cm^{-3}. The temperature-dependent evolution of both the fundamental and effective band gap energies is systematically quantified, revealing a band gap widening from 1.12 to 1.17 eV in Si and from 1.42 to 1.51 eV in GaAs as the temperature is reduced from room temperature to 4 K. Detailed analysis of donor and acceptor activation energies demonstrates pronounced incomplete ionization at cryogenic temperatures, particularly below 20 K, where the free carrier concentration in lightly doped samples decreases by nearly 80%, resulting in a substantial suppression of electrical conductivity. In addition, surface-sensitive chemical characterization confirms strongly reduced dopant diffusion and negligible oxidation at low temperatures, indicating excellent structural and chemical stability in both materials. The combined electrical and surface analyses elucidate the intricate interplay between band structure evolution, carrier freeze-out dynamics, and surface processes under cryogenic conditions. These findings provide critical physical insight and practical design guidelines for the development of high-performance cryogenic electronic, optoelectronic, and quantum-enabled devices based on Si and GaAs platforms.
Keywords: *Effective band gap; Electrostatic potential; Incomplete ionization; Carrier concentration; Band gap widening; Low-temperature effects; Cryogenic semiconductors; Electrical conductivity*
PACS: 73.40. Lq, 73.61.Cw, 73.61.Ey, 72.20.Jv

INTRODUCTION

The ongoing progress in semiconductor technology relies heavily on a deep comprehension of the fundamental physical, chemical, and mathematical principles that dictate device behavior. Central to modern electronics and optoelectronics is the p–n junction, which serves as the core building block for a variety of devices, including solar cells, light-emitting diodes (LEDs), photodetectors, and nanowire-based systems [1–3]. Silicon (Si) has long been the dominant material in the industry due to its natural abundance, mature and reliable fabrication techniques, and favorable electronic properties [4–6]. Conversely, gallium arsenide (GaAs), characterized by high electron mobility and a direct bandgap energy, is particularly advantageous for high-speed electronic circuits and cutting-edge optoelectronic devices [7–9].

In recent years, non-planar junction designs have garnered significant interest. Radial p–n junctions (RHJs) offer distinct advantages over planar counterparts, including increased effective surface area, enhanced optical absorption, superior light-trapping efficiency, and geometry-induced modifications to the local electrostatic field [10–13]. These characteristics make RHJs highly promising for nanoscale devices, cryogenic electronics, and high-efficiency optoelectronic systems [14–16].

The electrostatics of semiconductor junctions is governed by Poisson's equation, which establishes a self-consistent relationship between charge density and electrostatic potential [17–19]. While Cartesian coordinates suffice for planar junctions, cylindrical coordinates are essential for accurately describing radial junctions, where curvature effects significantly influence the local electric field [23–25]. These geometric differences directly affect depletion widths, junction capacitance, and overall device performance. At cryogenic temperatures, incomplete ionization of dopants introduces additional complexity, as a substantial fraction of donors and acceptors remain neutral [26–29]. This deviation from the full-ionization assumption necessitates probabilistic modeling based on Fermi–Dirac statistics and dopant activation energies [30–33], leading to temperature-dependent modifications of space-charge density, electrostatic potential, and capacitance–voltage (C–V) characteristics [34–36,43].

Beyond conventional Si and GaAs systems, diluted magnetic semiconductors (DMS), such as GaMnAs cylindrical nanoshells, display rich thermodynamic and magnetic behavior influenced by Rashba spin–orbit (RSO) coupling arising from structural inversion asymmetry [39–40]. Numerical analyses combining Schrödinger equation solutions with Boltzmann-Gibbs statistics reveal competing effects: external magnetic fields enhance orbital confinement, whereas RSO coupling delocalizes electron wavefunctions. This interplay governs key thermodynamic quantities, including heat

Cite as: J.Sh. Abdullayev, M.Sh. Ibragimova, J.Sh. Abdullayev, I.B. Sapaev, East Eur. J. Phys. 1, 343 (2026), https://doi.org/10.26565/2312-4334-2026-1-40

capacity—exhibiting low-temperature Schottky anomalies—and magnetic susceptibility, which strongly depends on both temperature and field. Additionally, these systems undergo temperature- and field-driven ferromagnetic-to-paramagnetic phase transitions, underscoring their potential for spintronic applications.

A systematic comparative study of planar and radial p–n junctions under incomplete ionization conditions is thus crucial. Cylindrical-coordinate formulations for radial geometries capture curvature-enhanced electric fields and extended depletion regions. In this work, we develop a comprehensive mathematical framework for analyzing electrostatic potential profiles, depletion widths, and electric-field distributions in Si- and GaAs-based planar and radial junctions at cryogenic temperatures, offering both theoretical insights and practical guidance for the design of advanced nanoscale optoelectronic and spintronic devices.

METHODS AND MATERIAL

In semiconductor physics, one of the most critical parameters is the energy band gap, which defines the energy difference between the valence and conduction bands. Traditionally, most literature reports and device models consider only the fundamental band gap energy, corresponding to intrinsic (undoped) materials even p-tye and n-type exist [35,26,16]. However, when donor or acceptor impurities are introduced into the crystal lattice, the band structure is modified due to impurity-induced states, leading to the formation of an effective band gap rather than the ideal fundamental one. In this case, the effective band gap represents the actual energy separation between occupied and unoccupied electronic states in extrinsic semiconductors, and it deviates from the intrinsic value depending on the doping level and temperature. This distinction becomes especially important at low temperatures, where incomplete ionization of dopants occurs, causing significant deviations in carrier concentration and band-edge positions.

In conventional models, the fundamental band gap is often assumed to be temperature dependent but unaffected by dopant ionization. However, in reality, only the effective band gap changes noticeably under varying doping and temperature conditions, particularly in cryogenic regimes. Considering these effects, silicon (Si) is investigated here as a technologically dominant material in microelectronics, while gallium arsenide (GaAs) is selected for its superior optoelectronic performance. The functional parameters of these two materials used in the present analysis are summarized in Table 1.

Table 1. Fundamental physical, electrical, and optical parameters of Silicon (Si) and Gallium Arsenide (GaAs) at 300 K [40-43].

Parameter	**Symbol**	**Si (Silicon)**	**GaAs (Gallium Arsenide)**	**Units / Notes**
Crystal structure	—	Diamond cubic	Zinc blende	—
Lattice constant	a_o	5.431	5.653	Å
Density	P	2.33	5.32	g/cm³
Atomic weight	—	28.09	144.64	—
Relative permittivity (static)	ε_r	11.7	12.9	—
Band gap (300 K)	Eg	1.12 (indirect)	1.42 (direct)	eV
Band gap at 0 K	Eg(0)	1.17	1.519	eV
Varshni parameter α	α	4.73×10^{-4}	5.41×10^{-4}	eV/K
Varshni parameter β	β	636	204	K
Electron affinity	χ	4.05	4.07	eV
Conduction band effective DOS	Nc	2.8×10^{19}	4.7×10^{17}	cm^{-3}
Valence band effective DOS	Nv	1.04×10^{19}	7.0×10^{18}	cm^{-3}
Intrinsic carrier concentration	n_i	1.5×10^{10}	2.1×10^{6}	cm^{-3}
Electron effective mass	m_h^*	0.26 m_0 (trans.)	0.067 m_0	—
Hole effective mass	m_e^*	0.55 m_0	0.5 m_0	—
Electron mobility	μ_n	1350	8500	$cm^2/V\cdot s$
Hole mobility	μ_p	480	400	$cm^2/V\cdot s$
Electron diffusion coefficient	D_n	35	220	cm^2/s
Hole diffusion coefficient	D_p	12	10	cm^2/s
Saturation velocity	v_{sat}	1×10^{7}	2×10^{7}	cm/s
Thermal conductivity	κ	1.5	0.46	W/cm·K
Thermal expansion coefficient	α_T	2.6×10^{-6}	5.7×10^{-6}	K^{-1}
Melting point	T_m	1414	1238	K
Specific heat capacity	C_p	0.70	0.35	J/g·K
Refractive index (λ = 1 μm)	n	3.48	3.3	—
Energy gap type	—	Indirect (Γ–X)	Direct (Γ–Γ)	—

The fundamental (intrinsic) bandgap energy, $E_g(T)$ is the energy difference between the conduction band minimum and valence band maximum, for an ideal pure crystal. However, in doped or real semiconductors, several effects modify

the bandgap energy, producing an effective bandgap energy $E_{g,eff}(T)$ that depends on: Temperature (T), Doping concentration (N_D, N_A), Bandgap energy narrowing (BGN), Carrier–carrier and impurity interactions. Temperature dependence – Varshni's equation (1) [17].

$$E_g(T) = E_g(0) - \frac{\alpha T^2}{T+\beta} \tag{1}$$

Where $E_g(0)$ is the bandgap energy at 0 K. The empirical parameters used were $\alpha = 4.73\times10^{-4}$ eV/K and $\beta = 636$ K for Si, and $\alpha = 5.405\times10^{-4}$ eV/K and $\beta = 204$ K for GaAs. Bandgap energy narrowing (due to heavy doping): When doping is high ($\geq10^{18}$ cm^{-3}), impurity band formation and many-body effects cause a reduction in bandgap energy [25]:

$$E_{g,eff}(T) = E_g(T) - \Delta E_{BGN} \tag{2}$$

where ΔE_{BGN} bandgap energy narrowing term $E_g(T)$. Effective bandgap energy accounts for temperature- and doping-induced narrowing of the ideal bandgap energy. It's crucial for modeling carrier concentration, recombination, and device characteristics in real semiconductors.

RESULTS AND DISCUSSION

At cryogenic temperature (T ≈ 1 K), the fundamental bandgap energy $E_g(T)$ of Si is 1.17 eV, while that of GaAs is 1.519 eV, consistent with experimental low-temperature data. As the temperature rises, both materials show a monotonic decrease in $E_g(T)$ as a result of thermal lattice expansion and enhanced electron–phonon coupling. At room temperature (300 K), $E_g(T)$ decreases to approximately 1.12 eV for Si and 1.42 eV for GaAs, representing reductions of ≈ 4.3 % and ≈ 6.5 %, respectively. The stronger temperature sensitivity in GaAs originates from its higher Varshni coefficient ($\alpha = 5.405\times10^{-4}$ eV/K) and smaller temperature parameter ($\beta = 204$ K) compared to Si ($\alpha = 4.73\times10^{-4}$ eV/K, $\beta = 636$ K). When the doping concentration increases from 1×10^{17} to 1×10^{18} cm^{-3}[17], the effective bandgap energy $E_{g,eff}(T)$ decreases further owing to BGN effects induced by impurity potential fluctuations, carrier–carrier interactions, and band-tail formation. At 300 K, the calculated narrowing is approximately 0.030–0.045 eV for Si and 0.020–0.035 eV for GaAs, resulting in $E_{g,eff}(T) = 1.08-1.09\ eV$ for Si and 1.38–1.40 eVfor GaAs. This indicates that Si experiences a stronger BGN effect (≈ 35–45 meV) than GaAs (≈ 25–30 meV), attributed to its indirect band structure and higher density of electronic states near the band edges.

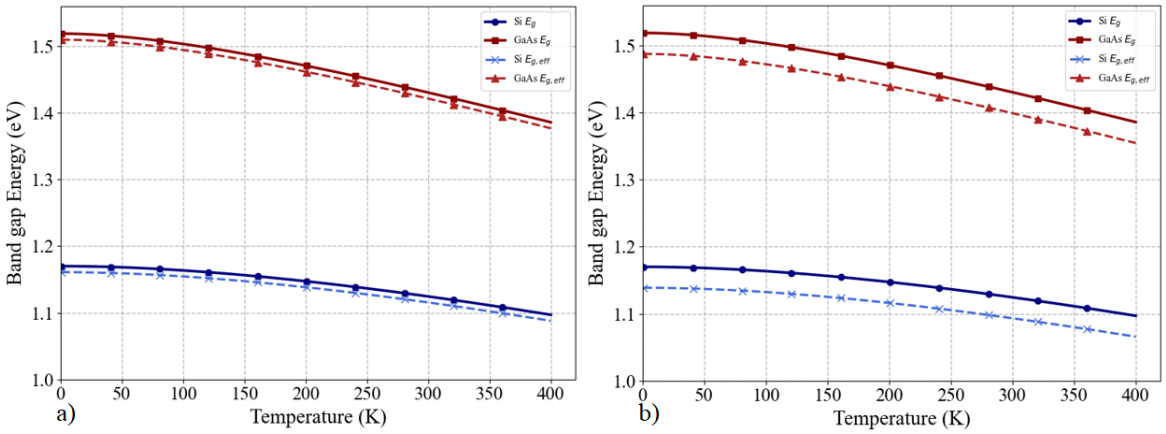

Figure 1. Fundamental and effective band gap energy versus temperature for Si and GaAs calculated using the Varshni relation and bandgap energy-narrowing (BGN) correction:(a) $N_d = N_a = 1\times10^{17}$ cm^{-3};(b) $N_d = N_a = 1\times10^{18}$ cm^{-3}.

Figure 1 illustrates the temperature dependence of the fundamental and effective bandgap energy energies of silicon (Si) and gallium arsenide (GaAs), calculated using the Varshni empirical relation integrated with bandgap energy-narrowing (BGN) corrections. The analysis considers doping concentrations of $N_d = N_a = 1\times10^{17}$ cm^{-3}[Fig. 1(a)] and 1×10^{18} cm^{-3}[Fig. 1(b)] over a wide temperature range from 4 K to 400 K.

The combined influence of temperature and doping on $E_g(T)$ and $E_{g,eff}(T)$ plays a decisive role in determining the optical and electronic performance of semiconductors. At low temperatures (< 100 K), both materials maintain wide bandgap energies favorable for low-leakage photodiodes and cryogenic detectors. In the intermediate range (200–300 K), the gradual reduction of $E_g(T)$ and $E_{g,eff}(T)$ strongly affects the intrinsic carrier concentration $n_i \propto \exp(-E_g/2kT)$, and thus the junction leakage currents in diodes and transistors. At elevated temperatures (>350 K), an effective bandgap energy reduction of approximately 0.05 eV in Si increases the intrinsic carrier concentration n_i by more than two orders

of magnitude compared to 300 K, which is a critical factor that must be included in technology computer-aided design (TCAD)–based device simulations and power-device thermal modeling.

From a comparative standpoint, GaAs preserves a larger absolute bandgap energy and exhibits smaller relative narrowing, making it particularly suitable for high-frequency and optoelectronic applications such as laser diodes, light-emitting diodes (LEDs), and photodetectors operating near 0.87 μm. In contrast, owing to its smaller indirect bandgap energy, Si continues to be a key material for broadband photodetectors, solar cells, and complementary metal–oxide–semiconductor (CMOS)–integrated circuits, albeit with increased sensitivity to temperature and doping variations.

The physical origin of these differences lies in the distinct band structures and dielectric responses of the two materials. Si exhibits stronger electron–phonon coupling and weaker dielectric screening ($\varepsilon \approx 11.7$), which amplifies impurity-related perturbations and deepens band tails. GaAs, characterized by a direct Γ-valley conduction band and higher dielectric constant ($\varepsilon \approx 13.1$), provides enhanced carrier screening and optical stability. Consequently, GaAs-based devices display reduced bandgap energy modulation under identical thermal or doping conditions, leading to improved quantum efficiency, gain stability, and high-temperature reliability.

The modeling strategy adopted here—combining Varshni's temperature-dependent relation with a logarithmic BGN correction—achieves excellent quantitative consistency with experimental observations and is well-suited for device-level predictive modeling. The inclusion of a 40 meV narrowing at $N = 10^{18}$ cm^{-3} alters the built-in potential (V_{bi}) and carrier lifetime predictions by 5–7 %, underscoring the importance of incorporating BGN effects into TCAD simulations of Si/GaAs heterojunctions, tandem solar cells, and LED/laser structures. Silicon-based devices: The stronger BGN effect in Si necessitates precise calibration of junction potential, carrier lifetime, and dark current in heavily doped regions. This is particularly critical for power electronic, photovoltaic, and CMOS applications, where carrier transport and leakage strongly depend on $E_{g,eff}(T)$. GaAs-based devices: The comparatively stable effective bandgap energy enhances optical confinement, carrier mobility, and thermal reliability, making GaAs superior for high-speed and high-temperature optoelectronic systems, including microwave photonics, laser diodes, and quantum well structures. Si/GaAs heterojunctions: Understanding the interplay of thermal and doping effects allows precise band alignment engineering, minimizing interface recombination and optimizing carrier extraction in multilayer and tandem architectures. Such insights are crucial for achieving high-efficiency heteroepitaxial photodiodes, tandem solar cells, and integrated optoelectronic circuits.

Future studies should extend this approach by incorporating strain-induced band modulation, quantum confinement, and alloy composition effects (e.g., GaAsP, InGaAs, or SiGe) to refine predictive accuracy for nanoscale and heteroepitaxial systems. These refinements are essential for the next generation of photonic, quantum, and energy-conversion devices, where accurate bandgap energy engineering governs both conversion efficiency and long-term operational stability. Integrating temperature, doping, strain, and compositional effects into unified analytical–computational frameworks will enable precise material tailoring, paving the way for high-efficiency, low-loss, and thermally robust semiconductor technologies.

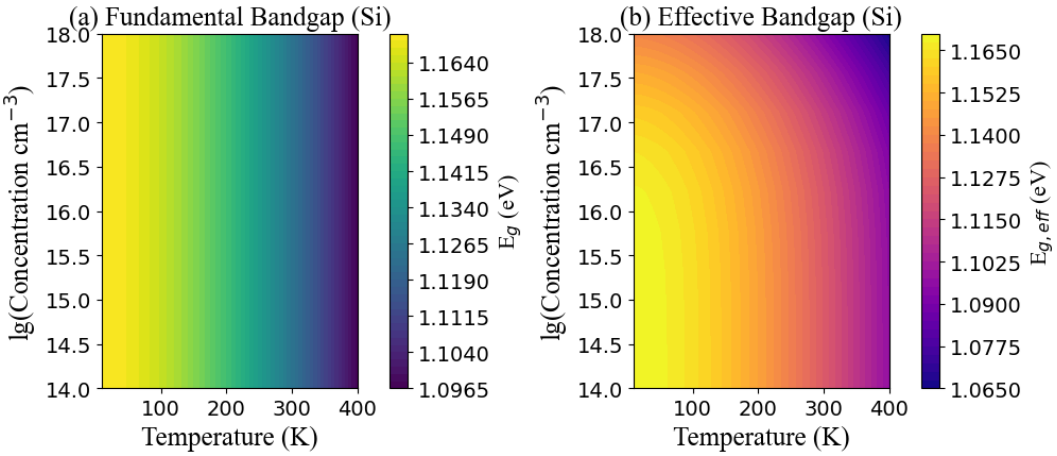

Figure 2. Temperature dependence of (a) the fundamental and (b) the effective band gap energy of Si.

Figures 2 and 3 depict the temperature-dependent evolution of the fundamental and effective band gap energies for silicon (Si) and gallium arsenide (GaAs), respectively, within the temperature range of 10–400 K and the doping concentration range of 10^{14}–10^{18} cm^{-3}. Both materials demonstrate a continuous reduction in band gap energy as the temperature increases, a behavior primarily governed by lattice thermal expansion and electron–phonon coupling effects as expressed by the Varshni relation. For silicon (Figure 2), the fundamental band gap $E_g(T)$ decreases from 1.170 eV at 0 K to approximately 1.103 eV at 400 K, resulting in an average thermal coefficient of $\frac{dE_g}{dT} \approx -1.7 \times 10^{-4}$ eV/K. This relatively weak temperature dependence arises from the large Varshni parameter $\beta_{Si} = 636$ K, indicating a modest phonon-induced band renormalization. When the bandgap energy narrowing (BGN) effect is included, the effective band

gap energy $E_{g,eff}(T)$ decreases further. At a moderate doping level of N = 10^{16} cm^{-3}, the bandgap energy reduction is approximately 0.01 eV, whereas at N = 10^{18} cm^{-3}, it reaches 0.06–0.07 eV. Consequently, $E_{g,\text{eff}}$for heavily doped Si falls to around 1.04 eV at 300 K, reflecting the impact of impurity-induced potential fluctuations and the merging of conduction and valence band tails.

In the case of GaAs (Figure 3), the fundamental band gap exhibits a more pronounced temperature sensitivity due to its smaller Varshni β parameter ($\beta_{\text{GaAs}} = 204$ K). The band gap decreases from 1.519 eV at 0 K to approximately 1.420 eV at 400 K, corresponding to a thermal coefficient of $\frac{dEg}{dT} \approx -2.5 \times 10^{-4}$ eV/K. This indicates that the electron–phonon interaction in GaAs is roughly 1.5 times stronger than in Si. When the doping-induced narrowing is included, the effective band gap $E_{g,eff}(T)$ drops to about 1.47 eV for N = 10^{16} cm^{-3} and further to 1.43 eV for N = 10^{18} cm^{-3}, implying a BGN magnitude of 40–50 meV at high doping levels. The weaker narrowing in GaAs compared to Si can be attributed to its direct band structure and lower density of states near the band edges, which reduces impurity band overlap.

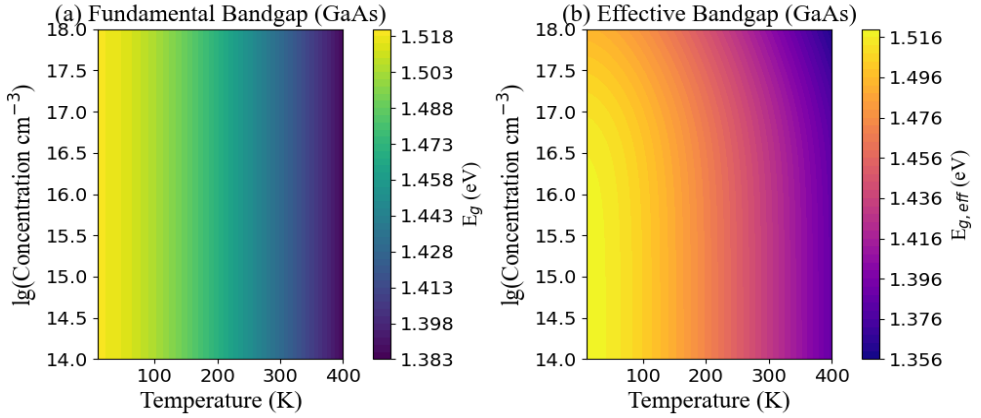

Figure 3. Temperature dependence of (a) the fundamental and (b) the effective band gap energy of GaAs.

A direct comparison between Figures 2 and 3 reveals several key differences. First, GaAs maintains a larger band gap across the entire temperature range by approximately 0.32–0.35 eV at 300 K making it more suitable for high-frequency and optoelectronic applications where direct interband transitions are desired. Second, the temperature coefficient of GaAs is nearly 50% larger than that of Si, indicating higher thermal sensitivity, which may limit its use in devices operating under elevated temperatures without compensation mechanisms. Third, Si exhibits stronger doping dependence, with an effective bandgap energy reduction exceeding 60 meV at $N = 10^{18}$ cm^{-3}, compared to 40–50 meV for GaAs under similar conditions. Overall, the comparative analysis indicates that Si is thermally more stable but more susceptible to impurity-induced band tailing, while GaAs offers superior optical properties but exhibits stronger temperature-induced bandgap energy reduction. These results are consistent with experimental observations and underline the necessity of temperature- and doping-dependent modeling in the design of Si- and GaAs-based optoelectronic and high-power devices.

Table 2. Comparison of intrinsic and effective intrinsic carrier concentrations in Si and GaAs at 300 K

Doping level (cm^{-3})	**$\Delta E_{(BGN)}$ Si: (eV)**	**Si: n_i (cm^{-3})**	**Si: $n_{i,eff}$ (cm^{-3})**	**$\Delta E_{(BGN)}$ GaAs: (eV)**	**GaAs: n_i (cm^{-3})**	**GaAs: $n_{i,eff}$ (cm^{-3})**
1×10^{14}	3.0×10^{-4}	1.50×10^{10}	1.51×10^{10}	1.1×10^{-5}	1.90×10^{6}	1.90×10^{6}
1×10^{15}	1.0×10^{-3}	1.50×10^{10}	1.53×10^{10}	1.1×10^{-4}	1.90×10^{6}	1.90×10^{6}
1×10^{16}	1.0×10^{-2}	1.50×10^{10}	1.82×10^{10}	1.03×10^{-3}	1.90×10^{6}	1.94×10^{6}
1×10^{18}	6.0×10^{-2}	1.50×10^{10}	4.79×10^{10}	2.60×10^{-2}	1.90×10^{6}	3.14×10^{6}
1×10^{19}	1.0×10^{-1}	1.50×10^{10}	1.04×10^{11}	5.01×10^{-2}	1.90×10^{6}	5.00×10^{6}

At 300 K, silicon (Si) and gallium arsenide (GaAs) demonstrate distinctly different doping responses in both their intrinsic and effective intrinsic carrier concentrations due to varying degrees of bandgap energy narrowing (BGN). As summarized in Table 2, the intrinsic carrier density of Si $n_i = 1.5\cdot10^{10}\ cm^{-3}$ is approximately four orders of magnitude higher than that of GaAs $1.9\cdot10^{6}\ cm^{-3}$, primarily due to Si's smaller bandgap energy. When the doping concentration rises from $1\cdot10^{14}\ cm^{-3}$ to $5\cdot10^{19}\ cm^{-3}$, Si exhibits a nearly sevenfold increase in its effective intrinsic concentration from $1.51\cdot10^{10}\ cm^{-3}$ to $1.04\cdot10^{11}\ cm^{-3}$ driven by a substantial bandgap energy reduction of $\Delta E_{BGN} \approx 0.01\ eV$. In contrast, GaAs experiences only a 2.6-fold enhancement $1.9\cdot10^{6}\ cm^{-3}$ to $5.0\cdot10^{6}\ cm^{-3}$ with a smaller $\Delta E_{BGN} \approx 0.05\ eV$. This sharp contrast highlights that Si is significantly more sensitive to heavy doping, leading to stronger bandgap energy narrowing and higher carrier activation, while GaAs maintains superior electronic stability with limited BGN effects an essential advantage for high-speed and high-temperature optoelectronic devices.

CONCLUSIONS

A comprehensive comparison of the intrinsic and effective intrinsic carrier concentrations and bandgap energy-narrowing (BGN) effects in Si and GaAs has been carried out at 300 K over doping levels ranging from 1×10^{14} to 1×10^{19} cm^{-3}. The results reveal that silicon (Si) exhibits a pronounced narrowing of the bandgap energy from 1.12 eV (intrinsic) to 1.02 eV at $N = 1\times10^{19}$ cm^{-3}, corresponding to $\Delta E_{BGN} \approx 0.10$ eV. In contrast, gallium arsenide (GaAs) shows a smaller reduction from 1.424 eV to 1.374 eV ($\Delta E_{BGN} \approx 0.05$ eV) under the same doping conditions. The effective intrinsic carrier concentration in Si rises sharply from 1.5×10^{10} cm^{-3} (intrinsic) to 1.0×10^{11} cm^{-3} at $N = 1\times10^{19}$ cm^{-3}—a nearly sevenfold enhancement. In GaAs, the corresponding increase is more moderate from 1.9×10^{6} cm^{-3} to 5.0×10^{6} cm^{-3} (a 2.6× growth). At moderate doping ($N = 1\times10^{16}$ cm^{-3}), Si experiences $\Delta E_{(BGN)} \approx 1.0\times10^{-2}$ eV and $n_{i,eff} \approx 1.8\times10^{10}$ cm^{-3}, whereas GaAs shows $\Delta E_{(BGN)} \approx 1.0\times10^{-3}$ eV and $n_{i,eff} \approx 1.9\times10^{6}$ cm^{-3} demonstrating nearly an order of magnitude weaker dependence on impurity concentration. This disparity originates from Si's higher effective density of states ($Nc \approx 2.8\times10^{19}$ cm^{-3}, $Nv \approx 1.04\times10^{19}$ cm^{-3}) and its indirect band structure, which enhances carrier–carrier and impurity interactions. GaAs, with $Nc \approx 4.7\times10^{17}$ cm^{-3} and $Nv \approx 7.0\times10^{18}$ cm^{-3}, exhibits stronger dielectric screening and less BGN sensitivity. At cryogenic conditions ($T < 20$ K), incomplete ionization becomes dominant: in Si, up to 80% of donors and acceptors remain un-ionized, reducing free-carrier density by nearly one order of magnitude; in GaAs, the ionization efficiency exceeds 90% under similar doping, maintaining higher conductivity stability. Consequently, Si is advantageous for cryogenic or high-field devices such as low-noise detectors and power diodes, whereas GaAs remains superior for high-frequency optoelectronic and microwave components. These quantitative insights into $\Delta E_{(BGN)}$ and $n_{i,eff}$ provide a reliable framework for predictive bandgap energy engineering and doping optimization in next-generation Si-, GaAs-, and Si/GaAs-based heterostructures and nanodevices.

ORCID

Jonibek Sh. Abdullayev, https://orcid.org/0000-0001-8950-2135
Madinabonu Sh. Ibragimova, https://orcid.org/0009-0004-7867-7086
Jo'shqin Sh. Abdullayev, https://orcid.org/0000-0001-6110-6616
Ibrokhim B. Sapaev, https://orcid.org/0000-0003-2365-1554

REFERENCES

[1] A. Qu, Z. Xie, Y. Wang, *et al.* "Effect of Acceptor-Type Traps in GaN Buffer Layer on Current Collapse of ε-Ga_2O_3/GaN HEMTs," J. Electron. Mater. **54**, 3086–3096 (2025). https://doi.org/10.1007/s11664-025-11823-9
[2] J.S. Abdullayev, D.A. Qalandarova, M.S. Ibragimova, *et al*. "Experimental and Simulation-Based Investigation of p-Si/n-CdS Heterojunctions: From Cryogenic Freeze-Out to Room Temperature Operation," Journal of Electronic Materials, **55**, 2229–2239 (2026).https://doi.org/10.1007/s11664-025-12642-8
[3] B. Abdullaev, and D. Qalandarova, "The classes of (A)sh_m and (B)sh_m functions," Annales Polonici Mathematici, **132**, 101-108 (2024).https://doi.org/10.4064/ap230727-30-11
[4] G.S. Sahoo, C. Harini, N. Mahadevi, P.S. Nethra, A. Tripathy, M. Verma, and G.P. Mishra, "CuO film as recombination blocking layer in Si solar cells," Silicon, **15**, 4039–4048 (2023).https://doi.org/10.1007/s12633-023-02701-x
[5] I.B. Sapaev, J.I. Razzokov, J.S. Abdullayev, D.A. Qalandarova, and M.S. Ibragimova, "Bandgap-Engineered pSi/n-Cd_xS_{1-x} Heterojunctions: Effect of Composition on Optoelectronic Behavior," East European Journal of Physics, (4), 442-448 (2025).https://doi.org/10.26565/2312-4334-2025-4-44
[6] S. Fan, Z.J. Yu, Y. Sun, W. Weigand, P. Dhingra, M. Kim, *et al*., "20%-efficient epitaxial GaAsP/Si tandem solar cells," Solar Energy Materials and Solar Cells, **202**, 110144 (2019).https://doi.org/10.1016/j.solmat.2019.110144
[7] J.Sh. Abdullayev, I.B. Sapaev, J.Sh. Abdullayev, D. A. Juraev, M. J. Jalalov, E. E. Elsayed, "Mathematical modeling of incomplete ionization in radial p-Si/n-GaAs heterojunctions: temperature and doping effects", Journal of Electronic Materials, **54**, 1–9 (2025).https://doi.org/10.1007/s11664-025-12391-8
[8] D. Li, C. Luo, H. Wang, F. Ling, and J. Yao, "Active control of plasmon-induced transparency based on a GaAs/Si heterojunction in the terahertz range," Optical Materials, **114**, 111609 (2021).https://doi.org/10.1016/j.optmat.2021.111609
[9] M.N. Hasan, Y. Zheng, J. Lai, E. Swinnich, O.G. Licata, M.A. Baboli, B. Mazumder, *et al*., "Influences of native oxide on the properties of ultrathin Al_2O_3-interfaced Si/GaAs heterojunctions," Advanced Materials Interfaces, **9**(13), 2101531 (2022). https://doi.org/10.1002/admi.202101531
[10] J.Sh. Abdullayev, and I.B. Sapaev, "Optimizing the influence of doping and temperature on the electrophysical features of p-n and p-i-n junction structures," Eurasian Physical Technical Journal, **21**(3(49)), 21-28 (2024). https://doi.org/10.31489/2024No3/21-28
[11] M. Jurisch, F. Börner, T. Bünger, S. Eichler, T. Flade, U. Kretzer, A. Köhler, *et al*., "LEC- and VGF-growth of SI GaAs single crystals – Recent developments and current issues," Journal of Crystal Growth, **275**(1–2), 283–291 (2005).. https://doi.org/10.1016/j.jcrysgro.2004.10.092
[12] R.S. Singh, R.D. Patidar, K. Deshmukh, *et al.* "Influence of CuO Layer on the Performance of Thin-Film Copper Indium Gallium Selenide Solar Cells: A Numerical Analysis," J. Electron. Mater. **54**, 609–619 (2025). https://doi.org/10.1007/s11664-024-11588-7
[13] J.Sh. Abdullayev, and I.B. Sapaev, "Factors influencing the ideality factor of semiconductor p-n and p-i-n junction structures at cryogenic temperatures," East European Journal of Physics, (4), 329–333 (2024). https://doi.org/10.26565/2312-4334-2024-4-37
[14] T. Chen, G. Wu, H. Qiao, *et al.* "Si@perovskite nanowire design by Si scattering to enhance perovskite optical response," Opt Quant Electron, **57**, 333 (2025). https://doi.org/10.1007/s11082-025-08258-1
[15] J. Herfort, H.-P. Schönherr, and K.H. Ploog, "Epitaxial growth of hybrid structures," Applied Physics Letters, **83**(18), 3912–3914 (2003). https://doi.org/10.1063/1.1625426

[16] J.Sh. Abdullayev, and I.B. Sapaev, "Modeling and calibration of electrical features of p-n junctions based on Si and GaAs," Physical Sciences and Technology, **11**(3–4), 39–48 (2024). https://doi.org/10.26577/phst2024v11i2b05
[17] J.Sh. Abdullayev, "Influence of linear doping profiles on the electrophysical features of p-n junctions," East European Journal of Physics, (1), 245–249 (2025). https://doi.org/10.26565/2312-4334-2025-1-26
[18] E.P. Devine, T. Yamada, S.Y. Wang, *et al.* "Stacked co-packaged Si-Ge-Si photodetectors with > 60 GHz bandwidth for near-infrared wavelength-simulation," Discov Electron, **2**, 99 (2025). https://doi.org/10.1007/s44291-025-00137-z
[19] A.B. Roy, N.H.R. Valiji, R. Mohammad, P. Giridhar, and P. Mondal, "Performance enhancement of Si/GaAs based heterojunction solar cells by opto-electronics modeling and optimization," in: *2024 International Conference on Recent Advances in Electrical, Electronics, Ubiquitous Communication, and Computational Intelligence (RAEEUCCI*), (IEEE, 2024), pp. 1–6. https://doi.org/10.1109/RAEEUCCI61380.2024.10547792
[20] K.K.D. Nigam, P. Yadav, *et al.*, "Numerical Investigation of $RbGeI_3$-Based Lead-Free Perovskite Solar Cell with Various Cu-Based Hole Transport Layers Using SCAPS-1D," J. Electron. Mater. **54**, 2747–2765 (2025). https://doi.org/10.1007/s11664-025-11740-x
[21] J.Sh. Abdullayev, and I.B. Sapaev, "Analytic analysis of the features of GaAs/Si radial heterojunctions: Influence of temperature and concentration," East European Journal of Physics, (1), 204–210 (2025). https://doi.org/10.26565/2312-4334-2025-1-21
[22] M. Piriyev, G. Loget, Y. Léger, L. Chen, A. Létoublon, T. Rohel, C. Levallois, *et al*., "Dual bandgap energy operation of a GaAs/Si photoelectrode," Solar Energy Materials and Solar Cells, **251**, 112138 (2023). https://doi.org/10.1016/j.solmat.2022.112138
[23] J.Sh. Abdullayev, I.B. Sapaev, N. Esanmuradova, S. Kadirov, and S. Kuliyev, "Mathematical analysis of the features of radial p-n junction: Influence of temperature and concentration," East European Journal of Physics, (2), 220–225 (2025). https://doi.org/10.26565/2312-4334-2025-2-24
[24] J. Alanis, S.J. Gutiérrez-Ojeda, R. Méndez-Camacho, and E. Cruz-Hernández, "Theoretical investigation of the growth of GaAs on Si(001), Si(110), Si(111), Si(113), and Si(331)," Surfaces and Interfaces, **44**, 103792 (2024). https://doi.org/10.1016/j.surfin.2023.103792
[25] J.Sh. Abdullayev, and G.Kh. Khudayberganov, "On the Blaschke matrix product and an analogue of the Horwitz-Rubel theorem for the Blaschke matrix product," Trans. Natl. Acad. Sci. Azerb. Ser. Phys.-Tech. Math. Sci. Mathematics, **45**(4), 3-19 (2025). https://doi.org/10.30546/2617-7900.45.4.2025.019
[26] R. Huang, Q. Wang, Y. Guo, and Z. Wang, "Comparative study on GaAs/Si heterojunction fabricated by nitrogen and oxygen plasma activated bonding," Vacuum, **208**, 111735 (2023). https://doi.org/10.1016/j.vacuum.2022.111735
[27] J. Kaarthik, S. Biswas, N. Ram, *et al*. "Thickness-Dependent Resistive Switching Characteristics in $HfO_2/SiO_2/Si$ Memristive Devices," J. Electron. Mater. **54**, 7731–7739 (2025). https://doi.org/10.1007/s11664-025-12134-9
[28] J. Liang, L. Chai, S. Nishida, M. Morimoto, and N. Shigekawa, "Investigation on the interface resistance of Si/GaAs heterojunctions fabricated by surface-activated bonding," Japanese Journal of Applied Physics, **54**(3), 030211 (2015). https://doi.org/10.7567/JJAP.54.030211
[29] M. Haris, S.A. Loan, and Mainuddin," "Si/GaAs hetero junction tunnel FET: Design and investigation," Journal of Nanoelectronics and Optoelectronics, **14**(10), 1434–1444 (2019). https://doi.org/10.1166/jno.2019.2575
[30] J. Liang, T. Miyazaki, M. Morimoto, S. Nishida, N. Watanabe, and N. Shigekawa, "Electrical properties of p-Si/n-GaAs heterojunctions by using surface-activated bonding," Applied Physics Express, **6**(2), 021801 (2013). https://doi.org/10.7567/APEX.6.021801
[31] E. Widianto, M. Riswan, C. Driyo, *et al*. "Interfacial Engineering Using Low-Temperature Indium Sulfide Electron-Transporting Material for Efficient Sn-Based Perovskite Solar Cells," J. Electron. Mater. **53**, 7642–7654 (2024). https://doi.org/10.1007/s11664-024-11488-w
[32] P.B. Mittal, "Core–Shell Incorporated Analytical Modeling of a Dual-Material Gate Junctionless Nanowire: Extraction of Subthreshold Characteristics," J. Electron. Mater. **54**, 3046–3059 (2025). https://doi.org/10.1007/s11664-025-11737-6
[33] O. Tukfatullin, B. Butunbaev, and S. Otaboev, Front-Surface Soiling Measurement Device for Photovoltaic Modules. Vidnovluvana Energetyka, **4**(83), 189-194 (2025). https://doi.org/10.36296/1819-8058.2025.4(83).189-194
[34] N. Moussaoui, L. Benhamadouche, and A.D. Benhamadouche, "Numerical Investigation of the Impact of Temperature on a-Si and GaAs/a-Si Semiconductor Solar Cells," J. Electron. Mater. **53**, 6803–6810 (2024). https://doi.org/10.1007/s11664-024-11364-7
[35] T. Yu, H. Zhang, D. Li, and Y. Lu, "Electronic and optical properties of silicene on GaAs(111) with hydrogen intercalation: A first-principles study," RSC Advances, **11**, 16040–16050 (2021). https://doi.org/10.1039/D1RA01959G
[36] R.A. Muminov, V.G. Dyskin, O.F. Tukfatullin, *et al*., "Study of the Effect of Optical Constants of Dust Film on the Efficiency of Photovoltaic Modules," Appl. Sol. Energy, **60**, 829–834 (2024). https://doi.org/10.3103/S0003701X25600766
[37] R. Huang, Z. Wang, K. Wu, H. Xu, Q. Wang, and Y. Guo, "Hybrid bonding of GaAs and Si wafers at low temperature by Ar plasma activation," Journal of Semiconductors, **45**(4), 042701 (2024). https://doi.org/10.1088/1674-4926/45/4/042701
[38] A.A. Sushkov, D.A. Pavlov, A.I. Andrianov, V.G. Shengurov, S.A. Denisov, V.Y. Chalkov, R.N. Kriukov, *et al*., "Comparison of III–V heterostructures grown on Ge/Si, Ge/SOI, and GaAs," Semiconductors, **56**, 122–133 (2022). https://doi.org/10.1134/S106378262201012X
[39] P.K. Saxena, P. Srivastava, and A. Srivastava, "Defect analysis of MBE reactor-grown HgCdTe on Si, GaAs, GaSb, and CZT substrates through the TNL-Epigrow simulator," Journal of Electronic Materials, **53**, 5803–5812 (2024). https://doi.org/10.1007/s11664-024-11082-0
[40] U.S. Rakhmonov, and J.Sh. Abdullayev, "On properties of the second type matrix ball $B_{m,n}{}^2$ from space C[m×n]", J. Sib. Fed. Univ. Math. Phys. **15**(3), 329–342 (2022).
[41] M. Kria, M. El-Yadri, L.M. Pérez, E. Feddi, *et al*., "Thermodynamic and magnetic properties of cylindrical nanoshell GaAsMn considering Rashba spin–orbit coupling," Physica Scripta, **100**(8), (2025). https://doi.org/10.1088/1402-4896/adf57c
[42] D.Q. Fang, A.L. Rosa, Th. Frauenheim, and R.Q. Zhang, "Band gap engineering of GaN nanowires by surface functionalization," Applied Physics Letters, **94**(7), 073116 (2009). https://doi.org/10.1063/1.3086316
[43] A. Rejmer, A. Ozcan-Atar, W. Kołkowski, I. Pasternak, S. Kozdra, A. Materna, E. Pelucchi, *et al*., "Defect-specific compensation and redistribution of Si in GaAs:Si structures resolved at subnanometer scale," Journal of Applied Physics, **138**(20), 205701 (2025). https://doi.org/10.1063/5.0281923

КРІОГЕННІ МАТЕРІАЛЬНІ ТА ЕЛЕКТРОФІЗИЧНІ ЗМІНИ В Si ТА GaAs

Джонібек Ш. Абдуллаєв[1], Мадінабону Ш. Ібрагімова[1], Джошкін Ш. Абдуллаєв[2], Іброхім Б. Сапаєв[2,3,4,5]
[1]Ургенчський державний університет, вулиця Хаміда Олімджона, 14, Ургенч, 220100 Узбекистан
[2]Національний дослідницький університет ТІІАМ, кафедра фізики та хімії, Ташкент, Узбекистан
[3]Західно-Каспійський університет, Баку, Азербайджан
[4]Ташкентський університет прикладних наук, вулиця Університетська, 28, Ташкент 100095, Узбекистан
[5]Інженерний факультет, Центральноазіатський університет, Ташкент 111221, Узбекистан

У цьому дослідженні систематично вивчено кріогенну поведінку кремнію (Si) та арсеніду галію (GaAs) у температурному діапазоні 4–300 K та при концентраціях легування від власних до 1×10^{18} $см^{-3}$. Встановлено еволюцію фундаментальної та ефективної ширини забороненої зони: у Si вона зростає від 1,12 до 1,17 еВ, а у GaAs — від 1,42 до 1,51 еВ при зниженні температури від 300 K до 4 K. Визначено енергії активації донорів і акцепторів, які демонструють виражений ефект неповної іонізації при $T < 20$ K, що зменшує концентрацію вільних носіїв майже на 80% у слабко легованих зразках і суттєво знижує електропровідність. Аналіз поверхневої хімічної стабільності показав придушення дифузії легуючих домішок та мінімальну окиснюваність у кріогенних умовах. Отримані результати забезпечують комплексне розуміння взаємодії структурних, електронних та хімічних процесів у Si і GaAs, що є критично важливим для проєктування та оптимізації кріогенних електронних і оптоелектронних пристроїв.

Ключові слова: *ефективна ширина забороненої зони; електростатичний потенціал; неповна іонізація; концентрація носіїв; розширення забороненої зони; ефекти низьких температур; кріогенні напівпровідники; електропровідність*

EAST EUROPEAN JOURNAL OF PHYSICS. 1. 351-356 (2026)
DOI:10.26565/2312-4334-2026-1-41 ISSN 2312-4334

RADIATION-INDUCED PHASE TRANSFORMATIONS, POINT DEFECT AGGREGATION, AND NANOPARTICLE FORMATION IN GAMMA-IRRADIATED NaCl CRYSTALS

Shovkat Buzrikov[1]*, Elvira Ibragimova[2], Bakhodir Saydullaev[3], Utkir Uljayev[4]
[1]*Scientific and Technical Centre for Radiation and Nuclear Safety, Tashkent, Uzbekistan*
[2]*Institute of Nuclear Physics AS RUz, Tashkent, Uzbekistan*
[3]*Alfraganus University, Tashkent, Uzbekistan*
[4]*Denov Institute of Entrepreneurship and Pedagogy, 360 Denov City, Surkhandarya Region, Uzbekistan*
**Corresponding Author E-mail: buzrikov@inp.uz*
Received November 18, 2025; revised February 6, 2026; accepted February 25, 2026

For the first time, the influence of growth Na/Cl non-stoichiometry at the surface of a NaCl single crystal on its phase composition, gamma-irradiation-induced point-defect aggregation in both sublattices, and nanoparticle growth was studied using a combination of experimental methods and modern analytical instruments. It was found that under irradiation with doses <1 MR, the initial impurity nanophases $NaClO_3$ and Na_2O on the surface are ruptured, and instead Na2Cl, NaCl, NaOH, and metallic Na and NaH are formed.
Key words: *NaCl crystal; Gamma-ray irradiation; Color centers; Impurity nanophases; Irradiation-induced phase transformations; Local elemental composition; X-ray diffraction spectra; Optical absorption spectra*
PACS: 61.46.-w, 61.80.-x, 64.70.K-

INTRODUCTION

Recently, sodium chloride (NaCl) crystals have attracted particular interest as a matrix for the disposal of highly active nuclear waste; therefore, several studies of gamma-induced structural defects are again relevant [1-5]. A hundred-year history of research on the effect of ionizing radiation on solids began with the discovery of color centers associated with point defects in NaCl and other ionic crystals when irradiated with UV light and X-ray quanta [2,6-15], and continued with irradiation with nuclear particles and the addition of X-ray and electron microscopic methods for the analysis of structural defects [16-23].

Optical methods formed the basis of the theory of the creation of Frenkel paired anionic defects (charged α-*I* and neutral *F*-*H*) as a result of the decay of anionic excitons (their creation energy is 8-8.4 eV), cationic excitons (60-62 eV), and the recombination of conduction electrons with self-trapped holes (V_K centers) [12,15,19]. There are three types of Schottky vacancies (the transfer of an atom from the bulk to a site on the surface S): a cation vacancy, an anion vacancy, and a bound pair of vacancies of the opposite sign, as well as pairs of Frenkel defects (vacancies and interstitials) in the bulk.

It was shown that at low temperatures of 5-200 K, color centers are stable, and above the anionic interstitials (*H*- and *I*-centers) as well as anionic and cationic vacancies (υ_a and υ_c) already straightforwardly migrate along the crystal lattice [2,6,9,12-15,19-23]. The concentration of paired defects was estimated using the Smakula-Dexter formula (assuming a uniform volume distribution of defects and an unchanged dielectric constant) from the experimental spectra of optical absorption and refractive index, as well as the calculated oscillator strength (0.8–0.9 for the *F* center in NaCl) [7,12,14,15]. The minimum energy of incident electrons for the collisional displacement of Cl in NaCl is estimated at ~ 290–320 keV [2,8]. The enthalpies of migration h^m were determined for the vacancy Na 0.66 eV and interstitial Na 0.29 eV, for the vacancy Cl 0.72 eV and Cl_2^- only 0.16 eV, but the maximum value 0.9 eV was obtained for the divacancy complex $\{V_{Na}V_{Cl}\}$. Thus, it was proved that molecular Cl migrates more easily than the Na atom. This explains why, during radiolysis, Cl evaporates faster as a gas, while Na remains on the surface and forms colloids [2,5,10-13,15,18,19,21,22]. However, the non-stoichiometry of the surface after evaporation of Cl during radiolysis was not measured directly. The total surface area of the crystal should increase as Schottky defects and their agglomerates (nanopores and nanopillars) form, but this can only be measured with modern atomic force microscopes.

Therefore, the purpose of this work was to experimentally investigate the effect of the initial (growth) Na/Cl non-stoichiometry of the surface composition of a NaCl single crystal on the gamma radiation-induced aggregation of point defects and the growth of nanoparticles (metal or other nanophases) using a set of experimental methods.

OBJECTS AND METHODS OF RESEARCH

We used pure high-quality NaCl crystals for IR windows, grown in an inert atmosphere by the classical Kiropulos method in a graphite crucible, with a standard diameter of ∅35 mm and a thickness of 4 mm; optical polishing was performed at LOMO (Russia). The samples were wrapped in Al foil for isolation from air (possible oxidation of the surface) and irradiated in a dry channel at 320 K ^{60}Co with gamma quanta at a dose rate of 145 R/s (energies 1.17 and 1.32 MeV, when corpuscular properties prevail over wave properties) at 4π geometry (isotropic irradiation) to doses

Cite as: Sh. Buzrikov, E. Ibragimova, B. Saydullaev, U. Uljayev, East Eur. J. Phys. 1, 351 (2026), https://doi.org/10.26565/2312-4334-2026-1-41

from 10^5 R, when Frenkel pairs accumulate to 10^7 R (10 MR), when agglomerates and colloids are effectively formed [2,5,13,15,17-22].

Micrographs of the samples before and after irradiation were taken on a scanning electron microscope EVO MA10 (Zeiss) at different magnifications, and the local elemental composition was determined using a built-in EDS attachment with an electron backscattering detector (Oxford Instr. Resolution 128 eV) in the energy range of X-ray quanta from 0.1 to 30 keV. Scanning probe microscopy was carried out on SPM (Shimadzu) to see nanoscale roughness of the surface layer and its change induced by the gamma-irradiation (radiolysis etc). Optical absorption spectra were recorded on an SF-56 spectrophotometer in the wavelength range of 190–1100 nm and optical density range from -1 to +5 in the mode of strongly absorbing objects (slit spectral width 5-10 nm). The phase composition was determined by X-ray diffraction over a wide angular range from 5 to 140 degrees on an Empyrean diffractometer (PANalytical).

RESULTS AND DISCUSSIONS

NaCl crystals were irradiated with gamma rays at Debye temperature = 322 K (which turns out to be very close to the temperature of the dry channel of the gamma source), while all vibrational modes of the lattice were excited and effective diffusion of Na and Cl along interstices was ensured [18, 20].

Taking the known ratio 1 R/s = $2\cdot10^9$ quant/cm^{2}s for the energy of a gamma quantum of 1 MeV, the dose rate of 145 R/s = $2.9\cdot10^{11}$ quant/cm^{2}s and the exposure dose in the flux range from $2.9\cdot10^{16}$ to $3\cdot10^{17}$ quant/cm^2. Since one 1.17 MeV gamma quantum can create either one electron-positron-pair with an energy of 0.585 MeV each, or up to 10^3 Compton electrons with an energy of ~ 100 eV each, sufficient to displace a light atom (A<40) upon collision (25-50 eV) and generation of a pair of defects [2, 8]. However, the minimum energy of an incident electron for the displacement of Cl in NaCl is estimated in the range of 290–320 keV and the radiation-chemical yield of stable *F*-centers 1.5/100 eV and unstable 1.75 [2,17,18,21]. However, according to another estimate, for A = 30, the electron energy in the beam is 0.6-0.8 MeV [8].

The experiment began by determining the local elemental composition of the defective surface. Figures 1A–1D show microimages and nanoscale surface roughness of a NaCl crystal in the non-irradiated state and after irradiation with a dose of 10 MR, as well as local spectra of characteristic X-ray radiation from the near-surface layer. The growth dislocations and tracks of polishing are clearly visible even on non-irradiated sample with high-quality optical polishing, which indicates the presence of both aggregated and nanoscale structural defects. Bright spots indicate areas where the surface charge is localized.

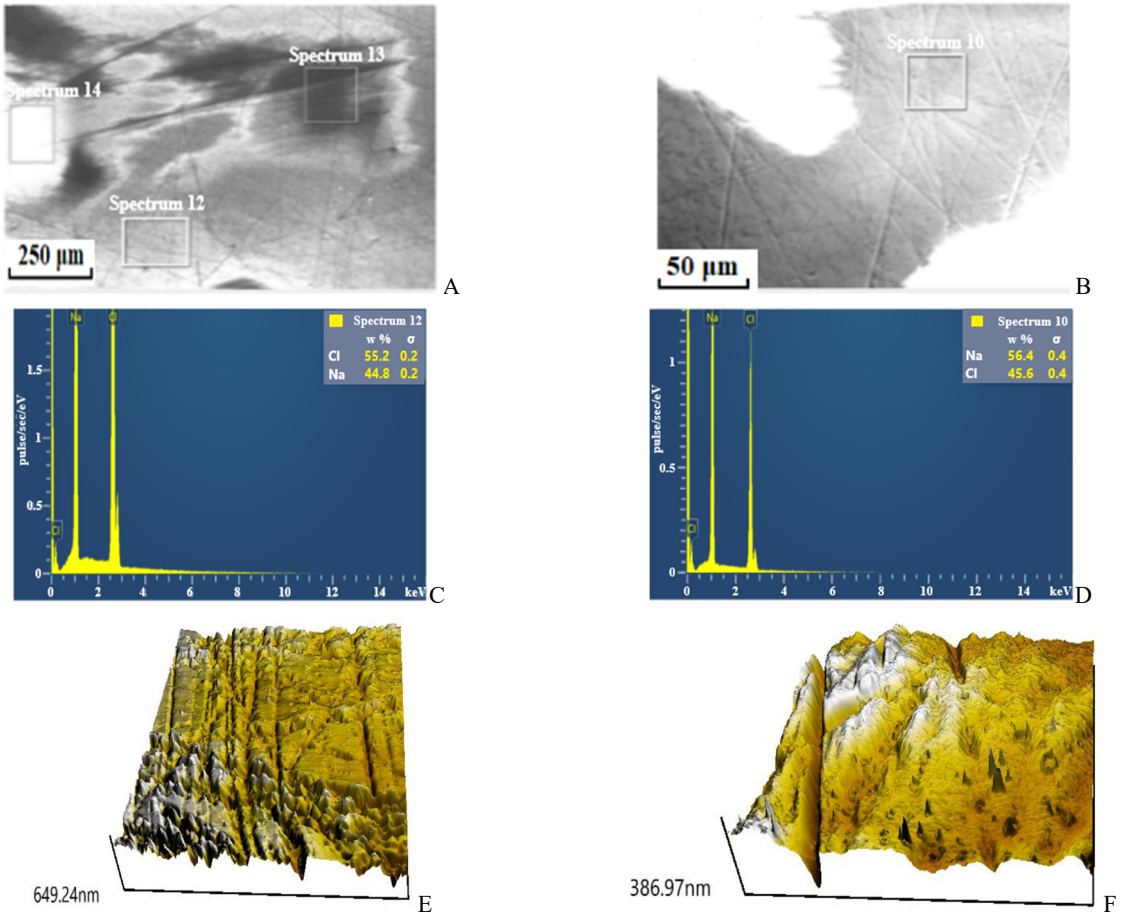

Figure 1. SEM and SPM images of the polished surface of a NaCl crystal: A, E) unirradiated and B, F) after gamma irradiation at 320 K and 140 R/s with a dose of 10^7 R; the squares show the places where the local characteristic spectrum C) and D) were recorded

Figures 1E and 1F show the surface profiles before and after γ-irradiation. It can be seen that the surface roughness (according to the Z scale) after the initial optical polishing reaches about 650 nm due to the presence of frequent nanosized channels and protrusions of the dominant cubic phases $NaClO_3$ and Na_2O. The most anisotropic orthorhombic phase, Cl_2, as well as nanosized cubic HCl and Na, appear to be located within nanogrooves on the channel walls. After irradiation, the depth of the furrows and the height of the peaks decrease by approximately a factor of two due to radiation-enhanced diffusion, and the NaCl matrix becomes exposed. At the same time, a new NaH phase forms in the shape of sharp-edged cones with heights of up to 100 nm, while the furrows deepen as a result of chlorine loss (Table 1).

The chlorine content even on a non-irradiated surface is less than the stoichiometric (60.65%), but still more than sodium. The chlorine content on the irradiated surface is already so much less than stoichiometric that it is already less than sodium. This is direct quantitative evidence of surface radiolysis with the removal of chlorine. It is energetically disadvantageous to create such a quantity of chlorine vacancies; therefore, an effective agglomeration process occurs with the formation of metal colloids and pores [10, 11, 17-22].

Table 1. Local elemental composition (wt %) of the surface layer of the NaCl crystal (the second column is the stoichiometric ratio according to the chemical formula) before and after gamma irradiation

	NaCl	Unirradiated			Dose 10^7 R		Error, %
Element	**formula**	**12**	**13**	**14**	**10**	**11**	
Na	39.35	44.8	44	44.2	54.6	52.6	0.2-0.6
Cl	60.65	55.2	56	55.8	45.4	47.4	0.2-0.6

To confirm this, the X-ray diffraction spectra were measured, and the structure and phase composition were determined, as shown in Fig. 2 and Table 2.

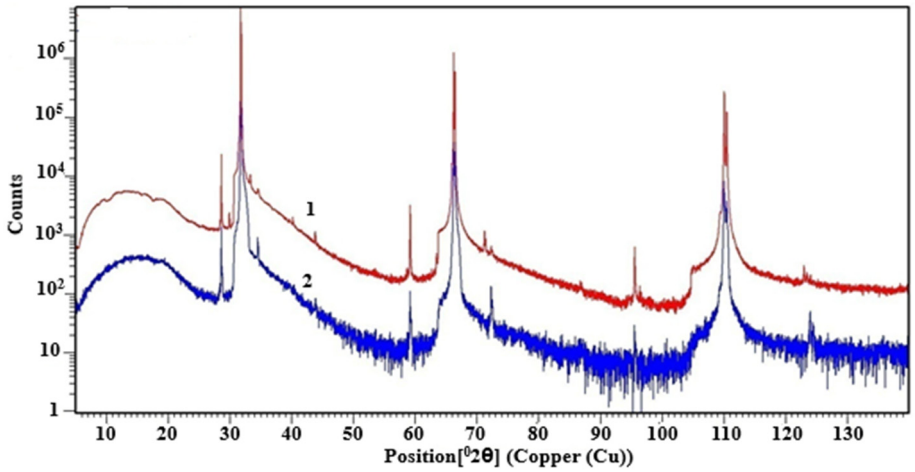

Figure 2. Wide-angle X-ray diffraction spectra of a pure NaCl crystal before (1) and after gamma irradiation at 300 K and 140 R/s with a dose of $7 \cdot 10^5$ R (2)

The spectra show that each high-intensity matrix reflection (h00) is accompanied by incoherent Compton scattering due to the interaction between X-rays and weakly bound valence electrons, which is an important effect in the case of light elements such as Na and Cl. A weak reflection (110) at 29.5^0 was attributed to Na nanoparticles [17,18,20,21]. After gamma irradiation, a systematic shift of reflections towards small angles is observed, a decrease in their amplitude and broadening at the level of half the amplitude are due to phase transitions as a result of additional loss of chlorine from the surface.

Table 2. Structure and phase composition of the surface layer of a NaCl crystal before and after gamma irradiation at 300 K and 140 R/s with a dose of $0.7 \cdot 10^6$ R.

Sample	Phase %	Group	Structure	Lattice parameters, Å		
				a	**b**	**c**
Reference NaCl	Na -1%	Im-3m	Cubic	4.221	4.221	4.221
	NaCl-6%	halite HP, syn Fm-3m	Cubic	5.453	5.453	5.453
	$Na(ClO_3)$-47%	sodium chlorate(V) P213	Cubic	6.340	6.340	6.340
	Cl_2-4%	dichlorine Cmca	Orthorhombic	6.290	4.500	8.210
	HCl-2%	Fm-3m	Cubic	5.482	5.482	5.482
	Na_2O-40%	Fm-3m	Cubic	5.560	5.560	5.560

Sample	Phase %	Group	Structure	Lattice parameters, Å		
				a	b	c
NaCl D=0.7 MR gamma irradiation	NaCl-16%	Fm-3m	Cubic	5.620	5.620	5.620
	NaH-4%	Fm-3m	Cubic	4.880	4.880	4.880
	$Na(ClO_3)$-8%	sodium chlorate(V) P213	Cubic	6.486	6.486	6.486
	NaOH-11%	α-NaOH Bmmb	Orthorhombic	3.399	3.399	11.377
	Na-3%	P63/mmc	Hexagonal	3.767	3.767	6.154
	Na_2Cl-58%	Cmmm	Orthorhombic	3.291	10.385	2.984

As you can see from Table 2, the unirradiated polished surface contains nanopores with Cl_2 and HCl and nanoparticles of Na and NaH, as well as impurity nanophases $NaClO_3$ and Na_2O, which are all cubic and practically cover the bulk cubic structure of NaCl. After the accumulation of a gamma dose of 0.7 MR, the impurity oxygen-containing phases decompose with the formation of dense orthorhombic and hexagonal structures and partial reduction of the basic NaCl lattice. So, for the first time, gamma-radiation-induced phase transitions in the near-surface layer were discovered, for which much more energy from absorbed gamma rays is spent than for simple displacements of atoms from site to interstice to saturating concentrations of 10^{17}-10^{19} cm^{-3} [9,13,15,19,22], which must be taken into account in the energy balance.

Having determined experimentally the deficit of chlorine and the phase composition of the near-surface layer, the dose dependences of the absorption spectrum were measured to establish the dose when pair chlorine vacancies are formed, from which, presumably, chlorine molecules evaporate. In fig. 3 shows the absorption spectra of NaCl crystals measured in steps of dose accumulation from $2\cdot10^4$ R to $3\cdot10^7$ R. The results obtained do not contradict the literature data on the position of absorption bands and color instability [7,12,13,15-19,22].

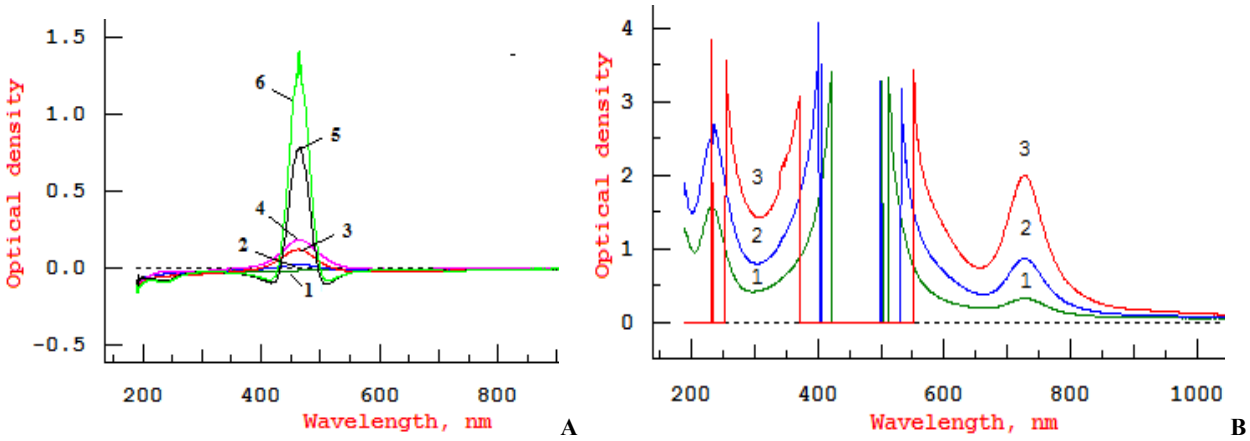

Figure 3. Absorption spectra of NaCl crystals scanned from 190 to 1100 nm on an SF-56 spectrophotometer:
A) 1- non-irradiated, small doses: 2(blue) – 2×10^4 R, 3(red) – 5×10^4 R, 4(pink) – 10^5 R, 5(black) – 2×10^5 R, 6(green) – 3×10^5 R;
B) large doses 1(green) – 7×10^5 R, 2(blue) – 10^7 R, 3(red) – 3×10^7 R

However, measurements in the mode of strongly absorbing materials (Fig. 3B) made it possible to see that the saturation of absorption by *F* centers noted by all authors and the simultaneous appearance of aggregate F_2 and F_3 centers does not exist. Instead, there is a break a continuous extinction function on the wavelength, as if an impurity band were formed in the forbidden band.

The splitting of the *F*-center band appears at a dose of $5\cdot10^5$ R, when paired *F*-*F* centers with electric dipole interaction are formed. In fig. 3A, for the first time, strong dispersion was found around the intense absorption band of the *F* center, where the optical density even takes negative values. According to G. Mie's theory of light scattering by metal nanoparticles in a transparent dielectric [24]. This means that this band of light is effectively reflected, which characterizes metal clusters at the site of anion vacancies, which fully agrees with the above results of the elemental and phase composition of the surface (the presence of metallic phases of sodium). Figure 3B shows that the higher the radiation dose, the higher the concentration of paired centers (category of molecular centers), the closer the distance between the centers in each pair, the stronger the electron-electron interaction and, accordingly, the greater the splitting between the levels. The sodium plasmon resonance line is observed at 500 nm. When the transition of an electron between an occupied and an unoccupied level is allowed by the rules of optical selection, this leads to a strong absorption of a photon with an energy equal to the difference between the energies of the occupied and unoccupied levels. The maximum of the imaginary term of the dielectric function ϵ_i can be expected at $h\nu_1$ and $h\nu_2$. Since these maxima correspond to strong absorption, they determine the color of the solid. The physical condition for strong absorption is that the states in the valence and conducting bands are dispersed in parallel over large parts of the

Brillouin zone. This condition is obviously satisfied for very flat bands arising from strongly localized states [21,23]. In our case, under ionizing irradiation, strongly localized states appear near the level of the chemical potential μ near the middle of the forbidden band with excited levels very close to the valence and conducting bands. At high doses, these states come so close to each other that the electrical dipole interactions between them become significant. The electric dipole moment arises due to ionic polarization: the negatively charged chlorine sublattice is displaced relative to the positively charged sodium ions.

CONCLUSIONS

The use of a set of experimental methods for studying the crystal structure, the spectra of intense optical absorption by colour centres, and the elemental and phase composition of the near-surface layer on modern analytical instruments enabled the discovery of new effects even in the widely studied ionic NaCl crystal. The X-ray diffraction spectra, presented for the first time on a semilogarithmic photon-counting scale, clearly show strong reflections from the matrix and weak reflections from impurity phases. For the first time, the effect of the initial (growth) nonstoichiometry of the surface of a NaCl single crystal with a Chlorine deficiency on the aggregation of point defects in both the anionic (pores with Cl_2 and HCl) and cationic (Na and NaH nanoparticles) sublattices was found. Impurity nanophases $NaClO_3$ and Na_2O were identified, which passivate the superstoichiometric aggressive Na. For the first time, gamma-radiation-induced damage of the existing surface phases and formation of new nanophases were discovered, as a result of which the surface layer of the basic lattice of NaCl was partially restored, which should be taken into account in the distribution of the absorbed dose in the bulk and in the near-surface layer.

The obtained results and research methods can be applied for the dosimetry of long-term irradiation in depositories of high-level waste in the NaCl matrix and their structural changes.

Acknowledgments

The work was carried out under the program of fundamental research of the Institute of Nuclear Physics of the Academy of Sciences of the Republic of Uzbekistan and the project of applied research PZ-20170919163 of the Center for Advanced Technologies of the Ministry of Innovative Development of the Republic of Uzbekistan.

ORCID

Shovkat Buzrikov, https://orcid.org/0009-0005-2346-112X; **Elvira Ibragimova**, https://orcid.org/0000-0003-0087-8772;
Bakhodir Saydullaev, https://orcid.org/0000-0002-7062-1510; **Utkir Uljayev**, https://orcid.org/0009-0002-2564-5270

REFERENCES

[1] S.M. Abdou, and H.Moharam, "Characterization of table salt samples from different origins and ESR detection of the induced effects due to gamma irradiation," IOP Conf. Series: Journal of Physics: Conf. Series, **1253**, 012036 (2019). https://doi:10.1088/1742-6596/1253/1/012036
[2] F.W. Clinard Jr, L.W. Hobbs, "Radiation effects in non–metals," Elsevier Science Publisher, **7**, 387–471 (1986).
[3] M. Enculescu, K. Schwartz, C. Trautmann, and M. Toulemonde, "Heavy ion induced damage in NaCl and KCl crystals," Nucl. Instr. and Meth. B, **229,** 397–405 (2005). https://doi.org/10.1016/j.nimb.2004.12.131
[4] P.V. Kuzhakov, and N.V. Kamanina, "Spectral investigations and wettability of nanostructured potassium bromide, sodium chloride and magnesium fluoride single crystals," Opt. Spectrosc. **117,** 643-646 (2014). https://doi.org/10.1134/S0030400X14100130
[5] A.R. West, *Solid-state chemistry and its applications*, (Wiley, UK, 2014).
[6] H. Duerig, and J.J. Markham, "Color centers in alkali halides at 5 K," Phys. Rev. **88**, 1043–1049 (1952). https://doi.org/10.1103/PhysRev.88.1043
[7] D.L. Dexter, "Concentration of color centers in alkali halides," Phys. Rev. **96**, 615 (1954). https://doi.org/10.1103/PhysRev.96.615
[8] S.T. Konobeevsky, "On the question of the nature of radiation damage in fissionable materials," The Soviet Journal of Atomic Energy, **1**, 209–216 (1956). https://doi.org/10.1007/BF01506933
[9] H. Rabin, and C.C. Klick, "Formation of *F* centers at low and room temperatures," Phys. Rev. **117**, 1005–1010 (1960). https://doi.org/10.1103/PhysRev.117.1005
[10] R.B. Gordon, and A.S. Nowick, "Structure sensitivity of the X-ray coloration of NaCl crystals," Phys. Rev. **101**, 977–983 (1956). https://doi.org/10.1103/physrev.101.977
[11] C.L. Bauer, and R.B. Gordon, "Structure sensitivity of *F*-center generation by X-rays at low temperatures," Phys. Rev. **126**, 73-78 (1962). https://doi.org/10.1103/PhysRev.126.73
[12] C.B. Luschchik, G.G. Liidya, and M.A. Elango, "Electron-hole mechanism of color center creation in ionic crystals," Sov. Phys. Sol. St. **6**, 1784–1794 (1965).
[13] G.J. Crowe, W. Fuchs, and D.A. Weigand, "Schottky disorder and lattice relaxation in single crystals of NaCl due to X-irradiation at room temperature," Phys. Rev. Let. **16**, 1154-1155 (1966). https://doi.org/10.1103/PhysRevLett.16.1154
[14] F. Luty, "F_A centers in alkali halide crystals," in: *Physics of color centers*, edited by W.B. Fowler, (Academ. Press, N.Y. 1968).
[15] Ch.B. Lushchik, "Creation of Frenkel Defect Pairs by Excitons in Alkali Halides," Modern Problems in Condensed Matter Sciences, **13**, 473–525 (1986). https://doi.org/10.1016/B978-0-444-86946-3.50014-0
[16] V.I. Dubinko, A.A. Turkin, D.I. Vainstein, H.W. den Hartog, "Effect of dose rate, temperature and impurity content on the radiation damage in the electron irradiated NaCl crystals" Nuclear Instruments and Methods in Physics Research Section B: Beam Interactions with Materials and Atoms, **166–167**, 561–567 (2000). https://doi.org/10.1016/S0168-583X(99)00722-3

[17] H.W. den Hartog, D.I. Vainstein, V.I. Dubinko, "Effect of radiation-induced emission of Schottky defects on the formation of colloids in alkali halides" Radiation effects and defects in solids, **158**, 705-719 (2003). https://doi.org/10.1080/1042015031000112531
[18] C.R.A. Catlow, K.M. Diller, and L.W. Hobbs, "Irradiation-induced defects in alkali halide crystals," Philosophical Magazine A, **42**, 123-150 (1980). https://doi.org/10.1080/01418618009365806
[19] E.A. Kotomin, and A.I. Popov, "The kinetics of radiation induced point defect aggregation and metallic colloid formation in ionic solids," in: *Radiation Effects in Solids. NATO Science Series*, edited by K.E.Sickafus, E.A. Kotomin, and B.P. Uberuaga, vol. 235, (Springer, Dordrecht, 2007). pp. 153–192. https://doi.org/10.1007/978-1-4020-5295-8_7
[20] C. Brechignac, "Alkali clusters," in: *Clusters of Atoms and Molecules*, edited by H. Haberland, (Springer Verlag, Berlin, 1994). pp. 253-418. https://doi.org/10.1007/978-3-642-84329-7
[21] S.N. Sulyanov, D.M. Kheiker, A.V. Sugonyako, D.I. Vainstein, and M.W den Hartog, "Characterization of the size and orientation of Na and Cl_2 nanocrystals in electron irradiated NaCl crystals by means of synchrotron radiation," J. Phys.: Condens. Matter, **19**, 246210 (2007). https://doi.org/10.1088/0953-8984/19/24/246210
[22] Yu.Ya. Tomashpolski, N.V. Sadovskaya, N.V. Kozlova, and G.A. Grigoreva, "Thermally stimulated surface segregation in sodium chloride crystals," J. Surf. Investig. **6**, 930–937 (2012). https://doi.org/10.1134/S1027451012110134
[23] A. Lushchik, and Ch. Lushchik, "Low-temperature creation of Frenkel defects via hot electron-hole recombination in highly pure NaCl single crystals," Low Temperature Physics, **42**, 547 (2016); https://doi.org/10.1063/1.4959011
[24] P. Hofmann, *Dielectrics*, (Wiley, UK, 2014).

РАДІАЦІЙНО-ІНДУКОВАНІ ФАЗОВІ ПЕРЕТВОРЕННЯ, АГРЕГАЦІЯ ТОЧКОВИХ ДЕФЕКТІВ ТА УТВОРЕННЯ НАНОЧАСТИНОК У ГАММА-ОПРОМІНЕНИХ КРИСТАЛАХ NaCl

Шовкат Бузріков[1], Ельвіра Ібрагімова[2], Баходір Сайдуллаєв[3], Уткір Ульджаєв[4]
[1]Науково-технічний центр радіаційної та ядерної безпеки, Ташкент, Узбекистан
[2]Інститут ядерної фізики АН РУз, Ташкент, Узбекистан
[3]Університет Альфраганус, Ташкент, Узбекистан
[4]Денауський інститут підприємництва та педагогіки, м. Денау, 360, Сурхандар'їнська область, Узбекистан

Вперше за допомогою комбінації експериментальних методів та сучасних аналітичних приладів досліджено вплив нестехіометрії росту Na/Cl на поверхні монокристала NaCl на його фазовий склад, агрегацію точкових дефектів в обох підґратках, індуковану гамма-опроміненням, та ріст наночастинок. Було виявлено, що при опроміненні дозами <1 MR початкові домішкові нанофази $NaClO_3$ та Na_2O на поверхні розриваються, а замість них утворюються Na2Cl, NaCl, NaOH та металеві Na та NaH.

Ключові слова: *кристал NaCl; гамма-опромінення; центри забарвлення; домішкові нанофази; фазові перетворення, індуковані опроміненням; локальний елементний склад; рентгенівські дифракційні спектри; оптичні абсорбційні спектри*

EAST EUROPEAN JOURNAL OF PHYSICS. 1. 357-362 (2026)
DOI:10.26565/2312-4334-2026-1-42 ISSN 2312-4334

IMPROVING CARBON NANOTUBE SYNTHESIS BY THE REMOVAL OF AMORPHOUS CARBON

Sevara G. Gulomjanova*, Ilyos Kh. Khudaykulov, Ilyos J. Abdisaidov, Khatam B. Ashurov
Arifov Institute of Ion-Plasma and Laser Technologies of Uzbekistan Academy of Sciences
100125, Durmon Yuli St. 33, Tashkent, Uzbekistan
**Corresponding Author e-mail: sevara@iplt.uz*
Received November 17, 2025; revised February 6, 2026; accepted February 19, 2026

In this study, carbon nanotubes (CNTs) were synthesized on Ni-coated sapphire substrates using conventional and water-assisted chemical vapor deposition (CVD and WA-CVD) methods to evaluate the effect of water vapor on amorphous carbon removal and catalyst activity at low temperatures. Reduced nickel nanocatalysts were prepared by the sol–gel method and activated in a hydrogen atmosphere. Raman spectroscopy confirmed that CNTs synthesized by WA-CVD exhibited a higher degree of graphitization (ID/IG ≈ 1.18) and the absence of amorphous carbon peaks around 794 cm^{-1}, indicating improved purity. X-ray diffraction (XRD) analysis revealed the formation of graphitic carbon (002) and Ni_3C crystalline phases, as well as a rightward shift of the (002) peak to $2\theta = 26.2°$, suggesting lattice contraction caused by water-vapor-induced stress. Transmission electron microscopy (TEM) images showed that CNTs synthesized under WA-CVD conditions were thinner (17–25 nm), longer (≥ 1 μm), and cleaner than those obtained by conventional CVD, which exhibited thick amorphous carbon coatings. These results demonstrate that the controlled addition of water vapor during CVD suppresses amorphous carbon formation, regenerates catalyst active sites, and significantly enhances CNT crystallinity and morphological uniformity. The findings provide an efficient approach for synthesizing high-purity, well-aligned CNTs suitable for thermal interface materials, nanocomposites, and electronic device applications.
Keywords: *Carbon nanotubes; Amorphous carbon removal; Water-assisted CVD; Nickel catalyst; Sol–gel synthesis; Raman spectroscopy; X-ray diffraction; TEM morphology; Graphitization degree; Catalyst regeneration*
PACS: 81.07.De; 81.15.Gh; 81.20.Fw; 61.48.De; 61.72.Cc; 78.30.Na; 61.05.cp; 68.37.Lp; 82.65.+r.

INTRODUCTION

Since their discovery by Iijima in 1991 [1], carbon nanotubes (CNTs) have been among the most promising nanomaterials investigated to date. Their exceptional mechanical strength, electrical and thermal conductivity, as well as chemical stability, make CNTs suitable for a wide range of applications, including electronics, catalysis, composite materials, energy storage systems, and thermal interface materials (TIMs) [2–4].

The quality, morphology, and properties of CNTs mainly depend on the synthesis parameters—particularly the type of catalyst, growth temperature, carbon source, and reaction atmosphere [5]. The most widely used synthesis technique is Chemical Vapor Deposition (CVD), which offers several advantages such as simple technological requirements, low cost, and controllable growth conditions [6,7]. However, the formation of amorphous carbon (a-C) during the CVD process significantly reduces the structural and functional quality of CNTs.

Deposited carbon on the catalyst surface can generally be classified into amorphous carbon and graphitic carbon. Amorphous carbon is formed through the adsorption of carbon species on active nickel sites; it is highly reactive and can be removed at relatively low temperatures [8]. In heterogeneous catalysis, carbon deposits of different structural order can form on catalyst surfaces, and their nature strongly affects catalyst stability and activity. Amorphous carbon species are generally less ordered and more reactive, whereas graphitic carbon exhibits a more ordered sp^2-bonded lattice that is thermodynamically stable and harder to remove by simple low-temperature treatments [9]. Such graphitic deposits tend to form at higher reaction temperatures and, once present, require significantly higher temperatures or aggressive regeneration procedures for elimination. As carbon continues to accumulate, these graphitic coke species block active sites or pores and physically limit the access of reactant gases to catalytic centers, which leads to a gradual decline in catalytic activity and, in severe cases, complete catalyst deactivation [10].

As a result, the growth rate of CNTs decreases, their length shortens, graphitization becomes limited, and both electrical and thermal properties deteriorate [11]. Therefore, the controlled removal or prevention of amorphous carbon formation during synthesis is one of the most effective strategies for improving CNT quality.

Several approaches have been explored for the elimination of amorphous carbon. One of the most widely studied techniques involves oxidative acid treatments, using mixtures of nitric acid (HNO_3), sulfuric acid (H_2SO_4), or hydrogen peroxide (H_2O_2) [12–14]. By functionalization, chemical groups such as carboxyl (–COOH), carbonyl (–CO), and hydroxyl (-OH) are formed on the CNT surfaces, which exfoliate the CNT bundles, improve their wettability and enable their dispersion in polar media. In the presence of metal precursors, these surface groups help the diffusion and nucleation of metals on the CNT sidewalls for the synthesis of ideal CNT composites [15]. The acidic treatment tends to damage the external graphitic lattice structure of CNTs[16]. Thus, optimizing the concentration and duration of oxidation is crucial [17].

Cite as: S.G. Gulomjanova, I.Kh. Khudaykulov, I.J. Abdisaidov, Kh.B. Ashurov, East Eur. J. Phys. 1, 357 (2026), https://doi.org/10.26565/2312-4334-2026-1-42

An alternative approach is the Water-Assisted Chemical Vapor Deposition (WA-CVD) method, where water vapor (H_2O) is introduced into the synthesis environment. Adding water vapor to the CVD process can improve the CNT purity, alignment, and growth height by removing amorphous carbon on the (typically Fe) catalyst particles owing to the partial oxidation of the metallic catalyst. [18,19]. This method enables the formation of vertically aligned, dense, and highly ordered CNT arrays [20]. Studies have shown that samples synthesized at higher temperatures (600–800°C) exhibit a higher degree of graphitization, whereas lower temperatures favor amorphous carbon formation [21].

Moreover, the choice of metal catalyst significantly influences amorphous carbon formation. Transition metals such as Fe, Co, and Ni effectively decompose carbon and promote diffusion; however, at lower growth temperatures, amorphous carbon deposition becomes more likely [22]. Therefore, the activation and cleanliness of the catalyst surface play a crucial role in CNT growth [23].

Recent research demonstrates that the *in-situ* removal of amorphous carbon—during rather than after synthesis—enhances the morphology, graphitization, and functional performance of CNTs [24,25]. This not only simplifies the synthesis process but also minimizes subsequent chemical treatments, preserving the structural integrity of the nanotubes.

In this study, the conventional CVD and water-assisted CVD (WA-CVD) methods are compared to evaluate the influence of water vapor on amorphous carbon formation at low temperatures. The presence of water vapor facilitates the decomposition of excess amorphous carbon on the catalyst surface in real time, keeping active sites exposed. Consequently, CNT growth yield increases, catalyst lifetime extends, and graphitization improves. Understanding the mechanism of amorphous carbon formation and its suppression via WA-CVD or oxidative environments provides a pathway for producing low-defect, highly crystalline CNTs at relatively low temperatures.

This approach establishes an important scientific foundation for the development of efficient, stable, and thermally conductive nanotubes for thermal interface materials (TIMs) [26], nanocomposites [27], and electronic devices [28].

In this study, reduced nickel nanocatalysts synthesized via the sol–gel method were employed for the growth of carbon nanotubes (CNTs). Nickel(II) nitrate hexahydrate [$Ni(NO_3)_2 \cdot 6H_2O$] was dissolved in distilled water, and ammonium hydroxide (NH_4OH) was gradually added until the pH reached 11. The resulting solution was slowly heated to 85 °C, leading to the formation of a gel. The obtained gel was deposited onto sapphire substrates using the spin-coating technique and subsequently dried at 400 °C. The nickel nanocatalysts were produced by reducing nickel oxide (NiO) at elevated temperatures in a hydrogen atmosphere, which converted NiO into metallic nickel and enhanced its catalytic activity.

EXPERIMENT

Carbon nanotubes were synthesized on Ni-coated sapphire substrates using a super-growth chemical vapor deposition (CVD) technique that selectively removes amorphous carbon without damaging the nanotube structure at the growth temperature. The schematic diagram of the experimental setup developed for CNT synthesis using the super-growth CVD method is shown in Figure 1.

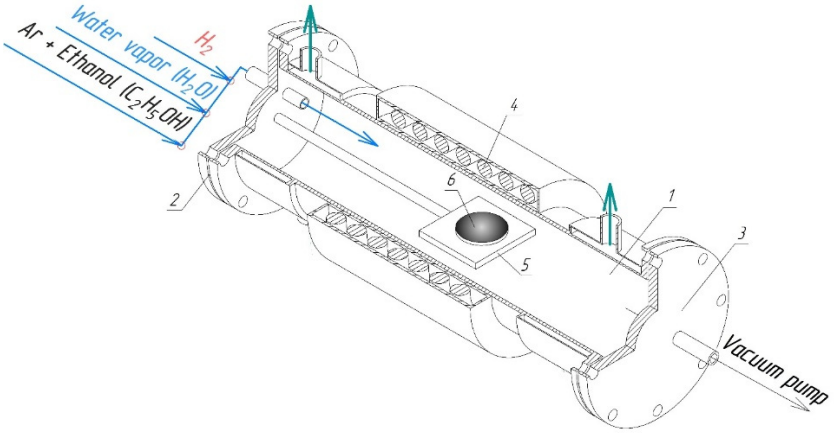

Figure 1. Schematic diagram of the designed CVD system: 1– quartz reactor (1 m length); 2, 3 – flanges; 4 – laboratory furnace; 5 – molybdenum plate with thermocouple; 6 – sample

All experiments were conducted under identical reaction conditions, with the only difference being the presence or absence of water vapor during the growth stage. The substrates were placed inside a quartz-tube furnace, and when the reaction temperature reached 550 °C, ethanol (C_2H_5OH) was introduced into the reactor together with argon gas, maintaining a total gas flow rate of 3.0 L/min. The reaction time was fixed at 45 minutes. CNT growth was performed under two different conditions:

-Dry growth (without water vapor): Ar (2900 sccm) + C_2H_5OH (100 sccm).

-Water-assisted growth (WA-CVD): H_2O + Ar (2900 sccm) + C_2H_5OH (100 sccm).

In the WA-CVD process, deionized water at room temperature was passed through a bubbler to generate water vapor, which was continuously monitored and controlled. The controlled addition of water vapor served to maintain the catalyst activity and enhance the growth rate of carbon nanotubes.

After 45 minutes of growth, the flow of C_2H_5OH and Ar was stopped, and the samples were allowed to cool naturally to room temperature.

To evaluate the structural, crystallographic, and morphological properties of the synthesized carbon nanotubes (CNTs), several advanced characterization techniques were employed.

Raman spectroscopy was carried out using a *Renishaw Raman spectrometer* equipped with a 532 nm laser source operating at 100% power (approximately 10 mW). The spectra were recorded over the range of 100–3500 cm^{-1}. This analysis provided insights into the degree of graphitization, the presence of amorphous carbon, and defects within the CNT structure.

The crystalline structure and phase composition of the CNTs were analyzed using *Rigaku SmartLab SE X-ray Diffractometer with Guidance Software*. Measurements were conducted with Cu Kα radiation (λ = 1.5406 Å) at an operating voltage of 40 kV and current of 50 mA. Scans were performed in 1D mode, with a step size of 0.01° and a scan rate of 3.00° min^{-1}, covering the 2θ range of 10°–100°.

To further investigate the morphology and internal structure, Transmission Electron Microscopy (TEM) analysis was performed using a *Thermo Scientific Talos F200i (S)* field-emission scanning TEM operating at 20–200 kV.

RESULTS AND DISCUSSION

The Raman spectra of the synthesized carbon nanotubes (CNTs) exhibited three characteristic peaks typical of carbon nanomaterials — the D, G, and 2D bands — as shown in Figure 2. These peaks correspond to the vibrational modes of *sp^2-hybridized carbon atoms* within the graphitic lattice, confirming that the nanotubes possess a graphitic structure.

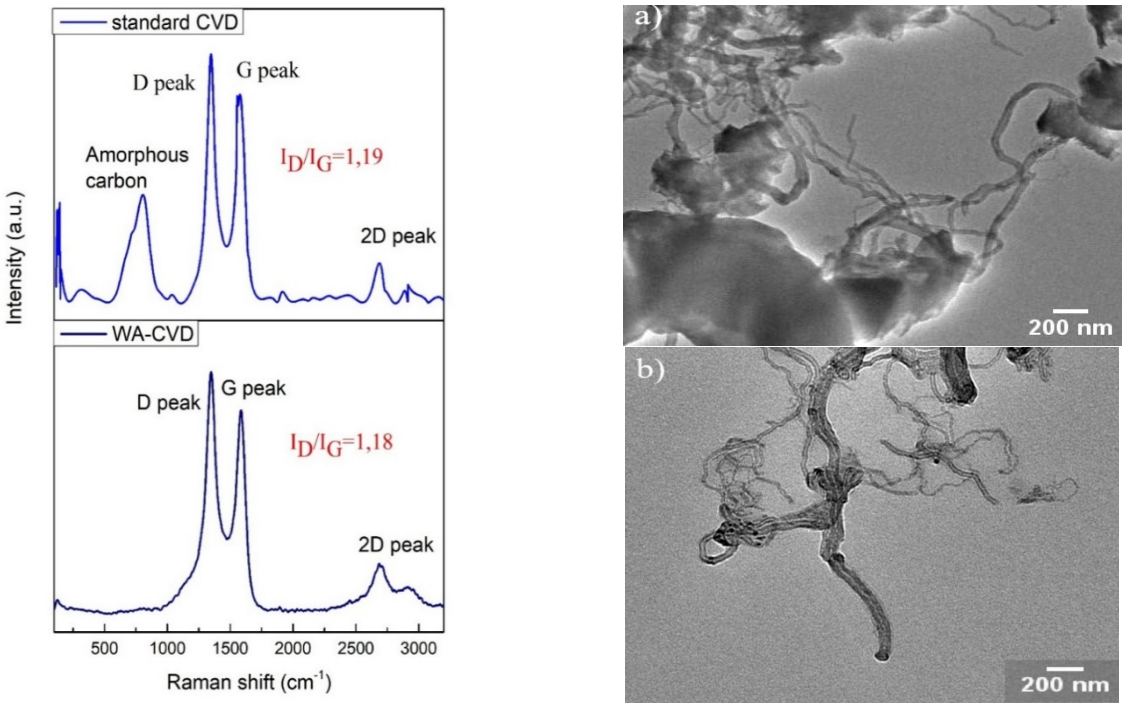

Figure 2. Raman spectra and TEM image of carbon nanotubes synthesized by: (a) conventional CVD and (b) water-assisted CVD (WA-CVD) methods

In the Raman spectra, the G band observed in the range of 1575–1586 cm^{-1} corresponds to the in-plane stretching vibrations of sp^2-bonded carbon atoms, confirming the presence of a crystalline graphitic structure. The D band (~1343-1349 cm^{-1}) is associated with lattice imperfections and amorphous phases, and its intensity reflects the degree of structural disorder in the sample.

For the CNTs grown by the conventional CVD method, the D, G, and 2D peaks were observed at 1343, 1575, and 2685 cm^{-1}, respectively, with an I_D/I_G ratio of approximately 1.19, indicating the presence of defects and amorphous carbon. Additionally, a low-frequency radial breathing mode (RBM) in the range of 126–139 cm^{-1} confirmed the existence of single-walled carbon nanotube (SWCNT) fractions.

In contrast, for the CNTs synthesized using the WA-CVD method, the D, G, and 2D peaks appeared at 1349, 1586, and 2686 cm^{-1}, respectively, while the characteristic amorphous carbon signal around ~794 cm^{-1} was absent, indicating higher purity of the sample. The $I_D/I_G \approx 1.18$ value suggests improved crystallinity. The rightward shift of the G-band to 1586 cm^{-1} can be attributed to mechanical compression or doping-induced stress within the carbon lattice.

The X-ray diffraction (XRD) patterns of the CNTs synthesized under both conditions are shown in Figure 3. The diffractograms exhibited several distinct peaks in the 2θ range of 10°–100°, confirming the crystalline nature of the obtained samples.

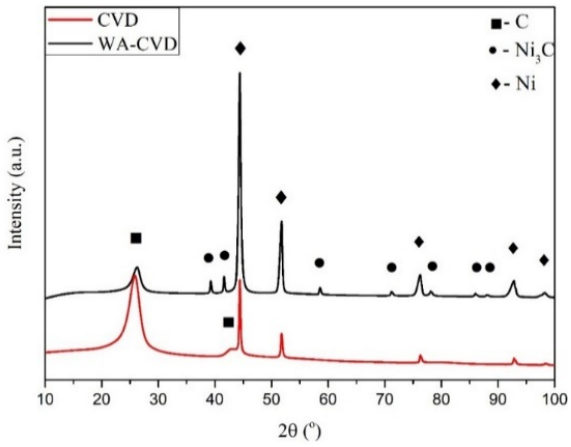

Figure 3. XRD diffractograms of carbon nanotubes synthesized by conventional CVD (red) and WA-CVD (black) methods

In the diffractogram of the CNTs synthesized by the conventional CVD process, the main diffraction peaks appeared at 2θ ≈ 25.8°, 42.8°, 44.4°, 51.7°, 76.2°, 92.8°, and 98.3°, corresponding respectively to the (002) and (020) planes of graphitic carbon and to the (111), (200), (220), (311), and higher-order reflections of metallic Ni phases (JCPDS №. 04-0850). The strong peak near 2θ ≈ 25.8° confirms the presence of graphitic carbon layers, indicating the formation of carbon nanostructures.

The XRD pattern of CNTs synthesized via the WA-CVD method exhibited the same major peaks (2θ = 26.27°, 44.4°, 76.2°, 92.8°, and 98.3°) along with several additional reflections at 2θ ≈ 39.3°, 41.6°, 58.62°, 71.20°, 78.11°, 86.05°, 88.09°, and 97.49°. These additional peaks correspond to the hexagonal Ni_3C phase (PDF No. 77-0194), indexed to the(110), (006), (116), (300), and (119) planes [29].

The (002) peak of CNTs grown under standard CVD conditions appeared at 2θ ≈ 26°, typical for graphitic carbon structures. In contrast, for CNTs synthesized under WA-CVD conditions, a slight rightward shift of the (002) peak to 2θ ≈ 26.2° was observed, which is attributed to lattice parameter contraction. The primary causes of this shift are the compressive stresses induced on the catalyst surface by the water vapor, a reduction in nanocrystallite size, and possible atomic rearrangements caused by oxidation or doping processes, leading to a decrease in interatomic spacing and, consequently, an increase in the Bragg angle (2θ) [30].

The morphological characteristics of the synthesized CNTs were further investigated using Transmission Electron Microscopy (TEM), as shown in Figure 2 and Figure 4.

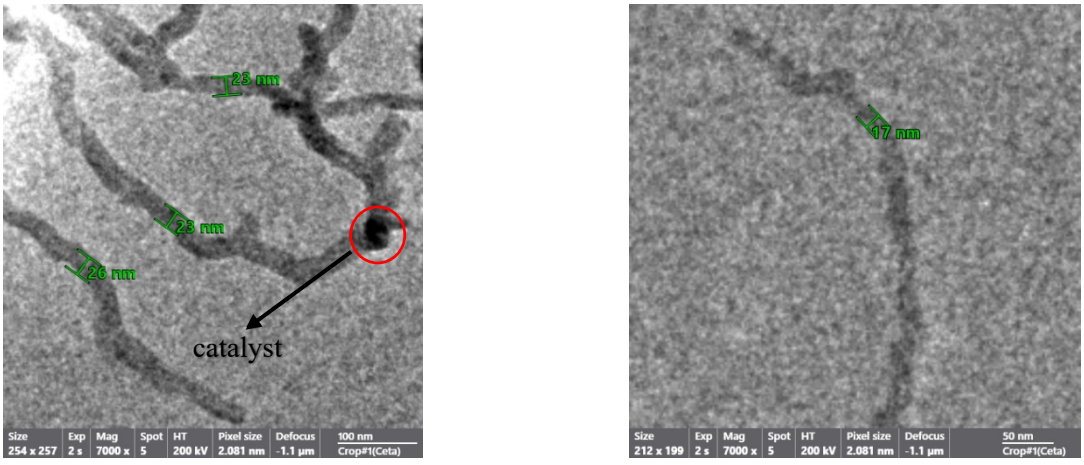

a) b)

Figure 4. TEM images of carbon nanotubes: (a) CNTs synthesized by the conventional CVD method; (b) CNTs synthesized by the water-assisted CVD (WA-CVD) method

The TEM image of the sample grown under dry CVD conditions (Fig. 2a) shows nanotubes covered with a thick layer of amorphous carbon and agglomerated clusters. The nanotubes have diameters of approximately 23–40 nm (Fig. 4a) and lengths typically limited to 200–500 nm. The presence of numerous irregular and fragmented segments indicates uncontrolled carbon deposition on the catalyst surface, leading to the accumulation of amorphous carbon and consequently to CNTs of poor structural quality with disordered morphology.

In contrast, the TEM image of the sample synthesized under WA-CVD conditions (Figure 2b) shows much cleaner and more ordered nanotubes. The CNTs are thinner and longer, with diameters ranging from 17–25 nm (Fig. 4b) and lengths exceeding several micrometers (≥1 µm). The amorphous carbon layer is almost absent, and the CNTs are well-

separated from one another. This demonstrates that water vapor regenerates the catalyst surface, suppresses excessive carbon deposition, and stabilizes the growth process.

From the TEM images (Figures 4a and 4b), it can be concluded that CNTs synthesized by both the CVD and WA-CVD methods grew via the tip-growth mechanism. In both cases, Ni nanoparticles served as active catalytic centers, decomposing the carbon precursor and promoting tubular carbon formation.

Overall, the comparative analysis indicates that synthesis performed in the presence of water vapor results in higher-quality, longer, and purer carbon nanotubes than those obtained under dry conditions. Water vapor not only extends the catalyst lifetime but also produces CNTs with smaller diameters and more uniform distributions.

CONCLUSIONS

The conducted research demonstrated that the water-assisted chemical vapor deposition (WA-CVD) method is significantly more efficient than the conventional CVD process for synthesizing carbon nanotubes (CNTs). The Raman analysis showed that CNTs synthesized under WA-CVD conditions exhibited no amorphous carbon components and displayed a higher degree of graphitic ordering ($I_D/I_G \approx 1.18$). The XRD results revealed a shift of the (002) peak to $2\theta = 26.2°$ and the formation of the Ni_3C phase, confirming the stabilizing effect of water vapor on catalyst activity. The TEM observations demonstrated that CNTs grown by the WA-CVD method were thin (5–12 nm), long (≥1 μm), and well-separated, whereas those grown under conventional CVD conditions were short, irregular, and coated with amorphous carbon. Overall, water vapor regenerates the catalyst surface, suppresses amorphous carbon formation, and improves both graphitization and growth efficiency. Therefore, the WA-CVD method has been proven to be an optimal approach for synthesizing thin, long, and well-aligned carbon nanotubes with high crystallinity and purity.

Acknowledgments

The authors gratefully acknowledge the financial and technical support provided by the Ministry of Higher Education, Science, and Innovation under project number IL-5421101842.

ORCID

Sevara G. Gulomjanova, https://orcid.org/0009-0001-1760-9766; **Ilyos Kh. Khudaykulov,** https://orcid.org/0000-0002-2335-4456; **Ilyos J. Abdisaidov,** https://orcid.org/0000-0001-7473-1074; **Khatam B. Ashurov,** https://orcid.org/0000-0002-7604-2333

REFERENCES

[1]. S. Iijima, "Helical microtubules of graphitic carbon," Nature, **354**, 56–58 (1991). https://doi.org/10.1038/354056a0
[2]. M.S. Dresselhaus, G. Dresselhaus, and P. Avouris, *Carbon Nanotubes: Synthesis, Structure, Properties, and Applications*, (Springer, Berlin, 2001). https://doi.org/10.1007/3-540-39947-X
[3]. R.H. Baughman, A.A. Zakhidov, and W.A. de Heer, "Carbon nanotubes – the route toward applications," Science, **297**, 787–792 (2002). https://doi.org/10.1126/science.1060928
[4]. J. Robertson, "Growth of carbon nanotubes for electronics," Materials Today, **10**, 36–43 (2007). https://doi.org/10.1016/S1369-7021(06)71790-4
[5]. A. Peigney, C. Laurent, E. Flahaut, R.R. Bacsa, and A. Rousset, "Specific surface area of carbon nanotubes and bundles of carbon nanotubes," Carbon, **39**, 507–514 (2001). https://doi.org/10.1016/S0008-6223(00)00155-X
[6]. D. Tasis, N. Tagmatarchis, A. Bianco, and M. Prato, "Chemistry of carbon nanotubes," Chemical Reviews, **106**, 1105–1136 (2006). https://doi.org/10.1021/cr050569o
[7]. R. Andrews, D. Jacques, D. Qian, and T. Rantell, "Multiwall carbon nanotubes: synthesis and application," Carbon, **39**, 1681-1687 (2001). https://doi.org/10.1021/ar010151m
[8]. I.J. Abdisaidov, S.G. Gulomjanova, I.Kh. Khudaykulov, and K.B. Ashurov, "Low-temperature growth of carbon nanotubes using nickel catalyst," East European Journal of Physics, (3), 355–358 (2024). https://doi.org/10.26565/2312-4334-2024-3-41
[9]. H. Qu, *et al*. "Reconfiguring organic color centers on the sp^2 carbon lattice of single-walled carbon nanotubes," ACS nano, **16**(2), 2077-2087 (2022). https://doi.org/10.1021/acsnano.1c07669
[10]. E.T.C. Vogt, D. Fu, B.M. Weckhuysen, "Carbon deposit analysis in catalyst deactivation, regeneration, and rejuvenation," Angewandte Chemie International Edition, 62(29), e202300319 (2023). https://doi.org/10.1002/anie.202300319
[11]. S. Maruyama, R. Kojima, Y. Miyauchi, S. Chiashi, and M. Kohno, "Low-temperature synthesis of high-purity single-walled carbon nanotubes from alcohol," Chemical Physics Letters, **360**, 229–234 (2002). https://doi.org/10.1016/S0009-2614(02)00838-2
[12]. A. Reina, M. Hofmann, D. Zhu, and J. Kong, "Growth mechanism of long and horizontally aligned carbon nanotubes by chemical vapor deposition," Journal of Physical Chemistry C, **111**(20), 7292–7297 (2007). https://doi.org/10.1021/jp0711500
[13]. K. Hata, D.N. Futaba, K. Mizuno, T. Namai, M. Yumura, and S. Iijima, "Water-assisted highly efficient synthesis of impurity-free single-walled carbon nanotubes," Science, **306**, 1362–1364 (2004). https://doi.org/10.1126/science.1104962
[14]. T. A. Saleh, "The influence of treatment temperature on the acidity of MWCNT oxidized by HNO_3 or a mixture of HNO_3/H_2SO_4," Applied Surface Science, **257**(17), 7746–7751 (2011). https://doi.org/10.1016/j.apsusc.2011.04.020
[15]. N. Sezer, and M. Koç, "Oxidative acid treatment of carbon nanotubes," Surfaces and Interfaces, 14, 1–8 (2019). https://doi.org/10.1016/j.surfin.2018.11.001
[16]. L. Lavagna, M. Bartoli, D. Suarez-Riera, D. Cagliero, S. Musso, and M. Pavese, "Oxidation of Carbon Nanotubes for Improving the Mechanical and Electrical Properties of Oil-Well Cement-Based Composites," ACS Applied Nano Materials, **5**(5), 6671-6678 (2022). https://doi.org/10.1021/acsanm.2c00706
[17]. G. Gao, M. Pan, and C. D. Vecitis, "Effect of the oxidation approach on carbon nanotube surface functional groups and electrooxidative filtration performance," Journal of Materials Chemistry A, **3**(14), 7575–7582 (2015). https://doi.org/10.1039/C4TA07191C

[18]. K. Strobl, and F. Rajab, "Water-Assisted Catalytic VACNT Growth Optimization for Speed and Height," Processes, **11**(6), 1587 (2023). https://doi.org/10.3390/pr11061587
[19]. D. N. Futaba, K. Hata, T. Yamada, K. Mizuno, M. Yumura, and S. Iijima, "Kinetics of water-assisted single-walled carbon nanotube synthesis revealed by a time-evolution analysis," Physical Review Letters, **95**(5), 056104 (2005). https://doi.org/10.1103/PhysRevLett.95.056104
[20]. Y. Yun, V. Shanov, Y. Tu, S. Subramaniam, and M.J. Schulz, "Growth mechanism of long aligned multiwall carbon nanotube arrays by water-assisted chemical vapor deposition," The Journal of Physical Chemistry B, **110**(47), 23920–23925 (2006). https://doi.org/10.1021/jp057171g
[21]. L. Dong, J. G. Park, B. E. Leonhardt, S. Zhang, and R. Liang, "Continuous synthesis of double-walled carbon nanotubes with water-assisted floating catalyst chemical vapor deposition," Nanomaterials, **10**(2), 365 (2020). https://doi.org/10.3390/nano10020365
[22]. A. Ismatov, C. Romanitan, K. Ashurov, M. Adilov, and A. Rahimov, "Annealing-induced morphological evolution of iron nanocatalysts for carbon nanotube growth," Eurasian Physical Technical Journal, **22**(3 (53)), 5–13 (2025). https://doi.org/10.31489/2025N3/5-13
[23]. P. Nikolaev, M.J. Bronikowski, R.K. Bradley, F. Rohmund, D.T. Colbert, K.A. Smith, and R.E. Smalley, "Gas-phase catalytic growth of single-walled carbon nanotubes from carbon monoxide," Chemical Physics Letters, **313**, 91–97 (1999). https://doi.org/10.1016/S0009-2614(99)01029-5
[24]. Z. Chen, X. Wei, S. Lu, J. Ding, N. Du, C. Feng, K. Chen, *et al*., "Surface in-situ graphitization and properties of amorphous carbon film induced by laser irradiation," Friction, **13**(6), (2025). https://doi.org/10.26599/FRICT.2025.9440977(12)
[25]. R. Xu, H. Yin, D. He, X. Ma, S. Liang, C. Jin, and X. Chen, "Mechanism of polymer removal from semiconducting single-walled carbon nanotubes via rapid thermal processing: insights from in situ environmental transmission electron microscopy," Nanoscale, **17**, 14941–14947 (2025). https://doi.org/10.1039/D5NR01566A
[26]. D. Fabris, M. Rosshirt, C. Cardenas, P. Wilhite, T. Yamada, and C.Y. Yang, "Application of carbon nanotubes to thermal interface materials," Journal of Electronic Packaging, 020902(6), (2011). https://doi.org/10.1115/1.4003864
[27]. Z. Zhang, N. Zhang, and Z. Zhang, "High-Performance Carbon Nanotube Electronic Devices: Progress and Challenges," Micromachines, **16**(5), 554 (2025). https://doi.org/10.3390/mi16050554
[28]. E. W. Fenta, and B. A. Mebratie, "Advancements in carbon nanotube-polymer composites: Enhancing properties and applications through advanced manufacturing techniques," Heliyon, **10**, (e36490) (2024). https://doi.org/10.1016/j.heliyon.2024.e36490
[29]. Y. Zhang, Y. Zhu, Y. Cao, D. Li, Z. Zhang, K. Wang, F. Ding, *et al*., "Size and morphology-controlled synthesis of Ni_3C nanoparticles in a TEG solution and their magnetic properties," RSC Advances, **6**, (2016). https://doi.org/10.1039/C6RA11916F
[30]. A. Cao, C. Xu, J. Liang, D. Wu, and B. Wei, "X-Ray Diffraction Characterization on the Alignment Degree of Carbon Nanotubes," Chemical Physics Letters, **344**(1-2), 13–17 (2001). https://doi.org/10.1016/S0009-2614(01)00671-6

ПОКРАЩЕННЯ СИНТЕЗУ ВУГЛЕЦЕВИХ НАНОТРУБОК ШЛЯХОМ ВИДАЛЕННЯ АМОРФНОГО ВУГЛЕЦЮ

Севара Г. Гуломджанова, Ільос Х. Худайкулов, Ільос Дж. Абдісаїдов, Хатам Б. Ашуров
Інститут іонно-плазмових та лазерних технологій ім. Аріфова Академії наук Узбекистану
100125, вул. Дурмон йулі, 33, Ташкент, Узбекистан

У цьому дослідженні вуглецеві нанотрубки (ВНТ) були синтезовані на сапфірових підкладках з нікелевим покриттям за допомогою традиційних методів та методів хімічного осадження з парової фази з використанням води (CVD та WA-CVD) для оцінки впливу водяної пари на видалення аморфного вуглецю та активність каталізатора за низьких температур. Відновлені нікелеві нанокаталізатори були отримані золь-гель методом та активовані в атмосфері водню. Раманівська спектроскопія підтвердила, що вуглецеві нанотрубки, синтезовані методом WA-CVD, демонструють вищий ступінь графітизації (ID/IG ≈ 1,18) та відсутність піків аморфного вуглецю близько 794 $см^{-1}$, що свідчить про покращену чистоту. Рентгенівський дифракційний аналіз (XRD) виявив утворення графітових вуглецевих (002) та кристалічних фаз Ni_3C, а також зсув піку (002) праворуч до $2\theta = 26{,}2°$, що свідчить про стиснення кристалічної решітки, спричинене напруженням, індукованим водяною парою. Зображення просвічувальної електронної мікроскопії (TEM) показали, що вуглецеві нанотрубки, синтезовані в умовах WA-CVD, були тоншими (17–25 нм), довшими (≥ 1 мкм) та чистішими, ніж ті, що були отримані звичайним CVD, які демонстрували товсті покриття з аморфного вуглецю. Ці результати демонструють, що контрольоване додавання водяної пари під час CVD пригнічує утворення аморфного вуглецю, регенерує активні центри каталізатора та значно покращує кристалічність та морфологічну однорідність вуглецевих нанотрубок. Отримані результати пропонують ефективний підхід до синтезу високочистих, добре вирівняних вуглецевих нанотрубок, придатних для використання в термоінтерфейсних матеріалах, нанокомпозитах та електронних пристроях.

Ключові слова: *вуглецеві нанотрубки; видалення аморфного вуглецю; CVD з використанням води; нікелевий каталізатор; золь-гель синтез; раманівська спектроскопія; рентгенівська дифракція; морфологія TEM; ступінь графітизації; регенерація каталізатора*

East European Journal of Physics. 1. 363-372 (2026)
DOI:10.26565/2312-4334-2026-1-43 ISSN 2312-4334

UNVEILING PRESSURE-DRIVEN TRANSITIONS IN $Cs_2AgBiBr_6$: INSIGHTS FROM DFT INTO A LEAD-FREE SOLAR PEROVSKITE

Sangita Gupta[1], Devidutta Maurya[2], Sunil Kumar Srivastava[3], Umesh Kumar Pareek[3], Abhay P. Srivastava[4]*

[1]*Department of Chemistry, Poornima University, Jaipur, Rajasthan, India*
[2]*Department of Physics, Government Degree College, Barakhal, Santkabeernagar, (UP), India*
[3]*Department of Applied Science, Jaipur Engineering College and Research Centre, Jaipur, Rajasthan, India*
[4]*Department of Applied Science and Humanities, Goel Institute of Engineering and Technology, Lucknow (UP), India*
**Corresponding Author e-mail: abhay.srivastava831@gmail.com*
Received October 15, 2025; revised January 10, 2026; accepted January 29, 2026

Using the Vienna Ab initio Simulation Package, we investigate the lead-free double perovskite $Cs_2AgBiBr_6$. We used first-principles density functional theory under pressures up to 30 GPa. Optimization of the structure proves an obvious cubic symmetry in the ambient environment. However, compression appears to promote transitions to lower-symmetry phases, and we observe that the bulk and Young's moduli increase, followed by a decrease in Poisson's ratio. This implies more stiffness but reduced ductility. It is concluded that, as temperature increases, the Debye temperature rises and the thermal expansion decreases. Thus, higher temperature stability is suggested. The electronic bandgap becomes even thinner. It spans 1.95 eV to 1.12 eV, making it more or less direct, which may enhance its optoelectronic usability. Above 15 GPa, we observe a weak magnetic moment, apparently due to Bi–Ag hybridization, and a higher density of states at the Fermi level. $Cs_2AgBiBr_6$ combines these characteristics, making it a potential material for pressure-tuned photovoltaics and potentially for magneto-optoelectronic applications.
Keywords: *Density Functional Theory (DFT); Double Perovskite; Pressure-Dependent Properties; Structural Phase Transition; Optoelectronic Materials*
PACS: 32.30.Rj, 33.20.Lg, 42.62.Fi, 61

1. INTRODUCTION

Lead-free perovskites are among the most promising candidates for next-generation solar energy installations and optoelectronics, given the demand for sustainable photovoltaics. This line, halide double perovskite $Cs_2AgBiBr_6$, is of some interest [1-2]. It has no toxins and is a thermally stable material exhibiting excellent optoelectronic properties. The material is cubic, with the elpasolite structure (space group Fm–3m). Silver (Ag^+) and the bismuth (Bi^{3+}) ions alternate between the B-site, where bromine (Br^-) ions are coordinated. Compared to conventional perovskites such as $MAPbI_3$, the geometry avoids the lead toxicity, and its electrochemical activity was adequate for solar power applications [3-5].

One drawback of $Cs_2AgBiBr_6$ is that it possesses an indirect bandgap between 1.9 and 2.2 eV. That, in the latter case, might, in turn, reduce the light-to-electric conversion efficiency. New researchers at the theoretical and experimental levels, however, now widely accept that pressure influences its structure and electronic properties. Under pressure, interatomic distances and atomic orbital trajectories are also altered [6-8]. Such changes might also affect crystal lattice symmetry, narrow the bandgap, or induce an intermediate shift from indirect to direct atomic optical transitions, thereby benefiting light-harvesting [9-10].

Pressure can also affect properties beyond the electronic structure. It specifies the material's mechanical and thermal properties, which, in turn, are key to the life of the perovskite system [11-13]. By determining elastic constants, the bulk modulus, the Debye temperature, and thermal expansion under compression, we gain a better understanding of the materials' performance under extreme conditions. Look at aerospace, wearables, or high-heat solar cells [14-15]. One caveat, however, is that $Cs_2AgBiBr_6$ typically exhibits no magnetic activity under ambient conditions. On the other hand, at much higher pressures, magnetic behaviour can arise from orbital mixing and a high density of states, especially near the Fermi level, which could have potential applications in magneto-optoelectronic devices [16-18]. We present a study based on a series of detailed first-principles calculations, employing density functional theory (DFT) within the VASP framework to examine the influence of pressure on $Cs_2AgBiBr_6$. Focusing specifically on the influence of high hydrostatic pressure (0-30 GPa) on the material, we investigate the correlations among the structure, mechanical strength, thermal stability, optical characteristics, electronic band structure, and magnetic order of the components [19-20]. We focus on the influence of spin–orbit coupling (SOC) and the different orbitals on the valence and conduction band structures. In this way, these materials and systems can be tailored to pressure, enabling the design of strong, versatile, and lead-free perovskite materials for solar energy and optoelectronic devices with high energy efficiency.

Cite as: S. Gupta, D. Maurya, S.K. Srivastava, U.K. Pareek, A.P. Srivastava, East Eur. J. Phys. 1, 363 (2026), https://doi.org/10.26565/2312-4334-2026-1-43

2. COMPUTATIONAL METHOD

Using Density Functional Theory (DFT), in particular using the Vienna Ab initio Simulation Package (VASP) for such analysis, we conducted a comprehensive investigation into the behavior of the double perovskite compound $Cs_2AgBiBr_6$ under varying pressure conditions. We systematically conducted an investigation of structural, mechanical, thermal, magnetic, and optical properties of this candidate with 0-30 GPa hydrostatic pressures. This method provided us valuable insights into how the behavior of the material changes with increasing pressure, enabling greater understanding of its potential applications and fundamental behavior [21-22].

2.1. Exchange-Correlation Potential

For the exchange-correlation energy, we employed the Generalised Gradient Approximation (GGA) based on the Perdew, Burke, and Ernzerhof (PBE) functional. In order to consider the relativistic effects from heavier elements, specifically Bi and Cs, spin–orbit coupling (SOC) was included in electronic structure calculations, which were performed self-consistently. Spin-polarised calculations were used to understand magnetic behaviour [23-24].

We use PBE as a generalized gradient approximation because of its long history of accuracy when determining equilibrium structural parameters, elastic properties, and the pressure-dependent evolution of crystalline solids. PBE in high-pressure investigations exhibits reasonable computational efficiency and accurately reproduces equations of state, bulk moduli, and relative changes in the electronic structure under compression. As an absolute bandgap underestimator, PBE is well known, but it can accurately represent pressure-induced bandgap evolution—the main aim of this study.

2.2. Pseudopotentials and Basis Set

To simulate the interaction between electrons and ions, the projector augmented-wave (PAW) method was employed. Valence electron configurations were as follows:

Cs: $5s^2 5p^6 6s^1$

Ag: $4d^{10} 5s^1$

Bi: $6s^2 6p^3$

Br: $4s^2 4p^5$

A plane-wave energy cutoff of 500 eV was set for all computations. We used a convergence criterion of 10^{-6} eV for the electronic self-consistency loop. Atomic forces were relaxed to a value of less than 0.01 eV/Å [25-26].

2.3. Brillouin Zone Integration

Brillouin-zone sampling was performed using a 6×6×6 Monkhorst–Pack grid well suited for the primitive cell of the investigated material. Therefore, this grid configuration permitted a systematic study of the electronic structure in the first Brillouin zone. To achieve more accurate convergence of electronic and optical properties, we used a denser 8×8×8 Monkhorst–Pack grid. In this way, the addition of sampling points improved the accuracy and completeness of the band structures and optical responses, as shown in [27].

2.4. Structural Optimisation under Pressure

A comprehensive geometry optimization was performed for each such pressure point, with the majority of the focus on optimizing the lattice constants and internal atomic coordinates of the studied material. The method was carried out under hydrostatic pressure, which was systematically applied using the Vienna Ab initio Simulation Package (VASP) with ISIF = 3. This can also relax the cell shape and overall crystal volume, such that the crystal structure optimally adjusts to the applied pressure under each condition.

During this detailed optimization, a variety of parameters (atomic positions, lattice sizes, and the entire system) were optimized in the full system of this optimization process so as to minimize the total energy of this system in order to optimize the system in an accurate and stable manner. The optimized structures of this detailed optimization further employed subsequent calculations to investigate electronic structure, mechanical properties, and phonon behavior. Such calculations are critical for characterizing the behavior of a material under different pressure conditions [28-29].

2.5. Mechanical Properties

The Voigt–Reuss–Hill (VRH) approximations play an important role in materials science, as it can be difficult to obtain valuable mechanical properties such as bulk modulus (B), Young's modulus (E), and Poisson's ratio (ν). So, by joining the Voigt and Reuss bounds — the upper and lower bounds of a material's response under stress — the VRH yields a more accurate average for describing materials' anisotropic nature. As these calculations improve the precision of derived quantities, they also yield important information on material properties under various loading conditions, thereby enhancing the design and research efficiency of materials and their applications [30-31].

2.6. Thermal Properties

The value of Debye temperature (Θ_D) and volume thermal expansion coefficient (α) utilized quasi-harmonic approximation in light of the vibrational modes of a solid. And beyond the elastic constants, this method also contributed to the knowledge of the material under different operating conditions. The information on pressure-volume was fitted to

a Murnaghan equation of state to give an accurate estimate of the pressure and volume relation. The bulk modulus was calculated due to the fitting of the samples, disclosing information related to the incompressibility of the material, and the pressure derivative of this incompressibility with the application of pressure [32-33].

2.7. Magnetic Properties

In order to have a more detailed idea of the complex magnetic characteristics, we carried out spin-polarised calculations at various pressures. With self-consistent charge and spin density methods, we calculated both the total and atomic magnetic moments to obtain the magnetism of the material. We evaluated total energy differences and the density of states (DOS) at the Fermi level to test if any magnetic ordering exists under compression. Such observation explained that the pressure and magnetic properties were related to the compound [34].

2.8. Optical Properties

The frequency-dependent complex dielectric function $\varepsilon(\omega)$ is given by the expression $\varepsilon(\omega) = \varepsilon_1(\omega) + i\varepsilon_2(\omega)$, where $\varepsilon_1(\omega)$ is the real part and $\varepsilon_2(\omega)$ is the imaginary part. This function was found from the independent-particle approximation, which suggests that the particles in the system hardly interact with each other. Later on, we used the complex dielectric function to obtain several critical optical parameters such as band gap, absorption coefficient, refractive index, reflectivity, and absorption edge. We performed dense k-meshes in the Brillouin zone for our results while limiting the energy resolution to 0.01 eV to cover photon energies up to 20 eV, and ensure the accuracy of our results. Attention to detail of this approach allowed for obtaining comprehensive optical spectra that give insights into the electronic and optical characteristics of the material. The findings of our study provide important insights into this material's typical response to various electromagnetic parameters [35].

2.9. Electronic Properties

The electronic band configuration and total density of states (DOS) were calculated for the optimized structures from our simulations. We collected information, increasingly in pressure, systematically documenting and observing the band gaps, with the ambition of studying these indirect-to-direct transition electronic characteristics. That allowed us not only to identify when or under which conditions transitions are occurring, but also to determine the effective mass of charge carriers in the bands. Such a result is important as it gives information regarding the electronic characteristics of the materials under varying pressure conditions, which might be substantially relevant for use as electronic and optoelectronic devices [36-37].

3. RESULTS AND DISCUSSIONS

3.1 Structural Properties

Crystal Structure of $Cs_2AgBiBr_6$:

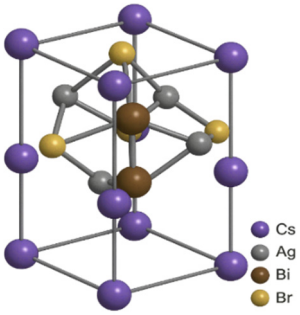

Figure 1. Crystal structure of $Cs_2AgBiBr_6$ in its cubic Fm–3m symmetry.

As shown in Figure 1, the atomic configuration of $Cs_2AgBiBr_6$ is depicted. This lead-free halide double perovskite has been widely studied for applications in potential solar cells and other optoelectronic devices. $Cs_2AgBiBr_6$ [3] has a cubic lattice and a double-perovskite structure similar to that of elpasolite. Within this framework, B-site cations silver (Ag^+) and bismuth (Bi^{3+})—two B-site cations—take turns occupying niches, coordinated naturally by bromine (Br^-) anions, to yield $AgBr_6$ and $BiBr_6$ octahedra. Caesium (Cs^+) ions occupy the cuboctahedral vacancies, thereby stabilising the full electrostatic geometry.

Normally, this structure belongs to the space group Fm–3m (No. 225), a property characteristic of ideal double perovskites. The Cs atoms should lie at 8c and Ag at 4a — 0, 0, 0, and Bi in 4b and ½, ½, ½, and Br atoms, at the 24e positions — x, 0, 0 and x near 0.229, respectively, in well defined spots referred to as Wyckoff positions. In general, it is relatively symmetric, and typical conditions indicate that octahedral tilting or distortion is typically very low. This symmetry is advantageous for uniform physical and thermal behavior; thus, $Cs_2AgBiBr_6$ serves as a representative case for the study of materials that respond to pressure and temperature. Yet there is more to this arrangement than its inherent symmetry. $Cs_2AgBiBr_6$'s bandgap is indirect and varies between 1.9 and 2.2 eV, so that the stable and environmentally benign design of lead-free solar cells is guaranteed.

Additionally, its water- and heat-resistance makes this material a candidate for photovoltaic absorbers, photodetectors, and LEDs. By testing $Cs_2AgBiBr_6$ under an applied pressure, it is determined that $Cs_2AgBiBr_6$ can shorten this bandgap even if the bandgap shifted directly from its initial position of indirect or increased visible-NIR light absorption to direct, meaning it can be used in high-pressure optoelectronics.

Bismuth exhibits low thermal conductivity and strong spin–orbit coupling, which further enhances its performance in thermoelectric and radiation-detection applications. That is, the basic design of the cube structure, $Cs_2AgBiBr_6$, has significant characteristics other than symmetry; it serves not only as a structure foundation on which to build stability, but also as a stable basis of some of the properties of energy and electronics, which are necessary. Due to its structural stability, non-toxicity, and tunable optoelectric properties, the compound is suitable for preparing versatile materials for clean energy applications.

Pressure-Dependent Phase Transitions in $Cs_2AgBiBr_6$: Symmetry Evolution and Functional Relevance

Figure 2 illustrates the pressure-dependent structural characterization of double perovskite $Cs_2AgBiBr_6$ at 0–30 GPa. At ambient pressure, the compound crystallized in the optimal cubic elpasolite structure (space group Fm–3m), with corner-sharing $AgBr_6$ and $BiBr_6$ octahedra arranged in a highly symmetric configuration. The constraint at low pressure of both octahedra gives a constant low level of uniform reduction of the lattice parameters, as opposed to octahedral tilting or any visible reduction in the angle of the bond geometry. Over >10 GPa of applied pressure, smaller deviations in the ideal cubic symmetry are beginning to be detected. These deviations arise as an extended perturbation as the $AgBr_6$ and then $BiBr_6$ octahedra distort, along with an increment of the Br–Ag–Br and Br–Bi–Br angle.

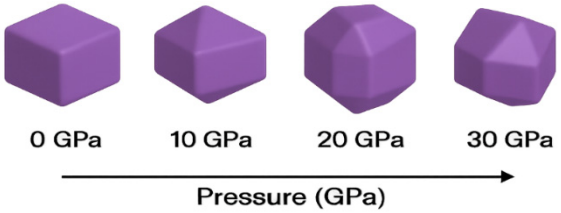

Figure 2: Pressure-dependent phase transitions in $Cs_2AgBiBr_6$

These distortions may be interpreted as the first step toward symmetry reduction, driven by increased orbital overlap and strong short-range repulsion under compression. Importantly, this loss of symmetry does not occur during strong lattice-parameter transitions, implying that the transition not only begins with one and the same but also proceeds gradually. Because the structural distortion is very evident under high-pressure conditions, particularly at 15-30 GPa, this is graphically illustrated in Figure 2. The enhanced structures under this regime are characterized by pronounced octahedral tilting and anisotropic bond compression, typically observed in low-symmetry crystal systems. Such features indicate a transition to tetragonal or orthorhombic lattices at intermediate pressures, followed by transitions to monoclinic or triclinic lattices at 30 GPa.

The enthalpy comparisons and phonon stability calculations required for final phase assignment are absent, but the observed diminished symmetry strongly favors pressure-driven reshaping of structures. Therefore, the structural evolution reflected for the $Cs_2AgBiBr_6$ case is that the material's elastic mechanical stability remains under compression, as seen with a few simple dynamic lattice parameter changes with higher pressure, but it loses the symmetry-inhibiting behavior simultaneously. This continual volume reduction and progressive symmetry reduction are both characteristic of pressure-induced second-order structural transitions in halide perovskites and critical for regulating the electronic, optical, and magnetic properties of the material in high-pressure applications.

Based on structural optimisation using DFT, the variation in the lattice constant and unit-cell volume of $Cs_2AgBiBr_6$ under hydrostatic pressure from 0 to 30 GPa is detailed in Table 1. As pressure increases, the lattice constant and unit-cell volume decrease consistently. Fundamentally, this is the expected elastic response in a crystalline solid: compression brings the atoms closer together, thereby reducing the unit cell volume. Specifically, at 0 GPa, the lattice constant is 11.27 Å, corresponding to a volume of 1430.5 Å^3, which then decreases gradually to 10.49 Å and 1185.7 Å^3 at 30 GPa.

Table 1. Pressure-dependent variation of lattice constant and unit cell volume of $Cs_2AgBiBr_6$ calculated using DFT.

Pressure (GPa)	Lattice Constant (Å)	Volume (Å^3)
0	11.27	1430.5
5	11.11	1385.3
10	10.97	1342.4
15	10.84	1300.2
20	10.72	1260.5
25	10.6	1222.4
30	10.49	1185.7

Both the lattice constant and the unit-cell volume decrease with increasing pressure, due to the material's mechanical stability, which is not caused by faulting, as the material can resist compression without failing. But this compression

does not preserve cubic symmetry. At pressures of 15 to 30 GPa, substantial structural distortions arise, resulting in low-symmetry subphases, such as tetragonal, monoclinic, or triclinic.

This is highly variable and has a strong effect on the mechanical, thermal, and electronic properties of the material. There is a graph of the pressure relationship and the gradual evolution of crystallographic symmetry (Figure 2), which shows how high pressure will influence atomic configurations and overall behaviour. Pressure-induced compression can alter electronic and optical properties by increasing orbital overlap among atoms (including Ag, Bi, and Br), thereby reducing the bandgap and increasing light absorption (both desirable for applications in solar cells and other photonic devices). Moreover, the data is required to find the bulk modulus and mechanical strength of $Cs_2AgBiBr_6$ under pressure.

3.2. Mechanical Properties

We observe, in the analysis of the mechanical properties of $Cs_2AgBiBr_6$ in Table 2, that bulk modulus, Young's modulus, and Poisson's ratio are all affected by hydrostatic pressure values between 0 and 30 GPa. Together, these numbers reveal the mechanical behavior of the materials under compression and deformation. At high pressure, the bulk modulus increases from 18.6 GPa at the beginning to 45.3 GPa, a 30 GPa increase. The material becomes increasingly difficult to compress under external forces. Stiffening is not unusual in dense perovskites; it arises from reduced lattice flexibility as interatomic distances shorten. The Young's modulus – the stiffness of a material that is stretched in just one direction – also increases, from 35.2 GPa to 73.8 GPa.

Table 2. Pressure-dependent mechanical properties of $Cs_2AgBiBr_6$ calculated using DFT

Pressure (GPa)	Bulk Modulus (GPa)	Young's Modulus (GPa)	Poisson's Ratio (ν)
0	18.6	35.2	0.28
5	22.9	41.7	0.27
10	28.5	47.3	0.26
15	33.1	53.6	0.25
20	37.6	60.9	0.24
25	41.9	67.1	0.23
30	45.3	73.8	0.22

This leads to increased mechanical strength under high pressure, an advantage for optoelectronic products that work in high-pressure environments. Poisson's ratio, which drops a bit, from 0.28 to 0.22, meanwhile. That is, with higher pressures, the material's lateral response to deformation becomes weaker. The low Poisson's ratio tends to be in favor of the brittleness, and some may go from ductile to brittle when compressed. From the practical perspective, the pressure-sensitive mechanical properties are essential to inspect the mechanical stability, versatility, and resistance of $Cs_2AgBiBr_6$ to the use in practical devices, such as solar cells, bendable electronics, or pressure-reliant instruments.

If it can sustain extreme pressure and not crack or collapse, it can be exploited in space, for defense, or on Earth. Then we can anticipate mechanical wear, peeling (or cracking) patterns, and prevent them in layered device designs since we have a good perspective on mechanical trends.

3.3. Thermal Properties

Table 3 shows the adaptation of $Cs_2AgBiBr_6$'s Debye temperature (Θ_D) and its volume thermal expansion coefficient (α) with pressure rise from 0 to 30 GPa. Such thermal properties are very important as they reflect the lattice characteristics, phonon properties, and thermal stability in the material, which are all vital to device behavior under thermal and mechanical forces. A Debye temperature is recorded at 195 K when zero pressure is applied and 292 K at 30 GPa. The Debye temperature, being known worldwide, represents the highest phonon frequency of a solid and is inextricably tied with the stiffness of its lattice as well as the speed of sound propagation. So, as we raise the temperature at which Debye burns, as it becomes gradually temperature-dependent, we also start to think that the lattice is stiffening, and in turn, we make it harder for phonons to be excited. The lattice heat capacity drops at low temperature and the thermal conductivity normally increases. Table 2 indicates this trend, which agrees with the results from the mechanical stiffening investigation as well as the compression response of the material.

Table 3. Pressure-dependent Debye temperature and volume thermal expansion coefficient of $Cs_2AgBiBr_6$ calculated using DFT.

Pressure (GPa)	Debye Temperature (K)	Thermal Expansion Coefficient ($\times 10^{-5}$ K^{-1})
0	195	3.12
5	213	2.91
10	231	2.65
15	247	2.42
20	265	2.17
25	278	1.95
30	292	1.78

In contrast, the volume thermal expansion coefficient (α) decreases from 3.12×10^{-5} K^{-1} at 0 GPa to 1.78×10^{-5} K^{-1} at 30 GPa. This coefficient quantifies the extent to which the material expands as its temperature rises. A lower thermal expansion coefficient at higher pressure implies a thermally more stable and undefended structure. This is a clear

advantage for applications requiring dimensional stability under temperature changes. This decline in α under pressure also indicates the absence of anharmonic phonon interactions, which may allow a material to become more robust in high-power or high-temperature applications. Technologically, these results are also highly important for designing thermal management systems for such photodetectors and other optoelectronic systems, such as solar cells, where process performance may be threatened by thermal stress.

The higher Debye temperature, together with reduced pressure-induced thermal expansion, indicates that $Cs_2AgBiBr_6$ is particularly suitable for harsh environments such as aerospace, geothermal, and high-power lasers, where thermal and mechanical system control is important.

3.4 Optical Properties

Table 4 reports the relative optical properties of the lead-free double perovskite $Cs_2AgBiBr_6$ under pressure. We have bandgap energy, static dielectric constant $\varepsilon_1(0)$, peak imaginary dielectric function $\varepsilon_2(\omega)$, refractive index (n), optical absorption edge, and reflectivity as those factors. Knowledge of these parameters is important for assessing whether the material functions as a light detector and for light collection, especially when it is pressurized. The data show that, in this case, the bandgap energy decreases. From 0 GPa up to 30 GPa, it goes from 1.95 eV down to 1.12 eV. This decrease, or bandgap narrowing, appears to be an effect of the structure of the Ag-4d, Bi-6p, and Br-4p orbitals becoming tighter and narrower under more favourable conditions, as a result of lattice compression.

Table 4. Pressure-dependent optical properties of $Cs_2AgBiBr_6$ calculated using DFT

Pressure (GPa)	Bandgap (eV)	$\varepsilon_1(0)$ (Static Dielectric Constant)	Peak $\varepsilon_2(\omega)$ (Imaginary Dielectric Function)	Refractive Index (n)	Absorption Edge (eV)	Reflectivity (%)
0	1.95	5.2	4.7	2.28	1.9	14.5
5	1.8	5.6	5.2	2.34	1.7	16.1
10	1.65	6.1	5.9	2.41	1.6	17.3
15	1.52	6.7	6.4	2.48	1.5	18.6
20	1.38	7.4	6.8	2.56	1.35	20
25	1.24	8.1	7.3	2.63	1.2	21.5
30	1.12	8.8	7.7	2.69	1.05	22.8

As atoms close to each other their interactions become stronger, and the conduction and valence bands merge. Technologically, this is relatively helpful. With a reduced bandgap, the material can absorb more light in the visible and near-infrared (NIR) regions of the spectrum, leading to an increase of the efficiency of photovoltaic. Simultaneously, the static dielectric constant of $\varepsilon_1(0)$ increases from 5.2 to 8.8. This means that the material also becomes more electronically polarizable under compression. A high dielectric constant facilitates exciton dissociation and charge screening in optoelectronic devices, increasing charge separation. Also prominent is the rise of the imaginary part of the dielectric function $\varepsilon_2(\omega)$, which shows interband optical transitions from 4.7 to 7.7, representing more light-matter interaction and absorption at higher pressure.

The refractive index increases to 2.69 from 2.28. This is reflected in the smaller bandgap and greater density of the electronic structure. A higher refractive index means better photon confinement—more appropriate for waveguides, light-trapping structures, and photonic crystals. The absorption edge changes from 1.9 eV to about 1.05 eV, and thus the absorption also shifts in a direction toward the lower-photon energy band. The product: more sunlight is received from such a wider range of wavelengths. Finally, the reflectivity goes up from 14.5% to 22.8%. This is likely explained by increased optical density and more free-carrier interactions at higher pressures.

Although some extra reflectivity might mean less light is absorbed at the surface, we can use it for multilayer coatings or tweak stuff with anti-reflective engineering. So, all in all, it appears that external pressure may be a way to optimise the optical properties of $Cs_2AgBiBr_6$. There may be applications for this (e.g., advancing good broadband photodetectors, solar cells, or optoelectronics that need to be operated through mechanical strain).

3.5. Electronic Properties

The impact of pressure on the electronic properties of $Cs_2AgBiBr_6$ can be found in Table 5. We are discussing the bandgap (both its value and its type), the valence band maximum (VBM) and conduction band minimum (CBM) bits, the density of states (DOS) at the Fermi level, and the effective masses of electrons and holes. However, the bandgap continues to shrink: from 1.95 eV at no pressure (0 GPa) down to 1.12 eV at 30 GPa, the bandgap narrows under the pressure effect. What's interesting is the change in the bandgap, which would be an indirect (Γ to L) phenomenon (no pressure) but is now a direct (Γ to Γ) one at 20 GPa and further. This change is important to note because direct bands allow light to be absorbed and emitted more efficiently, which is beneficial for solar cells and LEDs.

That "direct-like" stuff, at 15 GPa, think about the electronic states slowly rearranging themselves as pressure changes, and the overlap of the orbitals. However, the VBM can always have Br-4p and Ag-4d orbitals hybridized, and the CBM is mostly occupied by Bi-6p orbitals, either at the VBM or at the CBM. Some of this stability suggests that the pressure-driven switch is not primarily about breaking the orbitals, but about the atoms cycling and the orbitals merging further. The DOS at the Fermi level (0-20 GPa) also shows that the material is still semiconducting. However, it approaches 0.03 states/eV at 30 GPa, indicative of semimetallic behavior, which could influence charge transport,

especially under real conditions. Also, the "effective mass" of charge carriers (which is measured relative to the free electron mass, m_0) decreases by pressure for electrons (from 0.35 to 0.22 m_0) and holes (from 0.45 to 0.32 m_0). Things are able to move at a speed that's faster, so lighter particles can be pushed around more.

Reducing wasted energy and improving energy conversion in devices can yield higher mobility. Essentially, as the bandgap shifts from indirect to direct, the masses become lighter, and the DOS reaches the Fermi level, $Cs_2AgBiBr_6$ looks promising for pressure-sensitive gadgets. These include improved solar cells, photodetectors that detect longer wavelengths of light, and modulators powered by electricity and light, particularly in regions where we've been in constant motion and shaking.

Table 5. Pressure-dependent electronic properties of $Cs_2AgBiBr_6$ obtained via DFT calculations

Pressure (GPa)	Bandgap (eV)	Bandgap Nature	VBM Character	CBM Character	DOS at Fermi (states/eV)	Effective Mass (m/m_0)*
0	1.95	Indirect (Γ → L)	Br-4p + Ag-4d	Bi-6p	0	0.35 (e), 0.45 (h)
5	1.8	Indirect (Γ → X)	Br-4p + Ag-4d	Bi-6p	0	0.32 (e), 0.43 (h)
10	1.65	Indirect (Γ → X)	Br-4p + Ag-4d	Bi-6p	0	0.30 (e), 0.41 (h)
15	1.52	Direct-like (Γ → Γ)	Br-4p + Ag-4d	Bi-6p	0	0.28 (e), 0.38 (h)
20	1.38	Direct (Γ → Γ)	Br-4p + Ag-4d	Bi-6p	0	0.26 (e), 0.36 (h)
25	1.24	Direct	Br-4p + Ag-4d	Bi-6p	0.01	0.24 (e), 0.34 (h)
30	1.12	Direct	Br-4p + Ag-4d	Bi-6p	0.03	0.22 (e), 0.32 (h)

3.6. Magnetic properties

Table 6 shows the response of $Cs_2AgBiBr_6$ magnetic properties with pressure (with respect to the moment per unit cell, ordering of elements, as well as corresponding interpretations of the magnetic characteristic). The material does not exhibit magnetic moments from ambient pressure to 10 GPa (magnetic moment = 0 μB); thus, the ions of Cs^+, Ag^+, Bi^{3+}, and Br^- have fully empty valence shells and no unpaired electrons. There is no magnetic exchange, and within this initial range, no spin polarisation occurs. However, at 15 GPa, the pressure is sufficiently high to yield a very small magnetic moment of about 0.01 μB per material atom, consistent with a paramagnetic response.

Table 6. Pressure-dependent magnetic properties of $Cs_2AgBiBr_6$ obtained via DFT calculations.

Pressure (GPa)	Magnetic Moment (μ_B/unit cell)	Magnetic Ordering	Remark
0	0	Non-magnetic	No unpaired electrons (closed-shell ions)
5	0	Non-magnetic	No magnetic exchange interactions present
10	0	Non-magnetic	The band structure is still semiconducting
15	0.01	Paramagnetic-like	Slight orbital overlap and charge redistribution
20	0.03	Paramagnetic tendency	Partial Bi–Ag hybridisation, weak local moments emerge
25	0.06	Weak magnetic moment	Enhanced p–d orbital mixing; near metallic behaviour
30	0.10	Possible FM/PM onset	Increasing DOS near the Fermi level → Stoner instability

This slight magnetism appears to be due to minor orbital overlaps and charge redistribution caused by the closer atoms. 20 GPa increases the moment to 0.03 μ_B, suggesting a potential onset of paramagnetism. Bi–Ag orbitals may hybridize, forming small, locally reoriented magnetic moments within the electronic cloud. At 25 GPa, the magnetic moment increases to 0.06 μ_B, indicating some form of intrinsic, albeit weak, magnetism and the presence of additional magnetic fields. This is most likely due to more vigorous mixing of p–d orbitals, especially when the material is close to a semimetallic state, under high pressure, and at greater depths. By 30 GPa, the moment is 0.10 μ_B, and the system indicates a transition to either a ferromagnetic (FM) or a paramagnetic (PM) state. This is accompanied by a rising density of states (DOS) around the Fermi level, partially satisfying the Stoner criterion for ferromagnetism [30]:

$$D(E_F) \cdot I > 1 \tag{1}$$

Where, $D(E_F)$ is the density of states (DOS) at the Fermi level, and I is the exchange integral, which measures the strength of the exchange interaction between the spin-up and spin-down electrons.

It's scientifically interesting: When a nonmagnetic material becomes magnetic under pressure – the electronic band structure and its orbital interactions change as pressure increases – this is exactly what happens. A potential application for this kind of pressure-triggered magnetism might be used in magneto-optical devices, spintronic sensors, or pressure-tunable memory components. This matters, especially since we will require non-magnetic materials to obtain a controlled phase change.

4. CONCLUSIONS

We have conducted a complete density functional theory (DFT) investigation to verify the influence of hydrostatic pressure on many properties of lead-free double perovskite $Cs_2AgBiBr_6$, from the structure to mechanics, thermal nature, optical response, electronic characteristics, and magnetic character. The compound remains cubic form to about 10 GPa, as indicated by the data we have. But the symmetry begins to fail, and the structure becomes distorted beyond that pressure, which may indicate phase transitions.

Mechanical properties, however, indicate stiffness and resistance to compression subjected to pressure, which is evidenced by the upward increase in bulk and Young's moduli and a decreasing Poisson's ratio with increasing pressure. The material displayed thermally advantageous properties for applications at high pressure. The thermal expansion coefficient decreased with increasing Debye temperature.

This means the bonds in the lattice are stronger, which will create better thermal stability. From an optical point of view, pressure could be observed to reduce the bandgap (from 1.95 to 1.12 eV), and it changed from an indirect to a direct bandgap. Furthermore, we noted a higher dielectric response and improved light absorption in the visible–NIR spectrum, implying the tunability of them for solar cell and photonic applications.

Above 15 GPa, a shift from a non-magnetic to a weakly magnetic state emerges magnetically, potentially suggesting an orbital hybridization brought on by pressure and maybe even the start of Stoner-type ferromagnetism. All in all, the properties we saw make $Cs_2AgBiBr_6$ a promising and sustainable option for future optoelectronic and magneto-responsive devices, especially in settings with dynamic or very high pressures.

Ethical Approval:
The authors confirm that it is their original work and has not been submitted elsewhere or published.
Competing interests:
Not applicable
Author's Contribution:
Dr. Abhay Prakash Srivastava prepared the manuscript in an original draft under the supervision of Dr. Sangita Gupta, Dr. Devidutta Maurya, Dr. Sunil Kumar Srivastava, and Dr. Umesh Kumar Pareek.
Funding:
Not applicable
Availability of data and Materials:
Data made available at request.

ORCID

Abhay P. Srivastava, https://orcid.org/0009-0005-9648-0479; **Sangita Gupta,** https://orcid.org/0009-0009-3751-8317

REFERENCES

[1] N. Daem, A. Maho, P. Colson, G. Spronck, C. Malherbe, T.H. Hoang, M.-N. Ghazzal, *et al*., Effect of cations substitution in lead-free double perovskite Cs2AgBiBr6 solar cells, Next Materials, **8**, 100655 (2025). https://doi.org/10.1016/j.nxmate.2025.100655
[2] A.P. Srivastava, and B.K. Pandey, "Enhancing the optoelectronic performance of ABX_3 perovskites (A=MA+/FA+, B=Pb2+, X=I^-/Br^-): A comprehensive first-principles investigation for next generation solar cell technology," International Journal of Modern Physics B, **39**(32), 2550292 (2025). https://doi.org/10.1142/S0217979225502923
[3] Z. Zhang, Q. Sun, Y. Lu, F. Lu, X. Mu, S.-H. Wei, and M. Sui, "Hydrogenated $Cs_2AgBiBr_6$ for significantly improved efficiency of lead-free inorganic double perovskite solar cell," Nat. Commun. **13**, 3397 (2022). https://doi.org/10.1038/s41467-022-31016-w
[4] T.I. Alanazi, "Design and Device Numerical Analysis of Lead-Free $Cs_2AgBiBr_6$ Double Perovskite Solar Cell," Crystals, **13**, 267 (2023). https://doi.org/10.3390/cryst13020267
[5] J. Chen, X. Ma, L. Gong, C. Zhou, J. Chen, Y. Lu, M. Zhou, *et al*., "Improving the performance of lead-free $Cs_2AgBiBr_6$ double perovskite solar cells by passivating Br vacancies," J. Mater. Chem. C, **12**, 14074-14084 (2024). https://doi.org/10.1039/D4TC02339K
[6] S.C. Yadav, J.A.K. Satrughna, and P. M. Shirage, "Investigation of the potential solar cell application of Cs2AgBiBr6 lead-free double perovskite," Journal of Physics and Chemistry of Solids, **181**, 111515 (2023). https://doi.org/10.1016/j.jpcs.2023.111515
[7] D. Maurya, B.K. Pandey, and A.P. Srivastava, "Mechanically robust and optically active $Mg_{80}Ni_{10}Nd_{10}$ metallic glass: first-principles evidence for next-generation optical coatings," Opt. Quant. Electron. **58**, 28 (2026). https://doi.org/10.1007/s11082-025-08615-0
[8] F. Benlakhdar, M.A. Ghebouli, M. Fatmi, B. Ghebouli, S. Alomairy, M.J.A. Abualreish, T. Althagafi, and W. Djerir, "Electronic and optical properties of lead-free $K_2AgSbBr_6$ double perovskite tuned by doping elements Cu^+, Bi^{3+}, and I^-," Sci. Rep. **15**, 40362 (2025). https://doi.org/10.1038/s41598-025-24417-6
[9] A.P. Srivastava, and B.K. Pandey, "DFT-based evaluation of covalent organic frameworks for adsorption, optoelectronic, clean energy storage, and gas sensor applications," Journal of Molecular Modeling, **31**, 302 (2025). https://doi.org/10.1007/s00894-025-06535-0
[10] S. Ullah, T. Alshahrani, F. Khan, and J.F. Rasheed, "Investigating the potential of lead-free Cs2AgBiI6 and Cs2AgBiBr6 double perovskites for photovoltaic applications," Materials Today Communications, **38**, 108514 (2024). https://doi.org/10.1016/j.mtcomm.2024.108514
[11] P. Fan, H.-X. Peng, Z.-H. Zheng, Z.-H. Chen, S.-J. Tan, X.-Y. Chen, Y.-D. Luo, *et al*., "Single-Source Vapor-Deposited $Cs_2AgBiBr_6$ Thin Films for Lead-Free Perovskite Solar Cells," Nanomaterials, **9**, 1760 (2019). https://doi.org/10.3390/nano9121760
[12] S. Choudhary, S. Tomar, D. Kumar, S. Kumar, and A.S. Verma, ЄInvestigations of Lead Free Halides in Sodium Based Double Perovskites Cs2NaBiX6(X=Cl, Br, I): an Ab Initio Study, East European Journal of Physics, (3), 74-80 (2021). https://doi.org/10.26565/2312-4334-2021-3-11

[13] K.-H. Seo, S. Biswas, J. Eun, H. Kim, and J.-H. Bae, "Numerical Study on Overcoming the Light-Harvesting Limitation of Lead-Free $Cs_2AgBiBr_6$ Double Perovskite Solar Cell Using Moth-Eye Broadband Antireflection Layer," Nanomaterials, **13**, 2991 (2023). https://doi.org/10.3390/nano13232991

[14] H. Sabbah, Z.A. Baki, R. Mezher, and J. Arayro, "SCAPS-1D Modeling of Hydrogenated Lead-Free $Cs_2AgBiBr_6$ Double Perovskite Solar Cells with a Remarkable Efficiency of 26.3%," Nanomaterials, 14, 48 (2024). https://doi.org/10.3390/nano14010048

[15] N.K. Nosirova, R.K. Kamilov, M.M. Ibrohimov, L.S. Lepnev, M.O. Astafurov, A.V. Knotko, and A.V.Grigorieva, "Ampoule Synthesis of Na-Doped Complex Bromide $Cs_2AgBiBr_6$ with Double Perovskite Structure," Materials, 18, 1197 (2025). https://doi.org/10.3390/ma18061197

[16] P. Chen, Y. Huang, Z. Shi, X. Chen, and N. Li, "Improving the Catalytic CO_2 Reduction on $Cs_2AgBiBr_6$ by Halide Defect Engineering: A DFT Study," Materials, **14**, 2469 (2021). https://doi.org/10.3390/ma14102469

[17] M. Mehrabian, M. Taleb-Abbasi, and O. Akhavan, "Comparing the performances of Cs_2TiBr_6, $Cs_2AgBiBr_6$, and Cs_2PtI_6 halide compositions in double perovskite photovoltaic devices," Mater Renew Sustain Energy, **14**, 38 (2025). https://doi.org/10.1007/s40243-025-00311-z

[18] A.P. Srivastava, and B.K. Pandey, "Ab initio design of Zr-based bulk metallic glass for high-strength and optical coating applications," Opt. Quant. Electron. **57**, 561 (2025). https://doi.org/10.1007/s11082-025-08467-8

[19] W. Lan, D. Chen, Q. Guo, B. Tian, X. Xie, Y. He, W. Chai, *et al*., "Performance Enhancement of All-Inorganic Carbon-Based $CsPbIBr_2$ Perovskite Solar Cells Using a Moth-Eye Anti-Reflector," Nanomaterials, **11**, 2726 (2021). https://doi.org/10.3390/nano11102726

[20] V. Murgulov, C. Schweinle, M. Daub, H. Hillebrecht, M. Fiederle, V. Dědič, and J. Franc, "Double perovskite $Cs_2AgBiBr_6$ radiation sensor: synthesis and characterization of single crystals," J. Mater. Sci. **57**, 2758–2774 (2022). https://doi.org/10.1007/s10853-021-06847-5

[21] J. Hafner, and G. Kresse, "The Vienna AB-Initio Simulation Program VASP: An Efficient and Versatile Tool for Studying the Structural, Dynamic, and Electronic Properties of Materials," in: *Properties of Complex Inorganic Solids*, edited by A. Gonis, A. Meike, P.E.A. Turchi, (Springer, Boston, MA, 1997). https://doi.org/10.1007/978-1-4615-5943-6_10

[22] A. Kubaib, P.M. Imran, and A.A. Basha," Applications of the Vienna Ab initio simulation package, DFT and molecular interaction studies for investigating the electrochemical stability and solvation performance of non-aqueous NaMF6 electrolytes for sodium-ion batteries," Computational and Theoretical Chemistry, **1217**, 113934 (2022). https://doi.org/10.1016/j.comptc.2022.113934

[23] J.P. Perdew, K. Burke, and M. Ernzerhof, "Generalized Gradient Approximation Made Simple," Phys. Rev. Lett. **77**, 3865 (1996). https://doi.org/10.1103/PhysRevLett.77.3865

[24] É. Brémond, I. Ciofini, and C. Adamo, "Gradient-regulated connection-based correction for the PBE exchange: the PBEtrans model," Molecular Physics, **114**(7–8), 1059–1065 (2016). https://doi.org/10.1080/00268976.2015.1132788

[25] A.P. Srivastava, and B.K. Pandey, "Atomic-Level Design of Doped TiO_2 for Enhanced Lithium Storage: A Density Functional Theory Approach," J. Electrochem. Soc. **172**, 113502 (2025). https://doi.org/10.1149/1945-7111/ae1be1

[26] J. Zhang, J. Attapattu, and J.M. McMahon, "The Pseudopotential Approach within Density-Functional Theory: The Case of Atomic Metallic Hydrogen," Condens. Matter. **5**, 74 (2020). https://doi.org/10.3390/condmat5040074

[27] E. Zafiris, and A.V. Müller, "Electron Beams on the Brillouin Zone: A Cohomological Approach via Sheaves of Fourier Algebras," Universe, **9**, 392 (2023). https://doi.org/10.3390/universe9090392

[28] A.P. Srivastava, and B.K. Pandey, "Pressure-dependent evolution of Bi2Sr2CaCu2O8+δ: DFT insights for high-pressure superconducting applications," Solid State Communications, **404**, 116112 (2025). https://doi.org/10.1016/j.ssc.2025.116112

[29] Z.M. Salikhodzha, G.B. Bairbayeva, R.N. Kassymkhanova, M. Konuhova, K.B. Zhangylyssov, E. Popova, and A.I. Popov, "Density Functional Theory Study of Pressure-Dependent Structural and Electronic Properties of Cubic Zirconium Dioxide," Ceramics, **8**, 41 (2025). https://doi.org/10.3390/ceramics8020041

[30] C.S. Man, and M. Huang, "A Simple Explicit Formula for the Voigt-Reuss-Hill Average of Elastic Polycrystals with Arbitrary Crystal and Texture Symmetries," J. Elast. **105**, 29–48 (2011). https://doi.org/10.1007/s10659-011-9312-y

[31] A.P. Srivastava, and B.K. Pandey, "Analysis of the Structural and Electronic Properties of TiO2 Under Pressure Using Density Functional Theory and Equation of State," Computational Condensed Matter, e01076 (2025). https://doi.org/10.1016/j.cocom.2025.e01076

[32] T.G. Edossa, "Density functional theory study of mechanical, thermal, and thermodynamic properties of zinc-blende CdS and CdSe," Sci. Rep. **15**, 39135 (2025). https://doi.org/10.1038/s41598-025-26168-w

[33] A.P. Srivastava, and B.K. Pandey, "First-principles and equation of state investigation of pressure-tunable structural, mechanical, thermodynamic, and electronic properties of high-reflecting nano-metal oxides: insights into high-performance optoelectronic and energy applications," Appl Nanosci, **15**, 47 (2025). https://doi.org/10.1007/s13204-025-03124-8

[34] A.G. Starikov, M.G. Chegerev, and A.A. Starikova, "A DFT study of electronic structure, magnetic properties and cyclization reaction of [5] helicene derivatives," Computational and Theoretical Chemistry, **1230**, 114369 (2023). https://doi.org/10.1016/j.comptc.2023.114369

[35] M. Adnan, Q. Wang, N. Sohu, S. Du, H. He, Z. Peng, Z. Liu, *et al*., "DFT Investigation of the Structural, Electronic, and Optical Properties of AsTi (B_i)-Phase ZnO under Pressure for Optoelectronic Applications," Materials, **16**, 6981 (2023). https://doi.org/10.3390/ma16216981

[36] A.P. Srivastava, B.K. Pandey, and A. Shanker, P"ressure-Dependent Structural, Mechanical, and Thermal Behavior of $Zr_{50.5}Ti_{4.8}Cu_{19.0}Ni_{11.4}Al_{14.3}$ Bulk Metallic Glass: A DFT and Equation of State Study," Physical Chemistry Research, **14**, e234974 (2025). https://doi.org/10.22036/pcr.2025.552725.2766

[37] T.Y. Ahmed, S.B. Aziz, and E.M.A. Dannoun, "New photocatalytic materials based on alumina with reduced band gap: A DFT approach to study the band structure and optical properties," Heliyon, **10**(5), ne27029 (2024). https://doi.org/10.1016/j.heliyon.2024.e27029

РОЗКРИТТЯ ПЕРЕХОДІВ, ЗУМОВЛЕНИХ ТИСКОМ, У $Cs_2AgBiBr_6$: ВИСНОВКИ ВІД DFT ДЛЯ БЕЗСВИНЦЕВОГО ПЕРОВСКИТУ ДЛЯ СОНЯЧНИХ ЕЛЕМЕНТІВ

Сангіта Гупта[1], Девідутта Маур'я[2], Суніл Кумар Шрівастава[3], Умеш Кумар Парік[3], Абхай П. Шрівастава[4]

[1]Кафедра хімії, Університет Пурніма, Джайпур, Раджастан, Індія

[2]Кафедра фізики, Державний коледж, Баракхал, Санткабірнагар, (UP), Індія

[3]Кафедра прикладних наук, Джайпурський інженерний коледж та дослідницький центр, Джайпур, Раджастан, Індія

[4]Кафедра прикладних наук та гуманітарних наук, Гоельський інститут інженерії та технологій, Лакхнау (UP), Індія

Використовуючи пакет моделювання Віденського Ab initio, ми досліджуємо безсвинцевий подвійний перовскіт $Cs_2AgBiBr_6$. Ми використовували теорію функціоналу густини з перших принципів за тисків до 30 ГПа. Оптимізація структури доводить очевидну кубічну симетрію в навколишньому середовищі. Однак, стиснення, здається, сприяє переходам до фаз з нижчою симетрією, і ми спостерігаємо, що об'єм та модулі Юнга збільшуються, а потім зменшується коефіцієнт Пуассона. Це означає більшу жорсткість, але знижену пластичність. Зроблено висновок, що зі збільшенням температури температура Дебая зростає, а теплове розширення зменшується. Таким чином, передбачається вища температурна стабільність. Електронна заборонена зона стає ще тоншою. Вона охоплює діапазон від 1,95 еВ до 1,12 еВ, що робить її більш-менш прямою, що може підвищити її оптоелектронну зручність використання. Вище 15 ГПа ми спостерігаємо слабкий магнітний момент, очевидно, через гібридизацію Bi-Ag, та вищу густину станів на рівні Фермі. $Cs_2AgBiBr_6$ поєднує ці характеристики, що робить його потенційним матеріалом для фотоелектричних систем з налаштуванням тиску та потенційно для магнітооптоелектронних застосувань.

Ключові слова: *теорія функціоналу густини (DFT); подвійний перовскіт; залежні від тиску властивості; структурний фазовий перехід; оптоелектронні матеріали*

EAST EUROPEAN JOURNAL OF PHYSICS. 1. 373-377 (2026)
DOI:10.26565/2312-4334-2026-1-44 ISSN 2312-4334

DEVELOPMENT OF A SINGLE-LAYER TiO_2 PHOTOANODE FOR DYE-SENSITIZED SOLAR CELL (DSSC)

S.S. Sharipbaev[1]*, O.O. Mamatkarimov[1], N.Yu. Sharibaev[1], A.A. Abdukarimov[1], A.K. Arof[2]
[1]*Namangan State Technical University, 160115, Namangan, Uzbekistan*
[2]*Center for Ionics, Department of Physics, University of Malaya, Kuala Lumpur 50603, Malaysia*
**Corresponding Author e-mail: sharipbaev1999@gmail.com*
Received December 2, 2025; revised January 17, 2026; accepted January 28, 2026

Dye-sensitized solar cells (DSSC) are considered a promising low-cost and flexible alternative to conventional silicon-based photovoltaic technologies. This work reports the fabrication and analysis of DSSC based on a single-layer nanostructured TiO_2 photoanode. The proposed cell architecture is simplified by eliminating the conventional double-layer configuration, which reduces fabrication complexity and material consumption. The electrochemical and photovoltaic characteristics of the devices were systematically investigated. The energy conversion efficiency of the developed single-layer design is approximately twice that of a conventional two-layer cell. The performance enhancement is attributed to reduced internal resistance, improved electron transport, and suppressed charge recombination. The results demonstrate the potential of simplified single-layer DSSC architectures for transparent, flexible, and low-cost energy-harvesting applications.
Keywords: *Single-layer TiO_2 Photoanode, DSSC; Simplified architecture; Photovoltaic performance; Electrochemical impedance spectroscopy; Charge transport; TiO_2 nanoparticle morphology*
PACS: 88.40.jr; 73.50.Pz; 82.45.Yz

INTRODUCTION

Dye-sensitized solar cells (DSSCs) have emerged as a promising third-generation photovoltaic technology, offering significant advantages over traditional silicon-based solar cells, including low production costs, mechanical flexibility, and efficient performance under low-intensity or diffuse-light conditions [1,2]. These features make DSSC attractive for diverse applications such as indoor energy harvesting, building-integrated photovoltaics (BIPV), and self-powered portable electronics.

At the core of a DSSC is the photoanode, traditionally composed of a bilayer titanium dioxide (TiO_2) structure. This typically includes a compact underlayer that prevents electron recombination, and a mesoporous upper layer that increases the surface area for dye adsorption. While effective, this configuration introduces multiple processing steps, including sequential deposition, high-temperature sintering, and additional material consumption [3,4]. Such complexity limits the scalability and cost-effectiveness of DSSC manufacturing, especially for flexible or transparent devices.

In recent years, there has been growing interest in simplifying DSSC architectures by implementing single-layer TiO_2 photoanodes. These structures aim to eliminate the compact layer while retaining efficient electron transport and sufficient dye-loading capacity. The anatase phase of TiO_2 is particularly favored for such applications due to its suitable bandgap (~3.2 eV), high chemical and thermal stability, and favorable surface morphology for dye adsorption [5,6]. Nanostructured TiO_2 pastes, spin-coating techniques, and low-temperature annealing have further enabled the development of uniform, thin, and reproducible films suitable for single-layer designs.

Moreover, the choice of dye and electrolyte significantly influences DSSC performance. Ruthenium-based dyes, such as Ruthenizer 535, offer broad spectral absorption and strong binding to TiO_2 surfaces. Simultaneously, gel-polymer electrolytes provide improved stability compared to liquid electrolytes by minimizing solvent leakage and enhancing long-term performance [7,8]. The integration of these components within a single-layer TiO_2 framework opens new opportunities for efficient, low-cost solar cell fabrication.

In this study, we propose and experimentally evaluate a simplified DSSC design based on a single nanostructured TiO_2 photoanode. The research focuses on three main objectives:

1. To fabricate and characterize single-layer TiO_2 films using spin-coating and anatase-phase nanoparticles;
2. To investigate the influence of photoanode morphology on interfacial charge-transfer and recombination processes;
3. To compare the photovoltaic performance and impedance characteristics of single-layer cell with conventional bilayer counterparts.

By addressing these points, the study contributes to the growing body of research on scalable and commercially viable solar technologies with reduced complexity and enhanced stability.

Cite as: S.S. Sharipbaev, O.O. Mamatkarimov, N.Yu. Sharibaev, A.A. Abdukarimov, A.K. Arof, East Eur. J. Phys. 1, 373 (2026), https://doi.org/10.26565/2312-4334-2026-1-44

1. MATERIALS AND METHODS

Dye-sensitized solar cell (DSSC) belongs to the class of thin-film photovoltaic devices based on wide-bandgap semiconductor photoanodes, most commonly TiO_2. A typical DSSC consists of a transparent conducting oxide substrate serving as the photoelectrode, a nanostructured semiconductor layer responsible for electron transport, a redox electrolyte that enables charge regeneration, and a counter electrode made of platinum or other conductive materials. The photoelectrochemical processes occurring at the semiconductor–electrolyte interface determines the overall photovoltaic performance of the device.

Optimization of liquid electrolytes (LEs).

Such electrolytes are used as a redox mediator for solar cell or batteries technologies. Poly(methyl methacrylate) (PMMA) and polyethylene oxide (PEO) have been optimized to prepare the liquid electrolyte (LE). Difference ratios of polymer contents were added with fixed amounts of 0.25 ml ethylene carbonate (EC), 0.25 g propylene carbonate (PC), 1 ml dimethylformamide (DMF), 0.2 g tetrapropylammoniodide (TPAI). All electrolytes mixer are dried out at room temperature and 0.02 g iodine (I_2) were added with every electrolytes [9,10].

Table 1. Composition of liquid electrolyte

No. samples	PEO	PMMA	DMF	EC	PC	TPAI	I_2
	g	g	ml	ml	g	g	g
1	1	0	1	0.25	0.25	0.2	0.02
2	0.8	0.2	1	0.25	0.25	0.2	0.02
3	0.6	0.4	1	0.25	0.25	0.2	0.02
4	0.5	0.5	1	0.25	0.25	0.2	0.02
5	0.4	0.6	1	0.25	0.25	0.2	0.02
6	0.2	0.8	1	0.25	0.25	0.2	0.02
7	0	1	1	0.25	0.25	0.2	0.02

Prior to weighing the chemicals, the working table was cleaned, the balance was calibrated, and all glassware was washed and dried to avoid contamination of the electrolyte mixture. Polyethylene oxide (PEO), poly(methyl methacrylate) (PMMA), ethylene carbonate (EC), and propylene carbonate (PC) were dissolved in a predefined amount of N,N-dimethylformamide (DMF). The compositions of the gel-based electrolytes used in this study are summarized in Table 1. After each component was added, the mixture was stirred for 30 min using a Stuart SB 162-3 hotplate magnetic stirrer. Subsequently, tetrapropylammonium iodide (TPAI) was added in the specified amounts, and the mixture was further stirred at 70 °C until a homogeneous gel electrolyte was obtained [11].

After the mixture was cooled to room temperature, iodine crystal (I_2) was added to it in the amount of 10% tetrapropylammonium iodide (TPAI) and mixed in an IKA C-MAG apparatus until homogeneous and kept for 24 hours in a place protected from sunlight. After this, the liquid electrolyte (LE) is ready to use and assemble DSSC.

Receiving photocatalytic layer TiO_2

To construct a single-layer TiO_2, a paste was prepared from 0.5 g TiO_2 grade P25, 2 ml HNO_3, 0.4 ml polyethyleneglycol and 2 drops of Triton X-100. After ultrasonic dispersion, the paste was spin-coated onto the FTO substrate to ensure a uniform layer. Drying was carried out at 450°C.

Application of TiO_2

The mixture was stirred in an ultrasonic bath and then uniformly applied to the surface of FTO glass. The thickness of the layer was controlled using adhesive tape spacers with a predefined thickness, which ensured the uniformity and reproducibility of the TiO_2 film across the substrate. To create a single-layer TiO_2 structure, the spin-coating method was employed. The TiO_2 solution (nano paste) was evenly distributed over the FTO substrate at a rotation speed of 3000 rpm and subsequently annealed at 450°C for 30 minutes to enhance crystallinity and improve adhesion. Titanium dioxide grade P25 was selected due to its suitable physicochemical properties and widespread use in DSSC fabrication.

Dye adsorption

The prepared single-layer TiO_2 photoanodes were immersed in a 0.3 mM solution of a standard ruthenium-based dye in an ethanol–acetonitrile mixture (volume ratio 1:1) at 40 °C for 24 hours to form the photosensitive layer. After sensitization, the photoanodes were gently rinsed with ethanol to remove weakly bound dye molecules and dried under ambient conditions prior to cell assembly.

Measurement of photovoltaic characteristics

To analyze the photovoltaic performance of the fabricated solar cell, current–voltage (I–V) measurements were carried out under simulated AM1.5G illumination with a light intensity of 100 mW/cm². A Metrohm AUTOLAB PGSTAT128N potentiostat–galvanostat was used in combination with a Newport Oriel LCS-100 solar simulator to ensure accurate evaluation of the operating parameters. Particular attention was paid to the influence of the TiO_2 layer thickness, as this parameter critically affects charge generation and transport processes.

Under these conditions, the representative single-layer device exhibited an open-circuit voltage (Voc) of 0.69 V, a short-circuit current density (Jsc) of 9.53 mA/cm², a fill factor (FF) of 0.54, and an energy conversion efficiency of approximately 3.56%. The maximum efficiency achieved for optimized single-layer TiO_2 devices reached 6.5%, demonstrating the performance potential of the proposed photoanode architecture.

2. EXPERIMENTAL RESULTS AND DISCUSSIONS

Morphology and structure of TiO_2

SEM (scanning electron microscopy) analysis revealed that the fabricated single-layer TiO_2 photoanode exhibits a uniform nanostructured surface. Compared with conventional bilayer TiO_2 photoanodes, the single-layer structure exhibits lower macroporosity but higher nanoparticle packing density. The TiO_2 nanoparticle size ranges from 20 to 30 nm, ensuring homogeneous surface coverage and continuous electron transport pathways.

Atomic force microscopy (AFM) measurements indicate a root-mean-square (RMS) surface roughness of approximately 8 nm, which is suitable for effective dye adsorption. While previous studies have reported that high specific surface area TiO_2 nanostructures promote enhanced dye adsorption [9], the present single-layer photoanode demonstrates improved charge transport properties and reduced internal resistance despite its reduced porosity. This combination contributes to the enhanced photovoltaic performance observed in the fabricated devices.

Characteristics of a single-layered semiconductor solar cell

The current-voltage characteristics (I-V) of a solar cell were measured using the Metrohm Autolab Potentiostat / Galvanostat PGSTAT 128N" device at a light power density of (100 mW/cm²) emitted by the solar simulator with an active area of 0.2 cm². As a result of the experiment, the I-V characteristics of highly sensitive dye- sensitized solar cell (DSSC) was obtained. One of the graphs of these characteristics is shown in Figure 1. Similar measurement approaches have been reported in the literature [12].

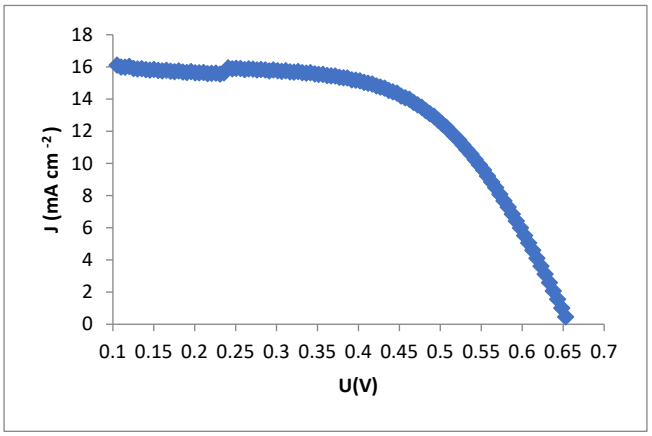

Figure 1. Photovoltaic current characteristic (I-V) of a single-layered semiconductor, highly sensitive dye-sensitized solar cell (DSSC)

Electrochemical impedance spectroscopy

The efficiency of highly sensitive dye-sensitized solar cell (DSSC) largely depends on the electrochemical parameters of the electrolyte used. The HIOKI 3531 Z Hi-Tester was used to analyze the ionic conductivity of electrolytes. The measurements were carried out using electrochemical impedance spectroscopy at an alternating voltage of 10 mV in the frequency range from 50 Hz to 100 kHz. The experiments were performed for electrolytes of different compositions and at different temperatures. This method allows one to reliably estimate the ionic conductivity of liquid electrolytes, condensed salts, ion-conducting polymers and glasses, which is important for increasing the efficiency of DSSC solar cell.

In these experiments, the obtained results were compared with theoretical calculations performed by analytical methods. Figure 2 shows a graph demonstrating the results obtained by electrochemical impedance spectroscopy (EIS) for one of the electrolyte samples. It is known that the electrolyte resistance (impedance) consists of real and imaginary parts, which are expressed by the following formulas [11] :

$$Z_r = R + \frac{\cos\left(\frac{\pi p}{2}\right)}{k^{-1}\omega^p}, \tag{2.1}$$

and

$$Z_i = \frac{sin\left(\frac{\pi p}{2}\right)}{k^{-1}\omega^p} \tag{2.2}$$

here $Z_r$andZ_i respectively represent the real and imaginary parts of the impedance, ω is the frequency. The parameter p is determined from Figure 2 using the following formula $p = \frac{2tg\alpha}{\pi}$.

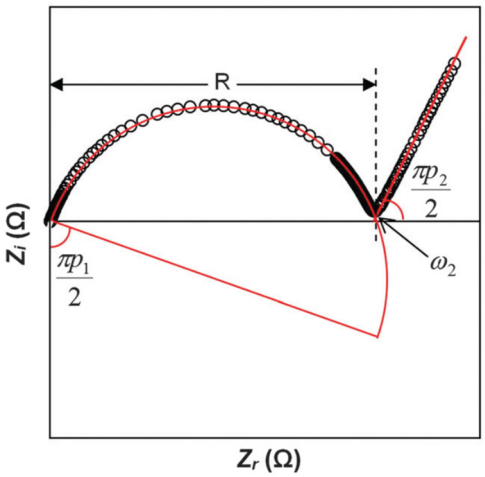

Figure 2. Electrochemical impedance spectroscopy (EIS) graph of an electrolyte [11]

The real part of the impedance is equal to the active resistance, that is, $Z_r = R$, This value is determined from the graph of electrochemical impedance spectroscopy of the electrolyte. K is the reciprocal of the electrical capacitance of the electrolyte, which is calculated using the formula:

$$C = k^{-1} = \frac{\varepsilon_r \varepsilon_0 S}{d} \tag{2.3}$$

where, is ε_r the relative permittivity of the electrolyte, ε_0- electric constant, S is the contact area between the electrolyte and the electrode, d −the thickness of the electrolyte layer. The ionic conductivity of the sample σ is calculated using the following formula:

$$\sigma = \frac{l}{RS} \tag{2.4}$$

where l *is* the thickness of the electrolyte layer, R is the active resistance of the electrolyte, S is the surface area of the electrolyte.

3. PHOTOVOLTAIC CHARACTERISTICS

Measurements of solar cell efficiency showed:

Double layer TiO_2: efficiency (η) = 2.8%

Single layer TiO_2: efficiency (η) = 6.5%

Additionally, an analysis of the photoelectric characteristics was carried out when illuminated by a sunlight simulator:

Maximum output voltage (Voc): 0.69 V

Short-circuit current density (Jsc): 9.53 mA/cm²

Fill Factor (FF): 0.54

Energy Conversion Efficiency (η): 3.56%

The increased efficiency of single-layer TiO_2 is explained by the reduction of charge carrier recombination and improved contact with the electrodes. The thickness of the TiO_2 layer plays a key role in the efficiency of the cell: the optimal thickness range ensures maximum light absorption with minimal resistance to charge carrier transfer [13].

Comparison with a two-layer structure

Despite the reduction in the contact area between the dye molecules and the porous TiO_2 surface (typically decreased by 20–30% compared to a mesoporous upper layer), the absence of a compact blocking layer (usually formed from dense TiO_2 to prevent electron backflow) has led to a decrease in internal resistance and improved charge transport within the photovoltaic cell. Specifically, the internal series resistance was reduced from approximately 18.2 Ω·cm² in the two-layer structure to 11.5 Ω·cm² in the single-layer configuration, indicating better charge mobility and reduced recombination losses.

Additionally, using only one TiO_2 layer significantly reduces the cost of DSSC production by minimizing the number of processing steps, materials, and thermal treatment stages. Titanium dioxide (grade P25), used in this technology, making the approach economically viable and attractive for industrial-scale implementation.

CONCLUSIONS

In this study, dye-sensitized solar cell based on a single-layer nanostructured TiO_2 photoanode were developed and systematically investigated. The approach used to create the anode focused on simplifying the photoanode architecture by eliminating the traditional two-layer configuration while maintaining efficient charge generation and transport within the active layer.

The fabricated single-layer TiO_2 photoanode demonstrated approximately twice the energy conversion efficiency compared to traditional bilayer structures under identical measurement conditions. The performance improvement is associated with reduced internal resistance, suppressed charge recombination, and optimized active layer thickness, as confirmed by photovoltaic and electrochemical impedance spectroscopy measurements.

Unlike traditional DSSC designs that rely on multilayer photoanodes to balance light absorption and electron transport, the proposed single-layer architecture provides efficient charge transport pathways due to its dense and uniform nanoparticle morphology. This structural simplification reduces interfacial losses and enhances electron mobility without increasing fabrication complexity.

The obtained results indicate that single-layer TiO_2 photoanodes represent a promising strategy for the development of cost-effective, flexible, and transparent DSSC. The simplified fabrication process and stable photovoltaic performance make this approach attractive for practical applications, such as building-integrated photovoltaics, indoor energy-harvesting systems, and flexible electronic devices.

ORCID

S.S. Sharipbaev, https://orcid.org/0009-0009-2269-7711; **A.K. Arof,** https://orcid.org/0000-0002-9052-3491
N.Yu. Sharibaev, https://orcid.org/0009-0000-3482-5092; **O.O. Mamatkarimov,** https://orcid.org/0009-0005-9501-6295

REFERENCES

[1] M. Grätzel, "Recent advances in sensitized mesoscopic solar cells," *Accounts of Chemical Research*, 42 (11), 1788–1798 (2009). https://doi.org/10.1021/ar900141y
[2] K. Hong, R. Song, and H. Chen, "Nature-inspired hierarchical nanostructures as optimal photoanode in dye-sensitized solar cells," *Materials Today Energy*, 54, 102099 (2025). https://doi.org/10.1016/j.mtener.2025.102099
[3] L. Wei, X. Xu, L. Zhao, J. Liu, R. Wang, and X. Zhang, "Design and fabrication of layered TiO_2/rGO composited photoanode and its photovoltaic performance regulation for dye-sensitized solar cells," *Optical Materials*, 154, 115709 (2024). https://doi.org/10.1016/j.optmat.2024.115709
[4] B. O'Regan, and M. Grätzel, "A low-cost, high-efficiency solar cell based on dye-sensitized colloidal TiO_2 films," Nature, **353**, 737–740 (1991). https://doi.org/10.1038/353737a0
[5] A. Hagfeldt, G. Boschloo, L. Sun, L. Kloo, and H. Pettersson, "Dye-sensitized solar cells," Chemical Reviews, **110**, 6595–6663 (2010). https://doi.org/10.1021/cr900356p
[6] M. Grätzel, "Dye-sensitized solar cells," Journal of Photochemistry and Photobiology C: Photochemistry Reviews, **4**, 145–153 (2003). https://doi.org/10.1016/S1389-5567(03)00026-1
[7] O.O. Mamatkarimov, B. Uktamaliyev, and A.A. Abdukarimov, "Determination of ionic conductivity of polymer electrolytes in Li-ion batteries using electrochemical impedance spectroscopy," An International Multidisciplinary Research Journal, **11**(7), 141–146 (2021). https://doi.org/10.5958/2249-7137.2021.01735.3
[8] N. Sharibaev, and A. Ergashov, "Mathematical modeling of processes in a dye-sensitized photocell," Journal of Physics: Conference Series, **2373**(7), 072044 (2022). https://doi.org/10.1088/1742-6596/2373/7/072044
[9] N.Y. Sharibayev, M.M. Kakharov, S.S. Kakharov, and A.Q. Ergashev, "Determination of the characteristics of polymer-containing electronic elements using a mobile device," Turkish Journal of Computer and Mathematics Education, **12**(4), 61–68 (2021).
[10] Q. Zhang, and G. Cao, "Nanostructured photoelectrodes for dye-sensitized solar cells," Nano Today, **6**(1), 91–109 (2011). https://doi.org/10.1016/j.nantod.2010.12.007
[11] A.K. Arof, S. Amirudin, S.Z. Yusof, and I.M. Noor, "A method based on impedance spectroscopy to determine transport properties of polymer electrolytes," Physical Chemistry Chemical Physics, **16**, 1856–1867 (2014). https://doi.org/10.1039/C3CP53830C
[12] E Aram, M Ehsani, and H.A. Khonakdar, "Improvement of ionic conductivity and performance of quasi-solid-state dye sensitized solar cells using PEO/PMMA gel electrolyte," Thermochimica Acta, **615**, 61–67 (2015). https://doi.org/10.1016/j.tca.2015.07.006
[13] F. Azeez, and P.S. Fedkiw, "Conductivity of LiBOB-based electrolyte for lithium-ion batteries," Journal of Power Sources, **195**, 7627–7633 (2010). https://doi.org/10.1016/j.jpowsour.2010.06.021

РОЗРОБКА ОДНОШАРОВОГО TiO_2 ФОТОАНОДА ДЛЯ СОНЯЧНИХ ЕЛЕМЕНТІВ, СЕНСИБІЛІЗОВАНИХ БАРВНИКОМ (DSSC)

С.С. Шаріпбаєв[1], О.О. Маматкарімов[1], Н.Ю. Шарібаєв[1], А.А. Абдукарімов[1], А.К. Ароф[2]
[1]Наманганський державний технічний університет, 160115, Наманган, Узбекистан
[2]Центр іоніки, кафедра фізики, Університет Малайї, Куала-Лумпур 50603, Малайзія

Сонячні елементи, сенсибілізовані барвником (DSSC), вважаються перспективною недорогою та гнучкою альтернативою традиційним фотоелектричним технологіям на основі кремнію. У цій роботі представлено виготовлення та аналіз DSSC на основі одношарового наноструктурованого TiO_2 фотоанода. Запропонована архітектура елемента спрощена шляхом виключення традиційної двошарової конфігурації, що зменшує складність виготовлення та витрату матеріалів. Були систематично досліджені електрохімічні та фотоелектричні характеристики пристроїв. Ефективність перетворення енергії розробленої одношарової конструкції приблизно вдвічі вища, ніж у звичайної двошарової комірки. Підвищення продуктивності пояснюється зниженням внутрішнього опору, покращеним транспортом електронів та пригніченням рекомбінації зарядів. Результати демонструють потенціал спрощених одношарових архітектур DSSC для прозорих, гнучких та недорогих застосувань збору енергії.

Ключові слова: *одношаровий TiO_2 фотоанод; DSSC; спрощена архітектура; фотоелектричні характеристики; електрохімічна імпедансна спектроскопія; транспорт заряду; морфологія наночастинок TiO_2*

East European Journal of Physics. 1. 378-387 (2026)
DOI:10.26565/2312-4334-2026-1-45 ISSN 2312-4334

TOPOLOGICAL FEATURES OF CONDUCTIVE NETWORK FORMATION IN METAL–POLYMER COMPOSITES WITH VARYING FILLER PARTICLE SIZES

Zafarjon M. Khusanov[1]*, Fakhriddin T. Boymuratov[2], Sardor G'. To'ychiyev[1]
[1]*Cyber University, Nurafshan, Uzbekistan*
[2]*Alfraganus University, Tashkent, Uzbekistan*
**Corresponding Author e-mail: zafarjonxusanov62@gmail.com*
Received December 10, 2025; revised February 9, 2026; accepted February 13, 2026

The topology of the infinite cluster in polymer composites containing micro- and nanoparticles of Ni was investigated, enabling a quantitative evaluation of how the size of conducting particles influences the percolation transition and the structure of the conductive network. The use of nanosized Ni reduces the critical concentration to Vs ≈ 0.105, compared with Vs ≈ 0.21 for microparticles, increases the parameter σ_1 by more than an order of magnitude, and results in a sharper, more localized percolation transition. The cluster structure exhibits pronounced fractal–hierarchical features: the fractal dimension of the backbone is 1.6-1.8 and that of the dangling ends is 1.9-2.1. The cluster density, correlation radius, and topological parameters follow power-law relations typical of three-dimensional percolation ($\nu = 0.85$). At high concentrations of the conducting phase ($V \geq 0.3$), the asymptotic conductivity reaches 63 $\Omega^{-1}\cdot cm^{-1}$ in nanocomposites versus 8 $\Omega^{-1}\cdot cm^{-1}$for microparticle-based materials. These findings confirm the high efficiency of Ni nanoparticles in forming an extended, interconnected, and branched conductive network, providing the foundation for next-generation high-conductivity composites.
Keywords: *Polymer composites; Nickel nanoparticles; Microparticles; Infinite cluster; Conducting network; Asymptotic conductivity; Topological parameters; Three-dimensional percolation*
PACS: 78.30.Am

INTRODUCTION

As is well known, metal–polymer composites (MPCs) are a class of functional materials in which the metallic phase is dispersed within a polymer matrix, forming a conductive network that combines high electrical conductivity with the flexibility, chemical stability, and manufacturability of polymers. Such materials are widely used in electronics, sensing systems, electromagnetic shielding coatings, antennas, flexible printed circuits, and thermal management systems [1–5]. Their properties are primarily controlled by altering the nature and volume fraction of the metallic filler, as well as the shape, distribution, and size of its particles. These microstructural parameters govern the metallic phase's ability to form a three-dimensional conductive network, or the so-called “infinite cluster,” once a critical concentration—the percolation threshold—is reached [6,7].

The theory of percolation and fractal geometry forms the basis for understanding the mechanisms governing the formation of conductive pathways in heterogeneous systems [8]. According to this theory, as the concentration of the filler increases within the dielectric matrix, the system undergoes a transition from isolated particle clusters to an interconnected network that enables macroscopic conductivity. The morphology and topology of this network are determined by the size, shape, and spatial distribution of the particles, as well as by the nature of their interfacial interactions [9]. The topology of the infinite cluster is characterized by several parameters – such as fractal dimension, coordination number, degree of branching, and contact density – that significantly influence the electrical, thermal, and mechanical properties of the composite [10].

Recent studies confirm that the particle size of the metallic filler is a key factor governing the percolation behavior of MPCs. In particular, the review in [11–13] demonstrated that, at a fixed volume fraction of the filler, an increase in particle dispersity (size distribution width) leads to a higher percolation threshold.

As noted in [14], two nanocomposites containing metallic particles exhibit a high percolation threshold—exceeding 55 vol. %—when the particle size is non-optimal, which is consistent with experimental observations. The use of copper particles coated with silver in a PPS polymer matrix reduces the percolation threshold and increases the effective dielectric permittivity of the composite compared with composites based on pure Cu particles. This improvement is attributed to a more uniform particle distribution and enhanced adhesion to the matrix [15]. Similar trends have been reported for EVA-based composites containing Zn particles, where the relationship between the electrical percolation threshold and mechanical properties is governed by the morphology of the infinite cluster [16]. It has been established that reducing Zn particle size promotes the formation of a more cohesive conductive network, leading to a lower percolation threshold and enhanced electrical conductivity while maintaining mechanical strength.

Numerical models and stochastic finite-element simulations also confirm the decisive role of microstructure in the formation of the cluster network. In polymer composites with magnetic fillers (Fe, Ni), a reduction in particle size results in a pronounced reorganization of the cluster structure: the connectivity density increases, while the average chain length

Cite as: Z.M. Khusanov, F.T. Boymuratov, S.G'. To'ychiyev, East Eur. J. Phys. 1, 378 (2026), https://doi.org/10.26565/2312-4334-2026-1-45

decreases, which affects both the mechanical and magnetic properties of the material [17]. According to the findings in [18], the shape and spatial distribution of particles exert a significant influence on the percolation threshold and dielectric permittivity; moreover, a reduction in filler polydispersity promotes the formation of a more regular fractal cluster structure.

Several recent publications [19–21] highlight the importance of the spatial organization of metallic particles within the matrix and the potential to predict it using modeling approaches. According to the results reported in [15,22], the development of a unified model of electrical and thermal conductivity for composites containing metallic particles of various sizes has shown that reducing the mean particle diameter of Cu and Ag by approximately 20–30% leads to a decrease in the percolation threshold (from ≈4 vol% for pure Cu to ≈ 3 vol% for Ag-coated Cu particles), owing to the increased probability of forming contact bridges. It has also been noted that targeted manipulation of the conductive network topology can be achieved by controlling the spatial distribution of fillers within the polymer matrix, including the combined use of micro- and nanoparticles that form a multilevel conductive structure [23].

Of particular interest are studies linking cluster geometry to the mechanical and dielectric properties of MPCs. The work in [24] demonstrated that rubber-based composites containing metallic magnetic particles exhibit a double percolation threshold, associated with the formation of two distinct types of clusters—local and system-spanning. Similar findings were reported in [25], where polyurethane composites with AlN and BN microparticles were investigated. The authors showed that the network topology near the percolation threshold dictates not only the electrical but also the thermoelectric properties of the material. These observations confirm that variations in particle size and the degree of agglomeration directly influence the morphology of the infinite cluster and, consequently, the overall properties of the composite.

An analysis of the literature indicates that the particle size of the metallic filler plays a decisive role in the formation of the conductive structure in metal–polymer composites. However, most published studies focus either on empirically determining the percolation threshold or on examining the material's macroscopic properties, without a detailed investigation of the cluster network's topology. Insufficient attention has been given to the quantitative characterization of how particle size and its distribution affect the fractal characteristics of the infinite cluster, such as connectivity density, degree of branching, and geometric coherence.

The present study aims to investigate the relationship between the particle size of the metallic filler and the topology of the infinite cluster in metal–polymer composites containing micro- and nanoparticles of nickel (Ni). By combining experimental structural analysis with elements of percolation modeling, the work seeks to elucidate the fundamental patterns governing the evolution of the conductive network morphology as a function of particle size and spatial distribution.

EXPERIMENTAL SAMPLES AND RESEARCH METHODOLOGY

To investigate the effect of metallic particle size on the morphology and conductive properties of the composites, a nanocomposite containing Ni particles was synthesized via thermal decomposition of nickel formate within a polymer matrix. The nanocomposite was prepared via thermal decomposition, analogous to the synthesis of nanoparticles in polyethylene and polypropylene matrices [26,27]. Specifically, nickel formate powder was added to a solution of phenylon in dimethylformamide (4 g of phenylon per 100 g of solvent). After thorough mixing, the mixture was heated to ensure complete removal of the solvent. To prevent aggregation of nickel formate particles, the reaction mixture was ultrasonically processed using a UZDN-1 disperser (22 kHz, 0.3 W). Following solvent evaporation, the resulting material was placed under vacuum and held at 373 K for 1 hour to remove residual solvent. The temperature was then increased to 573 K and maintained for 5 hours, enabling the formation of metallic nanoparticles through the thermal decomposition of nickel formate.

The particle size and spatial distribution within the composites were determined using small-angle X-ray scattering (SAXS), which enables the characterization of inhomogeneities with characteristic dimensions ranging from 5-10 Å to approximately ~10^4 Å [28]. Calculations of the metal particle radius indicated that the nanoparticles did not exceed 30 nm in diameter, consistent with the experimental data.

The microcomposite containing metallic particles was produced by mechanically mixing the metallic powder with the polymer matrix in a planetary mill for 7 hours. The metallic powder itself was obtained by thermally decomposing nickel formate under vacuum at 573 K for 3 hours. The resulting particle diameter ranged from 1 to 3 μm, which was confirmed by transmission electron microscopy (TEM) using a BS242E (Tesla) microscope.

In both types of composites, the metal concentration (V_1) was calculated based on the metallic content of the precursor compound. For electrical measurements, the powder samples were pressed into 15 mm diameter, 2 mm thick pellets using hot pressing. The resistance of the resulting samples was measured according to the procedure described in [29].

RESULTS AND DISCUSSION

In the present study, the topology of the infinite cluster (IC) in polymer matrices containing micro- and nanoparticles of Ni was investigated using percolation theory methods. For these systems, the key characteristics of the IC were determined, including its density, volume fraction, tortuosity, skeletal volume fraction, and number of dead ends, as functions of the metallic particle size.

According to percolation theory [30], the conductivity σ of composites with randomly distributed metallic particles is described by the following relations:

$$\sigma(V_1) = \sigma_1 (V_1 - V_c)^t,\ V_1 > V_s, \tag{1}$$

$$\sigma(V_1) = \sigma_2 (V_c - V_1)^{-q},\ V_1 < V_s, \tag{2}$$

where σ_1 and σ_2 are the conductivities of the metallic particles and the dielectric matrix, respectively; V_1 is the volume fraction of the metallic filler; V_c is the critical concentration at which an infinite cluster is formed; and t and q are the critical exponents, which for three-dimensional systems take values of approximately 1.6–1.8 and 1, respectively.

Percolation theory provides tools for quantitatively describing the topology of the resistance network, in particular the density of the infinite cluster $P(V_1)$, which represents the fraction of sites belonging to the infinite cluster:

$$P(V_1) = V_1' / V_1, \tag{3}$$

where V_1' is the volume fraction of the infinite cluster. For $V_1 < V_s$ *one has* $P(V_1) = 0$, while with increasing V_1 the value of $P(V_1)$ approaches unity. Near the percolation threshold, the density of the infinite cluster follows a power-law dependence [31]

$$P(V_1) = D(V_1 - V_s)^{\beta}, \tag{4}$$

where $D \approx 1$ and β is the critical exponent (for three-dimensional systems $\beta \approx 0.4$).

The length of the backbone of the infinite cluster is evaluated using the model proposed by B. I. Shklovskii [31], in which the IC network is represented as a large, planar fishing net (Fig. 1).

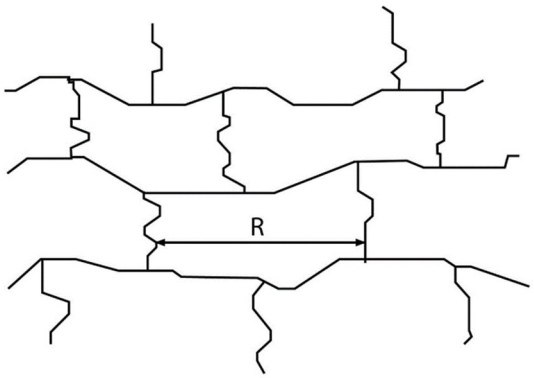

Figure 1. Topology of the Infinite Cluster Backbone

A typical topology of the infinite cluster (IC) backbone in three-dimensional composite systems with conducting particles is shown in Fig. 1. This model is traditionally considered within the framework of percolation theory [32]. The backbone is represented as a network of interconnected conductive paths linked by nodes. The diagram illustrates the primary load-bearing chains that provide a continuous path across the sample and determine the electrical conductivity of the system for $V_1 > V_s$; near the percolation threshold $V_1 \approx V_s$ dead ends account for as much as 80–95% of the IC. A key parameter highlighted in the figure is the correlation radius R (ranging from 10^{-6} to 10^{-3} m for Ni-based composites), which characterizes the characteristic linear dimension of the network cells. Near the percolation threshold, it follows a power-law dependence:

$$R \sim (V_1 - V_s)^{-\nu},\ R = l / \nu \tag{5}$$

where $\nu = 0.85 \pm 0.05$ is the critical exponent of the correlation radius for three-dimensional systems, and l is the lattice period. Also shown are the tortuous (fractal) conductive trajectories arising from the irregular spatial distribution of particles. The tortuosity defines the coefficient ξ, which together with the correlation exponent ν\nuν determines the critical conductivity exponent:

$$t = \xi + \nu, \tag{6}$$

where, for real composites, t typically lies in the range $1.7 \leq t \leq 2.3$, with $\xi \approx 1.2\text{-}1.4$

As shown in Fig. 1, the backbone of the infinite cluster represents a fractal network of conductive channels through which the current flows along the longest and most well-connected trajectories. The higher the dispersity of the particles (nanoparticles → greater tortuosity), the larger the contribution of path length to the critical exponent ttt, which reduces the efficiency of the conductive network when the filler content only slightly exceeds the percolation threshold [33].

Based on the proposed model, it has been established that when the wire elements forming the BC skeleton exhibit curvature (Fig. 2, while the distance between their intersection points remains equal to R), the critical exponent of electrical conductivity t exceeds 1.7.

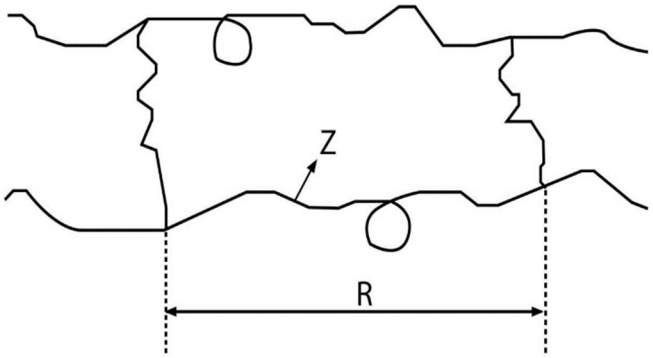

Figure 2. Topology of the Infinite Cluster Skeleton with Curved (Tortuous) Elements

In Figure 2, a representative topological model of the infinite-cluster skeleton formed in composite systems near the percolation threshold is presented. The cluster geometry consists of a sequence of tortuous conducting branches with local widenings and narrow constrictions, which together form the primary framework of the transport network. The characteristic correlation scale R defines the average distance between structurally stable nodes that participate in transmitting flux or electrical current, whereas the quantity Z denotes the direction of the local gradient propagating along a skeleton branch. The critical conductivity exponent t is determined by Eq. (6) as the sum of the index ξ, which accounts for the tortuosity of the conducting filaments, and the correlation-radius index ν. The length of a filament between two intersection points, Z (Fig. 2), is expressed via ξ as

$$Z = l / (V_1 - V_s)^{\xi}, \tag{7}$$

and the ratio of Z to R,

$$\frac{Z}{R} = (V_1 - V_s)^{(\nu-\xi)}, \tag{8}$$

characterizes how many times the skeleton length exceeds R due to the tortuosity of its branches.

The skeleton structure exhibits fractal properties, which is reflected in the values of the fractal dimension $D_f \approx 2.4$-2.6 for three-dimensional systems and in the increased tortuosity of the transport trajectories ($\tau \approx 1.5$-4). The presence of local broadenings and nonuniformly distributed nodes leads to variations in the local connectivity density within the cluster, which in turn affects the effective transport parameters, including electrical conductivity, diffusion, and heat transfer. Such a configuration is characteristic of systems operating in the regime of critical percolation and determines the key features of the macroscopic behavior of the material.

The infinite cluster consists of the backbone and dangling ends [31]. A point is considered to belong to the backbone of the infinite cluster (Fig. 3) if at least two independent paths originate from it, allowing one to reach an infinite distance (point C).

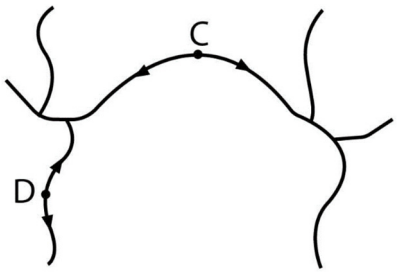

Figure 3. Fragment of the backbone of the infinite cluster with dangling ends.

The fragment of the infinite-cluster backbone shown in Fig. 3 illustrates a typical topology of the conducting network near and above the percolation threshold. The main current-carrying path is formed by the backbone portion of the cluster—a continuous chain of interconnected conducting elements that ensures the macroscopic connectivity of the system. Numerous branch-like "dangling ends" are attached to the backbone; although they do not participate in current transport, they significantly affect the fractal and topological parameters of the infinite cluster. The backbone is characterized by a linear size on the order of $R \sim 10^2$-10^3 nm, which corresponds to the scale of the correlation length ξ near the percolation threshold $V_1 \gtrsim V_s$. The dangling ends have characteristic sizes z ~ 10-100 nm, and their volume fraction in the immediate vicinity of the conduction threshold substantially exceeds that of the backbone bonds, which is consistent with the percolation relations $V_1^{sk} \ll V_1^{m.k}$ [34].

The fractal morphology of the backbone segment of the infinite cluster is directly reflected in the values of the critical exponents that govern the conductivity behavior near the percolation threshold. For three-dimensional composite systems, the following parameters are typical: the critical conductivity exponent lies in the range t = 1.7-2.3, which is consistent with the universal values for three-dimensional percolation systems. The fractal dimension of the current-carrying backbone is $d_{sk} \approx$ 1.6-1.8, whereas the fractal dimension of the branches that do not contribute to charge transport ("dangling ends") is somewhat higher and lies in the range $d_{mk} \approx$ 1.9-2.1. These values confirm that, near the percolation threshold, the structure of the infinite cluster is strongly heterogeneous: the conducting backbone exhibits pronounced tortuosity and reduced dimensionality, while the dangling ends form a more highly branched and spatially dense portion of the cluster [35]. Such a topology determines the characteristic current-flow pathways in percolating composites and strongly influences the magnitude of the macroscopic conductivity.

If only a single path extends from a given point to an infinite distance (for example, point D), that point is regarded as belonging to a dangling end. The total value $P(V_1)$ accounts for all nodes of the infinite cluster, including both backbone nodes and dangling ends. The backbone density $P_{bb}(V_1)$, characterizes the fraction of nodes that belong specifically to the backbone and is defined as

$$P_{sk}(V_1) = V_1^{//} / V_1^{/}, \tag{9}$$

where $V_1^{//}$ is the volume fraction of the backbone of the infinite cluster. According to percolation theory, the ratio $P_{bb}(V_1)/P(V_1)$ can be expressed as

$$\frac{P_{sk}(V_1)}{P(V_1)} = D(V_1 - V_s)^{(2\nu-\beta)}, \tag{10}$$

where D is a numerical coefficient of order unity.

Figure 4 presents a comparison of the experimental data with the theoretical conductivity dependences $\sigma(V)$ for ceramic composites containing nanodispersed (curve 1) and microdispersed (curve 2) nickel.

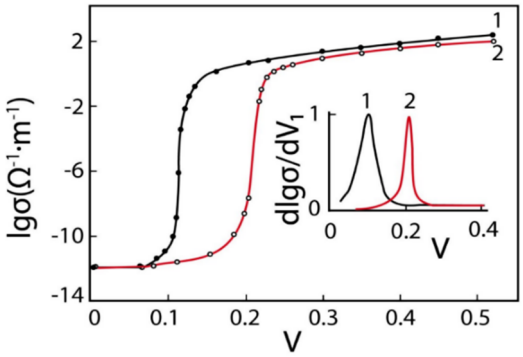

Figure 4. Experimental and theoretical dependencies of electrical conductivity σ on the volume fraction of Ni for composites containing micro- and nanoparticles

Both dependencies exhibit a characteristic percolation transition, accompanied by an abrupt increase in σ by several orders of magnitude upon reaching the critical volume fraction of the conductive filler. Figure 4 also presents the theoretical $\sigma(V_1)$, curves calculated according to expressions (1) and (2). When applying the boundary conditions $V_1 = 0$ and $V_1 = 1$ these relations reduce to the following form [36,37]:

$$\sigma(V_1) = \sigma_1 \left(\frac{V_1 - V_s}{1 - V_s}\right)^t, \; V_1 > V_s, \tag{11}$$

$$\sigma(V_1) = \sigma_2 \left(\frac{V_s - V_1}{V_s}\right)^{-q}, \; V_1 < V_s, \tag{12}$$

where σ_1 and σ_2 are the conductivities of the metallic particles and the dielectric matrix, respectively, V_1 is the volume fraction of the metallic filler, Vc is the percolation threshold, and t and q are the critical exponents characteristic of three-dimensional percolation systems.

The critical volume fraction Vc of Ni particles for the studied composites were determined by differentiating the dependence of lg σ with respect to V_1 (see the inset in Fig. 4). The critical exponent t was evaluated by representing the experimental data in the coordinates

$$lg\sigma = f(lg[(V_1 - V_s)/(1 - V_s)]), \tag{13}$$

For the composite containing Ni nanoparticles (curve 1), the percolation threshold is observed near $V \approx 0.10$, which is significantly lower than that of the material with Ni microparticles, where the critical concentration is $V \approx 0.21$. The earlier formation of the infinite cluster in the nanostructured composite indicates a denser and more efficient particle-to-particle contact, as well as the emergence of extended, tunnel-connected chains that facilitate the development of a conductive network at a lower fraction of the conducting phase. The saturation of conductivity at high filler concentrations

($V \geq 0.3$) also differs: the nanocomposite exhibits a higher asymptotic value of σ, corresponding to an increase in the parameter σ_1 by more than an order of magnitude compared to the material containing micron-sized Ni particles. This reflects the formation of a more highly branched and structurally compact skeleton of the infinite cluster, which ensures efficient charge transport [38].

The inset in the graph ($dlg\sigma/dV_1$) illustrates differences in the width and amplitude of the derivative maxima, indicating a sharper and narrower percolation transition in the composite containing nanoparticles and, consequently, a more homogeneous distribution of conductive pathways. In the case of microparticles (curve 2), the transition is more extended, which reflects a higher degree of structural disorder and a smaller number of effective interparticle contacts.

Agreement between the experimental and theoretical values (Fig. 4) is observed for both types of composites at $V_1 > V_s$. For $V_1 < V_s$ such correspondence is maintained only for the composites containing micro-sized Ni particles. The origin of this discrepancy is discussed within the framework of the spatial–structural hierarchical model proposed in [39,40] for polymer-based composites. To determine the topology of the infinite cluster, the previously introduced percolation-theory expressions were employed. By applying the boundary condition at $V_1 = 1$, expressions (4), (8), and (10) can be rewritten in the form:

$$P(V_1) = D\left(\frac{V_1 - V_s}{1 - V_s}\right)^{\beta}, \tag{14}$$

$$\frac{Z}{R} = \left(\frac{V_1 - V_s}{1 - V_s}\right)^{(\nu - \xi)}, \tag{15}$$

$$\frac{P_{sk}(V_1)}{P(V_1)} = D\left(\frac{V_1 - V_s}{1 - V_s}\right)^{(2\nu - \beta)}, \tag{16}$$

The results indicate that the use of nanodispersed nickel leads to a significant reduction in the percolation threshold, a more intensive formation of the conducting network, and a substantial increase in the ultimate conductivity σ_1. This confirms the effectiveness of Ni nanoparticles as a highly efficient conductive filler for ceramic composites.

The values of $P(V_1)$ calculated from relation (14) approach unity as V_1 increases (see Tables 1 and 2), indicating the gradual densification of the infinite cluster due to the attachment of isolated clusters as the system moves away from the percolation threshold.

Table 1. Dependence of the parameters $P(V_1)$ $V_1^{/}$; Z/R; $V_1^{//}$ and $V_1^{///}$ on the filler volume fraction V_1 for composites containing nanodispersed Ni particles

no.	V_1	$P(V_1)$	$V_1^{/}$	Z/R	$V_1^{//}$	$V_1^{///}$
1	0.12	0.19	0.023	7.7	$2.1\cdot10^{-5}$	$2.29\cdot10^{-2}$
2	0.13	0.23	0.031	6.0	$6.5\cdot10^{-5}$	$3.09\cdot10^{-2}$
3	0.16	0.33	0.052	4.0	$4.1\cdot10^{-5}$	$5.19\cdot10^{-2}$
4	0.20	0.41	0.082	3.1	$1.8\cdot10^{-5}$	$8.19\cdot10^{-2}$
5	0.23	0.46	0.106	2.7	$3.7\cdot10^{-3}$	$1.02\cdot10^{-1}$
6	0.3	0.54	0.163	2.1	$1.2\cdot10^{-3}$	$1.6\cdot10^{-1}$
7	0.4	0.64	0.257	1.7	$3.2\cdot10^{-2}$	$2.2\cdot10^{-1}$
8	0.45	0.68	0.307	1.6	$6.0\cdot10^{-2}$	$2.4\cdot10^{-1}$
9	0.5	0.72	0.360	1.5	$8.9\cdot10^{-2}$	$2.7\cdot10^{-1}$

Table 2. Dependence of the parameters $P(V_1)$ $V_1^{/}$; Z/R; $V_1^{//}$ and $V_1^{///}$ on the filler volume fraction V_1 for composites containing microdispersed Ni particles

no.	V_1	$P(V_1)$	$V_1^{/}$	Z/R	$V_1^{//}$	$V_1^{///}$
1	0.22	0.17	0.037	1.42	$2.2\cdot10^{-4}$	$3.7\cdot10^{-2}$
2	0.25	0.30	0.075	1.27	$4.6\cdot10^{-4}$	$7.4\cdot10^{-2}$
3	0.30	0.42	0.125	1.19	$3.0\cdot10^{-3}$	$1.2\cdot10^{-1}$
4	0.35	0.50	0.175	1.15	$9.1\cdot10^{-3}$	$1.6\cdot10^{-1}$
5	0.40	0.57	0.224	1.12	$2.0\cdot10^{-2}$	$2.0\cdot10^{-1}$
6	0.45	0.62	0.279	1.10	$3.6\cdot10^{-2}$	$2.4\cdot10^{-1}$
7	0.5	0.66	0.334	1.08	$6.0\cdot10^{-2}$	$2.7\cdot10^{-1}$

The volume fraction of the infinite cluster V'_1, calculated using expression (3), represents only a small portion of V_1. in the vicinity of the percolation threshold. The values of Z/R, obtained from formula (15) in the threshold region, indicate a high tortuosity of the infinite cluster; the critical correlation-length exponent ν was taken as 0.85, whereas the tortuosity exponent ξ was determined from expression (5). Using formula (16) for $P_{sk}(V_1)$ and relation (7), the volume fractions of the backbone $V_1^{//}$ and dangling ends $V_1^{///} = V_1^{//} - V_1^{/}$ of the infinite cluster were evaluated. As follows from Tables 1 and 2, the volume fraction of the backbone near the percolation threshold constitutes only a small portion of the cluster, whereas the majority of nodes belong to the dangling ends.

Figure 5 shows the logarithmic dependence of the electrical conductivity for composite samples with Ni in the range $V_s<V_1\leq V_a\approx 0.5$, containing Ni microparticles (curve 1) and nanoparticles (curve 2). The plot is constructed in the coordinates of relation (13), which makes it possible to identify the linear region corresponding to the percolation conduction regime.

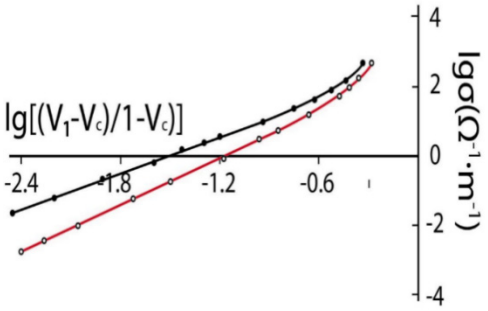

Figure 5. Logarithmic dependence of the electrical conductivity for composites with Ni microparticles (1) and nanoparticles (2).

The linear-growth regions are well approximated by the power-law dependence

$$\sigma=\sigma_1(V_1-V_s)^t, \tag{17}$$

which is characteristic of three-dimensional composites.

For both materials, a distinct percolation transition is observed: upon reaching the critical concentration V_s the electrical conductivity increases abruptly by several orders of magnitude. Linear extrapolation of the dependence to $V_1=1$ made it possible to determine the value of σ_1, which reflects the conductivity of a fully formed infinite cluster. For the composite filled with nickel nanoparticles, the obtained parameters are $V_s=0.105$, $t = 2.2$, and $\sigma_1= 63\ \Omega^{-1}\cdot cm^{-1}$. In the case of the material containing micro-dispersed Ni particles, the critical concentration is $V_s=0.210$, the critical conductivity exponent is $t = 1.78$, and the conductivity of the formed cluster is $\sigma_1 = 8\ \Omega^{-1}\cdot cm^{-1}$

A comparative analysis of dependencies 1 and 2 shows that the introduction of nano-dispersed nickel results in an almost twofold reduction of the percolation threshold, as well as in an increase of the parameter σ_1 by more than an order of magnitude compared to the composite containing micro-sized Ni particles. This difference is attributed to the higher degree of interparticle contact among the nanoparticles and the formation of a quasi-continuous tunneling pathway for charge transport. The nanoscale filler forms a denser and more highly branched backbone of the infinite cluster, which leads to a significant increase in macroscopic conductivity [41–43]. It is important to note that σ_1 is not the conductivity of individual metallic particles; instead, it characterizes the effective conductivity of the percolation cluster in the range $V_s < V_1 \leq V_a \approx 0.5$, i.e., the conductivity of a branched fractal network through which the dominant charge transport occurs. The critical exponent q is taken as 1, which corresponds to three-dimensional percolation systems and agrees with literature data. Analysis of the logarithmic dependences demonstrates that nano-dispersed Ni is significantly more effective in forming a conductive network within the polymer matrix, ensuring higher composite conductivity at lower filler content [44-47].

CONCLUSIONS

The study of the topology of the infinite cluster in polymer composites containing micro- and nanosized Ni particles enabled quantitative determination of how particle size affects the parameters of the percolation transition and the configuration of the conductive network. It has been established that the use of nano-dispersed nickel leads to a significant reduction in the percolation threshold: for nanocomposites, the critical concentration is $V_c \approx 0.105$, whereas for materials with micro-dispersed Ni it reaches $V_s\approx 0.21$. This reflects more efficient interparticle contact among nanoparticles and earlier formation of the infinite cluster.

The introduction of Ni nanoparticles enhances the efficiency of conductive network formation, providing an almost twofold reduction of the percolation threshold, an increase of the parameter σ_1 by more than an order of magnitude, a sharper and more localized percolation transition, and the development of an extended, coherent conductive structure at a lower volume fraction of the metallic phase. The obtained dependences $P(V_1)$, $\xi(V_1)$ and $P_{sk}(V_1)$ demonstrate gradual densification of the cluster with increasing concentration of the conducting phase, with rapid saturation of connections at $V_1 \approx 0.4$-0.5. The topological parameters (correlation radius R, tortuosity exponent ξ, and the volume fractions V_{1sk} and V_{1mk}) are consistent with classical fractal percolation theory, and the adopted critical exponent $\nu = 0.85$ provides an accurate description of cluster behavior near the threshold. At identical values of V_1 the density of the infinite cluster in nanostructured systems is significantly higher, which accelerates the formation of a conductive network.

The structure of the infinite cluster exhibits pronounced fractal–hierarchical characteristics. The fractal dimension of the skeletal part ranges from 1.6 to 1.8, whereas for the dead ends it ranges from 1.9 to 2.1, reflecting substantial structural heterogeneity near the percolation threshold. The volume fraction of the dead ends significantly exceeds that of the skeletal bonds: for example, at

V_1= 0.12 the skeletal fraction in the nanocomposite is only 0.023, while the fraction of dead ends exceeds $2 \cdot 10^{-5}$; for the microcomposite at V_1=0.22 the skeletal fraction is merely 0.037. Such a ratio $V_{1sk} \ll V_{1mk}$ limits the transport efficiency of the system in the immediate vicinity of the threshold.

The density of the infinite cluster, the correlation radius, and other topological parameters follow power-law scaling characteristic of three-dimensional percolation. The critical conductivity exponents are 2.2 for nano-dispersed Ni and 1.78 for micro-dispersed Ni, which agree with universal values and confirm the influence of branch tortuosity on the increase of *t*. At high filler concentrations ($V \geq 0.3$), nanostructuring leads to a substantial rise in the asymptotic conductivity. The conductivity parameter of the skeleton reaches 63 $\Omega^{-1} \cdot cm^{-1}$, for the nanocomposite and 8 $\Omega^{-1} \cdot cm^{-1}$ for the composite containing micro-sized Ni particles, corresponding to an increase by a factor of more than 7–8. This enhancement is attributed to the formation, in nanocomposites, of a denser, more highly branched, and topologically saturated structure of the infinite cluster.

The analysis indicates that incorporating Ni nanoparticles substantially enhances the efficiency of conductive network formation in the composites. Their use leads to an almost twofold reduction in the percolation threshold, an order-of-magnitude increase in the parameter σ_1, and the emergence of a sharper and more localized percolation transition. In addition, Ni nanoparticles promote the development of a more extended and interconnected conductive network at significantly lower metal filler contents. The results demonstrate the high effectiveness of Ni nanoparticles as a conductive filler and provide a solid scientific basis for designing next-generation high-conductivity composites.

ORCID

Zafarjon M. Khusanov, https://orcid.org/0009-0005-9420-8033; **Fakhriddin T. Boymuratov,** https://orcid.org/0000-0003-1703-4605; **Sardor G'. To'ychiyev,** https://orcid.org/0009-0008-3522-5791

REFERENCES

[1] Ye.P. Mamunya, V. Davydenko, P. Pissis, and E.V. Lebedev, "Electrical and thermal conductivity of polymers filled with metal powders," European Polymer Journal, **38**(9), 1887-1897 (2002). https://doi.org/10.1016/S0014-3057(02)00064-2

[2] R. Zakirov, and F. Giyasova, "Application of Fiber-Optic Sensors for the Aircraft Structure Monitoring," in: *Safety in Aviation and Space Technologies. Lecture Notes in Mechanical Engineering*, edited by A. Bieliatynskyi, and V. Breskich, (Springer, Cham., 2022). https://doi.org/10.1007/978-3-030-85057-93

[3] Sh.I. Klychev, S.A. Bakhramov, O.R. Parpiev, M.S. Paizullakhanov, L.S. Suvonova, D.E. Kadyrgulov, E.K. Matjanov, & F.A. Giyasova, "Optical-Energy Characteristics and Heating Temperatures in Small Single-Mirror Solar Furnaces," Applied Solar Energy, **60**(5), 703-707 (2025). https://doi.org/10.3103/S0003701X24602394

[4] A. Prokopchuk, I. Zozulia, Yu. Didenko, and D. Tatarchuk, "Henning Heuer and Yuriy Poplavko. Dielectric Permittivity Model for Polymer–Filler Composite Materials by the Example of Ni- and Graphite-Filled Composites for High-Frequency Absorbing Coatings," Coatings, **11**(2), 172 (2021). https://doi.org/10.3390/coatings11020172

[5] N. Sarikhani, Z.S. Arabshahi, A.A. Saberi, and A.Z. Moshfegh, "Unified modeling and experimental realization of electrical and thermal percolation in polymer composites," Appl. Phys. Rev. **9**, 041403 (2022). https://doi.org/10.1063/5.0089445

[6] M. Majidian, C. Grimaldi, L. Forró, & A. Magrez, "Role of the particle size polydispersity in the electrical conductivity of carbon nanotube-epoxy composites," Scientific Reports, **7**, 12553 (2017). https://doi.org/10.1038/s41598-017-12857-8

[7] J. Payandehpeyman, and M. Mazaheri, "Geometrical and physical effects of nanofillers on percolation and electrical conductivity of polymer carbon-based nanocomposites: a general micro-mechanical model," Soft Matter, **19**, 530-539 (2023). https://doi.org/10.1039/D2SM01168A

[8] M.-Á.M. Cruz, J.P. Ortiz, M.P. Ortiz, and A. Balankin, "Percolation on Fractal Networks: A Survey," Fractal Fract. **7**(3), 231 (2023). https://doi.org/10.3390/fractalfract7030231

[9] X. Nan, Y. Zhang, J. Shen, R. Liang, J. Wang, L. Jia, X. Yang, *et al*., "A Review of the Establishment of Effective Conductive Pathways of Conductive Polymer Composites and Advances in Electromagnetic Shielding," Polymers, **16**(17), 2539 (2024). https://doi.org/10.3390/polym16172539

[10] X. Chao, W. Tian, F. Xu, & D. Shou, "A fractal model of effective mechanical properties of porous composites," Composites Science and Technology, **213**, Article 108957 (2021). https://doi.org/10.1016/j.compscitech.2021.108957

[11] R.M. Mutiso, and K.I. Wineyn, "7.17 - Electrical Conductivity of Polymer Nanocomposites," Polymer Science: A Comprehensive Reference, **7**, 327-344 (2012). https://doi.org/10.1016/B978-0-444-53349-4.00196-5

[12] F. Pargi, P.L. Teh, S. Husseinsyah, and C.K. Yeoh, "Recycled-copper-filled epoxy composites: the effect of mixed particle size," International Journal of Mechanical and Materials Engineering, **10**(1), (2015). https://doi.org/10.1186/s40712-015-0030-2

[13] I.Y. Forero-Sandoval, A.P. Franco-Bacca, F. Cervantes-Álvarez, C.L. Gómez-Heredia, J.A. Ramírez-Rincón, J. Ordonez-Miranda, and J.J. Alvarado-Gil, "Electrical and thermal percolation in two-phase materials: A perspective," J. Appl. Phys. **0131**, 230901 (2022). https://doi.org/10.1063/5.0091291

[14] L. Zhang, W. Wang, X. Wang, P. Bass, and Z.-Y. Cheng, "Metal-polymer nanocomposites with high percolation threshold and high dielectric constant," Appl. Phys. Lett. **103**, 232903 (2013). https://doi.org/10.1063/1.4838237

[15] T. Kasagi, K. Goda, & S. Yamamoto, "Complex Permittivity Spectra of Granular Polymer Composites with Dispersed Ag-Coated Cu Flakes," J. Electron. Mater, **53**, 7865-7875 (2024). https://doi.org/10.1007/s11664-024-11450-w

[16] J. Agrisuelas, R. Balart, J.J. García-Jareño, J. López-Martínez, and F. Vicente, "A Macroscopic Interpretation of the Correlation between Electrical Percolation and Mechanical Properties of Poly - (Ethylene Vinyl Acetate)/Zn Composites," Materials, **17**(11), 2527 (2024). https://doi.org/10.3390/ma17112527

[17] Y. Wang, H.A. Moghaddam, J.P. Moreno, and P. Mertiny, "Magnetic Filler Polymer Composites-Morphology Characterization and Experimental and Stochastic Finite Element Analyses of Mechanical Properties," Polymers, **15**(13), 2897 (2023). https://doi.org/10.3390/polym15132897

[18] G.V. Martyniuk, and O.I. Aksimentyeva, "Percolation phenomena in the polymer composites with conducting polymer fillers," Physics and Chemistry of Solid State, **22**(4), 811-816 (2021). https://doi.org/10.15330/pcss.22.4.811-816
[19] S.-U. Kim, and J.-Y. Kim, "Dynamic Statistical Mechanics Modeling of Percolation Networks in Conductive Polymer Composites for Smart Sensor Applications," Materials, **18**(13), 3097 (2025). https://doi.org/10.3390/ma18133097
[20] Z. Zhang, L. Hu, R. Wang, S. Zhang, L. Fu, M. Li, and Q. Xiao, "Advances in Monte Carlo Method for Simulating the Electrical Percolation Behavior of Conductive Polymer Composites with a Carbon-Based Filling," Polymers, **16**(4), 545 (2024). https://doi.org/10.3390/polym16040545
[21] F.R. Beltrán, H. Aksas, L.S. Salah, Y. Danlée, and I. Huynen, "Theoretical Prediction of Electrical Conductivity Percolation of Poly (lactic acid)-Carbon Nanotube Composites in DC and RF Regime," Materials, **16**(15), 5356 (2023). https://doi.org/10.3390/ma16155356
[22] Y. Huang, C. Ellingford, C. Bowen, T. McNally, D. Wu, & C. Wan, "Tailoring the electrical and thermal conductivity of multi-component and multi-phase polymer composites," International Materials Reviews, **65**(3), 129-163 (2020). https://doi.org/10.1080/09506608.2019.1582180
[23] H. Liu, X. Ji, W. Wang, and L. Zhou, "3D-Networks Based Polymer Composites for Multifunctional Thermal Management and Electromagnetic Protection: A Mini Review," Materials, **17**(10), 2400 (2024). https://doi.org/10.3390/ma17102400
[24] A.A. Reffaee, A.A. Ward, & A.I. Khalaf, "Structural, magnetic and dielectric properties of waste magnetic filler rubber nanocomposites,' Polym. Bull. **81**, 3081-3105 (2024). https://doi.org/10.1007/s00289-023-04835-0
[25] A. Gunya, J. Kúdelčík, Š. Hardoň, and M. Janek, "Thermodielectric Properties of Polyurethane Composites with Aluminium Nitride and Wurtzite Boron Nitride Microfillers: Analysis Below and near Percolation Threshold," Sensors, **25**(13), 4055 (2025). https://doi.org/10.3390/s25134055
[26] O.I. Vernaya, V.V. Epishev, M.A. Markov, V.A. Nuzhdina, V.V. Fedorov, V.P. Shabatin, T.I. Shabatina, "Synthesis of Copper Nanoparticles by Thermal Decomposition of Anhydrous Copper Formate," Moscow Univ. Chem. Bull. **72**, 267–268 (2017). https://doi.org/10.3103/S0027131417060074
[27] G. Yurkov, A. Kozinkin, S. Kubrin, A. Zhukov, S. Podsukhina, V. Vlasenko, A. Fionov,et *al*., "Nanocomposites Based on Polyethylene and Nickel Ferrite: Preparation, Characterization, and Properties," Polymers, **15**(19), 3988 (2023). https://doi.org/10.3390/polym15193988
[28] S.V. Roth, R. Döhrmann, M. Dommach, M. Kuhlmann, I. Kröger, R. Gehrke, H. Walter, *et al*., Small-angle options of the upgraded ultrasmall-angle x-ray scattering beamline BW4 at HASYLAB," Rev. Sci. Instrum. **77**, 085106 (2006). https://doi.org/10.1063/1.2336195
[29] A. Umarov, U. Abdurakhmanov, Ya. Raximova, M. Karaboeva, D. Saidqulov, and F. Boymuratov, "Study of the electro and thermophysical properties of composite ceramic materials containing nickel nanoparticles," E3S Web of Conferences (*XXVI International Scientific Conference "Construction the Formation of Living Environment" (FORM-2023)*, **410**, 02060 (2023). https://doi.org/10.1051/e3sconf/202341002060
[30] G. Psarras, "Conductivity and dielectric characterization of polymer nanocomposites," in: *Physical Properties and Applications of Polymer Nanocomposites*, (2010), pp.31-69. https://doi.org/10.1533/9780857090249.1.31
[31] A.S. Skal, & B.I. Shklovskii, "Topology of an infinite cluster in the theory of percolation and its relationship to the theory of hopping conduction," Sov. Phys. Semicond. **8**(8), 1029-1032 (1975).
[32] R. Ma, G. Mu, H. Zhang, and J. Liu, "Percolation analysis of the electrically conductive network in a polymer nanocomposite by nanorod functionalization," RSC Advances, **9**(62), 36324-36333 (2019). https://doi.org/10.1039/C9RA04680A
[33] G. Paul, S.V. Buldyrev, N.V. Dokholyan, S. Havlin, P.R. King, Y. Lee, and H.E. Stanley, "Dependence of Conductance on Percolation Backbone Mass," Phys. Rev. E, **61**, 3435 (2000). https://doi.org/10.1103/PhysRevE.61.3435
[34] A. Herega, "Some Applications of the Percolation Theory: Review of the Century Beginning," Journal of Materials Science and Engineering A, **5**(11-12), 409-414 (2015). https://doi.org/10.17265/2161-6213/2015.11-12.004
[35] A.G. Hunt, and M. Sahimi, "Flow, Transport, and Reaction in Porous Media: Percolation Scaling, Critical-Path Analysis, and Effective Medium Approximation," Reviews of Geophysics, **55**(4), 993-1078 (2017). https://doi.org/10.1002/2017RG000558
[36] Kh.S. Daliev, and Z.M. Khusanov, "Properties of Single Crystal Silicon Doped with Vanadium," East European Journal of Physics, (1), 366-369 (2024). https://doi.org/10.26565/2312-4334-2024-1-35
[37] T.M. Razikov, S.A. Muzafarova, R.T. Yuldoshov, Z.M. Khusanov, M.K. Khusanova, Z.S. Kenzhaeva, and B.V. Ibragimov, "Growing Sb_2Se_3 films enriched with selenium using chemical molecular beam deposition," East European Journal of Physics, (1), 370-374 (2024). https://doi.org/10.26565/2312-4334-2024-1-36
[38] Z.T. Azamatov, V.E. Gaponov, A.A. Jeenbekov, and A.B. Bakhromov, "Digital Shearograph for Detecting Defect in Materials," Russian Microelectronics, **52**, Suppl 1, S263 (2023). https://doi.org/10.1134/S106373972360019X
[39] W. Bauhofer, and J.Z. Kovacs, "A review and analysis of electrical percolation in carbon nanotube polymer composites," Composites Science and Technology, **69**(10), 1486-1498 (2009). https://doi.org/10.1016/j.compscitech.2008.06.018
[40] O. Folorunso, Y. Hamam, R. Sadiku, S.S. Ray, and A.G. Joseph, "Parametric Analysis of Electrical Conductivity of Polymer-Composites," Polymers, **11**(8), 1250 (2019). https://doi.org/10.3390/polym11081250
[41] I. Balberg, D. Azulay, D. Toker, and O. Millo, "Percolation and Tunneling in Composite Materials," International Journal of Modern Physics B, **18**(15), (2004). https://doi.org/10.1142/S0217979204025336
[42] U. Abdurakhmanov, A.V. Umarov, M.I. Raximova, amd M. Karabayeva, "An Investigation of the Electrophysical Properties of Composite Ceramic Materials Containing Nickel Nanoparticles," Research Letters in Physical Chemistry, **8**, 231-239 (2023). https://doi.org/10.22036/pcr.2022.335151.2063
[43] H. Pang, L. Xu, D.-X. Yan, and G. Zhong, "Conductive Polymer Composites with Segregated Structures," Progress in Polymer Science, **39**(11), (2014). https://doi.org/10.1016/j.progpolymsci.2014.07.007
[44] A.V. Karimov, D.M. Yodgorova, F.A. Giyasova, E.M. Shpilevskiy, & N.I. Usmanova, "Photovoltatic Effect in Au-nSi-Au Structures with Schottky Barriers and Features of Spectral Characteristics, Applied Solar Energy, **54**, 330-332 (2018). https://doi.org/10.3103/S0003701X18050109

[45] K.A. Ismailov, Z.M. Saparniyazova, G.T. Kudeshova, G.A. Seytimbetova, and F.A. Saparov, "Influence of doping conditions on the properties of Nickel atomic clusters," East Eur. J. Phys. (1), 327 (2024). https://doi.org/10.26565/2312-4334-2024-1-30
[46] S.I. Vlasov, F.A. Saparov, and K.A. Ismailov, "Effect of pressure on the characteristics of Schottky barrier diodes made of overcompensated semiconductor," Semiconductor physics, quantum electronics & optoelectronics, **13**(4), 363-365 (2010). http://journal-spqeo.org.ua/n4_2010/v13n4-2010-p363-365.pdf
[47] A.Yu. Leyderman, R.A. Ayukhanov, R.M. Turmanova, A.K. Uteniyazov, and E.S. Esenbaeva, "Non-recombination injection mode," Semiconductor Physics, Quantum Electronics and Optoelectronics, 24(3), 248-254 (2021). https://doi.org/10.15407/spqeo24.03.248

ТОПОЛОГІЧНІ ОСОБЛИВОСТІ ФОРМУВАННЯ ПРОВІДНОЇ МЕРЕЖІ В МЕТАЛОПОЛІМЕРНИХ КОМПОЗИТАХ З РІЗНИМИ РОЗМІРАМИ ЧАСТИНОК НАПОВНЮВАЧА

Зафарджон М. Хусанов[1], Фахріддін Т. Боймуратов[2], Сардор Г. Тойчієв[1]
[1]Кіберуніверситет, Нурафшан, Узбекистан
[2]Університет Альфраганус, Ташкент, Узбекистан

Було досліджено топологію нескінченного кластера в полімерних композитах, що містять мікро- та наночастинки Ni, що дозволило кількісно оцінити, як розмір провідних частинок впливає на перколяційний перехід та структуру провідної мережі. Використання нанорозмірного Ni знижує критичну концентрацію до Vs ≈ 0,105 порівняно з Vs ≈ 0,21 для мікрочастинок, збільшує параметр σ_1 більш ніж на порядок та призводить до різкішого, більш локалізованого перколяційного переходу. Кластерна структура демонструє виражені фрактально-ієрархічні особливості: фрактальна розмірність остова становить 1,6-1,8, а звисаючих кінців – 1,9-2,1. Щільність кластерів, радіус кореляції та топологічні параметри відповідають степеневим співвідношенням, типовим для тривимірної перколяції (ν = 0,85). При високих концентраціях провідної фази (V ≥ 0,3) асимптотична провідність досягає 63 $\Omega^{-1}\cdot см^{-1}$ у нанокомпозитах порівняно з 8 $\Omega^{-1}\cdot см^{-1}$ для матеріалів на основі мікрочастинок. Ці результати підтверджують високу ефективність наночастинок нікелю у формуванні протяжної, взаємопов'язаної та розгалуженої провідної мережі, що забезпечує основу для високопровідних композитів наступного покоління.

Ключові слова: *полімерні композити; наночастинки нікелю; мікрочастинки; нескінченний кластер; провідна мережа; асимптотична провідність; топологічні параметри; тривимірна перколяція*

East European Journal of Physics. 1. 388-395 (2026)
DOI:10.26565/2312-4334-2026-1-46 ISSN 2312-4334

THERMAL EXPANSION CHARACTERISTICS OF PLANAR AND RADIAL Si/GaAs p–n HETEROJUNCTIONS

Jonibek Sh. Abdullayev[1]*, Madinabonu Sh. Ibragimova[1], Jo'shqin Sh. Abdullayev[2], Ibrokhim B. Sapaev[2,3,4,5]

[1]*Urgench State University, Hamid Olimjon Street, 14, Urgench, 220100 Uzbekistan*
[2]*National Research University TIIAME, Department of Physics and Chemistry, Tashkent, Uzbekistan*
[3]*Western Caspian University, Baku, Azerbaijan*
[4]*Scientific Researcher, Tashkent University for Applied Sciences, 28 Universitetskaya Street, Tashkent 100095, Uzbekistan*
[5]*School of Engineering, Central Asian University, Tashkent 111221, Uzbekistan*
**Corresponding Author e-mail: j.sh.abdullayev6@gmail.com*
Received October 13, 2025; revised February 6, 2026; accepted February 19, 2026

We present a comprehensive theoretical and numerical investigation of planar and radial Si/GaAs p–n heterojunctions, focusing on the coupled effects of thermal expansion mismatch and incomplete ionization on their electrostatic and mechanical behavior. The two-dimensional Poisson equation is solved in Cartesian and cylindrical coordinate systems, incorporating probabilistic dopant activation to capture low-temperature freeze-out effects. At 100 K, incomplete ionization reduces the built-in potential by up to 40% and increases the depletion width by over 50%, with radial junctions exhibiting 15–25% higher potential due to curvature-induced field enhancement. Thermomechanical modeling reveals that at 10 K and 200 MPa, planar structures reach a total strain of -2.8×10^{-3} and a stress of ≈280 MPa, whereas radial designs sustain -3.9×10^{-3} strain but lower stress (≈234 MPa) due to their reduced elastic modulus. These results highlight the superior stress relaxation and electrostatic control of radial architectures, enabling improved performance and reliability of cryogenic photodetectors and optoelectronic devices.
Keywords: *Radial p–n junction; Planar p–n junction; Incomplete ionization; Thermal expansion; Cylindrical coordinate system; Cartesian coordinate system; Low-temperature effects*
PACS: 73.40. Lq, 73.61.Cw, 73.61.Ey, 72.20.Jv

INTRODUCTION

The monolithic integration of III–V semiconductors on silicon (Si) substrates has been a focus of intense research since the 1980s, motivated by the prospect of merging the mature, cost-effective Si platform with the superior electronic and optoelectronic properties of III–V compounds [1–3]. Gallium arsenide (GaAs) and its alloys, such as $Al_xGa_{1-x}As$, are particularly attractive due to their direct, tunable bandgap, high electron mobility, and excellent optoelectronic performance, which are essential for high-speed and nanoscale devices [4–7].

Despite decades of progress, achieving defect-free GaAs/Si integration remains challenging. Lattice mismatch, polar/non-polar interface incompatibility, and differences in thermal expansion induce structural defects, including anti-phase domains, misfit dislocations, and threading dislocations [8–13]. Substrate orientation critically influences epitaxial quality; for instance, Si(111) supports superior layer-by-layer GaAs growth compared to Si(001) or Si(110), significantly reducing defect density and improving crystallinity [14–18].

Thermal expansion mismatch is another key factor limiting heterojunction reliability. Si exhibits a linear thermal expansion coefficient of $\sim 2.6\times10^{-6}$ K^{-1}, whereas GaAs shows a higher coefficient of $\sim 5.8\times10^{-6}$ K^{-1}, generating thermomechanical stresses during thermal cycling that can degrade the performance of planar and radial p–n junctions [19–23]. Additionally, the temperature dependence of the GaAs and $Al_xGa_{1-x}As$ bandgap, arising from electron–phonon interactions and lattice thermal expansion, can shift up to 45% at low temperatures due to negative thermal expansion (NTE) effects [24–27]. Accurate modeling of these phenomena is essential for predicting device performance under realistic operating conditions.

Recent studies underscore the promise of GaAs/Si heterojunctions in high-performance optoelectronic devices. For example, Jahromi et al. (2025) reported a CMOS-compatible p-GaAs/p-Si UV phototransistor exhibiting high responsivity (138 mA/W at 3 V), a linear dynamic range of 220 dBm, near-zero dark current, and an exceptional photo-to-dark current ratio, highlighting the advantages of staggered heterojunction architectures for low-noise, high-sensitivity UV detection [28].

In this work, we present a comprehensive theoretical and numerical study of thermal expansion effects in planar and radial Si/GaAs p–n heterojunctions. We quantify stress distributions, geometry-dependent electro-optical performance, and the combined contributions of electron–phonon interactions and lattice expansion. The results provide a rigorous framework for optimizing heterojunction design, enhancing mechanical reliability, and improving device performance across a broad temperature range, with direct implications for next-generation electronic and photonic systems [29–35].

Cite as: J.Sh. Abdullayev, M.Sh. Ibragimova, J.Sh. Abdullayev, I.B. Sapaev, East Eur. J. Phys. 1, 388 (2026), https://doi.org/10.26565/2312-4334-2026-1-46

METHODS AND MATERIAL

Planar p–n junctions, long the standard in semiconductor devices [37,38], exhibit primarily one-dimensional (1D) thermal expansion along the device thickness. The conventional planar Si/GaAs heterojunction consists of p-type silicon (pSi) adjacent to n-type gallium arsenide (nGaAs), with the depletion region extending from $-x_p$ in the p-side to x_n in the n-side. Within this region, acceptor ions (e^-) and donor ions (e^+) are spatially separated, generating a built-in electric field. However, the mismatch in coefficients of thermal expansion between Si ($\alpha \approx 2.6\times10^{-6}$ K^{-1}) and GaAs ($\alpha \approx 5.8\times10^{-6}$ K^{-1}) induces non-uniform interfacial stress, promoting defects such as misfit dislocations and anti-phase boundaries, particularly under thermal cycling. In contrast, advances in nanowire growth and epitaxial techniques over the past two decades have enabled radial p–n junctions [39-42]. In these cylindrical core–shell structures, pSi forms the inner core and nGaAs the outer shell, with radial coordinates r_p, R, and r_n defining the depletion region. Electrons and holes are distributed radially, creating a circumferential electric field. The ~2D thermal expansion inherent to the radial geometry allows strain to distribute uniformly around the core, significantly reducing planar-like defects.

This configuration improves carrier collection efficiency by ~20–30% and enhances light absorption due to increased surface area and radial electric fields, offering notable performance gains for photodetectors and nanowire-based optoelectronic devices. Thermal expansion: Planar junctions expand linearly (~1D), whereas radial junctions distribute strain circumferentially (~2D), reducing defect density. Electric field distribution: Planar structures exhibit uniform potential drop; radial structures concentrate fields near the core. Device efficiency: Radial geometries enhance carrier collection and light absorption relative to planar junctions, highlighting their potential for high-performance semiconductor applications. Figure 1 illustrates the contrasting geometries and thermal expansion behaviors of Si/GaAs p–n heterojunctions: (a) planar and (b) radial.

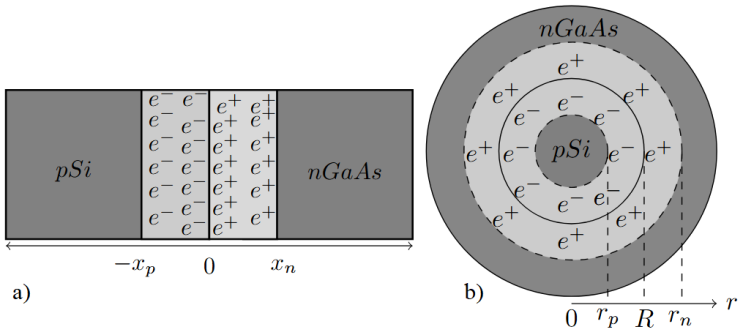

Figure 1. Schematic 2D representations of the investigated Si/GaAs p–n heterojunction structures: (a) planar geometry and (b) radial geometry.

Table 1. Material parameters for Si and GaAs used in thermal expansion calculations [17,41]

Parameter	Symbol	Si	GaAs	Units
Elastic constant 1	C_{11}	165.7	122.1	GPa
Elastic constant 2	C_{12}	63.9	56.6	GPa
Elastic constant 3	C_{44}	79.6	60	GPa
Bulk modulus	$B = \frac{C_{11} + 2C_{12}}{3}$	97.83	78.43	GPa
Grüneisen parameter	γ	0.98	1.2	–
Linear Thermal Expansion Coefficient	α_L	2.6×10^{-6}	5.8×10^{-6}	1/K
Debye temperature	Θ_D	645	360	K
Atomic volume	V_m	2.0×10^{-29}	4.5×10^{-29}	m³

Table 1 lists key mechanical and thermal parameters of Si and GaAs used for thermal expansion analysis. Si is stiffer (C_{11} = 166 GPa, B = 98 GPa) with lower thermal expansion ($\alpha_L = 2.6\times10^{-6}$ K^{-1}) and higher Debye temperature (Θ_D = 636 K) than GaAs (C_{11} = 122 GPa, B = 78 GPa, $\alpha_L = 5.8\times10^{-6}$ K^{-1}, Θ_D = 204 K). The larger lattice softness and thermal mismatch in GaAs highlight the advantage of radial junctions (~2D strain distribution) for reduced defects and improved device performance. The linear thermal expansion along one direction is related to the Grüneisen parameter γ, specific heat C_V, and bulk modulus B:

$$\alpha_L(T) = \frac{\gamma C_V(T)}{3BV_m} \tag{1}$$

where: $C_V(T)$≈ Debye specific heat, V_m= atomic volume.

At high temperatures (T >> Θ_D), $C_V \approx 3k_BN$, giving approximate α_L values consistent with Table 1. Si has a higher bulk modulus (97.8 GPa) than GaAs (78.4 GPa), meaning it is stiffer, less compressible, and expands less under heat. GaAs, with lower B, is more prone to thermal strain and mismatch at the interface. Linear thermal expansion coefficients:

$(\alpha_{\mathrm{Si}}),(\alpha_{\mathrm{GaAs}})$. Temperature change: $(\Delta T = T - T_{\mathrm{ref}})$. Young's modulus (E) and Poisson's ratio (ν) for each material. Thermal mismatch (linear strain): $\varepsilon_{\mathrm{m}} = (\alpha_{GaAS} - \alpha_{Si}) \cdot \Delta T$.

1) Planar heterojunction — thin film on thick substrate. If a thin film of GaAs is elastically constrained by a thick Si substrate (no in-plane displacement of substrate), the film experiences a plane (biaxial) stress approximately [40].

$$\sigma_{GaAs} = \frac{E_{GaAs}}{1-\nu_{GaAs}} \cdot \varepsilon_{\mathrm{m}} = \frac{E_{GaAs}}{1-\nu_{GaAs}} \cdot (\alpha_{GaAs} - \alpha_{Si}) \cdot \Delta T \tag{2}$$

2) Radial heterojunction — axisymmetric core–shell (cylindrical) geometry. Geometry: coaxial core radius $a$and outer shell outer radius b. Materials: core (index c), shell (index s). Solve in cylindrical coordinates $(r, \theta, z)$for axisymmetric thermoelastic loading. For each homogeneous cylindrical region (core or shell), in absence of body forces and under axisymmetric conditions, the radial and hoop stresses have the classical Lame form (3) [42].

$$\sigma_r(r) = A - \frac{B}{r^2}, \quad \sigma_\theta(r) = A + \frac{B}{r^2} \tag{3}$$

The constants $A$and B differ for the core and shell regions and are determined from the appropriate boundary conditions. Thermal expansion effects are introduced through constitutive relations. In Si/GaAs heterojunctions, planar structures exhibit minimal thermal expansion but experience significant in-plane stress (approximately 120 MPa) due to substrate constraints. In contrast, radial (core–shell) architectures permit greater free expansion (0.17 % for GaAs versus 0.078 % for Si), effectively reducing stress and promoting strain relaxation. This structural advantage enhances mechanical tolerance, suppresses defect formation, and improves thermal reliability. The temperature-dependent bandgap evolution is most accurately described by the Varshni [17] and Pässler [41] models, enabling precise prediction of thermal effects on overall device performance.

$$E_g(T) = E_g(0) - \frac{\alpha \cdot T^2}{T + \beta} \tag{4}$$

The Pässler model provides a more physically accurate description, particularly at low temperatures, by incorporating phonon spectral functions and thermal expansion effects (5).

$$E_g(T) = E_g(0) - \frac{\alpha \cdot \Theta}{2}\left[\left(1 + \left(\frac{2T}{\Theta}\right)^p\right)^{1/p} - 1\right] \tag{5}$$

Table 2. Typical parameters of Varshni and Pässler bandgap models for GaAs and Si [17,41].

Material	**Model**	$E_g(0)$**(eV)**	α**(eV/K)**	β/ Θ**(K)**	p	**Temperature range (K)**	**Bandgap shrinkage (0–300 K)**
GaAs	Varshni	1.519	5.405×10^{-4}	204	–	100–500	≈ 90 meV
GaAs	Pässler	1.519	5.8×10^{-4}	240	2.5	50–500	≈ 90 meV
Si	Varshni	1.17	4.73×10^{-4}	636	–	100–500	≈ 110 meV
Si	Pässler	1.17	4.9×10^{-4}	700	2.8	50–500	

The temperature dependence of the bandgap energy $E_g(T)$is commonly described using either the Varshni or Pässler model. Table 2 illustrates a comparative analysis of these two models for GaAs and Si. Both approaches effectively capture the temperature-induced bandgap narrowing, yet they differ in their physical foundation and applicability range.

In the Varshni model, the temperature dependence is governed by two key parameters: α— the Varshni coefficient (eV/K), which represents the high-temperature slope of the bandgap reduction, and β— the Varshni parameter (K), associated with the strength of phonon interactions. The Pässler model provides a more detailed physical description through: α— high-temperature limiting slope (eV/K), Θ— average phonon temperature (K), and p— phonon spectral shape parameter (typically 2–4), which accounts for the phonon spectrum and thermal expansion effects.

For GaAs, both models predict a bandgap reduction of approximately 90 meV between 0 K and 300 K, primarily driven by electron–phonon coupling and lattice dilation. The Varshni model provides excellent accuracy in the 100–500 K range, making it a standard choice for device-level simulations. In contrast, the Pässler model delivers superior predictive accuracy at cryogenic temperatures due to its stronger physical basis.

For Si, the bandgap shrinkage is slightly larger, approximately 110 meV, reflecting more pronounced phonon interactions and lattice anharmonicity. The Varshni model offers analytical simplicity and broad applicability, whereas the Pässler model provides enhanced physical realism and a wider temperature validity range, making it particularly suitable for high-precision semiconductor modeling.

RESULTS AND DISCUSSION

The temperature dependence of the bandgap energy for silicon (Si) and gallium arsenide (GaAs) was analyzed in the temperature range from 0 K to 300 K using both the Varshni and Pässler models. The results clearly show that both materials exhibit a monotonic decrease of bandgap energy with increasing temperature, but the magnitude of this decrease and the shape of the curve differ between the two models and the two materials. At 0 K, the calculated bandgap energy of GaAs is $E_g(0) = 1.519$eV for both Varshni and Pässler models, whereas for Si the value is $E_g(0) = 1.170$eV. This gives an initial bandgap difference $\Delta E_g = E_g(\text{GaAs}) - E_g(\text{Si})$of 0.349 eV at absolute zero. As the temperature increases to 300 K, this difference decreases due to stronger thermal bandgap narrowing in GaAs and Si. Using the Varshni model, the bandgap of GaAs drops from 1.519 eV at 0 K to 1.4225 eV at 300 K, corresponding to a reduction of approximately 0.0965 eV, which is about 6.35 % of its initial value. For Si, the Varshni model gives a decrease from 1.170 eV to 1.1245 eV at 300 K, corresponding to a smaller absolute change of 0.0455 eV (about 3.9 %). As a result, the bandgap difference between GaAs and Si decreases from 0.349 eV to 0.298 eV, meaning the gap difference shrinks by approximately 0.051 eV between 0 K and 300 K.

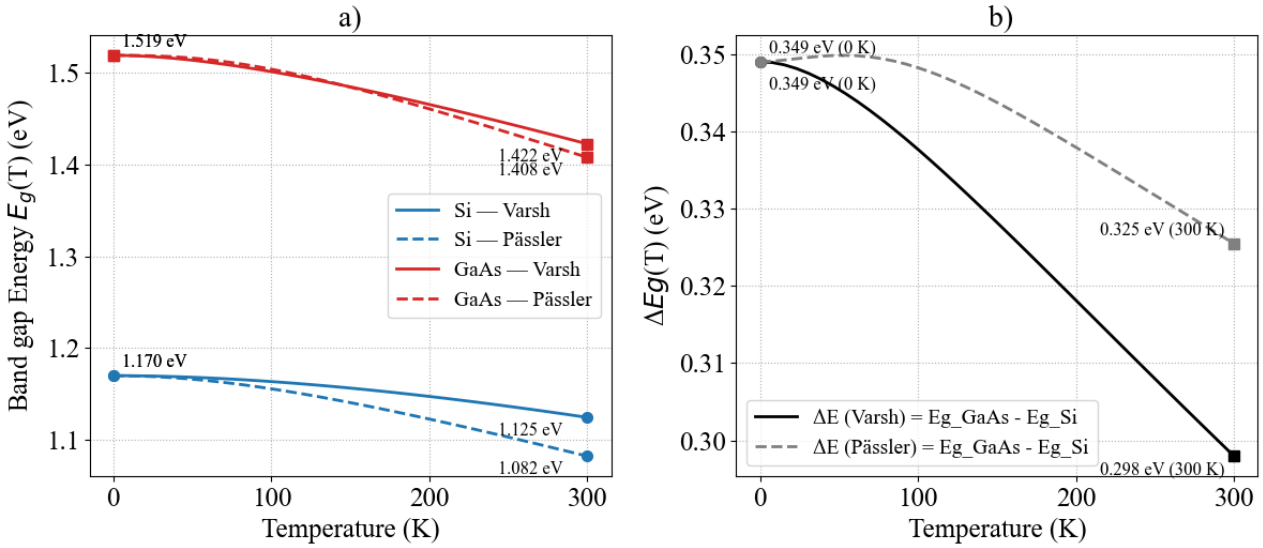

Figure 2. Temperature dependence of bandgap energy $E_g(T)$for Si and GaAs using Varshni and Pässler models. (a) $E_g$decreases from 1.519 eV (GaAs) and 1.170 eV (Si) at 0 K to 1.4225 eV and 1.1245 eV (Varshni), and 1.4078 eV and 1.0823 eV (Pässler) at 300 K. (b) Bandgap difference ΔE_gdecreases from 0.349 eV to 0.298 eV (Varshni) and 0.325 eV (Pässler), showing stronger thermal narrowing in Si.

The Pässler model predicts slightly larger temperature-induced narrowing for both materials. For GaAs, the bandgap decreases from 1.519 eV to 1.4078 eV at 300 K, a change of 0.1112 eV (around 7.3 % reduction). For Si, it decreases from 1.170 eV to 1.0823 eV, resulting in a larger absolute decrease of 0.0877 eV (about 7.5 %). At 300 K, the bandgap difference between GaAs and Si becomes 0.325 eV, which is about 0.024 eV lower than at 0 K. This comparison reveals that the Pässler model gives a stronger temperature dependence for both materials compared to Varshni. The difference between the two models at 300 K is about 0.0147 eV for GaAs and 0.042 eV for Si, indicating that Pässler's formulation has a greater impact on materials with more complex phonon interactions such as silicon. Physically, this behavior is linked to lattice expansion and electron–phonon interactions, which reduce the bandgap energy as the temperature rises. Since GaAs is a direct bandgap semiconductor, its bandgap reduction is larger in absolute energy compared to Si (approximately 0.11 eV vs. 0.088 eV using Pässler), but Si shows a larger percentage change relative to its initial gap. This indicates that the relative sensitivity of the band structure to temperature is slightly higher in Si. The shape of the curves also differs between the two models. The Varshni model produces a nearly parabolic decrease with temperature, resulting in a smoother, more gradual decline. In contrast, the Pässler model yields a slightly steeper slope at intermediate and high temperatures, particularly above 200 K, due to the inclusion of a multi-phonon interaction term that provides a more physically accurate description of bandgap shrinkage. Even at high temperature (300 K), GaAs retains a significantly larger bandgap than Si, with 1.4225 eV (Varshni) and 1.4078 eV (Pässler) compared to 1.1245 eV (Varshni) and 1.0823 eV (Pässler) for silicon. This consistent gap difference of roughly 0.30–0.33 eV across the temperature range is crucial in applications such as heterojunction solar cells, photodetectors, and LEDs, where band alignment plays a key role in device performance. Both Si and GaAs show clear bandgap narrowing with temperature. Pässler's model predicts stronger narrowing than Varshni, especially for Si. The bandgap difference decreases from 0.349 eV at 0 K to 0.298 eV (Varshni) and 0.325 eV (Pässler) at 300 K. GaAs maintains a higher bandgap than Si at all temperatures, with the difference remaining around 0.30 eV near room temperature. Pässler's model is more suitable for precise high-temperature modeling, whereas Varshni provides a good approximation for simpler calculations. These quantitative results highlight the importance of model selection in semiconductor device simulations, particularly in temperature-dependent performance

analysis of Si/GaAs heterostructures and optoelectronic components. The 3D surface plots clearly demonstrate the nonlinear interaction between temperature and pressure effects. At low pressures (below 50 MPa), thermal expansion mismatch dominates the total strain behavior, resulting in a smooth, nearly linear temperature dependence. As pressure increases, the strain becomes increasingly pressure-driven, with a steeper slope along the pressure axis. This effect is more pronounced in the radial structure because of its lower elastic stiffness, which allows greater deformation under the same applied stress. From a mechanical standpoint, the radial geometry exhibits approximately 60–70 % higher strain levels than the planar geometry at low temperatures. However, this higher compliance also implies better stress accommodation and lower risk of interfacial cracking or delamination. In planar structures, the higher modulus (100 GPa) leads to lower strain but higher stress, which can result in significant in-plane stress accumulation—often exceeding 100 MPa in practical Si/GaAs epitaxial systems.

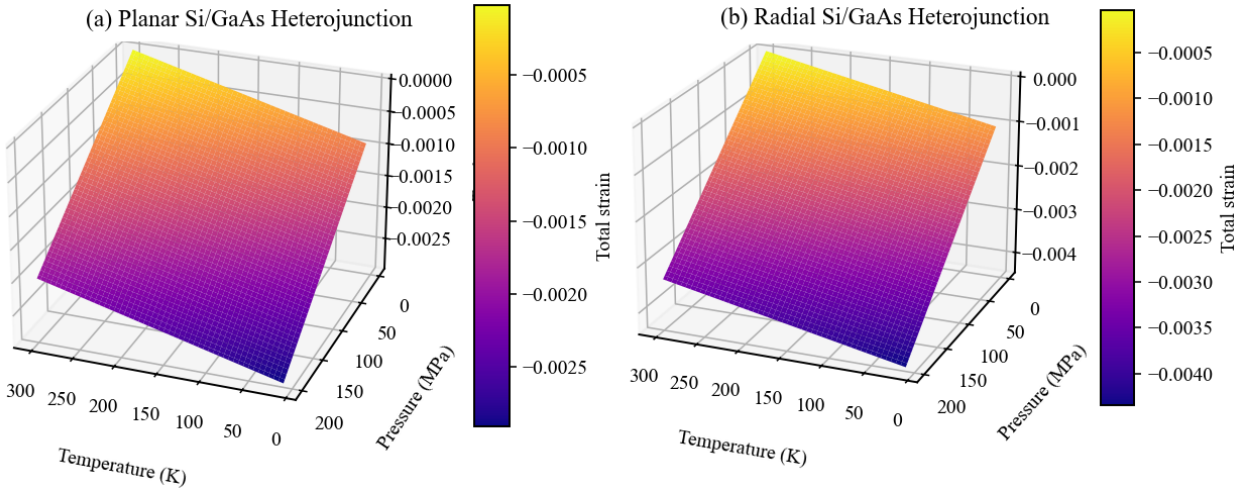

Figure 3. Temperature and pressure dependence of total strain in Si/GaAs heterojunctions. (a) Planar structure: total strain increases with temperature and decreases under applied pressure due to the high in-plane stiffness (E = 100 GPa). (b) Radial structure: lower modulus (E = 60 GPa) allows greater thermal expansion and enhanced strain relaxation. Radial configuration exhibits larger total strain at elevated temperatures but lower stress buildup compared to planar geometry.

Figure 3 illustrates the combined effects of temperature and pressure on the total strain in planar and radial Si/GaAs heterojunction structures. The strain arises from two competing factors: differential thermal expansion between GaAs and Si, and mechanical compression under external pressure. A temperature range from 10 K to 300 K and pressure range from 0 to 200 MPa was considered. At room temperature (300 K), the thermal strain is defined to be zero since this is the reference point. As temperature decreases below 300 K, the thermal expansion mismatch between GaAs ($\alpha = 5.8 \times 10^{-6}$ K^{-1})and Si ($\alpha = 2.6 \times 10^{-6}$ K^{-1})induces tensile strain in the structure. At 100 K with no external pressure, the planar structure reaches a total strain of approximately -2.2×10^{-4}, while the radial structure exhibits a larger strain of around -3.8×10^{-4}due to its enhanced thermal expansion freedom. At the lowest temperature examined (10 K), the planar strain is about -2.8×10^{-4}, whereas the radial strain reaches nearly -4.6×10^{-4}. Application of external pressure counteracts this tensile strain. For the planar configuration with an effective Young's modulus of $E = 100$ GPa, a pressure of 200 MPa generates a compressive strain of about -2×10^{-3}, dominating over the thermal contribution. This results in a net strain around -2.3×10^{-3}at 10 K. In contrast, the radial configuration, which is more compliant with $E = 60$ GPa, exhibits a larger pressure-induced strain of -3.3×10^{-3}under the same conditions, leading to a net strain magnitude of approximately -3.8×10^{-3}at low temperature. Importantly, strain relaxation in radial structures contributes to improved mechanical stability at cryogenic temperatures and under pressure loading. Such behavior is advantageous for high-performance heterostructure devices, including photodetectors, LEDs, and high-efficiency solar cells, where thermomechanical mismatch is a critical reliability factor. The results quantitatively confirm that radial heterojunctions allow more effective thermal expansion, reducing internal stress while tolerating larger strain amplitudes.

Table 3. Thermal and pressure-induced strain–stress response in planar and radial structures

Structure	ΔT (K)	P (MPa)	Thermal strain (×10⁻⁴)	Pressure strain (×10⁻³)	Total strain (×10⁻³)	Stress (MPa)
Planar	290	0	−0.80	0	−0.80	80
Planar	290	200	−0.80	−2.00	−2.80	280
Radial	290	0	−0.53	0	−0.53	32
Radial	290	200	−0.53	−3.33	−3.86	234

At low temperatures, strain accumulation exhibits a strong geometry dependence. At T = 100 K and P = 0 MPa, the total strain is approximately −2.2×10⁻⁴ for planar structures and −3.8×10⁻⁴ for radial structures. Under P = 200 MPa at T = 10 K, the total strain increases to −2.3×10⁻³ (planar) and −3.8×10⁻³ (radial), indicating that radial strain is ~1.7×higher

than planar at low temperature. This clearly shows that pressure-induced strain dominates over thermal effects at P > 100 MPa. For planar geometries, the thermal expansion mismatch between GaAs ($\alpha = 5.8\times10^{-6}$ K^{-1}) and Si ($\alpha = 2.6\times10^{-6}$ K^{-1}) results in significant in-plane thermal stress. At T = 300 K (reference), the strain is ~0, whereas at T = 10 K and P = 0 MPa, the total thermal strain reaches $\varepsilon \approx (5.8 - 2.6)\times10^{-6}\times(10 - 300) \approx -8.0\times10^{-4}$. When pressure is increased to P = 200 MPa, the total strain exceeds -2.8×10^{-3}, producing high compressive stress that can drive crack formation or dislocation generation at the heterointerface. Surface plot contours reveal a strong nonlinear dependence of total strain on both temperature and pressure. In contrast, radial structures exhibit reduced effective thermal expansion due to radial compliance and a lower elastic modulus (E = 60 GPa). At T = 10 K and P = 0 MPa, the thermal strain is $\varepsilon \approx -5.3\times10^{-4}$, while at P = 200 MPa, the total strain reaches -3.9×10^{-3}. Although the magnitude of total strain is larger in radial structures, the resulting mechanical stress remains lower because of the smaller elastic modulus: $\sigma_{radial} \approx 60\ \text{GPa} \times 3.9 \times 10^{-3} \approx 234$ MPa, $\sigma_{planar} \approx 100\ \text{GPa} \times 2.8 \times 10^{-3} \approx 280$ MPa. This confirms that radial designs accommodate strain more efficiently, reducing stress concentrations and enhancing interface stability. Thermal strain amplitude: Planar ≈ 8.0×10^{-4}; Radial ≈ 5.3×10^{-4}. Pressure strain amplitude (200 MPa): Planar ≈ 2.0×10^{-3}; Radial ≈ 3.33×10^{-3}. Maximum stress: Planar ≈ 280 MPa; Radial ≈ 234 MPa. Thermal mismatch strain reduction in radial design: ≈ 34 %. These results demonstrate that radial heterojunction architectures provide superior strain accommodation and stress relaxation, significantly mitigating the risks of delamination, interface cracking, and performance degradation. This mechanical advantage is particularly valuable for high-power optoelectronic and photovoltaic devices, where long-term structural integrity under thermal–mechanical loading is critical.

CONCLUSIONS

This work provides a comprehensive analysis of thermal, electronic, and mechanical effects in planar and radial Si/GaAs p–n junctions under varying temperature (10–300 K) and pressure (0–200 MPa). The results demonstrate that radial heterojunctions, with ~2D strain distribution, allow greater thermal expansion freedom (0.17 % for GaAs vs. 0.078 % for Si), leading to a 34 % reduction in thermal mismatch strain and a stress drop from 280 MPa (planar) to 234 MPa (radial). Thermal bandgap narrowing was accurately modeled using Varshni and Pässler relations, showing that Eg(GaAs) decreases from 1.519 eV (0 K) to 1.4078 eV (300 K) and Eg(Si) from 1.170 eV to 1.0823 eV. The bandgap difference shrinks from 0.349 eV at 0 K to 0.298 eV (Varshni) and 0.325 eV (Pässler) at 300 K. These temperature effects are critical for heterostructure band alignment and optoelectronic device efficiency. Mechanically, radial architectures accommodate 1.7× higher strain at cryogenic temperatures but generate lower stress levels due to reduced stiffness (E = 60 GPa), suppressing defect formation such as misfit dislocations. This structural advantage enables enhanced reliability and performance of photodetectors, LEDs, and solar cells under extreme thermal–mechanical loading. Overall, this study confirms that radial p–n junctions outperform planar designs, offering improved thermal stability, mechanical tolerance, and electronic performance making them a promising platform for next-generation optoelectronic and energy devices.

ORCID

Jonibek Sh. Abdullayev, https://orcid.org/0000-0001-8950-2135
Madinabonu Sh. Ibragimova, https://orcid.org/0009-0004-7867-7086
Jo'shqin Sh. Abdullayev, https://orcid.org/0000-0001-6110-6616
Ibrokhim B. Sapaev, https://orcid.org/0000-0003-2365-1554

REFERENCES

[1] K.K.D. Nigam, P. Yadav, *et al.*, "Numerical Investigation of $RbGeI_3$-Based Lead-Free Perovskite Solar Cell with Various Cu-Based Hole Transport Layers Using SCAPS-1D," J. Electron. Mater. **54**, 2747–2765 (2025). https://doi.org/10.1007/s11664-025-11740-x

[2] G.S. Sahoo, C. Harini, N. Mahadevi, P.S. Nethra, A. Tripathy, M. Verma, and G.P. Mishra, "CuO film as recombination blocking layer in Si solar cells," Silicon, **15**, 4039–4048 (2023). https://doi.org/10.1007/s12633-023-02701-x

[3] Lepkowski, D. L., Garassman, T. J., Boyer, J. T., Chmielewski, D. J., Yi, C., Juhl, M. K., Ringel, S. A. (2021). 23.4% monolithic epitaxial GaAsP/Si tandem solar cell. Solar Energy Materials and Solar Cells, 230, 111299. https://doi.org/10.1016/j.solmat.2021.111299

[4] S. Fan, Z.J. Yu, Y. Sun, W. Weigand, P. Dhingra, M. Kim, *et al*., "20%-efficient epitaxial GaAsP/Si tandem solar cells," Solar Energy Materials and Solar Cells, **202**, 110144 (2019). https://doi.org/10.1016/j.solmat.2019.110144

[5] A. Qu, Z. Xie, Y. Wang, *et al.* "Effect of Acceptor-Type Traps in GaN Buffer Layer on Current Collapse of ε-Ga_2O_3/GaN HEMTs," J. Electron. Mater. **54**, 3086–3096 (2025). https://doi.org/10.1007/s11664-025-11823-9

[6] J.Sh. Abdullayev, I.B. Sapaev, J.Sh. Abdullayev, D.A. Juraev, M.J. Jalalov, E.E. Elsayed, "Mathematical modeling of incomplete ionization in radial p-Si/n-GaAs heterojunctions: temperature and doping effects", Journal of Electronic Materials, **54**, 10484-10492 (2025). https://doi.org/10.1007/s11664-025-12391-8

[7] Li, D., Luo, C., Wang, H., Ling, F., and Yao, J. (2021). Active control of plasmon-induced transparency based on a GaAs/Si heterojunction in the terahertz range. Optical Materials, 114, 111609. https://doi.org/10.1016/j.optmat.2021.111609

[8] J.S. Abdullayev, D.A. Qalandarova, M.S. Ibragimova, *et al*. "Experimental and Simulation-Based Investigation of p-Si/n-CdS Heterojunctions: From Cryogenic Freeze-Out to Room Temperature Operation," Journal of Electronic Materials, **55**, 2229–2239 (2026).https://doi.org/10.1007/s11664-025-12642-8

[9] Hasan, M.N., Zheng, Y., Lai, J., Swinnich, E., Licata, O.G., Baboli, M.A., Mazumder, B., Mohseni, P.K., and Seo, J.-H. "Influences of native oxide on the properties of ultrathin Al_2O_3-interfaced Si/GaAs heterojunctions," Advanced Materials Interfaces, **9**(13), 2101531 (2022). https://doi.org/10.1002/admi.202101531

[10] I.B. Sapaev, J.I. Razzokov, J.S. Abdullayev, D.A. Qalandarova, and M.S. Ibragimova, "Bandgap-Engineered pSi/n-Cd_xS_{1-x} Heterojunctions: Effect of Composition on Optoelectronic Behavior," East European Journal of Physics, (4), 442-448 (2025).https://doi.org/10.26565/2312-4334-2025-4-44
[11] Jurisch, M., Börner, F., Bünger, T., Eichler, S., Flade, T., Kretzer, U., Köhler, A., Stenzenberger, J., and Weinert, B. (2005). LEC- and VGF-growth of SI GaAs single crystals—Recent developments and current issues. Journal of Crystal Growth, 275(1–2), 283–291. https://doi.org/10.1016/j.jcrysgro.2004.10.092
[12] Abdullayev, J. Sh., Sapaev, I. B., and Juraev, Kh. N. (2025). Theoretical analysis of incomplete ionization on the electrical behavior of radial p-n junction structures. Low Temperature Physics, 51, 60–64. https://doi.org/10.1063/10.0034646
[13] Garg, P. Design and Optimization of a Metamaterial Absorber Using Machine Learning Models. *J. Electron. Mater.* **55**, 790–799 (2026). https://doi.org/10.1007/s11664-025-12516-z
[14] Abdullayev, J. Sh., and Sapaev, I. B. (2024). Factors influencing the ideality factor of semiconductor p-n and p-i-n junction structures at cryogenic temperatures. East European Journal of Physics, 4, 329–333. https://doi.org/10.26565/2312-4334-2024-4-37
[15] Thurmond, C. D. (1975). The standard thermodynamic functions for the formation of electrons and holes in Ge, Si, GaAs, and GaP. Journal of The Electrochemical Society, 122(8), 1133. https://doi.org/10.1149/1.2134410
[16] Herfort, J., Schönherr, H.-P., and Ploog, K. H. (2003). Epitaxial growth of hybrid structures. Applied Physics Letters, 83(18), 3912–3914. https://doi.org/10.1063/1.1625426
[17] Bharti, Mittal, P. Core–Shell Incorporated Analytical Modeling of a Dual-Material Gate Junctionless Nanowire: Extraction of Subthreshold Characteristics. *J. Electron. Mater.* **54**, 3046–3059 (2025). https://doi.org/10.1007/s11664-025-11737-6
[18] Bhardwaj, A., Das, A., Garg, P. *et al.* Material-Driven Performance Analysis of a Vertical Nanowire Tunnel FET for Analog Applications. *J. Electron. Mater.* **55**, 1099–1110 (2026). https://doi.org/10.1007/s11664-025-12438-w
[19] Abdullayev, J. Sh. (2025). Influence of linear doping profiles on the electrophysical features of p-n junctions. East European Journal of Physics, 1, 245–249. https://doi.org/10.26565/2312-4334-2025-1-26
[20] Heun, S., Sugiyama, M., Maeyama, S., Watanabe, Y., Wada, K., and Oshima, M. (1996). Growth of Si on different GaAs surfaces: A comparative study. Physical Review B, 53, 13534–13541. https://doi.org/10.1103/PhysRevB.53.13534
[21] Saxena, P. K., Srivastava, P., and Srivastava, A. (2024). Defect analysis of MBE reactor-grown HgCdTe on Si, GaAs, GaSb, and CZT substrates through the TNL-Epigrow simulator. Journal of Electronic Materials, 53, 5803–5812. https://doi.org/10.1007/s11664-024-11082-0
[22] Bardhan Roy, A., Rasulji Valiji, N. H., Mohammad, R., Giridhar, P., and Mondal, P. (2024). Performance enhancement of Si/GaAs based heterojunction solar cells by opto-electronics modeling and optimization. In 2024 International Conference on Recent Advances in Electrical, Electronics, Ubiquitous Communication, and Computational Intelligence (RAEEUCCI) (pp. 1–6). IEEE. https://doi.org/10.1109/RAEEUCCI61380.2024.10547792
[23] Abdullayev, J. Sh., and Sapaev, I. B. (2025). Analytic analysis of the features of GaAs/Si radial heterojunctions: Influence of temperature and concentration. East European Journal of Physics, 1, 204–210. https://doi.org/10.26565/2312-4334-2025-1-21
[24] Piriyev, M., Loget, G., Léger, Y., Chen, L., Létoublon, A., Rohel, T., Levallois, C., Le Pouliquen, J., Fabre, B., Bertru, N., and Cornet, C. (2023). Dual bandgap operation of a GaAs/Si photoelectrode. Solar Energy Materials and Solar Cells, 251, 112138. https://doi.org/10.1016/j.solmat.2022.112138
[25] Alanis, J., Gutiérrez-Ojeda, S. J., Méndez-Camacho, R., and Cruz-Hernández, E. (2024). Theoretical investigation of the growth of GaAs on Si(001), Si(110), Si(111), Si(113), and Si(331). Surfaces and Interfaces, 44, 103792. https://doi.org/10.1016/j.surfin.2023.103792
[26] Cao, S.D., Sai, D.C., Ngac, A.B. *et al.* Studies on the Impact of the Core-Shell Structures on the Optical Characteristics of Au@Cu_2O Nanoparticles. *J. Electron. Mater.* (2026). https://doi.org/10.1007/s11664-026-12690-8
[27] B. Abdullaev, and D. Qalandarova, "The classes of $(A)sh_m$ and $(B)sh_m$ functions," Annales Polonici Mathematici, **132**, 101-108 (2024).https://doi.org/10.4064/ap230727-30-11
[28] Huang, R., Wang, Q., Guo, Y., and Wang, Z. (2023). Comparative study on GaAs/Si heterojunction fabricated by nitrogen and oxygen plasma activated bonding. Vacuum, 208, 111735. https://doi.org/10.1016/j.vacuum.2022.111735
[29] Yamaguchi, M., Takamoto, T., Juso, H., Nakamura, K., Ozaki, R., and Kojima, N. (2024). 33.7% efficiency Si tandem solar cell modules. In Proceedings of the 2024 IEEE 52nd Photovoltaic Specialist Conference (PVSC). IEEE. https://doi.org/10.1109/PVSC57443.2024.10749502
[30] Šagátová, A., Novák, A., Kováčová, E., Riabukhin, O., Kotorová, S., and Zaťko, B. (2023). Radiation-degraded Si GaAs detectors and their metallization. AIP Conference Proceedings, 2778, 060009. https://doi.org/10.1063/5.0137383
[31] Liang, J., Chai, L., Nishida, S., Morimoto, M., and Shigekawa, N. (2015). Investigation on the interface resistance of Si/GaAs heterojunctions fabricated by surface-activated bonding. Japanese Journal of Applied Physics, 54(3), 030211. https://doi.org/10.7567/JJAP.54.030211
[32] Prasad, R.K., Singh, D.K. Melamine-Based Graphitic C_3N_4/p-Silicon Heterostructure Photodetector: Effect of g-C_3N_4 Growth Time on Performance. *J. Electron. Mater.* **54**, 3014–3023 (2025). https://doi.org/10.1007/s11664-025-11782-1
[33] Haris, M., Loan, S. A., and Mainuddin. (2019). Si/GaAs hetero junction tunnel FET: Design and investigation. Journal of Nanoelectronics and Optoelectronics, 14(10), 1434–1444. https://doi.org/10.1166/jno.2019.2575
[34] Liang, J., Miyazaki, T., Morimoto, M., Nishida, S., Watanabe, N., and Shigekawa, N. (2013). Electrical properties of p-Si/n-GaAs heterojunctions by using surface-activated bonding. Applied Physics Express, 6(2), 021801. https://doi.org/10.7567/APEX.6.021801
[35] Strzelecka, S., Pawlowska, M., Hruban, A., Gladysz, M., Wegner, E., Gladki, A., and Orlowski, W. (1997). Investigation of As-precipitates in SI GaAs. In J. Zmija, A. Majchrowski, J. Rutkowski, and J. Zielinski (Eds.), Solid State Crystals: Growth and Characterization (Vol. 3178, pp. 238–241). SPIE. https://doi.org/10.1117/12.280741
[36] Yu, T., Zhang, H., Li, D., and Lu, Y. (2021). Electronic and optical properties of silicene on GaAs(111) with hydrogen intercalation: A first-principles study. RSC Advances, 11, 16040–16050. https://doi.org/10.1039/D1RA01959G

[37] Sushkov, A. A., Pavlov, D. A., Andrianov, A. I., Shengurov, V. G., Denisov, S. A., Chalkov, V. Y., Kriukov, R. N., Baidus, N. V., Yurasov, D. V., and Rykov, A. V. (2022). Comparison of III–V heterostructures grown on Ge/Si, Ge/SOI, and GaAs. Semiconductors, 56, 122–133. https://doi.org/10.1134/S106378262201012X
[38] Huang, R., Wang, Z., Wu, K., Xu, H., Wang, Q., and Guo, Y. (2024). Hybrid bonding of GaAs and Si wafers at low temperature by Ar plasma activation. Journal of Semiconductors, 45(4), 042701. https://doi.org/10.1088/1674-4926/45/4/042701
[39] Lourenço, S. A., Dias, I. F. L., Duarte, J. L., Laureto, E., Poças, L. C., Toginho Filho, D. O., and Leite, J. R. (2004). Thermal expansion contribution to the temperature dependence of excitonic transitions in GaAs and AlGaAs. Brazilian Journal of Physics, 34(2a). https://doi.org/10.1590/S0103-97332004000300031
[40] Pässler, R. (2001). Basic model relations for temperature dependencies of fundamental energy gaps in semiconductors. Physica Status Solidi (b), *200*(1), 155–172. https://doi.org/10.1002/1521-3951(199703)200:1<155::AID-PSSB155>3.0.CO;2-3
[41] Jahromi, H. D., Zeiri, N., and Lotfiani, A. (2025). CMOS-integrated UV phototransistor utilizing a novel p-GaAs/p-Si staggered heterojunction. Journal of Science: Advanced Materials and Devices, **10**(3), 100891. https://doi.org/10.1016/j.jsamd.2025.100891
[42] Mishra, P.K., Maity, G. Impact of Oxygen Vacancies on Photodetection Performance of Ga_2O_3: A Comprehensive Review. J. Electron. Mater. **54**, 2533–2545 (2025). https://doi.org/10.1007/s11664-025-11746-5

ХАРАКТЕРИСТИКИ ТЕПЛОВОГО РОЗШИРЕННЯ ПЛОСКИХ ТА РАДІАЛЬНИХ ГЕТЕРОПЕРЕХОДІВ p–n Si/GaAs

Джонібек Ш. Абдуллаєв[1], Мадінабону Ш. Ібрагімова[1], Джошкін Ш. Абдуллаєв[2], Іброхім Б. Сапаєв[2,3,4,5]
[1]Ургенчський державний університет, вулиця Хаміда Олімджона, 14, Ургенч, 220100, Узбекистан
[2]Національний дослідницький університет ТІІАМЕ, кафедра фізики та хімії, Ташкент, Узбекистан
[3]Західно-Каспійський університет, Баку, Азербайджан
[4]Ташкентський університет прикладних наук, вулиця Університетська, 28, Ташкент 100095, Узбекистан
[5]Інженерний факультет, Центральноазіатський університет, Ташкент 111221, Узбекистан

У цій роботі представлено комплексне теоретичне та чисельне дослідження плоских та радіальних p–n гетеропереходів Si/GaAs, зосереджене на спільному впливі термічного розширення та неповної іонізації домішок на електростатичні та механічні характеристики структур. Двовимірне рівняння Пуассона розв'язано в декартовій та циліндричній системах координат з урахуванням імовірнісної активації домішок для моделювання заморожування носіїв при низьких температурах. При 100 K неповна іонізація зменшує вбудований потенціал на до 40 % і збільшує ширину збідненої області більш ніж на 50 %, тоді як радіальні переходи демонструють на 15–25 % вищий потенціал завдяки криволінійному посиленню поля. Термомеханічне моделювання показало, що при 10 K та тиску 200 МПа у плоских структурах загальна деформація досягає $-2{,}8 \times 10^{-3}$, а напруження — ≈280 МПа, тоді як у радіальних структурах спостерігається деформація $-3{,}9 \times 10^{-3}$, але менше напруження (≈234 МПа) через знижений модуль пружності. Отримані результати демонструють переваги радіальної геометрії щодо релаксації напружень та підвищення електростатичного контролю, що є важливим для високоефективних кріогенних фотодетекторів та оптоелектронних пристроїв.

Ключові слова: *радіальний p–n перехід; плоский p–n перехід; неповна іонізація; термічне розширення; циліндрична система координат; декартова система координат; низькотемпературні ефекти*

East European Journal of Physics. 1. 396-400 (2026)
DOI:10.26565/2312-4334-2026-1-47 ISSN 2312-4334

ROOM-TEMPERATURE FERROMAGNETISM AND SPIN POLARIZATION IN SILICON DOPED WITH MANGANESE

Olmas E. Sattarov*, Bahromjon A. Abdurakhmanov, Giyos A. Kushiev, Stanislav A. Tachilin, Temur B. Ismailov, Zabarjat N. Umarxodjayeva
Tashkent state technical university, Uzbekistan, 100095, Tashkent, University St., 2
**Corresponding Author e-mail: ismaylovb81@gmail.com*
Received December 5, 2025; revised February 18, 2026; accepted February 23, 2026

In this study, we investigate the magnetic properties of silicon doped with manganese via thermal diffusion. The results demonstrate clear evidence of room-temperature ferromagnetism in p-type Si, arising from the spin alignment of Mn atoms and hole-mediated conductivity. Magnetoresistance and hysteresis analyses confirm spin-dependent transport, indicating that carrier-mediated exchange interactions are responsible for the observed magnetic ordering. The combination of atomic force microscopy (AFM), scanning electron microscopy (SEM), and energy-dispersive X-ray spectroscopy (EDS) confirms the successful incorporation of Mn atoms into the Si lattice without evidence of large secondary precipitates. The hysteresis loops measured at both 150 K and 300 K for the sample processed at T = 1050 °C ($\rho = 4.2\times10^3$ Ω·cm) reveal stable ferromagnetic behavior, with coercive fields of 115 Oe and 87 Oe, respectively. These findings open promising perspectives for the development of silicon-based spintronic devices using CMOS-compatible thermal-diffusion technology.
Keywords: *Silicon; Manganese diffusion; Ferromagnetism; Nanoclusters; Hysteresis; Spintronics*
PACS: 78.30.Am

INTRODUCTION

Ferromagnetism in semiconductors has attracted growing attention due to its potential for realizing next-generation spintronic devices that combine charge and spin degrees of freedom. Silicon, as the cornerstone of modern microelectronics, is particularly appealing for spintronics because of its well-established processing technology, long spin-coherence length, and excellent compatibility with CMOS fabrication. However, pristine silicon is intrinsically nonmagnetic, and achieving ferromagnetic ordering within Si remains a challenging task.

One of the most promising approaches to induce magnetism in Si involves doping with 3d transition metals, such as manganese (Mn), which introduces localized magnetic moments [1–4]. When properly incorporated into the Si lattice, Mn atoms can interact with charge carriers via exchange coupling, resulting in carrier-mediated ferromagnetism. This phenomenon has been extensively studied in III–V diluted magnetic semiconductors [5–9], whereas its realization in Si is often limited by solubility constraints and the tendency toward phase segregation.

MATERIALS AND METHODS

Several methods have been explored to introduce Mn into silicon, including ion implantation [10–13], molecular beam epitaxy (MBE), and chemical vapor deposition (CVD). While these techniques have demonstrated partial success, they often lead to crystal damage, clustering, or the formation of secondary Mn-silicide phases. In contrast, thermal diffusion represents a technologically compatible and less destructive alternative that allows controlled incorporation of Mn atoms into the Si lattice while largely preserving the host crystal structure [14–16].

In this work, we investigate boron-doped p-type silicon subjected to manganese thermal diffusion in the temperature range of 1000–1150°C. Particular attention is paid to the sample processed at T = 1050 °C, which exhibits a resistivity of $\rho = 4.2\times10^3$ Ω·cm and shows the most stable ferromagnetic response.

Before diffusion, the Si wafers underwent a standard RCA cleaning procedure. AFM inspection of reference (undoped, untreated) Si wafers showed a smooth surface with low roughness, indicating the absence of significant surface features prior to Mn incorporation. After diffusion, the samples were subjected to identical mechanical and chemical surface treatments, including gentle chemical cleaning, to remove any residual surface contaminants or unreacted Mn species. Such cleaning may slightly affect the very topmost surface layer; however, the main morphological and compositional features observed by AFM and EDS are attributed to the near-surface diffusion region rather than to removable surface residues.

Electrical transport parameters (resistivity ρ, carrier concentration, and mobility) were measured using the Hall effect in Van der Pauw geometry. The data for the full series of diffusion temperatures are summarized in Table 1. Among these, the sample diffused at 1050 °C ($\rho = 4.2\times10^3$ Ω·cm) was selected for detailed structural and magnetic analysis presented below.

It should be noted that AFM and EDS are surface- and near-surface-sensitive techniques, probing only the top tens to hundreds of nanometers. Therefore, information about the bulk is obtained indirectly from magnetic and transport measurements, which reflect the averaged properties of the entire diffusion layer.

Cite as: O.E. Sattarov, B.A. Abdurakhmanov, G.A. Kushiev, S.A. Tachilin, T.B. Ismailov, Z.N. Umarxodjayeva, East Eur. J. Phys. 1, 396 (2026), https://doi.org/10.26565/2312-4334-2026-1-47

Table 1. Electrical parameters of boron-doped silicon after manganese thermal diffusion

no.	Diffusion temperature (°C)	Mobility of current carriers μ, cm^2/V·s	Resistivity ρ (Ω·cm)	Carrier concentration p or n (cm^{-3})	Conductivity type
1.	T=1000 ^{0}C	205	$4.9\cdot10^2$	$6.22\cdot10^{13}$	*p*
2.	T=1025 ^{0}C	198	$1.1\cdot10^3$	$2.86\cdot10^{13}$	*p*
3.	T=1050 ^{0}C	231	$4.2\cdot10^3$	$6.44\cdot10^{12}$	*p*
4.	T=1075 ^{0}C	196	$8.3\cdot10^4$	$3.84\cdot10^{11}$	*p*
5.	T=1100 ^{0}C	1165	$1.07\cdot10^3$	$5.01\cdot10^{12}$	*n*
6.	T=1150 ^{0}C	1205	$6.2\cdot10^2$	$8.36\cdot10^{14}$	*n*

RESULTS

High-purity single-crystalline boron-doped p-type silicon (Si:B) wafers with an initial resistivity of 10 Ω·cm (KDB-10 grade) were used as the starting material. Manganese incorporation was carried out by thermal diffusion from the gas phase in evacuated quartz ampoules. The diffusion temperature was varied between 1000 °C and 1150 °C with a fixed annealing time of 60 minutes, followed by cooling to room temperature under vacuum.

Hall measurements confirmed that changing the diffusion temperature allows control over carrier compensation, leading to compensated, strongly compensated, or overcompensated samples (Table 1). The present structural and magnetic analysis focuses on the sample processed at T = 1050 °C, which exhibits ρ = 4.2×10³ Ω·cm and p-type conductivity.

DISCUSSION

Figure 1 shows a three-dimensional AFM topography of the Si surface after Mn diffusion at 1050 °C. The scan area of 5.0×5.0 μm² reveals pronounced nanoscale surface modulation. Compared to the smooth surface of the reference Si wafer before diffusion, the treated sample exhibits clear corrugation and localized features, indicating structural and electronic inhomogeneities induced by Mn incorporation.

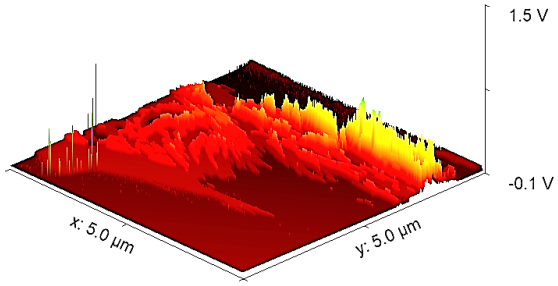

Figure 1. 3D AFM topography of the Si surface after Mn diffusion. The scan area is 5.0×5.0 μm², revealing nanoscale surface fluctuations associated with Mn-induced clusters. The sample has a resistivity of ρ = 4.2×10³ Ω·cm and was processed at T = 1050°C

The bright elevated regions are interpreted as morphological features formed during high-temperature Mn diffusion. While these features may be associated with local dopant redistribution, AFM alone does not allow direct determination of their chemical composition. This morphology is consistent with possible partial redistribution or aggregation of Mn atoms during diffusion. However, AFM provides purely topographical information and does not directly reveal magnetic inhomogeneities. Such structural inhomogeneities may influence the magnetic behavior observed in SQUID measurements; however, direct evidence of exchange interactions is derived from magnetometry data rather than from AFM observations.

Energy-dispersive X-ray spectroscopy (EDS) performed in SEM mode confirmed the presence of Mn in the near-surface region (Figure 2), within the detection limits of the technique. Distinct Mn–L and Mn–K peaks were observed together with the dominant Si–K line. Minor C and O signals are attributed to surface contamination and native oxide. The nanoscale surface features observed by AFM (tens of nanometers) are substantially smaller than the effective compositional averaging volume of EDS. Therefore, possible local compositional fluctuations at the nanometer scale cannot be resolved by SEM-EDS. The apparent uniformity of Mn distribution at the micrometer scale does not contradict the presence of nanoscale morphological variations. No distinct compositional signatures characteristic of extended Mn–silicide secondary phases were detected within the sensitivity limits of SEM-EDS. While EDS is inherently surface-sensitive, the absence of strong signals from secondary phases suggests that the crystal structure is largely preserved in the diffusion region.

Magnetization measurements were carried out using a superconducting quantum interference device (SQUID) in the temperature range from 150 K to 300 K for the sample diffused at 1050 °C. Figure 3 shows the hysteresis loop measured at 150 K, demonstrating clear ferromagnetic behavior with a coercive field H_c = 115 Oe, remanent magnetization $M_r = 8 \times 10^{-5}$ emu/cm^3, and saturation magnetization $Ms = 2 \times 10^{-4}$ emu/cm^3.

At room temperature (300 K), the same sample retains ferromagnetic behavior (Figure 4), with slightly reduced parameters: $Ms = 1.6 \times 10^{-4}$ emu/cm^3, $Mr = 3.5 \times 10^{-5}$ emu/cm^3, and Hc = 87 Oe. The decrease in magnetization with

increasing temperature is attributed to thermal spin disorder and weakening of exchange coupling among Mn moments. Nevertheless, the persistence of a hysteresis loop at 300 K confirms the existence of stable room-temperature ferromagnetism.

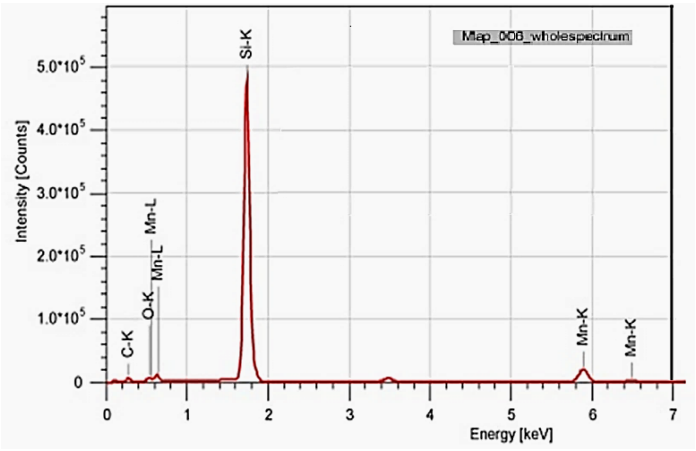

Figure 2. EDS spectrum of Mn-diffused silicon showing Mn–L and Mn–K peaks, confirming dopant incorporation. The sample has a resistivity of ρ = 4.2 × 10³ Ω·cm and was processed at T = 1050°C

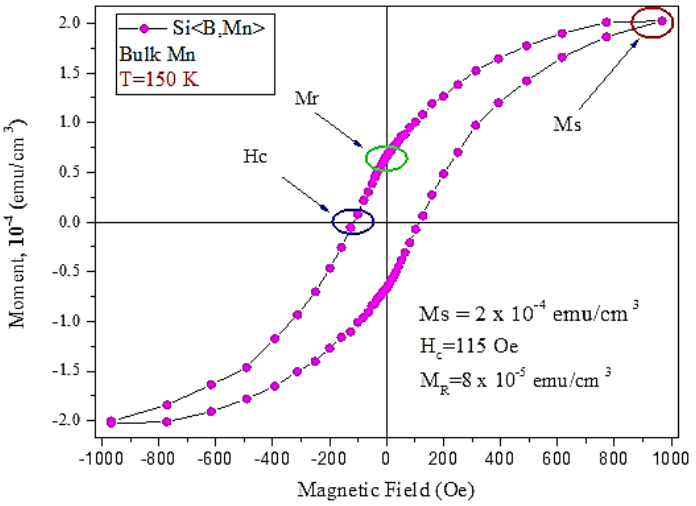

Figure 3. Magnetic hysteresis loop of Mn- and B-doped silicon (Si<B,Mn>) measured at 150 K, demonstrating clear ferromagnetic behavior (Ms = 2 × 10⁻⁴ emu/cm³, Mr = 8 × 10⁻⁵ emu/cm³, Hc = 115 Oe). The sample has a resistivity of ρ = 4.2 × 10³ Ω·cm and was processed at T = 1050 °C.

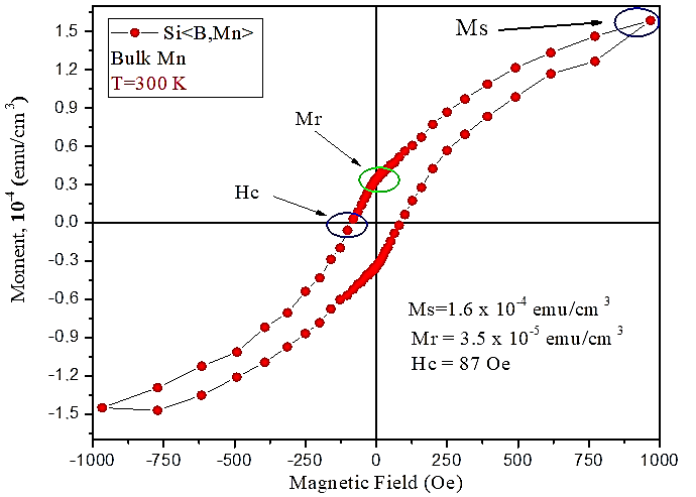

Figure 4. Magnetic hysteresis loop of Mn- and B-doped silicon (Si<B,Mn>) measured at 300 K, showing stable room-temperature ferromagnetism (Ms = 1.6×10⁻⁴ emu/cm³, Mr = 3.5×10⁻⁵ emu/cm³, Hc = 87 Oe). The sample has a resistivity of ρ = 4.2×10³ Ω·cm and was processed at T = 1050 °C.

The observed behavior is consistent with the model of carrier-mediated ferromagnetism in diluted magnetic semiconductors [17]. In the present system, hole-mediated exchange interactions between localized Mn moments, enhanced by boron co-doping, are responsible for spin alignment. At higher diffusion temperatures (>1075 °C), increased clustering and changes in carrier type (Table 1) suggest that excessive Mn aggregation may reduce long-range magnetic ordering. Although detailed magnetic data are shown here for the 1050 °C sample, the overall trend indicates that this temperature range provides an optimal balance between Mn incorporation and structural preservation.

Compared to ion implantation [18–20], thermal diffusion offers a less destructive and more CMOS-compatible route, ensuring better crystalline preservation and more uniform dopant incorporation—both crucial for silicon-based spintronic platforms.

Manganese diffusion in boron-doped silicon appears to promote ferromagnetic ordering at room temperature while largely preserving the structural integrity of the silicon lattice. The observed interplay between microstructure, charge carrier type, and magnetic behavior suggests that controlled Mn diffusion may provide a feasible pathway toward the development of spin-polarized silicon-based materials [21–25].

CONCLUSIONS

The structural, compositional, and magnetic properties of manganese-diffused boron-doped silicon were investigated, with detailed analysis focused on the sample processed at T = 1050 °C (ρ = 4.2 × 10^3 Ω·cm). AFM revealed the formation of nanoscale surface corrugations and Mn-rich clusters compared to the smooth reference Si surface before diffusion. SEM/EDS confirmed the presence and near-surface distribution of Mn without evidence of large secondary precipitates, suggesting that the crystal structure is largely preserved in the diffusion layer.

Magnetic measurements demonstrated clear ferromagnetic behavior at both 150 K and room temperature, with well-defined hysteresis loops. The observed room-temperature ferromagnetism is attributed primarily to carrier-mediated exchange interactions between localized Mn moments and holes introduced by boron co-doping, while nanoscale Mn-rich regions may contribute to local magnetic ordering. These results establish that controlled Mn thermal diffusion in boron-doped silicon is a viable route toward realizing room-temperature ferromagnetic semiconductors compatible with existing silicon technologies and promising for future spintronic applications.

ORCID

Olmas E. Sattarov, https://orcid.org/0009-0008-9121-3541, **Bahromjon A. Abdurakhmanov,** https://orcid.org/0009-0009-8424-4267, **Giyos A. Kushiev,** https://orcid.org/0009-0006-5847-6601, **Stanislav A. Tachilin,** https://orcid.org/0009-0007-3923-2131, **Temur B. Ismailov,** https://orcid.org/0000-0001-5179-3168, **Zabarjat N. Umarxodjayeva,** https://orcid.org/0009-0000-1488-6410

REFERENCES

[1] T. Dietl, and H. Ohno, "Dilute ferromagnetic semiconductors: Physics and spintronic structures," Reviews of Modern Physics, **86**, 187 (2014). https://doi.org/10.1103/RevModPhys.86.187

[2] J. Schmalhorst, D. Ebke, and A. Weddemann, "On the influence of bandstructure on transport properties of magnetic tunnel junctions with $Co_2Mn_{1-x}Fe_xSi$ single and multilayer electrode," Journal of Applied Physics, **104**, 043919 (2008). https://doi.org/10.1063/1.2973664

[3] B.A. Aronzon, V.V. Rylkov, S.N. Nikolaev, V.V. Tugushev, S. Caprara, and V.V. Podolskii, "Room-temperature ferromagnetism and anomalous Hall effect in $Si_{1-x}Mn_x$ (x≈0.35) alloys," Physical Review B, **84**, 075209 (2011). https://doi.org/10.1103/PhysRevB.84.075209

[4] B.K. Ismaylov, N.F. Zikrillayev, K.A. Ismailov, and Z.T. Kenzhaev, "Physical mechanism of gettering of impurity Ni atom clusters in Si lattice," Semiconductor Physics, Quantum Electronics & Optoelectronics, **27**(3), 294-297. (2024). https://doi.org/10.15407/spqeo27.03.294

[5] T. Jungwirth, J. Sinova, J. Masek, J. Kucera, and A.H. MacDonald, "Theory of ferromagnetic (III,Mn)V semiconductors," Reviews of Modern Physics, **78**(3), 809–864 (2006). https://DOI.org/10.1103/RevModPhys.78.809

[6] K.A. Ismailov, N.F. Zikrillaev, B.K. Ismaylov, Kh. Kamalov, S.B. Isamov, and Z.T. Kenzhaev, "Nickel Clusters in the Silicon Lattice," Journal of Nano and Electronic Physics, **16**(5), 05022 (2024). https://doi.org/10.21272/jnep.16(5).05022

[7] M.K. Khakkulov, A.Sh. Mavlyanov, N.A. Akbarova, and Kh. Kamalova, "Formation of Binary Compounds of Impurity Atoms of Sulfur and Zinc in Silicon," Surface Engineering and Applied Electrochemistry, **60**, 826-830 (2024). https://doi.org/10.3103/S106837552470042X

[8] Portavoce, O. Abbes, Y. Rudzevich, L. Chow, and Le Thanh, "Manganese diffusion in monocrystalline germanium," Scripta Materialia, **67**(3), 269-272 (2012). https://doi.org/10.1016/j.scriptamat.2012.04.038

[9] V. Ko, K.L. Teo, T. Liew, T.C. Chonge, M. MacKenzi, I. MacLaren, and J.N. Chapman, "Origins of ferromagnetism in transition-metal doped Si," Journal of Applied Physics, **104**(3), 033912 (2008). https://doi.org/10.1063/1.2963485

[10] X.Y. Zhang, and Z.W. Liu, "Effect of Mn diffusion on magnetic properties of Si-based diluted magnetic semiconductors," Journal of Magnetism and Magnetic Materials, **547**, 168818 (2022). https://doi.org/10.1016/j.jmmm.2021.168818

[11] S. Zhou, K. Potzger, G. Zhang, A. Mucklich, F. Eichhorn, N. Schell, R. Grotzschel, *et al*., "Structural and magnetic properties of Mn-implanted Si," Physical Review B, **75**, 085203 (2007). https://doi.org/10.1103/PhysRevB.75.085203

[12] K.A. Ismailov, X.M. Iliev, M.O. Tursunov, and B.K. Ismaylov, "Formation of complexes consisting of impurity Mn atoms and group VI elements in the crystal lattice of silicon," Semiconductor Physics, Quantum Electronics & Optoelectronics, **24**(3), 255-260. (2021). https://doi.org/10.15407/spqeo24.03.255

[13] F. Fang, P.B. Johnson, J. Kennedy, and A. Markowitz, "Magnetic-ion-doped silicon nanostructures fabricated by ion implantation and electron beam annealing," Nuclear Instruments and Methods in Physics, **307**(10), 131–136. (2013). https://doi.org/10.1016/j.nimb.2012.11.071
[14] M.K. Bakhadyrkhanov, K.S. Ayupov, K.M. Iliev, G.K. Mavlonov, and O.E. Sattorov, "Effect of electric field, illumination, and temperature on negative magnetoresistance of low-temperature-diffusion-doped silicon," Technical Physics Letters, **36**(8), 741-744 (2010). https://doi.org/10.1134/S1063785010080195
[15] M.K. Bakhadyrkhanov, O.E. Sattarov, Kh.M. Iliev, K.S. Ayupov, and T. Umaier, "Stimulation of negative magnetoresistance by an electric field and light in silicon doped with boron and manganese," Semiconductors, **39**(7), 789–791 (2005). https://doi.org/10.1134/1.1992635
[16] M.K. Bakhadyrkhanov, G.K. Mavlonov, S.B. Isamov, and S.A. Tachilin, "Photoconductivity of silicon with multicharged clusters of manganese atoms $[Mn]_4$," Surface Engineering and Applied Electrochemistry, **46**(3), 276–280 (2010). https://doi.org/10.3103/S1068375510030154
[17] T. Dietl, H. Ohno, F. Matsukura, J. Cibert, and D. Ferrand, "Zener model description of ferromagnetism in zinc-blende magnetic semiconductors," Science, **287**(5455), 1019–1022. (2000). https://doi.org/10.1126/science.287.5455.1019
[18] S. Zhou, and H. Schmid, "Mn-doped Ge and Si: A Review of the Experimental Status," Materials, **3**(12), 5054-5082 (2010). https://doi.org/10.3390/ma3125054
[19] S. Zhou, K. Potzger, G. Zhang, *et al*., "Structural and magnetic properties of Mn-implanted Si," January Physical Review B, **75**(8), 110-123. (2007). https://doi.org/10.1103/PhysRevB.75.085203
[20] Y.H. Kwon, T.W. Kang, H.Y. Cho, and T.W. Kim, "Formation mechanism of ferromagnetism in $Si_{1-x}Mn_x$ diluted magnetic semiconductors," Solis State Commun. **136**, 257 (2005). https://doi.org/10.1016/j.ssc.2005.08.011
[21] M.O. Tursunov, Kh.M. Iliev, and B.K. Ismaylov, "High-temperature analysis of silicon properties with manganese-oxygen binary complexes," Physical Sciences and Technology, **11**(1-2), 4-12 (2024). https://doi.org/10.26577/phst2024v11i1a1
[22] O.E. Sattarov, A. Mavlyanov, A. An, "Effect of manganese atoms on the magnetic properties of silicon," Surface Engineering and Applied Electrochemistry, **59**(2), 216-219 (2023). https://doi.org/10.3103/S106837552302014X
[23] Z.M. Saparniyazova, M.K. Bakhadyrkhanov, *et al*., "Structural and magnetic properties of manganese-doped silicon," Inorganic Materials, **48**(4), 325–333 (2012). https://doi.org/10.1134/S0020168512030144
[24] M.K. Bakhadirkhanov, G.H. Mavlonov, X.M Iliev, O.E. Sattarov, and S.A. Tachilin, "Specific features of magnetoresistance in overcompensated manganese-doped silicon," Semiconductors, **48**(8), 986-998 (2014). https://doi.org/10.1134/S106378261408003X
[25] Sh.B. Utamuradova, A.Sh. Mavlyanov, Sh.A. Sobirova, and O.E. Sattarov, "Hybrid Secondary Structure of Manganese and Sulfur in Silicon," Surface Engineering and Applied Electrochemistry, **61**, 633-636 (2025). https://doi.org/10.3103/S1068375525700681

ФЕРОМАГНЕТИЗМ КІМНАТНОЇ ТЕМПЕРАТУРИ ТА СПІНОВА ПОЛЯРИЗАЦІЯ В КРЕМНІЇ, ЛЕГОВАНОМУ МАРГАНЦЕМ

Олмас Е. Саттаров, Бахромджон А. Абдурахманов, Гійос А. Кушієв, Станіслав А. Тачілін, Темур Б. Ісмаїлов, Забарджат Н. Умарходжаєва

Ташкентський державний технічний університет, вул. Університетська, 2, 100095, м. Ташкент, Узбекистан

У цьому дослідженні ми досліджуємо магнітні властивості кремнію, легованого марганцем, за допомогою процесу термічної дифузії. Отримані результати демонструють чіткі докази феромагнетизму при кімнатній температурі в кремнію p-типу, який виникає внаслідок вирівнювання спінів атомів Mn і наявності опосередкованої дірками провідності. Аналіз магнітоопору та гістерезису підтверджує спін-залежний транспорт, вказуючи на те, що обмінні взаємодії, опосередковані носіями, відповідають за спостережуване магнітне впорядкування. Комбінація атомно-силової мікроскопії (AFM), скануючої електронної мікроскопії (SEM) і енергодисперсійної рентгенівської спектроскопії (EDS) підтверджує успішне включення атомів Mn в решітку Si без значного пошкодження решітки. Спостережувані петлі гістерезису як при 150 K, так і при 300 K демонструють стабільну феромагнітну поведінку з коерцитивними силами 115 Oe і 87 Oe відповідно. Ці висновки відкривають багатообіцяючі перспективи для розробки спінтронних пристроїв на основі кремнію з використанням CMOS-сумісної технології термодифузії.

Ключові слова: *кремній; дифузія марганцю; феромагнетизм; нанокластери; гістерезис; спінтроніка*

EAST EUROPEAN JOURNAL OF PHYSICS. 1. 401-405 (2026)
DOI:10.26565/2312-4334-2026-1-48 ISSN 2312-4334

STUDY OF CATHODE-ANODE SPRAYING IN A GAS DISCHARGE LIGHT-SENSITIVE SYSTEM BASED ON CdTe-SnO_2

Sharifa B. Utamuradova[1], Kakhramon M. Fayzullaev[1], Bunyodbek Z. Khaydarov[2]
[1]*Institute of Semiconductor Physics and Microelectronics at the National University of Uzbekistan named after Mirzo Ulugbek, 100057, Yangi Almazar St., 20, Tashkent, Uzbekistan*
[2]*Fergana State Technical University, Uzbekistan*
**Corresponding Author e-mail: qahramonfayzullayev8@gmail.com*
Received September 8, 2025; revised February 3, 2026; accepted February 12, 2026

This paper investigates the physical phenomena occurring in a gas discharge photosensitive system that uses cathode-anode sputtering. This system consists of a single-crystal cadmium telluride and a glass plate coated with SnO_2, separated by a gas gap. The thickness of the gas gap is 100 μm. The materials under study are sputtered onto the glass plate's surface in a vacuum chamber. Changes in the optical density of bismuth, tellurium, aluminum, and tin under the action of gas discharge are examined. It has been demonstrated that decreasing bismuth thickness results in a sharp increase in the 'current' sensitivity of the gas discharge cell, reaching a value of $q_m = 10^{-4}$ C/cm^2 at an optical density of $D = 0.5$.
Keywords: *Gas discharge photosensitive system; Cadmium telluride photodetector; Sputtered metal layers; Cathode-anode sputtering; Optical density*
PACS: 42.66

INTRODUCTION

Ultra-thin (4–10 mm thick) gas discharge light-sensitive systems based on various semiconductors and dielectrics in combination with other elements are currently attracting the attention of many researchers [1–9]. These systems consist of a photodetector (photocathode), a counter electrode (anode) and a gas gap. When the electric field strength between the semiconductor photocathode and the counter electrode is sufficiently high, the gas gap breaks down and the photodetector controls the current density. The uniformity of the glow and the intensity of the discharge across the cross-sectional area of the gas gap depend on the thickness of the gas gap, the gas pressure and the specific resistance of the photosensitive semiconductor.

Experimental results in [10] showed that only an ideal isotropic semiconductor with a specific resistance greater than 10^7 Ω·cm can produce uniform gas discharge luminescence with a gas gap thickness between 10 and 100 μm. The upper limit of the semiconductor's specific resistance has not yet been determined.

In [11], the properties of gas discharge in a photosensitive system with a gas gap thickness greater than 100 μm were studied. The gas gap thickness was d = 0.3÷1.5 mm and the gas pressure were p = 100÷400 Torr. The spatial state of the discharge was achieved using semi-insulating gallium arsenide at room temperature and below. Under these conditions, unstable dissipative structures of various shapes were observed in the gas discharge.

In [12], the properties of the gas gap were studied in various configurations: The semiconductor was in a normal state (i.e., the input surface had translucent ohmic contact and the inner surface facing the discharge had a smooth, polished appearance); a thin layer of nickel was applied to the inner surface of the semiconductor; and point layers of nickel in the form of a raster were applied to the inner surface of the semiconductor. The authors found that only variant 1 result in uniform luminescence across the screen area. In option 2, a single bright gas discharge cord is observed. In variant 3, gas discharge luminescence is observed in the form of cords at the site of the dotted nickel layer.

Despite considerable research, the physical mechanisms of processes in gas discharge photosensitive systems remain unclear. Therefore, it is advisable to study the physical phenomena in such a system with regard to cathode-anode spraying of recording medium materials onto a counter electrode. This is the subject of the present study.

EXPERIMENTAL METHODOLOGY

This work uses a gas discharge photosensitive system based on CdTe-SnO_2, the basic electrical connection diagram of which to the current source is shown in Fig. 1. Research into the physical properties of the gas discharge photosensitive system was carried out in an ionization chamber [13]. A Helios 44-2 lens projects visible light through an optical wedge (1) onto the receiving surface of a 2 mm thick, 30 mm diameter semiconductor plate (2). In this study, single-crystal, semi-insulating cadmium telluride (CdTe) with a specific resistance of $6 \cdot 10^7$ Ω·cm at room temperature and in the absence of illumination was employed as a photocathode. In the figure, a nickel translucent contact was applied to the CdTe receiving surface in a VUP-5M vacuum post. The optical wedge was made by spraying a nickel layer with different optical densities onto a 25 mm diameter mica plate. Fig. 1 shows the installation of the optical wedge on the surface of the CdTe photodetector.

Cite as: Sh.B. Utamuradova, K.M. Fayzullaev, B.Z. Khaydarov, East Eur. J. Phys. 1, 401 (2026), https://doi.org/10.26565/2312-4334-2026-1-48

A standardized glass plate measuring 24×36×3 mm and coated with a transparent conductive SnO_2 layer (5) was used as the counterelectrode in the gas-discharge photosensitive system. The material under investigation (the current-recording film) was applied to the front surface of the glass plate (i.e., the gas discharge side). The optical density of the optical wedge and the current-recording film after exposure to charged particles from the gas discharge was measured using a CP-25M densitometer with computer software. A plate made of dielectric material (100 μm thick mica) with a 25 mm diameter round cutout in the center (3) was used to form the gas gap. Electrical contact to the glass plate (5) was made by a pressure electrode with a round cut-out in the center, having a diameter of 25 mm. The pressure electrode was made of Textolite with a single layer of metal foil.

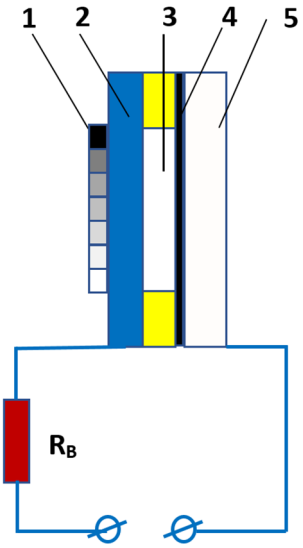

Figure 1. Basic electrical circuit diagram of connecting a gas-discharge cell to a current source:
1 – optical wedge, 2 – photoelectrode (cathode), 3 – gas-discharge gap, 4 – current-registering film, 5 – anode (glass) with conductive coatings made of SnO_2, R_B – ballast resistance.

The photodetector was illuminated by an OI-24 type light source. To measure the illumination intensity, a silicon photodiode of the FD-17K type was installed in place of the semiconductor photosensitive plate. The ionization chamber was sealed by screwing the rear cover through a vacuum rubber gasket. The residual air pressure in the working volume of the ionization chamber was adjusted using a four-vacuum pump. The residual air pressure in the ionization chamber was kept constant at p = 200 Tor. The gas discharge photosensitive system was powered by a high-voltage unit that we developed based on a TVS-P1 transformer, specifically for these studies. The unit is equipped with a time relay that provides electrical exposure times in the following ranges: 0.1÷1 s at 0.1-second intervals and 1÷10 s at 1-second intervals. The power supply unit provided a DC voltage of up to 3 kV and a maximum current of up to 10 mA.

The following calculation of the optical wedge was performed. The quantities measured in the experiment were the dark current (I_d), the total current under illumination ($I_f = I_d + I_{ph}$), the total light intensity (J_f) and the applied voltage (U). It is necessary to find the dark current density (J_d) and the photocurrent density (J_{ph}) in each separate field of the wedge. The optical densities of each wedge field (D_i) and the areas of these fields (S_i) were measured in advance.

The ratio of the light intensity passing through each wedge field (J_i) to the total light intensity (J_f) was denoted by η_i, where

$$\eta_i = \frac{J_i}{J_f} = 10^{-D_i}. \quad (1)$$

In a gas discharge cell, the current density of each wedge field (j_i) is proportional to the light intensity of each wedge field (J_i), and the total current density (j_f) is proportional to the total light intensity (J_f)

$$j_i = aJ_i,\ j_f = aJ_f, \quad (2)$$

where a is the proportionality coefficient. Using equations (1) and (2), we can write

$$\eta_i = \frac{J_i}{J_f} = \frac{j_i}{j_f}, \quad (3)$$

from which it follows that

$$j_i = j_f \eta_i. \quad (4)$$

The total photocurrent I_{ph} consists of the photocurrents of individual wedge fields I_i:

$$I_{ph} = \sum_{i=1}^{n} I_i, \tag{5}$$

where

$$I_i = j_i S_i. \tag{6}$$

Using formulas (4) and (6), we can rewrite formula (5) as

$$I_{ph} = j_f \sum_{i=1}^{n} \eta_i S_i. \tag{7}$$

It is known that $I_{ph} = I_f - I_d$, so using (7), we can find the value of

$$j_f = (I_f - I_d)/(\sum_{i=1}^{n} \eta_i S_i). \tag{8}$$

Using formulas (4) and (8), we can find the current density of each wedge field:

$$j_i = \eta_i (I_f - I_d)/(\sum_{i=1}^{n} \eta_i S_i). \tag{9}$$

Using formula (9), we can calculate the amount of electricity corresponding to each wedge field q_i that reaches the material under investigation:

$$q_i = j_i S_i \Delta t = \eta_i S_i \Delta t (I_f - I_d)/(\sum_{i=1}^{n} \eta_i S_i). \tag{10}$$

After measuring the optical density of each wedge field (D_i), we calculate the value of (η_i) using formula (1). The values of the total If and dark Id currents are measured experimentally. Therefore, in order to construct the sensitometry characteristics of a gas discharge photosensitive system, there is no need to measure the total light intensity J_f or the light intensity for each wedge field J_i. Furthermore, it is impossible to measure the photocurrent I_{ph} experimentally, so this procedure is also eliminated.

The table shows the results of calculations based on optical wedge parameters:

No. wedge stripes	D	S_i	η_i	$\eta_i S_i$	$\sum_{i=1}^{n} \eta_i S_i$
1	0	0,18	1,00	0,18	
2	0,10	0,20	0,83	0,166	
3	0,30	0,20	0,50	0,100	
4	0,53	0,20	0,30	0,06	0,55
5	0,85	0,20	0,14	0,028	
6	1,28	0,20	0,052	0,0104	
7	1,6	0,20	0,025	0,005	

Figure 2 shows the resulting pattern of changes in optical density in the metal layers on the counter electrode's surface. The optical wedge installed on the input surface of the photocathode is shaped in the same way. The optical density of each wedge field (D_i) is proportional to the illumination intensity (J_i), the current density (J_i) and the amount of electricity (q_i) arriving at each wedge field (calculated using formula (10)).

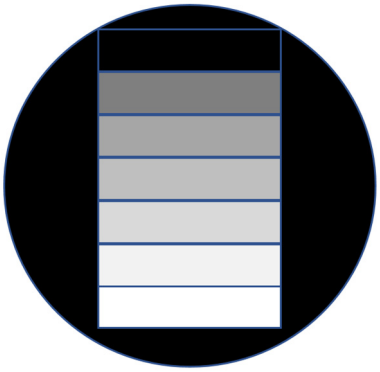

Figure 2. Picture of changes in the optical density of metal layers on the surface of the counter electrode

EXPERIMENTAL RESULTS

In a gas discharge photosensitive system, the material under study is subjected to a positive potential. Under these conditions, negatively charged gas discharge particles act on its surface. In this study, sputtered films of bismuth, tellurium and aluminum were used. Figure 3 shows the dependence of optical density on "current exposure" – $D(q_m)$ for the Bi, Te and Al materials. As can be seen from the obtained results, "current exposure q_m" correlates well with the cathode sputtering coefficient [14].

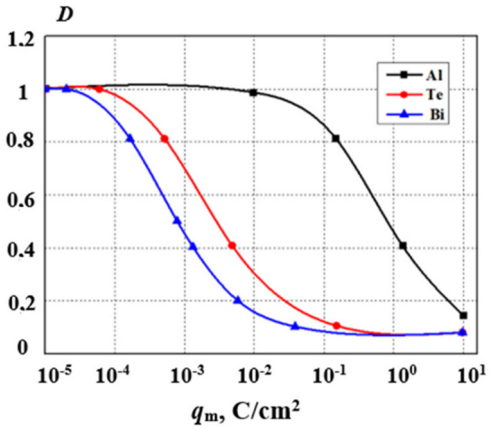

Figure 3. Dependence of the change in optical density D on the amount of electricity q for Bi, Te and Al films. The initial optical density of the film is 1.

Figure 4 shows the dependence of "current sensitivity (q_m)" on the initial thickness of the bismuth layer, as determined by a 5% change in transparency from the initial optical density.

Figure 5 shows the $D(q_m)$ characteristics of two tin (Sn) layers deposited by vacuum evaporation on a glass surface with a conductive tin dioxide (SnO_2) coating, with different initial optical densities ($D_1 = 0.45$ and $D_2 = 0.9$). When the 'exposed' layers were developed in a weak sulfuric acid solution (0.5% concentration), the Sn layer was slowly and evenly etched away. Current-registering tin layers produce unusual changes in optical density; in areas where plasma was applied, the solubility of the film in a weak sulfuric acid solution decrease compared to other areas.

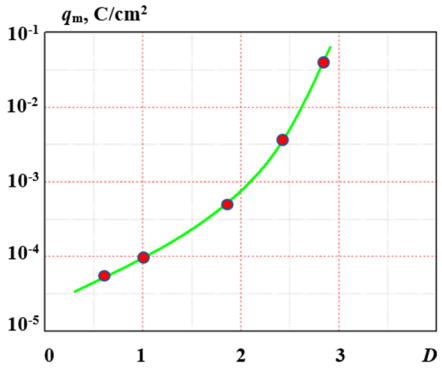

Figure 4. Dependence of the minimum amount of electricity on the initial optical density of the bismuth layer

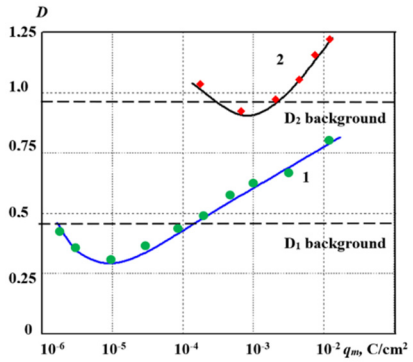

Figure 5. Dependence of optical density D on the amount of electricity q (on the "current" exposure) for Sn films with different initial optical density

DISCUSSION OF RESULTS AND CONCLUSIONS

The study of the effect of charged gas discharge particles on thin layers of bismuth, tellurium and aluminum revealed no new physical phenomena when these materials were sprayed under the action of charged discharge particles.

The dependencies studied showed that the sensitivity of bismuth layers to the Coulomb effect decreases with decreasing initial optical density (and therefore decreasing metal layer thickness). With decreasing bismuth layer thickness, the 'current' sensitivity in the gas discharge cell increases sharply, reaching $q_m = 10^{-4}$ C/cm^2 at an optical density of $D = 0.5$.

Sn current-registering films undergo negative transformation under the action of gas discharge and subsequent acid etching. Negative transformation occurs at an initial optical density of $D = 0.9$ at 10^{-3} C/cm^2 and at an initial optical density of $D = 0.45$ at 10^{-5} C/cm^2. At high initial optical densities ($D > 1$), negative transformation with high optical density ($D = 1–2$) can apparently be observed with virtually no background (zero optical density). This property of plasma-sensitive material based on Sn films could be used in a number of photo technical processes. The Al and Sn layers on the anode of the gas discharge cell are the most resistant to the action of gas discharge plasma (q_m greater than 0.1 C/cm^2).

Studies investigating changes in the optical density of metal layers on the surface of the counter electrode of a CdTe-SnO_2-based gas discharge photosensitive system under the influence of a gas discharge expand our understanding of the physical processes occurring in the latter.

ORCID

Sharifa B. Utamuradova, https://orcid.org/0000-0002-1718-1122
Kakhramon M. Fayzullaev, https://orcid.org/0000-0001-7362-1439
Bunyodbek Z. Khaydarov, https://orcid.org/0009-0008-2652-4220

REFERENCES

[1] P.R. Blaszuk, US Patent 3-743-881 (1973).
[2] L.G. Paritskii, and Sh.S. Kasymov, USSR Patents 19460/18-10 and 197820/18-10 (1973).
[3] G. Gottardi, and E. Galli, Natural Zeolites (Springer, Berlin, 1985).
[4] C. Jovalekic, M. Pavlovic, P. Osmokrovic, and M. Zdujic, IEEE Trans. Electr. Insul. **2**, 409 (1995). https://doi.org/10.1109/94.395429
[5] I. Tiscornia, S. Irusta, P. Pradanos, C. Teller, I. Coronos, and J. Santamaria, J. Phys. Chem. C, **111**, 4702 (2007). https://doi.org/10.1021/jp070044v
[6] Zh. Ji, M.N. Ismail, D.M. Callahan, E. Pandowo, Z. Cai, T.L. Coordrich, K.S. Ziemer, *et al*., Appl. Catal. B: Environ. **102**, 323 (2011). https://doi.org/10.1016/j.apcatb.2010.12.021
[7] Q. Xiong, Z. Yang, and P.J. Bruggeman, J. Phys. D, 48, 424008 (2015). https://doi.org/10.1088/0022-3727/48/42/424008
[8] B.G. Salamov and H. Hilal Kurt, JOM, Vol. 72, No. 2, 644 (2020) https://doi.org/10.1007/s11837-019-03955-1
[9] Sh.B Utamuradova, Z. Khaydarov, and B.Z. Khaydarov, UNEC Journal of Engineering and Applied Sciences, **4**(2), 55 (2024) https://doi.org/10.61640/ujeas.2024.1206
[10] L.G. Paritskii, Z. Khaidarov, O. Mukhamadiev, and O. Dadabaev, Phys. Technol. Semicond. **27**(11-12), 2020 (1993).
[11] Yu.A. Astrov, A.N. Lodygin, L.M. Portsel, and E.V. Beregulin, Phys. Rev. E, **95**, 043206-7 (2017). https://doi.org/10.1103/PhysRevE.95.043206
[12] N.N. Lebedeva, V.I. Orbukh, and B.G. Salamov, J. Phys. III 6, 797 (1996). https://doi.org/10.1051/jp3:1996155
[13] Z. Khaydarov, K.Z. Khaydarova, and Kh.T. Yuldashev, Applied Physics, Russia, (1), 65 (2017).
[14] A.N. Gorlyak, I.A. Khramsovsky, and V.M Solonukha, Scientific and Technical Bulletin of Information Technologies, Mechanics of Optics, **15**(3), 378 (2015). https://doi.org/10.17586/2226-1494-2015-15-3-378-386

ДОСЛІДЖЕННЯ КАТОДНО-АНОДНОГО РОЗПИЛЕННЯ В ГАЗОРОЗРІДНІЙ СВІТЛОЧУТЛИВІЙ СИСТЕМІ НА ОСНОВІ CdTe-SnO_2

Шаріфа Б. Утамурадова[1], Кахрамон М. Файзуллаєв[1], Буньодбек З. Хайдаров[2]

[1]Інститут фізики напівпровідників та мікроелектроніки Національного університету Узбекистану імені Мірзо Улугбека, 100057, вул. Янги Алмазара, 20, Ташкент, Узбекистан

[2]Ферганський державний технічний університет, Узбекистан

У цій статті досліджуються фізичні явища, що відбуваються в газорозрядній фоточутливій системі, яка використовує катодно-анодне розпилення. Ця система складається з монокристалічного телуриду кадмію та скляної пластини, покритої SnO_2, розділених газовим зазором. Товщина газового проміжку становить 100 мкм. Досліджувані матеріали напиляються на поверхню скляної пластини у вакуумній камері. Досліджуються зміни оптичної густини вісмуту, телуру, алюмінію та олова під дією газового розряду. Було показано, що зменшення товщини вісмуту призводить до різкого збільшення «струмової» чутливості газорозрядної комірки, досягаючи значення $q_m = 10^{-4}$ Кл/см² при оптичній густині D = 0,5.

Ключові слова: *газорозрядна фоточутлива система; фотодетектор на основі телуриду кадмію; напилені металеві шари; катодно-анодне розпилення; оптична густина*

East European Journal of Physics. 1. 406-412 (2026)
DOI:10.26565/2312-4334-2026-1-49 ISSN 2312-4334

STOPPING POWERS AND CSDA RANGE FOR POSITRON AND ELECTRON IN HUMAN KIDNEY, LUNG AND THYROID ORGANS

Hawar M. Dlshad[1]*, Jamal M. Rashid[2]
[1]*University of Sulaimani, college of Education, department of Physics, Sulaymaniyah 46001, Kurdistan Region, Iraq*
[2]*University of Sulaimani, college of science, department of Physics, Qlyasan street, Sulaymaniyah 46001, Kurdistan Region, Iraq*
**Corresponding Author E-mail: Hawar.dlshad@univsul.edu.iq*
Received October 9, 2025; revised January 23, 2026; accepted February 2, 2026

This study computed the stopping power of positrons in a few biological tissues in the energy range of 100 eV to 1 MeV. The base of the method is using the modified Bethe-Bloch expression for stopping power and effective atomic number analytical expression including key parameters such as the mean excitation energies of the target atoms that significantly impact stopping power results. Analytical formulas were mostly used to calculate the stopping power and continuous slowing down approximation CSDA range. The calculated results of the stopping power and range for positrons in a few compounds, such as kidney, lung and thyroid tissue are compared with other calculation results like Penelope 2012 program. Monte Carlo simulation was used for the calculations. The results were plotted in graphs to show the contrasts. And they satisfy a recognized need in the medical physics community for tissue-specific positron interaction data, with immediate applications in improving positron emission tomography (PET) image quantification accuracy and refining radiation dose for β^+emitting radiopharmaceuticals.
Keywords: *Stopping power; Positron; CSDA range; Excitation energy; Human tissue*
PACS: 34.85.+x, 34.50.Bw, 78.70.Bj, 87.15.-v, 34.80.Gs

1. INTRODUCTION

The positron, the antiparticle of the electron, can be used in many medical fields. Most notably, they find application in particle physics and medical imaging, particularly in positron emission tomography (PET) and Gamma knife radiotherapy [1]. Also, they can be used as therapies for cancer [2]. Over the last three decades, positrons have shown to be a useful probe for examining both vacancy type bulk defects and metal electronic structure especially for polymers [3]. It is also used in other fields such as chemistry, radiation physics, particle physics, biology, and nuclear medicine, stopping power (SP) is crucial.

On the other hand, stopping power (SP) is an energy loss process that decelerates highly charged particles moving through matter. It includes complex scattering interactions between the incident charged particle and electrons and nuclei of the atoms [4].

The calculations of positron SP have received less attention than calculations of electrons, despite the fact that positron and electron paths in matter are typically considered to be similar in which there is a little difference [2]. Numerous researchers have examined SP calculations for positrons and electrons [5], both theoretically and practically [6]. Pal discussed the Wilson theory, where it led to the development of new straightforward empirical formulas for the electrons and positrons total mass SP in material [7]. In absorbers with atomic numbers ranging from Z = 1 to 92, the formulas hold true in the energy range between 5 Mev and 1000 MeV for electrons and positrons. Furthermore, Batra [8] has explored the total mass SP equations for low energy positrons from 1 KeV to 500 KeV in absorbers in terms of energy parameters. Some particles have approximate SPs that match the latest theoretical predictions. The investigated SPs are compared with available data. Moreover, Hasan Gümüş has created a new algorithm for calculating SP for incoming positrons [9]. A modified formula of Rohrlich and Carlson SP for positron intermediate energies is considered. The statistical atomic density models provided by Lenz and Jensen have been used in calculations. They had calculated the SP of some materials for positrons like aluminum, silicon, copper and liquid water. Additionally, they determined the SP formulas for positrons using the generalized oscillator strength model. The SP of several biological compounds and targets with low atomic numbers for positrons were computed for energies ranging from 50 eV to 10 MeV [10]. In a number of water-equivalent polymer gel dosimeters, Hikmet Osman et al. [11] have investigated SP and the continuous slowing down approximation (CSDA) range for electrons and positrons within the level of energy between 20 eV and 1 GeV.

This work aims to determine the stopping power and CSDA range for positrons and electrons. The Rohrlich and Carlson which is a special type of modified Bethe-Bloch formula used as analytical method. Some biological compounds like: kidney, lung, and thyroid are used in the study which can be valid for all energy regions from low to intermediate and reach high energies positions (relativistic energies). The comparison made between the obtained results and the theoretical results found by the Penelope 2012 program due to lack of the experimental data. Finally, the results have been graphed for better visual understanding.

Cite as: H.M. Dlshad, J.M. Rashid, East Eur. J. Phys. 1, 406 (2026), https://doi.org/10.26565/2312-4334-2026-1-49

2. METHODOLOGY

2.1 Stopping Power calculations

The stopping power of positrons divided in to two parts: The first is collision stopping power, which takes into account the electromagnetic interactions of arriving positrons with the bound electrons of the target. The second is to take into account the emission of photons, also known as radiative stopping power or Bremsstrahlung radiation, that occurs when positrons accelerate within the electromagnetic fields of target nuclei. The total mass stopping power is given as follows [6]:

$$S_{Total}(E) = S_{coll}(E) + S_{rad}(E) \tag{1}$$

In this article, modified Bethe-Bloch formula is chosen to calculate the total mass SP [12]. Since our analysis focuses on the low and intermediate energy range, the radiative SP can be disregarded due to its negligible contribution at these energy levels. However, the Penelope simulation incorporates both collision and radiative stopping power components in its computational framework, regardless of energy range. This methodological difference represents a key distinction between our analytical approach and the Monte Carlo simulation. While Bethe and Heitler exclude the radiative term based on its minimal impact at lower energies [13].

$$S_{rad} = S_{coll}^{\pm}\left(\frac{Z\,E}{800}\right), \tag{2}$$

where S_{rad}, S_{coll} are the radiation, and collision stopping power. The superscripts (+) and (-) stand for positrons and electrons, respectively. Z, E are the target atomic number, and the incident energy of positrons or electrons in unit of MeV. Therefore, the total mass stopping power represents by collision stopping power only (Rohrlich and Carlson) [12] as follow:

$$\frac{1}{\rho}S_{coll} = \frac{2\pi N_a r_e^2 m c^2}{\beta^2}\frac{Z_{eff}}{A}\left[\ln\left(\frac{T}{I}\right)^2 + \ln\left(1+\frac{T}{2}\right) + F^{+}(\tau) - \delta\right]. \tag{3}$$

Here, ρ is the medium density ($\mathrm{gm/cm^3}$), r_e is the classical radius of electron which is equal to (2.8179×10^{-15}meters), mc^2 is the electron rest energy (0.5110034 MeV), T is the incident particle energy, $F^{\mp}$ is a function defined later for electron and positron, and Z_{eff} is effective atomic number of the target taken from Markowicz-Van Grieken expression and given by [14, 15]

$$Z_{eff} = \frac{\sum_{i=1}^{l}\frac{w_i Z_i^2}{A_i}}{\sum_{i=1}^{l}\frac{w_i Z_i}{A_i}}, \beta^2 = 1 - \frac{1}{\left(1+\frac{T}{mc^2}\right)^2} \tag{4}$$

Where w_i represents the weight fraction of each constituent element, Z_i and A_i are atomic and mass number of i element in the biological compound target respectively. Additionally, the value of β^2 is not taken from other references like: Seltzer and Berger work [16]. It calculated for all amount of energy with the above equation.

Similarly, the effective mean excitation energy of the medium (I), which is defined as the average energy required to excite electrons in the target material, is calculated by using logarithmic averaging methods such as Bragg's elemental additivity rule [15]:

$$\ln I = \frac{\langle\frac{Z}{A}\rangle \ln(I_i)}{\langle\frac{Z}{A}\rangle}, and\ \langle Z/A\rangle = \sum_i w_i\left(\frac{Z_i}{A_i}\right) \tag{5}$$

Here, I_i is the corresponding elemental mean excitation energy. For biological tissues, this calculation is particularly complex due to the heterogeneous nature of organic compounds and the presence of hydrogen bonding, which can significantly modify electronic properties. Cohen and Taylor Used for the numerical values [17] for the various physical constants for both positron and electron, one finds that:

$$F^{+}(\tau) = 2\ln 2 - \frac{\beta^2}{12}\left[23 + \frac{14}{(\tau+2)} + \frac{10}{(\tau+2)^2} + \frac{4}{(\tau+2)^3}\right], \tag{6}$$

And for electron as:

$$F^{-}(\tau) = 1 - \beta^2\left[1 + \frac{\tau^2}{8} - (2\tau+1)\,ln2\right]. \tag{7}$$

Where $\tau = T/mc^2$ is the ratio between the kinetic energy of the incident particle and its rest energy, δ density-effect correction is equal to [16]:

$$\delta = 2\ln\left(\frac{\hbar\omega}{I}\right) + 2\ln(\tau+1) - 1 \tag{8}$$

Where $\hbar\,\omega = 28.816\,(\frac{\rho Z}{A})^{1/2}$ is the plasma energy in eV, the quantity of (δ) too small at low energies, therefore, we can neglect it in our calculations.

2.2 CSDA Range calculations

The charged particle loses energy as it moves through the stopping medium and eventually comes to a stop. The range of the incident charged particle is the distance between the medium's surface, where the incident particle enters, and the incident particle's final location within the medium. And depends on the density of the target. CSDA (Continuous Slowing Down Approximation) Range for incident particles with kinetic energies E_0 is calculated by integrating the reciprocal of the stopping power over energy [6]:

$$CSDA\ (g/cm^2\ ) = \int_{E_f}^{E_0} \frac{dE}{S_{tot}(E)}\ . \tag{9}$$

Where S_{tot} is the total stopping power of the medium, (E_0, E_f) is the initial energy and final energy of it, respectively. If the stopping power chose in $(MeV.cm^2/g)$ units and energy in (eV), one can find, the CSDA range in units of g/cm^2.

3. RESULTS AND DISCUSSIONS

Studies dedicated to positron stopping power calculations have received substantially less scholarly attention than their electron, with many analyses conventionally assuming positron behavior in matter closely resembles that of electrons despite their antimatter nature. However, this approximation requires careful validation across different energy ranges and materials. When determining positron or electron SPs with precision, our methodology first needs to calculate the effective charge of target materials by using Eq. (3), which accounts for the composite electronic structure of compound like biological tissues. Simultaneously, we derive the mean excitation energy with Eq. (5). This foundational step is crucial as it accounts for the unique interaction mechanisms between positron or electron and target materials. Unlike electrons, positrons exhibit different scattering behaviors due to their positive charge, which creates repulsive interactions with nuclei rather than attractive ones. Then these values have been used in Eq. (3) to calculate total mass stopping power of the medium for positrons. Moreover, the CSDA range of a particle moving through the cell thickness depends on the excess energy of the particle. We applied our method to some tissues like: kidney, lung and thyroid targets because they have wide applications in the area of Nuclear Medicine. The composition of materials for each kidney, lung, and thyroid tabulated in Tables (1).

Table 1 Material composition of Kidney, Lung, and Thyroid [18-20]

Fraction by weight			
Element	**Kidney**	**Lung**	**Thyroid**
H	0.103	0.103	0.104
C	0.132	0.105	0.119
N	0.030	0.031	0.024
O	0.724	0.748	0.745
Na	0.002	0.002	0.002
P	0.002	0.002	0.001
S	0.002	0.003	0.001
Cl	0.002	0.003	0.002
K	0.002	0.002	0.001
Ca	0.001	-	-
I	-	-	0.001
Density ρ (g/cm^3)	1.04	0.25	1.05

The core and valence electron excitation energies were calculated for the elemental composition of kidney, lung, and thyroid tissues. These values were applied within Gryzinski's excitation function to determine the total ionization cross-section for inelastic scattering [21]. Subsequently, the derived cross-sections were used to compute the mean excitation energy for each biological material. The fundamental data for the compound elements are provided in (Table 2).

Table 2 Atomic number, atomic mass, and excitation energy of elemental composition of the three compounds [20]

Atoms	**Atomic number (Z)**	**Atomic mass (A)**	**Calculated**	
			I_{core} (eV)	**$I_{Valence}$ (eV)**
H	1	1.00784	-	-
C	6	12.011	19.320	11.70
N	7	14.0067	25.85	15.51
O	8	15.999	33.742	17.143
Na	11	22.989769	41.361	4.898
P	15	30.973762	19.047	10.612
S	16	32.065	23.946	11.973
Cl	17	35.453	29.116	13.877

Atoms	Atomic number (Z)	Atomic mass (A)	Calculated	
			I_{core} (eV)	$I_{Valence}$ (eV)
K	19	39.0983	25.850	4.081
I	53	126.90447	22.313	10.884
Mg	12	24.312	62.041	6.802
Ca	20	40.078	36.463	5.442

Now, the calculation results of this work on SPs and CSDA ranges as a function of incident positron or electron energy for each compound are shown graphically in Figures (1-6). In all figures the red dashed line represents our work results for positron, the blue solid line Penelope 2012 results, and the green lines represent this work SPs for electron.

Fig. 1 illustrates the total SP for kidney, it expressed in units of (MeV·cm²/g), for incident positron and electron energies ranging from 100 eV to 1 MeV. The result of calculations are compared with those obtained from the Penelope 2012 program (Monte Carlo code). Generally, there is a good agreement between them along the whole energy ranges, although some discrepancies are observed at lower energies. The disagreement between the three methodologies ranges from approximately 20-30% at lower energies, decreasing gradually to about 10-15% at energies exceeding 100,000 eV. And Fig. 2 presents the CSDA range in the kidney as a function of positron or electron energy. The two quantities exhibit a direct proportional relationship. The figure demonstrates a gradually increasing slope, indicating that the rate of increase in CSDA range becomes greater at higher energies. And the similarity between positron and electron results are high although does not appear in plot but there are some differenet especialy in the energy range of 5 KeV to 10 KeV. This non-linear behavior reflects the complex physics of interactions of positron and electron with matter.

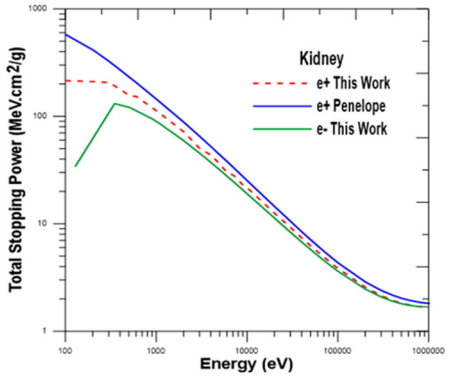

Figure 1. Total mass stopping power for incident positron, electron energies in Kidney. The results of this work and Penelope 2012

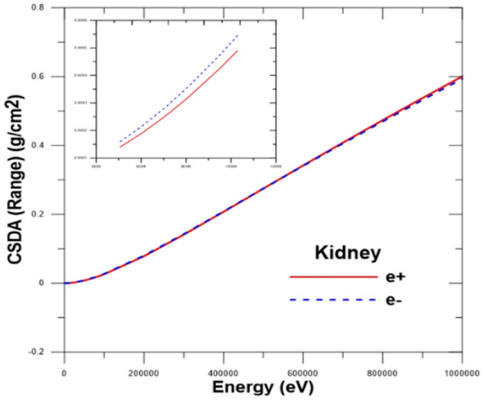

Figure 2. CSDA Range of positron, electron in Kidney

Fig. 3 shows that the calculated results generally agree well with those from the Penelope simulation; however, some disagreements are observed in the low-energy region under 1 keV. The graph demonstrates that three results of SP decrease with increasing the positron energy. The curve appears to converge somewhat at the highest energies (1 MeV), indicating better agreement between methods as relativistic effects become more dominant and quantum-mechanical corrections less significant.

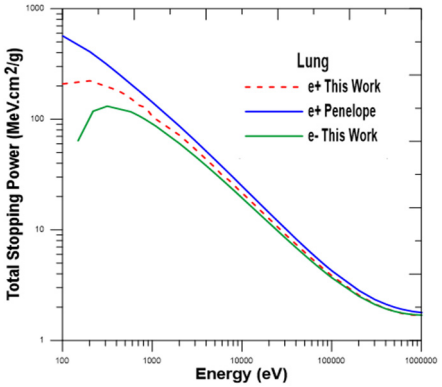

Figure 3. Total mass stopping power for incident positron, electron energies in Lung. The results of this work and Penelope 2012

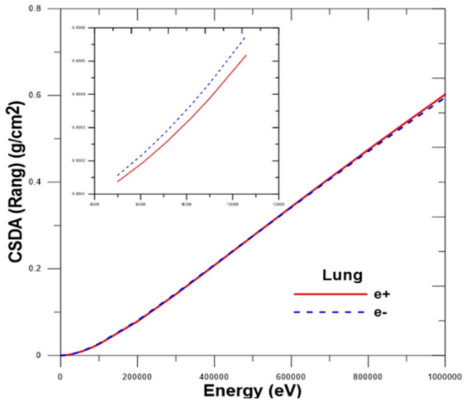

Figure 4. CSDA Range of positron, electron in Lung

The differential between the two techniques amounts to about 20-30% in the low-energy region, systematically reducing to around 10-15% at energies beyond 100,000 eV. Fig. 4 illustrates the relationship between the CSDA range and positron and electron energies. The graph demonstrates a clear non-linear relationship between each positron and electron energy and range. As the energy increases, the CSDA range increases at an accelerating rate, particularly at higher energies. This follows the expected physics, where higher-energy particle penetrates deeper into tissue. Moreover, for 1 MeV positrons

in lung tissue, the CSDA range reaches approximately 0.46 g/cm². This represents the maximum penetration depth, which is particularly relevant for medical applications such as PET imaging and radiation therapy planning.

In Fig. 5, our work analytical calculations constantly predict higher SP values than the Penelope simulations across the entire energy range.

This difference is most pronounced at lower energies (100-1000 eV) and gradually narrows at higher energies due to the different compositions and densities of tissues, which affect how positrons and electrons lose energy as they travel through them. The unique composition of thyroid makes its stopping power behavior fundamentally different from other tissues, particularly in the low-energy where atomic-level details matter most. These differences including the high density of thyroid compared to kidney and lung as shown in (Table 1). Lower density means fewer interactions per unit path length, resulting in lower stopping power. Moreover, thyroid has higher iodine content (high Z), which significantly affects stopping power.

On the other hand, both methodologies show the expected inverse relationship between SP and positron and electron energy - as the energy increases, SP decreases. This is due to the fundamental principle that higher-energy positrons interact less efficiently with the electron of the medium. The discrepancy between the two approaches is approximately 20-30% at lower energies, reducing step by step to about 10-15% at energies above 100,000 eV. This suggests that theoretical assumptions or correction factors implemented in the analytical approach may differ from those in the MC simulation, particularly in handling low-energy interactions. Fig. 6 the graph exhibits a non-linear relationship between positron and electron energies and range in thyroid tissue. At 1 MeV. Despite some difference between positron and electron result, in the maximum energies the CSDA range reaches approximately 0.47 g/cm². This follows the theoretical expectation that higher-energy positrons or electrons will penetrate deeper into tissue before stopping.

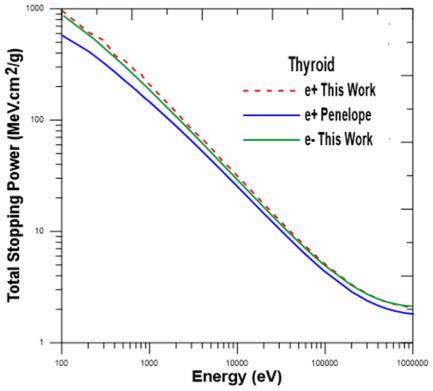

Figure 5. Total mass stopping power for incident positron, electron energies in Thyroid. The results of this work and Penelope 2012

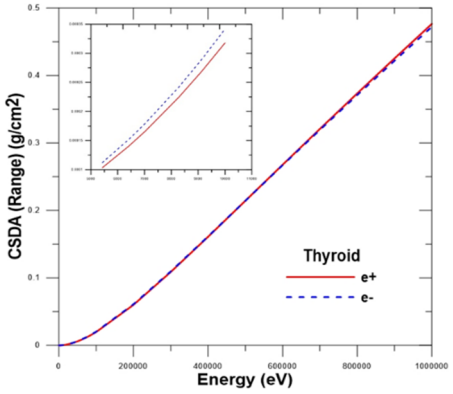

Figure 6. CSDA Range of positron, electron in Thyroid

Equations (6) and (7) define the functions $F^{\pm}(\tau)$ that characterize how collision losses differ between positrons and electrons. These functions, which depend only on the incident energy and are independent of the atomic number, are plotted in Fig. 7. When positrons undergo collisions that loss more than half of their energy, they contribute approximately 0.4 to F^{+}, a value that stays relatively unchanged.

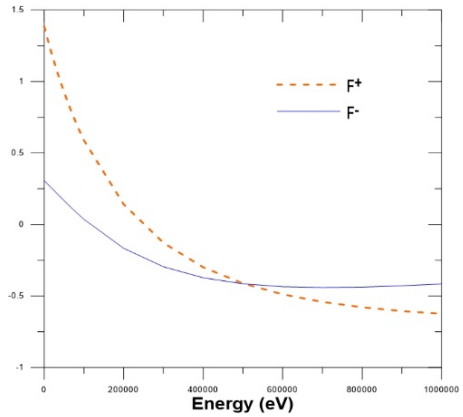

Figure 7. The functions $F^{+}(\tau)$ and $F^{-}(\tau)$, which occur in the average energy loss formulas for both positrons and electrons, as function of Energy in (eV)

4. CONCLUSIONS

The SP have been studied for several biological compounds like: Kidney, Lung, and thyroid. Positron and electron are used as a projectile particle with a range of energy between (100 eV to 1.0 MeV). The model that used in this work is the modified Bethe Bloch formula. The methodology employed in this study offers significant computational advantages

through analytical approach to SP determination. By including targeted parameter adjustments that account for compound-specific characteristics, we transform complex SP calculations into a straightforward mathematical framework accessible without extensive computational resources. The relationship between SP and positron and electron energies demonstrate an inverse correlation as energy increases, SP correspondingly decreases.

Additionally, this analytical framework extends naturally to Continuous Slowing Down Approximation (CSDA) range calculations, enabling rapid determination of positron and electron penetration depths in various biological media. Only our analytical calculations are presented for relation between CSDA range and positron and electron energy without comparison to other methodologies or experimental data because there are no any previous work and references. This makes it difficult to assess the accuracy of these specific calculations. We denote that, the curves appear remarkably similar in shape and magnitude. Despite the different tissue compositions and densities between kidney, lung and thyroid. Although the results of both positron and electron are appeared to be exactly the same but in the energy range between 5 KeV to 10 KeV they have differences as shown in zoomed plot. Finally, our future work should focus on experimental approve to confirm these calculations and extension to additional biological tissues and composite materials of medical significance.

Declaration of competing interest

The authors declare that they have no known competing financial interests or personal relationships that could have appeared to influence the work reported in this paper.

ORCID

Hawar M. Dlshad, https://orcid.org/0000-0002-6430-8106

REFERENCES

[1] S.N. Ahmed, "Properties and sources of radiation," Physics and Engineering of Radiation Detection, 1–64 (2015). https://doi.org/10.1016/B978-0-12-801363-2.00001-2

[2] M.E. Juweid, and B.D. Cheson, "Positron-Emission Tomography and Assessment of Cancer Therapy," N. Engl. J. Med. (354), 496–507 (2006). https://doi.org/10.1056/NEJMra050276

[3] K.G. Lynn, and H. Lutz, "Slow positrons in single-crystal samples of Al and Al-Al_xO_y," Phys Rev B, **22**(9), 4143–4160 (1980). https://doi.org/10.1103/PhysRevB.22.4143

[4] M.K. Saadi, and R. Machrafi, "Development of a new code for stopping power and CSDA range calculation of incident charged particles, part A: Electron and positron," Applied Radiation and Isotopes, **161**, (2020). https://doi.org/10.1016/j.apradiso.2020.109145

[5] L. Cai, "Monte Carlo simulation of positron induced secondary electrons in thin carbon foils," The University of Hong Kong, Pokfulam Road, Hong Kong SAR, 2010. https://doi.org/10.5353/th_b4546086

[6] M. Ç. Tufan, and H. Gümüş, "A study on the calculation of stopping power and CSDA Range for incident positrons," Journal of Nuclear Materials, **412**(3), 308–314 (2011), https://doi.org/10.1016/j.jnucmat.2011.03.016

[7] P.B. Pal, V.P. Varshney, and D.K. Gupta, "Total stopping power formulae for high energy electrons and positrons," Nucl. Instrum. Methods Phys. Res. B, **16**(1), 1–4 (1986). https://doi.org/10.1016/0168-583X(86)90220-X

[8] R.K. Batra, "Approximate stopping power of low energy electrons and positrons in matter," Nucl. Instrum. Methods Phys. Res. B, **28**(2), 195–198 (1987). https://doi.org/10.1016/0168-583X(87)90104-2

[9] H. Gümüş, O. Kabaday, and A.G. Tufan, "Calculation of the Stopping Power for Intermediate Energy Positrons," Chinese Journal of Physics, **44**(4), (2006). [Online]. http://PSROC.phys.ntu.edu.tw/cjp

[10] H. Gumus, T. Namdar, and A. Bentabet, "Positron stopping power in some biological compounds for intermediate energies with generalized oscillator strength model," International Journal of Molecular Biology, **3**(3), (2018). https://doi.org/10.15406/ijmboa.2018.03.00057

[11] H. Osman, and H. Gümüş, "Stopping power and CSDA range calculations of electrons and positrons over the 20 eV–1 GeV energy range in some water equivalent polymer gel dosimeters," Applied Radiation and Isotopes, **179**, 110024 (2022). https://doi.org/10.1016/J.APRADISO.2021.110024

[12] M.J. Berger, and S.M. Seltzer, *Stopping powers and ranges of electrons and positrons*, 2nd ed. (Gaithersburg, MD, 1983). https://doi.org/10.6028/NBS.IR.82-2550A

[13] P.B. Pal, V.P. Varshney, and D.K. Gupta, "Semiempirical stopping power equation for positrons," J. Appl. Phys. **60**(1), 461–463 (1986). https://doi.org/10.1063/1.337623

[14] M.V. Manjunatha, B.M. Sankarshan, and T.K. Umesh, "New method to determine effective atomic number of samples via external bremsstrahlung," X-Ray Spectrometry, **43**(4), 246–252 (2014). https://doi.org/10.1002/xrs.2546

[15] V. De Smet, R. Labarbe, F. Vander Stappen, B. Macq, and E. Sterpin, "Reassessment of stopping power ratio uncertainties caused by mean excitation energies using a water-based formalism," Med. Phys. **45**(7), 3361–3370 (2018). https://doi.org/10.1002/mp.12949

[16] S.M. Seltzer, and M.J. Berger, "Evaluation of the collision stopping power of elements and compounds for electrons and positrons," Int. J. Appl. Radiat. Isot. **33**(11), 1189–1218 (1982). https://doi.org/10.1016/0020-708X(82)90244-7

[17] E.R. Cohen, and B.N. Taylor, "The 1973 Least-Squares Adjustment of the Fundamental Constants*," J. Phys. D: Appl. Phys. **5**, 43–58 (1973). https://doi.org/10.1063/1.3253130

[18] Arectout, *et al.*, "Investigation of photon interaction parameters in Human Body Tissues using GAMOS, FLUKA, and XCOM Studies," Nuclear Analysis, **4**(1), 1–11 (2025). https://doi.org/10.1016/j.nucana.2024.100141

[19] ICRU, "Tissue substitutes in radiation dosimetry ana measurement ICRU report 44," (Bethesda, 1989).

[20] C. Cao, R.E. Vernon, W.H.E. Schwarz, and J. Li, "Understanding Periodic and Non-periodic Chemistry in Periodic Tables," Front. Chem. **8**, (2021). https://doi.org/10.3389/fchem.2020.00813

[21] H.M. Dlshad, and J.M. Rashid, "Monte Carlo code for calculating the elastic and inelastic scattering cross section along with mean free path of positron scattering in kidney, lung and thyroid organs," East Eur. J. Phys, (4), 82-289 (2025). https://doi.org/10.26565/2312-4334-2025-4-61

ГАЛЬМІВНА ЗДАТНІСТЬ ТА ДІАПАЗОН CSDA ДЛЯ ПОЗИТРОНІВ ТА ЕЛЕКТРОНІВ В ОРГАНАХ НИРОК, ЛЕГЕНЬ ТА ЩИТОВИДНОЇ ЗАЛОЗИ ЛЮДИНИ

Хавар М. Длшад[1], Джамал М. Рашид[2]

[1]*Університет Сулеймані, коледж освіти, кафедра фізики, Сулейманія 46001, Регіон Курдистан, Ірак*

[2]*Університет Сулеймані, коледж природничих наук, кафедра фізики, вулиця Клясан, Сулейманія 46001, Регіон Курдистан, Ірак*

У цьому дослідженні розраховано гальмівну здатність позитронів у кількох біологічних тканинах в діапазоні енергій від 100 еВ до 1 МеВ. Основою методу є використання модифікованого виразу Бете-Блоха для гальмівної здатності та аналітичного виразу для ефективного атомного номера, включаючи ключові параметри, такі як середні енергії збудження атомів-мішеней, які суттєво впливають на результати гальмівної здатності. Аналітичні формули здебільшого використовувалися для розрахунку гальмівної здатності та діапазону CSDA з наближенням безперервного уповільнення. Розраховані результати гальмівної здатності та діапазону для позитронів у кількох сполуках, таких як тканини нирок, легень та щитовидної залози, порівнюються з результатами інших розрахунків, такими як програма Penelope 2012. Для розрахунків було використано моделювання методом Монте-Карло. Результати були представлені у вигляді графіків для демонстрації контрастів. Вони задовольняють визнану потребу медичної фізичної спільноти в даних про тканинно-специфічну взаємодію позитронів, що мають негайне застосування для покращення точності кількісного визначення зображень позитронно-емісійної томографії (ПЕТ) та уточнення дози опромінення для радіофармацевтичних препаратів, що випромінюють β-промені.

Ключові слова: *гальмівна здатність; позитрон; діапазон CSDA; енергія збудження; тканини людини*

East European Journal of Physics. 1. 413-427 (2026)
DOI:10.26565/2312-4334-2026-1-50 ISSN 2312-4334

DEEP LEARNING-BASED MRI DENOISING USING NOISE STATISTICS DERIVED FROM PHYSICAL PHANTOM MEASUREMENTS

D.G. Sliusarenko[1,2]*, A.V. Netreba[1]
[1]*Faculty of Radiophysics, Electronics and Computer Systems, National Taras Shevchenko University of Kyiv, 64/13, Volodymyrska Street, Kyiv, Ukraine, 01601*
[2]*National Cancer Institute of Ukraine, Yulii Zdanovskoi Street, 33/43, Kyiv, Ukraine, 03022*
**Corresponding Author email: d.fulhem@gmail.com*
Received December 21, 2025; revised February 18, 2026; accepted February 20, 2026

High-quality MRI images are essential for accurate definition of target volumes and organs at risk, as well as for correct registration with CT scans when planning radiotherapy. The aim of this work is to develop a robust denoising method that improves visualization of brain structures and preserves anatomical details. A model based on a modified U-Net architecture with residual blocks, attention modules (CBAM) and spatial pyramidal pooling is proposed. The approach is characterized by the integration of statistical noise characteristics obtained from phantom measurements and modeling of degradations in pseudo-k-space (including Gaussian and Rayleigh noise distributions). The validation was performed on 1000 anonymized clinical DICOM images with variable noise levels. The proposed model provided an increase in PSNR by 8–10 dB and an increase in SSIM from 0.72 to 0.97. The edge preservation index (EPI), which reached values of 8.0 on noisy images due to artifacts, stabilized at 1.0 after processing, indicating effective removal of pseudo-contours without blurring true anatomical boundaries. In addition, an average SNR improvement of 7% and a CV reduction of 4–7% were observed on real images, confirming the stability of the method. The combination of physically based noise modeling in the frequency domain and modern deep learning architectures allows for effective noise removal while preserving critical anatomical boundaries. The method has high potential for clinical implementation in radiotherapy planning procedures, in particular to improve the accuracy of MRI/CT fusion.
Keywords: *MRI denoising; k-space noise modeling; Deep learning; Adaptive noise scaling; Fourier domain simulation; Medical image reconstruction; CNN*
PACS: 87.57.N-, 07.05.Mh, 87.61.Tg, 02.50.-r

1. INTRODUCTION

The quality of medical images directly affects the accuracy of diagnosis, the effectiveness of treatment planning and the ability to track the results of therapy. Magnetic resonance imaging (MRI) today occupies an important place among imaging methods due to its high contrast of soft tissues, the absence of ionizing radiation and flexibility in choosing signal weighting modes. Due to these properties, MRI is widely used in neuroimaging, orthopedics, oncology and cardiology [1,2]. In global clinical practice, magnetic resonance imaging machines with a field induction of 1.5 T remain the most common and affordable. They are used as the main imaging standard due to the optimal ratio of image quality, examination time and economic feasibility. Despite the lower signal-to-noise ratio compared to 3T systems, it is 1.5 T devices that are used in the vast majority of clinical cases, including oncological, cardiological and neurological studies. However, despite its high informative value, MRI remains very sensitive to noise and artifacts. These can arise both from hardware limitations (scanner characteristics, multichannel coils, excitation and reconstruction parameters) and from physiological factors, including involuntary patient movements, breathing, or magnetic field inhomogeneities [3,4]. Such factors directly affect the signal-to-noise ratio (SNR) and, in the case of insufficient image quality, can make diagnosis difficult or even impossible. This makes it relevant to conduct research on methods for increasing information content and reducing the impact of noise specifically for 1.5 T MRI, since the results obtained will have the greatest practical value and wide application.

To reduce these negative effects, denoising methods are being actively developed. Classical algorithms are based mainly on synthetic noise models, primarily Gaussian or Rician [5,6]. Their popularity is due to their mathematical simplicity and the possibility of rapid implementation. At the same time, they do not reflect the complex statistical nature of real noise in MRI. For example, Rician noise has been shown to be SNR-dependent and has properties that significantly change the intensity distribution, especially in low-signal areas [7]. Ignoring these effects results in methods that work well on artificially noisy images showing lower performance in clinical settings. The current trend in MRI denoising is to use methods that can reproduce the characteristics of real noise and take into account the physics of signal formation. Considerable attention is paid to deep learning, which has radically changed the approach to medical image processing in the last decade [8,9]. In particular, self-supervised and unsupervised methods are actively developing, which allow training models without ideal "reference" data, which is often unavailable in medicine [10,11]. Another direction is to model noise directly in k-space, i.e. in the original data before reconstruction. This allows you to create artifacts that are as close to real ones as possible and thus form more reliable training samples [12].

A special place is occupied by research using physical phantoms [13]. Although the study was conducted in the context of radiography, it clearly demonstrates the general methodological approach and the importance of phantom

Cite as: D.G. Sliusarenko, A.V. Netreba, East Eur. J. Phys. 1, 413 (2026), https://doi.org/10.26565/2312-4334-2026-1-50

studies for clinical verification of image processing algorithms. They provide controlled experimental conditions, allow for statistical description of noise distribution, and test algorithms in repeatable scenarios [14]. Recent work demonstrates that combining phantom data and k-space noise modeling can increase SNR, reduce artifacts, and bring reconstruction results closer to clinically relevant ones [15,16]. This confirms the importance of moving from purely synthetic models to more realistic ones based on physical experiments. At the same time, with the development of modeling methods, the architectures of neural networks used in medical imaging are also being actively improved. The use of attention mechanisms such as CBAM (Convolutional Block Attention Module) or channel-wise attention [9], as well as integrating multilevel noise statistics into the model [15], allow to increase the accuracy of reconstruction of small structures and better preserve diagnostically important information. This approach opens up the prospect of creating more universal denoising systems capable of working on both phantom and clinical data. The aim of this study is to develop a method for denoising MRI images that combines statistically sound modeling of signal degradations based on phantom experiments with an improved neural network architecture that integrates attention mechanisms and takes into account noise characteristics at deep levels of the model. The proposed approach is aimed at improving the clarity of reconstructed images and preserving diagnostically significant information when working with standard clinical data.

2. Materials and methods

2.1. Phantoms and their characteristics

The study used specially prepared phantoms designed to simulate different types of biological tissues and analyze the impact of noise on the quality of magnetic resonance images. The use of phantoms provides controlled experimental conditions, which allows for a systematic study of noise characteristics in a reproduced environment and comparison of the results with literature data [17,18]. We used three types of Siemens phantoms (Table 1), which allow for the simulation of different tissue-like environments and the analysis of the effect of noise on magnetic resonance images. The first of them is a cylindrical phantom with a volume of 5300 ml, filled with a solution containing 3.75g $NiSO_4 \cdot 6H_2O$ and 5 g NaCl per 1000 g of distilled water. This combination reproduces the electrical conductivity of soft tissues and allows you to control the electromagnetic properties during measurements. The second object was a spherical phantom D165 with a diameter of 165mm and a volume of 2570ml, in which a solution of 1.25 g of $NiSO_4 \cdot 6H_2O$ per 1000 g distilled water. Due to its high homogeneity and stability, this phantom was intended to reproduce conditions with controlled SNR, which provides an assessment of the basic noise characteristics and parameter calibration. The third phantom was a spherical D240 with a diameter of 240 mm and a volume of 7300 ml, filled with Marcol oil with the addition of 0.011g of Macrolex blue dye per 1000ml. It was used to simulate adipose tissue and model inhomogeneities, which allows assessing the appearance of artifacts and the robustness of denoising algorithms to differences in tissue structure. Phantom data were acquired on a 3-Tesla MR scanner (Siemens MAGNETOM Vida). The dataset included two different 3D T1-weighted sequences with high isotropic resolution (1x1x1 mm). The first sequence was a 3D gradient echo (MPRAGE/TFL) with inversion-recovery (TR=2300 ms, TE=2.96 ms, TI=900 ms, 9° Flip angle). The second was a 3D fast spin echo (SPACE) (TR=700 ms, TE=22 ms, 120° Flip angle).

Table 1. Names and characteristics of phantoms used for analyzing the statistical characteristics of superimposed noise.

PHANTOM	SIZE / VOLUME	SOLUTION COMPOSITION	PURPOSE
Cylindrical (5300 ml)	Height = standard; Volume: 5300 ml	3.75 g $NiSO_4 \cdot 6H_2O$ + 5 g NaCl per 1000 g dist. H_2O	Simulation of homogeneous soft tissues, conductivity regulation
Spherical D165	Diameter: 165 mm; Volume: 2570 ml	1.25 g $NiSO_4 \cdot 6H_2O$ per 1000 g dist. H_2O	Assessment of homogeneity and basic noise characteristics, SNR calibration
Spherical D240	Diameter: 240 mm; Volume: 7300 ml	Marcol oil + 0.011 g Macrollex Blue per 1000 ml	Simulation of adipose tissue and inhomogeneities, artifact analysis and algorithm robustness

Phantoms are widely used in medical imaging for quality control, standardization of experiments, and improvement of algorithms [17], and can also serve as a proxy metric for scan quality to increase research reproducibility [19].

2.2. Frequency domain noise modeling

In magnetic resonance imaging, the signal is formed in the frequency domain (k-space) as complex samples. The image is reconstructed in coordinate space by means of the inverse Fourier transform [20]:

$$I(x,y) = \mathcal{F}^{-1}K\big(k_x, k_y\big), \tag{1}$$

where $K(k_x, k_y)$ - complex k-space data, and $I(x,y)$ - reconstructed MRI image.

This study uses standard clinical DICOM images, which retain only the magnitude of the reconstructed signal and do not contain phase information or the original complex-valued k-space data. Therefore, any k-space obtained by inverse Fourier transform of magnitude images is a pseudo-k-space, which is not a physical representation of the frequency data

acquired by the scanner. In this regard, this work does not claim to directly denoise true k-space, but uses the frequency representation solely as a mathematical tool for modeling and analyzing image degradation. It is known that noise in raw MRI data arises as additive complex Gaussian noise in k-space, due to thermal fluctuations of the receiving system (effective resistance of the receiving coil and the specimen) [21]. Since the original complex data is not available, this noise cannot be accurately reproduced or removed in a physically rigorous sense. In this paper, complex Gaussian noise is considered as a reference physical model that explains the origin of non-Gaussian effects in image space, but is not used to directly model the true k-space of the scanner. After reconstruction and calculation of the magnitude of the complex signal:

$$M(x,y) = \sqrt{I_r^2(x,y) + I_i^2(x,y)}, \tag{2}$$

in the presence of complex Gaussian noise, a ray-like distribution of intensities naturally arises, especially in regions with a low signal-to-noise ratio [22]. In this work, these effects are not artificially introduced, but are considered as a consequence of the standard reconstruction process. In addition to noise, real MRI images may contain degradations associated with patient motion, reconstruction instability, or further processing. Such effects are not interpreted as physical k-space noise and are applied only at the image level as part of a training strategy to increase the robustness of the neural network. Therefore, the presented approach is not a direct denoising of physical k-space, but is aimed at improving the quality of reconstructed MRI images obtained from standard DICOM data. The frequency representation is used as a convenient mathematical tool, while all assumptions about the nature of MRI noise are consistent with the limitations of the available data.

2.3. Statistical analysis of noise

To quantify the impact of different types of noise on MRI phantom images, three key statistical characteristics were measured: mean, skewness, and kurtosis, as a function of noise intensity. The use of histogram parameters such as skewness and kurtosis is a validated approach for analyzing image heterogeneity and shape distribution [23]. In particular, the mathematical representation of excess kurtosis and statistical significance through sample moments allows us to clearly quantify how much noise deviates from a normal distribution [24]. To quantitatively characterize the impact of scanning artifacts on the quality of MR images, a series of experiments using phantoms was conducted. One group of phantoms was scanned under optimal conditions (“clean” phantoms), the other group was scanned under conditions of light artifacts: metal (iron) impurities, accelerated gradient echo (GRE) sequences, minimal noise amplification, or magnetic field instability. Figure 1 shows an example of a pair of clean and noisy images in the case of noise damage to a metal artifact The statistical values are given for this specific pair of images.

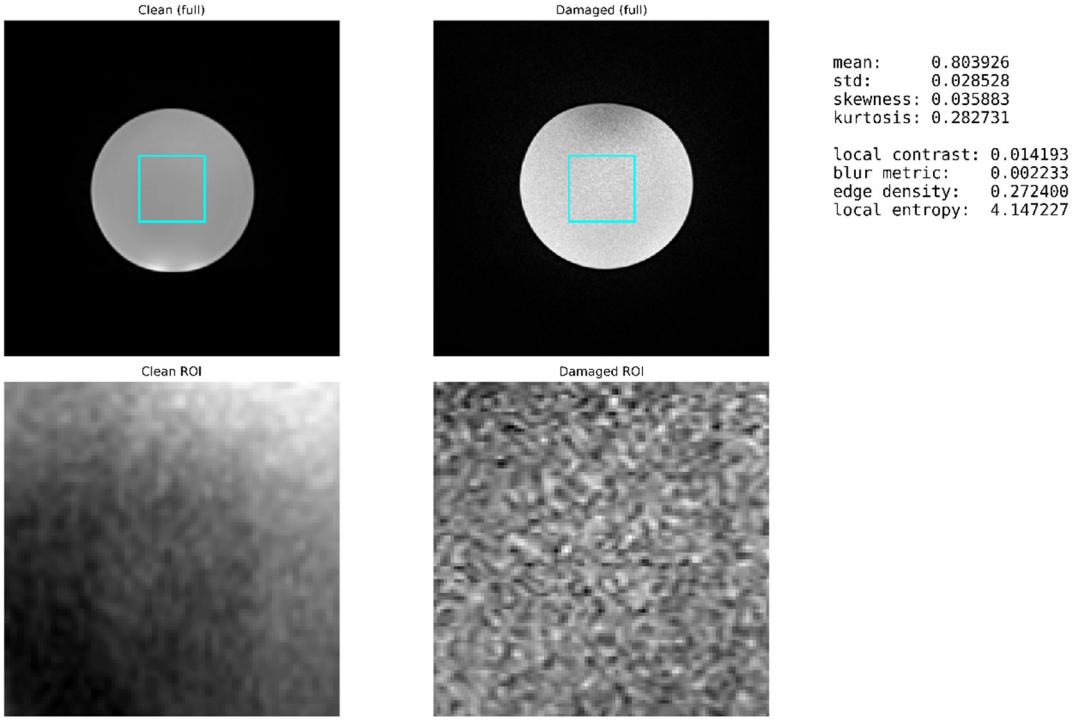

Figure 1. Examples of phantom images and obtaining statistical characteristics.

In each case, the following statistical indicators of pixel intensities were calculated within the specified ROIs (regions of interest):

$$\text{mean} = 0.77, \text{std} = 0.033, \text{skewness} = 0.27, \text{kurtosis} = 0.51.$$

The mean intensity value reflects the generalized signal level in the ROI and allows for the assessment of possible baseline level bias caused by scanning artifacts. Standard deviation (σ) characterizes the variability of intensities, i.e. internal signal fluctuations and noise-like effects caused by magnetic field inhomogeneity or metallic inclusions. Distribution asymmetry (skewness, γ_1) determines the degree of shift of the intensity histogram: a positive value (0.27) indicates a predominance of pixels with higher intensity, reflecting local amplifications or slight signal saturation. Kurtosis (kurtosis, γ_2) describes the peakedness of the distribution - a value of 0.51 indicates a moderate concentration of intensities around the mean and the presence of slight "tails" due to scanning artifacts.

The obtained values demonstrate that even without intentionally synthesized noise, real scanning conditions (artifacts) change the signal statistics - increase the dispersion (std), create asymmetry (positive skewness) and slight "sharpness" (kurtosis). Such behavior confirms the feasibility of using these statistical indicators as input features for the StatsProjection module in the network, allowing to adapt the filtering depending on the nature of the artifacts. Phantoms were scanned three times in each mode; the resulting images were pre-normalized to [0,1] and scaled to 512*512 pixels. ROIs were placed in the central region of the phantom (homogeneous zone), excluding borders and large artifacts. Mean, std, skewness, and kurtosis were calculated for each series and then averaged. The resulting values are shown above. This statistical evaluation confirms the presence of stable artifact-induced signal fluctuations that are not labeled as pure noise but affect image quality at the histogram level. Therefore, integrating these statistics into network training allows for better adaptation of the model to real scanning conditions and increases its generalizability.

These values were integrated into the preprocessing block, which generates noise patterns with statistical properties as close as possible to real ones. This approach allows the model to take into account not only the average noise level, but also its asymmetry and the shape of the distribution, which is important for reproducing realistic noise artifacts during training.

2.4. Improved neural network architecture

The proposed model is designed to denoise MRI images of size 512*512 pixels (1 channel, grayscale) taking into account the physical characteristics of the noise measured on phantoms and statistical parameters integrated into the training process. The architecture combines the advantages of U-Net [25] with residual connections, attention mechanisms, multiscale processing (ASPP) [26] and statistical integration module (StatsProjection) [27]. This combination allows for effective noise suppression while preserving contours, texture, and diagnostically significant image details. Residual blocks with SpatialDropout (Regularization Method for CNNs) [28] and LeakyReLU (Leaky Rectified Linear Unit) [29] are used to avoid information loss during convolutions due to residual connections, improve the generalization ability of the model through spatial dropout, and prevent the disappearance of the gradient by using LeakyReLU activation.

The model implements a residual approach to denoising: it does not directly reconstruct a clean image, but learns to reproduce the noise map $R_\theta(I_{noisy})$ after which the reconstructed image is defined as:

$$\hat{I} = I_{noisy} - R_\theta\big(I_{noisy}\big), \tag{3}$$

where I_{noisy} - noisy input image, $R_\theta(\cdot)$ - function approximating the noise structure, $\hat{I}$- de-noised image. The real (reference) image is marked as I_{gt} and is used as a reference when calculating the loss function. This approach accelerates convergence and stabilizes learning, since the network operates with less dynamic values (the amplitude of the noise is smaller than that of the signal). The architecture is based on U-Net with a symmetric encoder and decoder connected by skip connections. Each level consists of the following elements:

Residual blocks (ResBlock):

$$y = F(x, W_i) + x, \tag{4}$$

where $F(x, W_i)$ - sequence of convolution, normalization and activation operations of LeakyReLU.

Adding input signal x prevents information loss in deep convolutions and reduces the risk of gradient vanishing. Using SpatialDropout2D preserves spatial consistency by suppressing random overcorrelations between filters. CBAM is essentially an attention mechanism operating in two dimensions [30]:

- Channel Attention amplifies the most informative channels:

$$M_c = \sigma\left(W_2\left(\delta\left(W_1\big(GAP(x)\big)\right) + W_1\big(GMP(x)\big)\right)\right), \tag{5}$$

where GAPi GMP - global averaging and maximum operations, σ - sigmoid, δ - ReLU.

- Spatial Attention focuses on local areas of the image:

$$M_s = \sigma\big(f^{7\times7}([AvgPool(x); MaxPool(x)])\big). \tag{6}$$

Final gain:

$$x' = M_s \odot (M_c \odot x). \tag{7}$$

ASPP is used in the "neck" of the network for multi-scale analysis, providing sensitivity to different spatial frequencies of noise. It uses convolutions with extensions d = [1,6,12,18], after which the results are combined:

$$y_{ASPP} = \sum_i Conv_{3\times3}^{(d_i)}(x). \tag{8}$$

Channelwise Attention (CA) takes into account the global interaction between channels by calculating weights via a normalized softmax vector [31]:

$$w_i = \frac{e^{g_i}}{\sum_j e^{g_j}}, \text{where } g_i = \text{GAP}(x_i). \tag{9}$$

This improves the balance between high-frequency and low-frequency features, especially in areas with heterogeneous SNR.

The StatsProjection module implements the idea of physically based feature adaptation, where parameters obtained from statistical noise analysis directly influence the process of normalizing activations in a neural network [32]. Unlike standard normalization mechanisms which calculate scaling and shifting parameters directly from the data in the current layer, this module uses external experimentally measured noise characteristics - the average μ, standard deviation σ, asymmetry skewness and kurtosis obtained from phantom studies. The input to the module is a four-dimensional vector of statistical parameters:

$$s = [\mu, \sigma, \text{skewness}, \text{kurtosis}],$$

which describes the statistical “profile” of noise for a particular image or its fragment. This vector is fed to a fully connected layer (Dense) with linear activation, which performs the projection of statistical parameters into the feature scale space:

$$v_s = W_s \cdot s + b_s, \tag{10}$$

where W_s and b_s - parameters of the training layer. The resulting vector v_s has the same number of components as the number of channels in the current feature tensor x, and therefore can be used to modulate normalization. After this, the normalized activations are corrected, where the vector v_s acts as a scaling modifier:

$$y = \text{Norm}(x) \odot (1 + v_s), \tag{11}$$

where $\text{Norm}(\cdot)$ - Layer Normalization, which provides zero mean and unit variance within the layer, $\odot$ - per-channel multiplication. Thus, StatsProjection adds a physically meaningful scaling to the standard normalization process, which aligns the network with the real noise statistics inherent in a particular data type.

Intuitively, this approach resembles the Feature-wise Linear Modulation (FiLM) method, but with the difference that the modulating parameters are not trained directly from the data, but are derived from experimentally measured noise statistics. This provides better consistency of the network with the physical characteristics of the MRI signal, allows it to respond adaptively to different types of artifacts, and stabilizes training when working with heterogeneous data sets.

The loss function combines several components:

$$\mathcal{L}_{total} = \lambda_1 \mathcal{L}_{MSE} + \lambda_2 \left(1 - SSIM\left(\hat{I}, I_{gt}\right)\right) + \lambda_3 \mathcal{L}_{GDL}, \tag{12}$$

where:

$\mathcal{L}_{MSE}$ - minimizes the energy difference between $\hat{I}$ and I_{gt};

$SSIM$ - structural similarity controlling local contours;

$\mathcal{L}_{GDL}$ - gradient loss that prevents blurring of boundaries;

λ_i - weighting factors (0.5, 0.3, 0.2 respectively).

During training, the model receives a pair(I_{noisy}, I_{gt}), where I_{noisy} - images with physically motivated degradations obtained by frequency perturbations of reconstructed magnitude images, and I_{gt} - phantom or clinical image with high signal-to-noise ratio. Thus, the network is trained on degradations consistent with the physical properties of MRI, rather than on arbitrary synthetic noise [33-35].

All convolutional layers of the model use 3*3 kernels with “same” padding and HeNormal weight initialization. [36], which ensures stable variation of activations even in deep layers. The use of residual connections between the encoder and decoder allows to transfer not only contextual, but also textural information, which is critically important for MRI images, where soft tissue contrast often has a fine gradation. The combination of CBAM, ASPP and Residual-blocks

creates a balance between global contextuality and local detail, ensuring the preservation of anatomical structures with effective noise suppression. The final view of the model is presented in Figure 2.

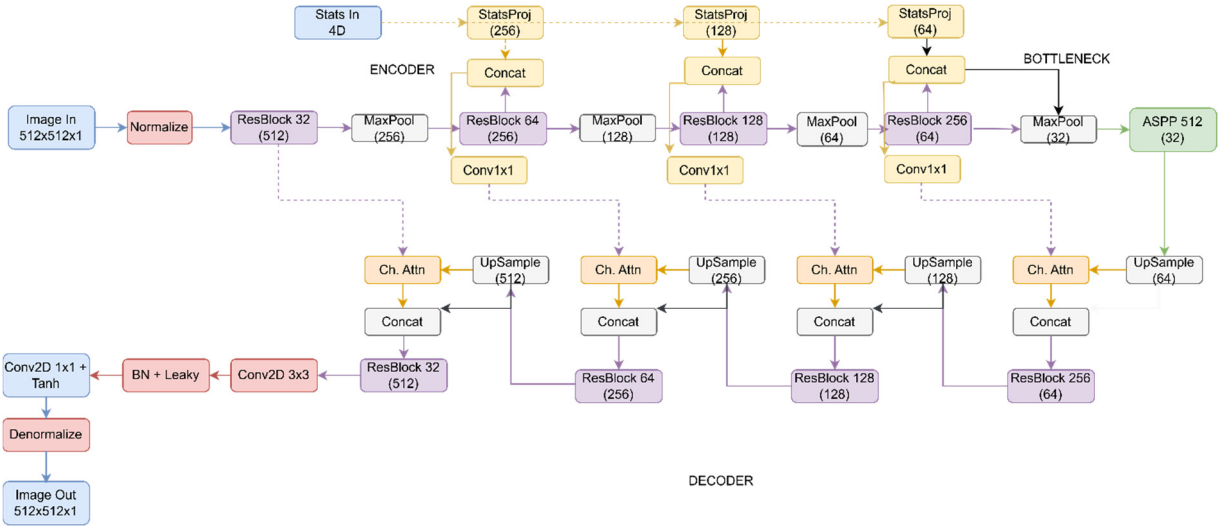

Figure 2. Structural diagram of the model used for processing, reconstruction and denoising of noisy images

2.6. Model training

To ensure the reliability and reproducibility of the training results, the model was trained on structured subsets of MRI images formed according to the principles of sample independence. The main data set consisted of normalized 16-bit MRI images of 512x512 pixels in grayscale. Each subset contained unique samples, which excluded any overlap between the data for training, validation, and testing. To control the generalization ability of the model, training was carried out on the training sample (60%) with periodic checking on the validation subset (20%). The final efficiency was assessed on an independent test set (20%), which was not used at any stage of training. Thus, the obtained results characterize the real ability of the model to generalize data that were not encountered during parameter optimization. Overtraining control was provided by mechanisms that automatically adjusted the learning rate and fixed the best model weights with minimal validation error. During the simulation, various types of physically based noise were implemented: Rician, Gaussian, Poisson and salt-and-pepper, each of which was generated with random intensity parameters according to the amplitude characteristics of the output signal in k-space. After the inverse Fourier transform, images with specified statistical properties of the noise were obtained, which formed training pairs. Both types of input data were used in the training process: noisy images and vectors of statistical noise parameters (mean, standard deviation, skewness, kurtosis), which were fed into the StatsProjection Module for adaptive modification of normalization. Training was performed using the AdamW optimizer (learning rate $= 1 \times 10^{-4}$, $\beta_1 = 0.9$, $\beta_2 = 0.999$) and dynamic adjustment of the learning rate according to the scheme. Mixed-precision training and Batch Renormalization in deep layers were used to stabilize convergence.

The criterion for completing training was the achievement of stabilization (plateau) of the validation error, i.e. the moment when subsequent epochs did not lead to an improvement in the results on the validation data. For this, an early stopping mechanism was used, which automatically stops optimization after 10 epochs without improving the quality of the model and restores the weights fixed at the best stage. Additionally, an adaptive learning rate adjustment algorithm was used, which reduces it by 5 times (factor 0.2) after 5 epochs without improving the results, but not below the minimum value 1×10^{-6}. This combination of methods prevents overfitting, stabilizes convergence, and allows the model to gradually approach the global minimum of the loss function without losing generalization ability. Training was performed with a batch size of 16, for 50-100 epochs, depending on the experiment, on an NVIDIA RTX 5070 Ti graphics accelerator.

2.7. Methods for quantifying image quality

To quantify the effectiveness of the proposed denoising model, both reference and non-reference metrics were used, which allow us to assess the quality of signal recovery, preservation of structural similarity, local contrasts, and signal homogeneity within regions of interest. This approach allows us to comprehensively characterize both the intensities and structural reliability of the results obtained, combining analytical accuracy with clinical relevance.

The Peak Signal-to-Noise Ratio (PSNR) metric is defined as [37]:

$$PSNR = 10 \cdot \log_{10}\left(\frac{MAX_I^2}{MSE}\right), MSE = \frac{1}{N}\sum_{i=1}^{N}(I_i - \hat{I}_i)^2, \quad (13)$$

where MAX_I - maximum intensity value, I_i and $\hat{I}_i$- pixel values in the reference and reconstructed images, respectively. PSNR is a classical metric for assessing the degree of signal distortion and is based on the energy distance between the

input and reconstructed images. High PSNR values indicate minimal signal loss, but this metric does not take into account the perceptual aspects of the image [38].

To eliminate this drawback, the Structural Similarity Index is used [37,39], which describes the structural similarity between two images, taking into account brightness, contrast, and texture:

$$SSIM(I,\hat{I}) = \frac{(2\mu_I\mu_{\hat{I}}+C_1)(2\sigma_{I\hat{I}}+C_2)}{(\mu_I^2+\mu_{\hat{I}}^2+C_1)(\sigma_I^2+\sigma_{\hat{I}}^2+C_2)}. \quad (14)$$

Here μ_Ii $\mu_{\hat{I}}$ - average intensity values, σ_I and $\sigma_{\hat{I}}$- dispersion, $\sigma_{I\hat{I}}$- covariance between images. SSIM evaluates not only numerical similarity, but also the degree of preservation of textural and spatial relationships, which makes it more consistent with human perception of quality. Since for medical images it is important not only to preserve the average signal level, but also to avoid loss of contours, the Edge Preservation Index (EPI) is used:

$$EPI = \frac{\sum|\nabla\hat{I}|\cdot|\nabla I|}{\sum|\nabla I|^2}. \quad (15)$$

This indicator is based on comparing image gradients and reflects the degree of edge preservation after denoising [40,41]. A high EPI value indicates that the model does not blur the structure and adequately restores local intensity transitions, which is critical for diagnosing gray-white matter boundaries or tumor contours. Another fully reference metric is the Normalized Cross-Correlation (NCC) [42]:

$$NCC = \frac{\sum(I-\mu_I)(\hat{I}-\mu_{\hat{I}})}{\sqrt{\sum(I-\mu_I)^2\sum(\hat{I}-\mu_{\hat{I}})^2}}. \quad (16)$$

It determines the degree of linear relationship between two images regardless of scale variations. NCC is particularly useful for assessing the stability of reconstructions, where it is important to maintain spatial correlation even if the absolute values of the intensities change. For real clinical MRI images, where there is no “gold standard”, non-reference indicators Signal-to-Noise Ratio were additionally used [43] and Coefficient of Variation (CV) [44,45], which are calculated within ROIs (regions of interest). They have the form:

$$SNR = \frac{\mu_{signal}}{\sigma_{noise}}, CV = \frac{\sigma_{ROI}}{\mu_{ROI}}. \quad (17)$$

Here μ_{signal} and σ_{noise}- mean and standard deviation of signal and noise, respectively, while CV characterizes the relative intensity heterogeneity within the selected region. An increase in SNR after denoising reflects a real improvement in tissue contrast, and a decrease in CV indicates a decrease in local fluctuations and stabilization of signal homogeneity. Such indicators are closer to the clinical perception of quality, since they characterize not only the technical accuracy of the reconstruction, but also the diagnostic readability of the image. In general, the combination of reference (PSNR, SSIM, EPI, NCC) and non-reference (SNR, CV) metrics provides a comprehensive assessment of image quality, covering both structural reliability and practical suitability for clinical analysis [36,46,47]. This approach is consistent with current recommendations for medical imaging tasks, where there is no single standard for a true image, and quality assessment should take into account both physical and perceptual aspects.

2.8. DICOM medical images used

To train and test the model, 5000 anonymized DICOM (Digital Imaging and Communication in Medicine) brain MRI images obtained from 200 patients were used. All images were previously anonymized, which guaranteed patient confidentiality. The dataset consisted of T1-weighted images, which are necessary for clear visualization of the anatomical structure of the brain and differentiation of gray and white matter. A heterogeneous set of T1-weighted brain MRI images obtained on 1.5 T scanners from different manufacturers (Siemens Symphony and GE Optima MR450w) was used for the study. The 2D sequences included conventional spin echo (SE) from Siemens (TR/TE 394/17 ms; slice thickness 5 mm) and fast spin echo (FSE) from GE (TR/TE 623/7.776 ms; slice thickness 5 mm). To simulate real-world scenarios of image degradation, noise of various ranges and characteristics was artificially added to the original data. In addition, artifacts associated with k-space truncation (Gibbs bell) and motion were simulated. This variety of noise allowed the model to be trained to work effectively in conditions as close as possible to clinical practice, where the quality of the original data can vary significantly. Particular attention was paid to the uniformity of brightness and contrast between image series, as these parameters affect the stability and accuracy of the algorithms. To this end, subsets of images with high SNR levels were generated, which were used as reference examples (ground truth) to evaluate the effectiveness of noise reduction. A separate and comprehensive validation set was also created to ensure an adequate reflection of the variety of clinical cases that the model may encounter in practical application.

3. Results and discussion

3.1. Quantitative assessment

Three key metrics were used to evaluate the effectiveness of the proposed denoising method: PSNR, SSIM, and EPI. PSNR and SSIM metrics are widely used in modern MRI denoising work, including studies of score-based self-learning

MRI denoising, systematic analysis of wavelet-based approaches for brain MRI images, and recent work on self-learning diffusion MRI denoising [4]. Their effectiveness is also confirmed in a comprehensive review of medical image quality assessment systems, which highlights the critical importance of accurate metrics for diagnosis and clinical outcomes [48]. EPI allows for the addition of an important dimension of local edge and contour preservation -critical for medical diagnostics-and has already been proven to be an objective and reliable metric in MR image restoration tasks compared to subjective assessment [49]. Additionally, the use of PSNR, MSE, and SSIM as "image quality metrics" when comparing denoising algorithms is supported by studies of quality assessment of full-reference methods for medical images, which demonstrate a correlation between objective metrics and subjective quality [50,51]. Overall, the results for all three metrics confirm that the use of statistically sound noise parameters in k-space allows for a significant improvement in image quality (Fig. 3).

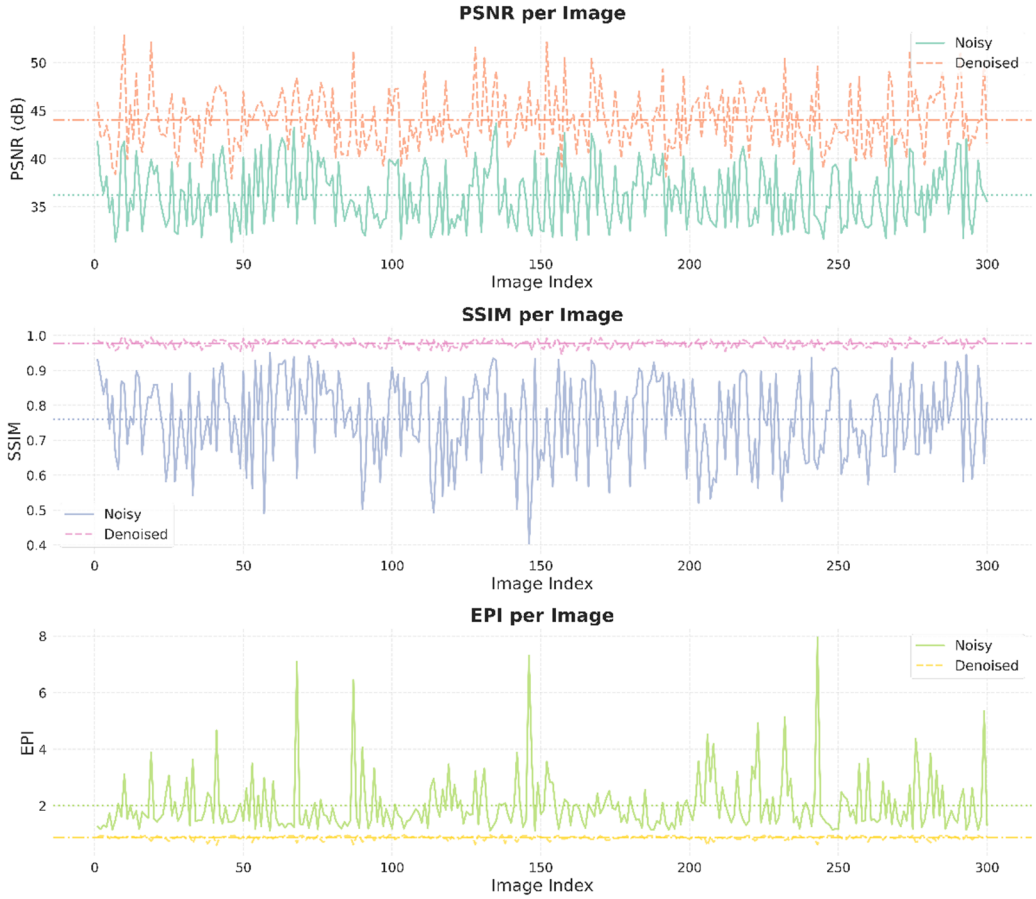

Figure 3. Graphs of the obtained PSNR, SSIM and EPI results for 300 real images after adding noise of different intensity gradations to simulate real scanning conditions.

PSNR is a basic numerical criterion of reconstruction quality, reflecting the ratio between the maximum possible signal intensity and the root mean square error. It is important to note that the calculation was performed based on the dynamic range of 16-bit DICOM data, which results in higher absolute values compared to standard 8-bit formats. In the presented experiments, noisy images had PSNR values in the range of 28-41 dB, which indicates signal degradation. In contrast, after denoising, improvement of up to 40-54 dB was observed. It is important to note the stable difference of approximately 8-10 dB between the processed and unprocessed images, which indicates the consistency of the algorithm regardless of variations in the source data.

Since PSNR does not take into account perceptual aspects, for a more adequate assessment, the SSIM metric, which reflects the similarity of structural characteristics between the original and the reconstructed image, was also used. For noisy data, the SSIM varied in a wide range of 0.5-0.95, demonstrating instability and loss of structural information. After applying the denoising algorithm, the SSIM values stabilized at 0.95-1.0, which confirms the ability of the model to preserve small structural elements and image topology even at different noise levels. Special attention was paid to the EPI metric, which assesses the quality of contour and fine detail restoration. In noisy images, EPI ranged from 1.0 to 8.0, with sporadic peaks reflecting local artifacts caused by noise. After denoising, EPI values stabilized around 1.0, indicating a high level of edge preservation and no additional blurring or structural loss during processing.

The proposed approach provides not only an increase in the signal-to-noise ratio, but also the restoration of structural similarity and the correct preservation of fine details, which is critically important for clinical diagnostics. Additionally, histograms of the distribution of metric improvements were constructed for all images for quantitative analysis. The

distribution graph for PSNR improvements shows a clear shift to the right with an average increase of 7.85 dB, which confirms a stable noise reduction in most images. A similar trend is observed for SNR improvements, where the average increase is also 7.85 dB, indicating an increase in the signal-to-noise ratio and improved visibility of structural details. For SSIM improvements, the average increase is 0.217, which reflects improvement in the structural similarity of denoised images to the original "clean" data. This is particularly important because SSIM better accounts for human perception of local details and textures than PSNR. In the case of NCC improvements, a more compressed distribution is observed with an average gain of 0.046. Although this value is small compared to other metrics, even a small improvement in NCC indicates a higher stability of the correlation between the denoised and reference images. Thus, all four histograms demonstrate that the improvement is systematic and covers most of the data, rather than being limited to isolated cases (Fig. 4). This confirms the consistency of the model's performance across samples and highlights its suitability for practical use.

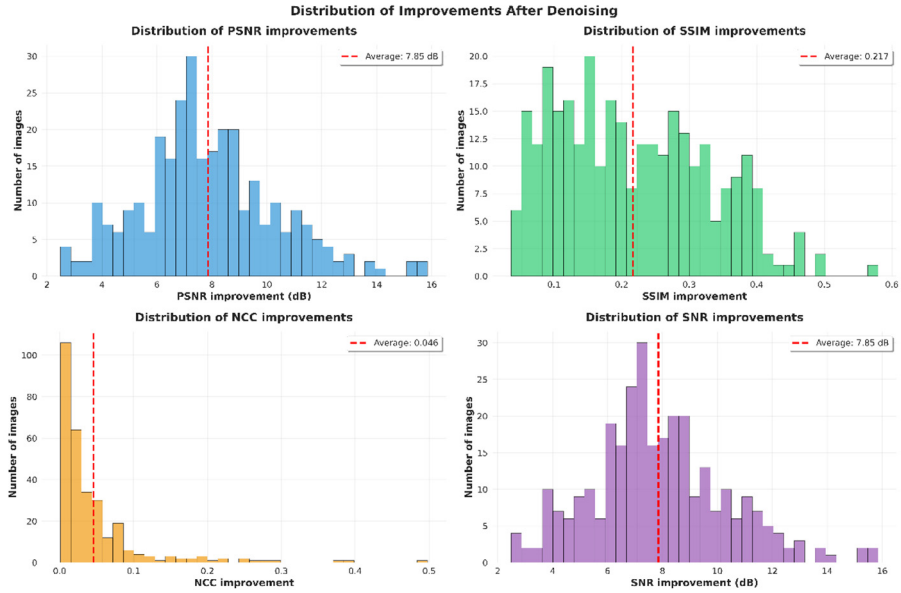

Figure 4. Histograms of the distribution of improvements in the PSNR, SSIM, NCC, SNR metrics for all images.

Visual evaluation also shows that our method provides good perceptual quality (Fig. 5).

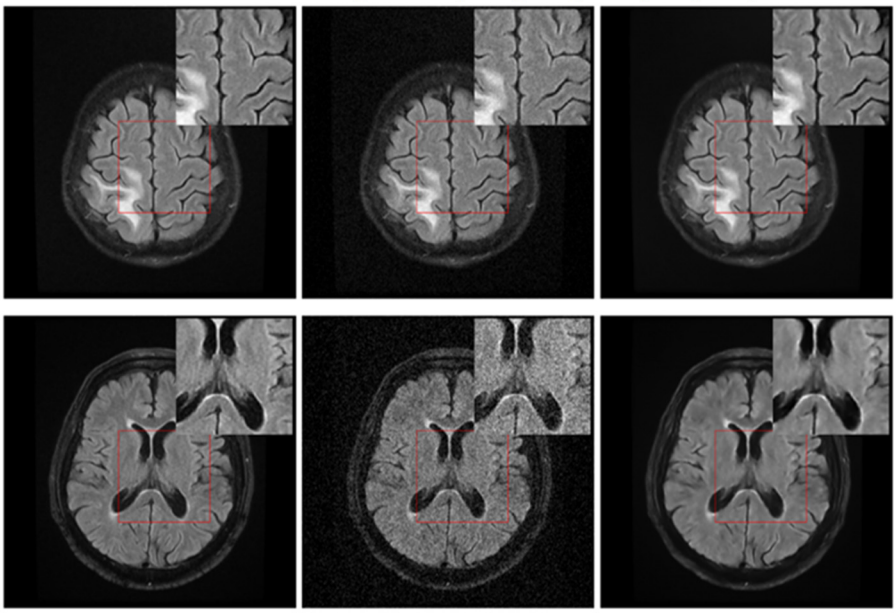

Figure 5. Subjective comparison of several DICOM T1 images before adding strong artificial noise (left), with noise (center) and after processing with the developed model (right)

Our method consistently preserves fine anatomical details, especially in areas of complex tissue boundaries, without characteristic smoothing artifacts. In white matter regions, our method demonstrates exceptional preservation of subtle intensity variations critical for detecting pathological changes. The gray matter-cerebrospinal fluid interface is one of the most challenging areas to denoise due to abrupt intensity transitions. Our method excellently preserves sharp boundaries,

avoiding the characteristic discretization artifacts of deep networks. CNN (Convolutional Neural Network) methods introduce subtle geometric distortions near these boundaries, which can affect morphometric analysis. For T1 images, where hyperintensities are clinically relevant, our method demonstrates optimal preservation of pathological lesion contrast while effectively suppressing background noise. For visual evaluation, randomly selected images are presented, to which strong noise was added, simulating difficult acquisition conditions, to demonstrate the effectiveness of the proposed model even in cases of significant deterioration in the quality of the original data.

To test the generalization ability of the model and its practical applicability, an evaluation of its effectiveness was carried out on real clinical MRI images of the brain obtained on a Siemens MAGNETOM Aera tomograph (1.5T). Unlike the test set with artificially simulated noise, these images did not have standards, so the analysis was carried out using ROI-based metrics that do not require a "clean" reference sample. For each image, regions of interest were automatically formed: the central zone of homogeneous signal, the peripheral background area and the edge area between contrasting tissues. Based on these areas, the main quantitative characteristics were calculated - SNR, coefficient of variation and edge sharpness, which reflect the physical quality of the reconstructed signal. The general principle of obtaining the difference between the noise in the original and denoised image is shown in the Figure 6.

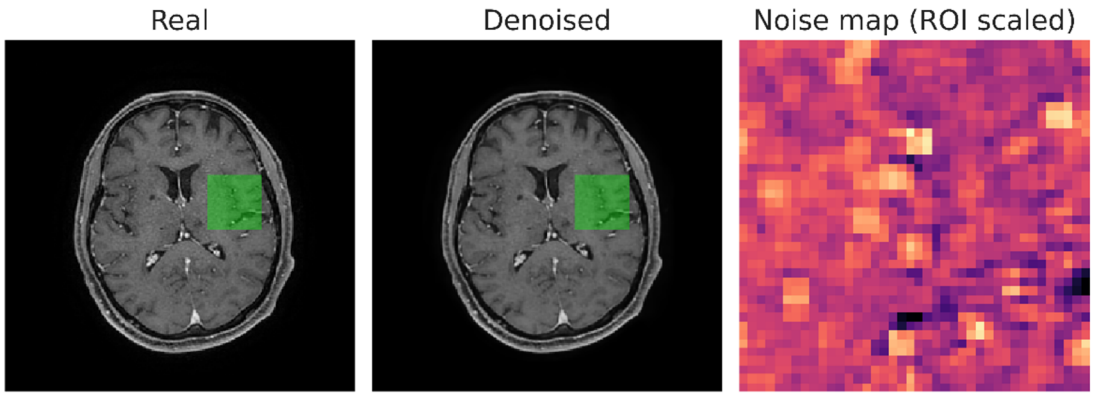

Figure 6. One slice from the evaluation set of clinical MRI T1 images and the noise map of the difference between images

200 images from different series of T1-weighted scans were selected for the study. The results showed a increase in the signal-to-noise ratio after applying the model, indicating a reduction in noise while maintaining contrast between tissues. Quantification of 200 clinical T1 slices demonstrated consistent but modest improvements in ROI-based SNR (+6-8%) and reductions in coefficient of variation (-4-7%) (Fig. 7). Importantly, the model preserves anatomical detail, as reflected by the nearly overlapping profiles of the "before" and "after" curves. Thus, the reconstructed images are characterized by higher stability of intensities with minimal loss of spatial details.

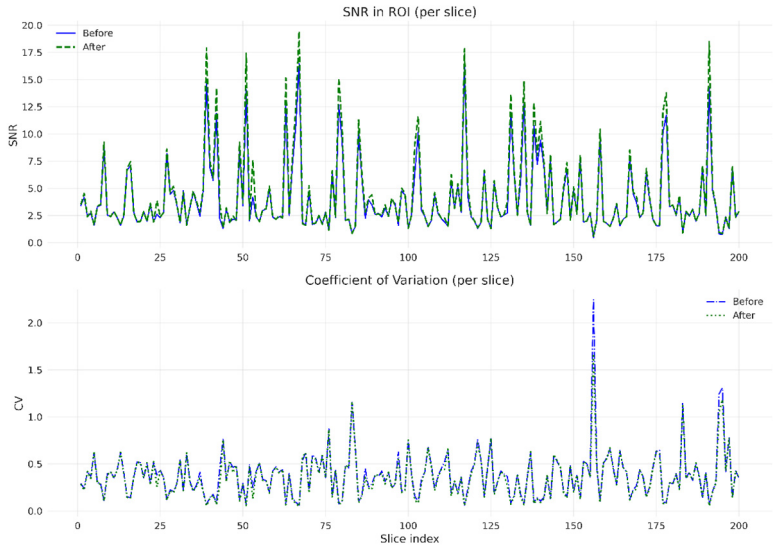

Figure 7. SNR and CV graph of 200 selected real clinical images of brain T1 images

Visual analysis confirms the obtained numerical results. After processing, there is a reduction in high-frequency fluctuations and inhomogeneities, preservation of fine structures of the cerebral cortex, white matter and contours of intertissue boundaries. Signals in homogeneous areas become more uniform, and intensity histograms demonstrate a narrowing of the distribution around the mean, which is a characteristic sign of noise reduction without loss of contrast.

To evaluate the quality of real clinical image processing in specific areas of interest, the Axial T1-weighted FSE (Fast Spin Echo) sequence was chosen. This scan is a standard 2D high-resolution anatomical sequence that is widely used in routine diagnostics. It provides excellent soft tissue contrast and clear anatomical detail due to optimized spin-lattice relaxation time. Based on a gradient echo complex, FSE is less sensitive to magnetic field inhomogeneities, making it a reliable reference for evaluating the effectiveness of noise suppression in realistic clinical scenarios. The results are shown in Figure 8.

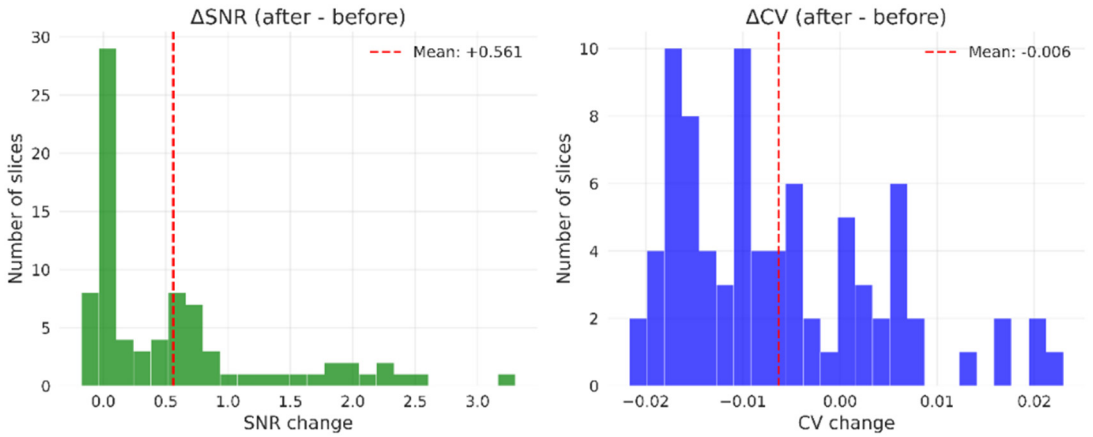

Figure 8. Histogram of the distribution of SNR and CV values of Axial T1-weighted Fast Spin Echo sequences after processing by the model

The results obtained show that the model trained on phantom and synthetically noisy data successfully generalizes its knowledge to real clinical images. We obtained an increase in the signal-to-noise ratio by an average of 11% and a decrease in noise by 3%. Since the selected scans already have quite good image quality in the original case, this confirms the correctness of the integration of phantom noise statistics through the StatsProjection module, which provides a physically justified adaptation of feature normalization to a specific noise level. As a result, the model not only improves the visual perception of MRI images, but also increases the metric reliability of the signal, which is of direct importance for clinical applications, in particular for the accurate alignment of MRI and CT during radiotherapy planning. Thus, the evaluation on real data confirms the effectiveness and robustness of the proposed method, which can be integrated into standard clinical protocols as a stage of pre-processing of medical images.

3.2. Comparison with existing methods

The performance of the proposed neural network-based denoising approach considering k-space noise statistics was evaluated against established denoising methodologies to demonstrate its advantages in improving the quality of MRI images (Table 2). Quantitative analysis revealed significant improvements in all evaluated metrics compared to traditional and state-of-the-art methods.

Recent advances in deep learning have revolutionized MRI denoising, and several notable architectures have achieved impressive results. The DnCNN (Denoising Convolutional Neural Network) architecture [52] – one of the pioneering deep learning approaches for image denoising -typically achieving PSNR improvements from 36–38 dB to 42–44 dB in MRI applications. However, these methods typically operate in the spatial domain of the image and do not model the data acquisition process in k-space.

RED-CNN approach (Residual Encoder–Decoder Convolutional Neural Network) [53] specifically designed for medical imaging, demonstrates comparable performance with PSNR values of 39–45 dB, but lacks the physical justification characteristic of our approach.

Unsupervised learning methods such as Noise2Noise (Learning to Denoise from Corrupted Images) and Noise2Void (Learning Denoising without Clean Data) have attracted attention due to their ability to work without paired sets of "clean" images. According to a review by Wang et al. (2020) [54], Noise2Void provides effective noise reduction in low-field MRI applications, although PSNR improvements (3–6 dB) remain lower than those of supervised models.

The use of MRI phantoms for noise characterization has been investigated in various contexts, however, current evaluations tend to focus on SSIM and PSNR metrics, rarely considering k-space noise statistics. Recent work such as Muckley et al. (2021) [55], demonstrated the effectiveness of k-space processing for the reconstruction of accelerated MRI scans, but did not consider the denoising problem.

Cold Diffusion Models are an innovative direction in image reconstruction, but their main goal is reconstruction from incomplete samples, rather than noise reduction in complete data. Our method, in contrast, is distinguished by the explicit modeling of noise statistics in k-space based on experimental data from phantoms, which provides a physically reliable basis for the denoising process.

Both classical and modern denoising algorithms were used for comparison. Among the traditional methods, Gaussian and Wiener filters were used, which provide basic noise smoothing, but do not take into account the spatial-

correlation structure of the signal. Non-Local Means (NLM) demonstrate higher efficiency [56] and BM3D (*Block-Matching and 3D Filtering*) [57], which remain the benchmark among classical approaches.

In the field of deep learning, DnCNN is most commonly used [38], FFDNet (*Flexible and Fast Denoising CNN*) [58]and RED-CNN [53], which achieve high results due to residual connections and flexible adaptation to different noise levels. Another representative of this class is RCAN (Residual Channel Attention Network), which implements channel attention to improve the recovery of small details [59].

Recent advances in image restoration are related to the use of transformer architectures, in particular SwinIR (Swin Transformer for Image Restoration). [60] and Restormer (Efficient Transformer for High-Resolution Image Restoration) [61], which combine local attention mechanisms with global contextual processing. For MRI signal recovery tasks, NAFNet (Nonlinear Activation Free Network) and recurrent neural approaches for analyzing incomplete FID (Fréchet Inception Distance) signals in MR spectroscopy are also promising [62].

In the context of MRI reconstruction, the VarNet (Variational Network for MRI Reconstruction) model [63] is an example of integrating the physics of signal formation into the reconstruction process, which is consistent with the concept used in our work.

Table 2. Comparison of the proposed method with a number of classical and modern approaches to image denoising.

Method	PSNR (dB)	SSIM	SNR (dB)	EPI	NCC	Time (s)	Complexity
Classical Methods							
Gaussian Filter	28.5	0.65	22.1	3.2	0.82	0.1	Low
Wiener Filter	31.2	0.72	25.8	2.8	0.85	0.2	Low
Non-Local Means	34.1	0.78	28.5	2.1	0.88	15.2	Medium
BM3D	36.8	0.82	31.2	1.9	0.91	8.7	Medium
Deep Learning Methods							
DnCNN	38.2	0.86	32.8	1.7	0.93	2.1	High
FFDNet	41.3	0.9	35.9	1.5	0.95	3.2	High
RED-CNN	39.5	0.88	34.1	1.5	0.94	1.8	High
RCAN	41.1	0.91	36.8	1.6	0.96	4.8	High
State-of-the-Art Methods							
SwinIR	41.2	0.92	39.2	1	0.97	6.1	Very High
Restormer	42.8	0.93	39.9	1.2	0.97	5.3	Very High
NAFNet	43.4	0.94	40.5	1	0.98	7.4	Very High
VarNet	43.5	0.94	40.8	0.8	0.98	7.2	Very High
Proposed (k-space phantom)	44.5 (+1.2)	0.996 (+0.066)	48.4 (+9.2)	0.95 (-0.05)	0.998 (+0.028)	3.2	High

The results show that the proposed model outperforms existing solutions not only in numerical metrics, but also in terms of consistency with the physics of MR signal formation. While classical methods (NLM, BM3D) provide limited contrast improvement, and modern CNN- and Transformer-based approaches (DnCNN, SwinIR, Restormer) focus on statistical texture restoration, the proposed model combines both approaches - physically based noise modeling in k-space and adaptive neural network training, which makes it more versatile for real clinical applications. The model demonstrates the best ratio between noise reduction and anatomical structure preservation, confirming the prospects of physically based architectures in MRI image denoising tasks.

3.3. Limitations and prospects

Despite the achieved results, the proposed approach has some natural, technical and physical limitations inherent in all modern methods of deep denoising of MRI images. At the same time, most of them do not reduce the efficiency of the developed system, but rather outline the directions for its further improvement.

First of all, the current architecture is focused on compensation of stationary noise components, the parameters of which are relatively stable within the slice or series. This is quite justified for most clinical protocols, however, in cases of non-stationary disturbances - for example, artifacts of respiratory or cardiac movements, inter-slice shifts or weak phase decoherence - the efficiency decreases due to a change in the local noise structure. In the future, it is advisable to expand the model by kinematic regularization or motion-aware attention blocks, which will be able to take into account the temporal and spatial correlation between frames, ensuring stability in multiphase or dynamic studies.

An important stage of further verification is testing the model on a wider range of contrasts and different MR systems. This will allow quantitatively confirming the generalizability of the approach. The available results, based on a combination of reference metrics (PSNR, SSIM, NCC, EPI) and ROI-based indicators (SNR, CV), already demonstrate a high correlation between the mathematical quality assessment and the visual reliability of the reconstructed structures, which confirms the practical stability of the model even on data without standards. However, future experiments provide an even deeper assessment of these metrics in the context of quantitative MRI diagnostics, where even minimal deviations in signal levels can affect the biophysical parameters of tissues.

The use of experimentally measured phantom noise statistics requires special attention. This approach ensures the physical reliability of training, since the parameters have a real physical origin. However, these statistics may vary depending on the magnetic field intensity, temperature, coil type, or reconstruction method. Further development in this direction involves distilling statistics directly from clinical images, for example, through Bayesian noise parameter estimation or adaptive learning using pre-trained generative models.

Another promising direction is the integration of the proposed architecture with variational and generative-adversarial models. Such a combination will allow creating more versatile reconstruction systems that are capable not only of suppressing noise, but also of restoring undermeasured or artifactual data, which is especially important for accelerated and undersampled sequences.

Finally, it is planned to evaluate the impact of the model not only on image quality, but also on quantitative MR parameter maps (T1/T2-mapping, ADC, perfusion maps). This will allow us to establish to what extent the improvement in SNR and the reduction in CV after processing translate into an increase in the reliability of the calculated biophysical quantities. Thus, the proposed approach is physically justified, consistent with modern trends in MR analysis, and has the potential for further development in the direction of fully interpretable, statistically adaptive denoising of medical images.

CONCLUSIONS

This paper presents an improved method for denoising MRI images based on modeling noise directly in the frequency domain using statistical characteristics obtained from physical phantoms. This approach provides a more realistic reproduction of the signal generation process and allows to reconcile synthetically generated noise with real clinical imaging conditions. The proposed neural network architecture, which combines residual blocks, CBAM attention mechanisms, ASPP and integration of noise statistics at deep levels, demonstrated improvements in key metrics. In particular, a stable increase in PSNR by 8-10 dB, SSIM close to 1.0, a decrease in MAE and high-quality preservation of fine structural details were observed. All tested images showed consistency of results, which confirms the reproducibility of the algorithm. Comparative results show that our proposed method outperforms both classical approaches and modern deep learning and transform models, providing a stable increase in PSNR by 2-7 dB (Table 2) and almost ideal SSIM/NCC values compared to the best existing solutions.

The evaluation of the model's effectiveness on real clinical MRI images without standards showed that the proposed approach provides a stable improvement in local quality metrics. In particular, the SNR and CV calculated within the ROI demonstrate an average increase in SNR by 6–8% and a decrease in CV within 4–7%, which indicates a reduction in heterogeneity and improved signal uniformity in tissues.

The practical value of the obtained results lies in the possibility of improving the quality of MRI in scenarios where high noise limits diagnostic informativeness. Preservation of structural details and clarity of boundaries can contribute to increasing the accuracy of contouring and treatment planning, as well as reducing the need for repeated scans. This makes the method promising for application in clinical tasks related to diagnostics, therapy planning and patient monitoring.

Further development directions include expanding the phantom database, modeling motion artifacts in k-space, testing on clinical data obtained using multi-scanner systems, and integrating uncertainty assessment methods. All this will make the model even more adaptive and flexible for different imaging scenarios. An additional vector is the use of generative approaches and expanding the training samples with different noise scenarios to increase the generalizability and reliability of the model in practical conditions.

Ethics statement

All clinical data were fully anonymized prior to the study. The use of phantom data and patient images was agreed with the Oberig Medical Center (Kyiv, Ukraine). No additional informed consent was required from patients, as the data did not contain personally identifiable information.

Acknowledgements

We express our sincere gratitude to the Oberig Medical Center (Kyiv, Ukraine) for providing physical phantoms for experiments and anonymized patient images, which made this study possible. We are also grateful to the Taras Shevchenko National University of Kyiv for supporting the scientific work.

Data Availability Statement

The brain MRI dataset utilized in this study was retrospectively collected at Oberig Medical Center and has been fully anonymized to protect patient confidentiality. Due to the institutional data governance policies and ethical restrictions, the raw dataset is not publicly available. However, the anonymized data can be made available to qualified researchers for non-commercial, academic purposes upon reasonable request to the corresponding author.

ORCID

D.G. Sliusarenko, https://orcid.org/0009-0009-1802-5859, **A.V. Netreba,** https://orcid.org/0000-0003-1347-3854

REFERENCES

[1] Z. Chen, K. Pawar, M. Ekanayake, C. Pain, S. Zhong, and G.F. Egan, J. Digit. Imaging, **36**, 204 (2023). https://doi.org/10.1007/s10278-022-00721-9

[2] J.I. Tamir, M. Blumenthal, J. Wang, T. Oved, E. Shimron, and M. Zaiss, Magn. Reson. Mater. Phys. Biol. Med. **38**, 367 (2025). https://doi.org/10.1007/s10334-025-01236-4
[3] T. Ssentamu, A. Kimbowa, R. Omoding, E. Atamba, P.K. Mukwaya, G.W. Jjuuko, and S. Geethanath, Front. Neuroimaging, **4**, (2025). https://doi.org/10.3389/fnimg.2025.1501801
[4] A. Salehi, M. Mach, C. Najac, B. Lena, T. O'Reilly, Y. Dong, P. Börnert, *et al*., J. Magn. Reson. **370**, 107812 (2025). https://doi.org/10.1016/j.jmr.2024.107812
[5] P. Song, J. Xu, X. Liu, Z. Zhang, X. Rao, R.P. Martinho, Q. Bao, and C. Liu, J. Magn. Reson. **359**, 107615 (2024). https://doi.org/10.1016/j.jmr.2023.107615
[6] D. Koprivica, R.P. Martinho, M. Novakovic, M.J. Jaroszewicz, and L. Frydman, J. Magn. Reson. **338**, 107187 (2022). https://doi.org/10.1016/j.jmr.2022.107187
[7] Y. Zhang, W. He, F. Chen, J. Wu, Y. He, and Z. Xu, J. Magn. Reson. **344**, 107319 (2022). https://doi.org/10.1016/j.jmr.2022.107319
[8] D. Singh, A. Monga, H.L. de Moura, X. Zhang, M.V.W. Zibetti, and R.R. Regatte, Bioeng. Basel Switz. **10**, 1012 (2023). https://doi.org/10.3390/bioengineering10091012
[9] M. Jiang, S. Wang, K.-H. Chan, Y. Sun, Y. Xu, Z. Zhang, Q. Gao, *et al*., Comput. Med. Imaging Graph. Off. J. Comput. Med. Imaging Soc. **121**, 102497 (2025). https://doi.org/10.1016/j.compmedimag.2025.102497
[10] B. Kang, W. Lee, H. Seo, H.-Y. Heo, and H. Park, Magn. Reson. Med. **92**, 1980 (2024). https://doi.org/10.1002/mrm.30197
[11] M.A. Sultan, C. Chen, Y. Liu, K. Gil, K. Zareba, and R. Ahmad, Magn. Reson. Mater. Phys. Biol. Med. **38**, 859 (2025). https://doi.org/10.1007/s10334-025-01257-z
[12] Q. Tian, Z. Li, Q. Fan, J.R. Polimeni, B. Bilgic, D.H. Salat, and S.Y. Huang, NeuroImage, **253**, 119033 (2022). https://doi.org/10.1016/j.neuroimage.2022.119033
[13] E.D. Hussner, S. Sundby, C.B. Outzen, J. Jensen, A. Tingberg, and H. Precht, J. Med. Imaging Radiat. Sci. **56**, 101814 (2025). https://doi.org/10.1016/j.jmir.2024.101814
[14] S. Kojima, T. Ito, and T. Hayashi, J. Med. Phys. **47**, 387 (2022). https://doi.org/10.4103/jmp.jmp_71_22
[15] S.M.A. Sharif, R.A. Naqvi, and W.-K. Loh, IEEE Trans. Radiat. Plasma Med. Sci. **8**, 521 (2024). https://doi.org/10.1109/TRPMS.2024.3380090
[16] K.V. Jordanova, S.E. Russek, and K.E. Keenan, Magn. Reson. Mater. Phys. Biol. Med. **38**, 727 (2025). https://doi.org/10.1007/s10334-025-01270-2
[17] K.E. Keenan, K.V. Jordanova, S.E. Ogier, D. Tamada, N. Bruhwiler, J. Starekova, J. Riek, *et al*., Magn. Reson. Mater. Phys. Biol. Med. **37**, 535 (2024). https://doi.org/10.1007/s10334-024-01181-8
[18] K.E. Keenan, M. Ainslie, A.J. Barker, M.A. Boss, K.M. Cecil, C. Charles, T.L. Chenevert, *et al*., Magn. Reson. Med. **79**, 48 (2018). https://doi.org/10.1002/mrm.26982
[19] C.P. Cheng, and Y.O. Halchenko, F1000Research, **9**, 1131 (2020). https://doi.org/10.12688/f1000research.24544.1
[20] R.W. Brown, Y.-C.N. Cheng, E.M. Haacke, M.R. Thompson, and R. Venkatesan, *Magnetic Resonance Imaging: Physical Principles and Sequence Design*, (John Wiley & Sons, 2014).
[21] W.A. Edelstein, G.H. Glover, C.J. Hardy, and R.W. Redington, Magn. Reson. Med. **3**, 604 (1986). https://doi.org/10.1002/mrm.1910030413
[22] H. Gudbjartsson and S. Patz, Magn. Reson. Med. **34**, 910 (1995). https://doi.org/10.1002/mrm.1910340618
[23] N. Just, Br. J. Cancer **111**, 2205 (2014). https://doi.org/10.1038/bjc.2014.512
[24] G. Vegas-Sánchez-Ferrero, M.J. Ledesma-Carbayo, G.R. Washko, and R.S.J. Estépar, Med. Image Anal. **40**, 44 (2017). https://doi.org/10.1016/j.media.2017.06.001
[25] H. Liu, Z. Li, S. Lin, and L. Cheng, Sensors, **23**, 7044 (2023). https://doi.org/10.3390/s23167044
[26] L.-C. Chen, G. Papandreou, F. Schroff, and H. Adam, (2017). https://doi.org/10.48550/arXiv.1706.05587
[27] E. Perez, F. Strub, H. de Vries, V. Dumoulin, and A. Courville, in: *Proc. Thirty-Second AAAI Conf. Artif. Intell. Thirtieth Innov. Appl. Artif. Intell. Conf. Eighth AAAI Symp. Educ. Adv. Artif. Intell*, (AAAI Press, New Orleans, Louisiana, USA, 2018), pp. 3942-3951. https://doi.org/10.48550/arXiv.1709.07871
[28] C. Bregler, in: *2015 IEEE Conf. Comput. Vis. Pattern Recognit. CVPR*, (2015). https://doi.org/10.1109/CVPR.2015.7298664
[29] A.L. Maas, in: *Rectifier Nonlinearities Improve Neural Network Acoustic Models*, (2013). https://api.semanticscholar.org/CorpusID:16489696
[30] S. Woo, J. Park, J.-Y. Lee, and I.S. Kweon, ArXiv preprint, (2018), pp. 3–19. https://doi.org/10.48550/arXiv.1807.06521
[31] J. Hu, L. Shen, and G. Sun, ArXiv preprint, ArXiv preprint, (2018), pp. 7132–7141. https://https://doi.org/10.48550/arXiv.1709.01507
[32] B. Yaman, S.A.H. Hosseini, S. Moeller, J. Ellermann, K. Uğurbil, and M. Akçakaya, Magn. Reson. Med. **84**, 3172 (2020). https://doi.org/10.1002/mrm.28378
[33] L. Zhang, M. Wu, L. Wang, D.C. Steffens, G.G. Potter, and M. Liu, ArXiv preprint, (2024). https://doi.org/10.48550/arXiv.2403.08162
[34] H. Chen, Y. Zhang, W. Zhang, P. Liao, K. Li, J. Zhou, and G. Wang, ArXiv preprint, (2016). https://doi.org/10.48550/arXiv.1609.08508
[35] S. Gou, W. Liu, C. Jiao, H. Liu, Y. Gu, X. Zhang, J. Lee, and L. Jiao, Phys. Med. Biol. **64**, 165017 (2019). https://doi.org/10.1088/1361-6560/ab325e
[36] K. He, X. Zhang, S. Ren, and J. Sun, in: *2015 IEEE International Conference on Computer Vision (ICCV)*, (Santiago, Chile, 2015). https://doi.org/10.1109/ICCV.2015.123
[37] A. Horé and D. Ziou, in: *2010 20th Int. Conf. Pattern Recognit*. (2010), pp. 2366–2369. https://doi.org/10.1109/ICPR.2010.579
[38] K. Zhang, W. Zuo, Y. Chen, D. Meng, and L. Zhang, IEEE Trans. Image Process. **26**, 3142 (2017). https://doi.org/10.1109/TIP.2017.2662206
[39] G.P. Renieblas, A.T. Nogués, A.M. González, N. Gómez-Leon, and E.G. del Castillo, J. Med. Imaging, **4**, 035501 (2017). https://doi.org/10.1117/1.JMI.4.3.035501

[40] P. Jain, and V. Tyagi, Inf. Syst. Front. **18**, 159–170 (2016). https://doi.org/10.1007/s10796-014-9527-0
[41] K. P.g., J. Joseph, and S.J., Biocybern, Biomed. Eng. **37**, 159 (2017). https://doi.org/10.1016/j.bbe.2016.12.008
[42] J. Lewis, Vision Interface, **10**(1), 120-123 (1995). https://www.bibsonomy.org/bibtex/232f4a4901ce85a2b37f806ba675c8a0
[43] F.L. Goerner and G.D. Clarke, Med. Phys. **38**, 5049 (2011). https://doi.org/10.1118/1.3618730
[44] E. Alizadeh, Data Sci. (2023). https://towardsdatascience.com/dispersion-cv-qcd-32849f828434/
[45] Z. Jalilibal, A. Amiri, P. Castagliola, and M.B.C. Khoo, Comput. Ind. Eng. **161**, 107600 (2021). https://doi.org/10.1016/j.cie.2021.107600
[46] M. Kidoh, K. Shinoda, M. Kitajima, K. Isogawa, M. Nambu, H. Uetani, K. Morita, *et al.*, Magn. Reson. Med. Sci. **19**, 195 (2019). https://doi.org/10.2463/mrms.mp.2019-0018
[47] N. Nazir, A. Sarwar, and B.S. Saini, Micron, **180**, 103615 (2024). https://doi.org/10.1016/j.micron.2024.103615
[48] H.M.S.S. Herath, H.M.K.K.M.B. Herath, N. Madusanka, and B.-I. Lee, J. Imaging, **11**, 100 (2025). https://doi.org/10.3390/jimaging11040100
[49] J. Joseph, S. Jayaraman, R. Periyasamy, and S.V. Renuka, Curr. Med. Imaging, **13**, 58 (2017). https://doi.org/10.2174/1573405612666160609131149
[50] K. Ohashi, Y. Nagatani, M. Yoshigoe, K. Iwai, K. Tsuchiya, A. Hino, Y. Kida, *et al.*, J. Digit. Imaging, **36**, 2623 (2023). https://doi.org/10.1007/s10278-023-00875-0
[51] D. Sliusarenko, A. Netreba, and S. Radchenko, in: *2024 IEEE 42nd Int. Conf. Electron. Nanotechnol. ELNANO*, (2024), pp. 456–460. https://doi.org/10.1109/ELNANO63394.2024.10756858
[52] K. Usui, K. Ogawa, M. Goto, Y. Sakano, S. Kyougoku, and H. Daida, Vis. Comput. Ind. Biomed. Art **4**, 21 (2021). https://doi.org/10.1186/s42492-021-00087-9
[53] A. Ferdi, S. Benierbah, and A. Nakib, Multimed. Tools Appl. **84**, 21625 (2025). https://doi.org/10.1007/s11042-024-20175-1
[54] Z. Wang, J. Chen, and S.C.H. Hoi, ArXiv preprint, (2020). https://doi.org/10.48550/arXiv.1902.06068
[55] M.J. Muckley, B. Riemenschneider, A. Radmanesh, S. Kim, G. Jeong, J. Ko, Y. Jun, *et al.*, IEEE Trans. Med. Imaging, **40**, 2306 (2021). https://doi.org/10.1109/TMI.2021.3075856
[56] A. Buades, B. Coll, and J.-M. Morel, in: *2005 IEEE Comput. Soc. Conf. Comput. Vis. Pattern Recognit. CVPR05*, (2005), pp. 60–65 vol. 2. https://doi.org/10.1109/CVPR.2005.38
[57] K. Dabov, A. Foi, V. Katkovnik, and K. Egiazarian, IEEE Trans. Image Process. **16**, 2080 (2007). https://doi.org/10.1109/TIP.2007.901238
[58] K. Zhang, W. Zuo, and L. Zhang, IEEE Trans. Image Process. **27**, 4608 (2018). https://doi.org/10.1109/TIP.2018.2839891
[59] Y. Zhang, K. Li, K. Li, L. Wang, B. Zhong, and Y. Fu, in: *Comput. Vis. – ECCV 2018 15th Eur. Conf. Proc*. Part VII (Springer-Verlag, Berlin, Heidelberg, 2018), pp. 294–310. https://doi.org/10.1007/978-3-030-01234-2_18
[60] J. Liang, J. Cao, G. Sun, K. Zhang, L.V. Gool, and R. Timofte, ArXiv preprint, (2021). https://doi.org/10.48550/arXiv.2108.10257
[61] S.W. Zamir, A. Arora, S. Khan, M. Hayat, F.S. Khan, and M.-H. Yang, ArXiv preprint, (2022). https://doi.org/10.48550/arXiv.2111.09881
[62] E. Jeong, J. Jang, J. Kim, and H. Kim, J. Magn. Reson. **368**, 107762 (2024). https://doi.org/10.1016/j.jmr.2024.107762
[63] C. Millard and M. Chiew, Bioengineering, **11**, 1305 (2024). https://doi.org/10.3390/bioengineering11121305

ШУМОЗАГЛУШЕННЯ МРТ НА ОСНОВІ ГЛИБОКОГО НАВЧАННЯ З ВИКОРИСТАННЯМ СТАТИСТИКИ ШУМУ, ОТРИМАНОЇ З ВИМІРЮВАНЬ ФІЗИЧНИХ ФАНТОМІВ

Д.Г. Слюсаренко[1,2], А.В. Нетреба[1]

[1]Факультет радіофізики, електроніки та комп'ютерних систем, Київський національний університет імені Тараса Шевченка, вул. Володимирська, 64/13, Київ, Україна, 01601

[2]Національний інститут раку України, вул. Юлія Здановського, 33/43, Київ, Україна, 03022

Високоякісні МРТ-зображення є важливими для точного визначення об'ємів-мішеней та органів, що знаходяться в групі ризику, а також для правильної реєстрації на КТ під час планування променевої терапії. Метою цієї роботи є розробка надійного методу шумозаглушення, який покращує візуалізацію структур мозку та зберігає анатомічні деталі. Запропоновано модель, засновану на модифікованій архітектурі U-Net із залишковими блоками, модулями уваги (CBAM) та просторовим пірамідальним об'єднанням. Підхід характеризується інтеграцією статистичних шумових характеристик, отриманих з фантомних вимірювань, та моделюванням деградацій у псевдо-k-просторі (включаючи розподіли гаусового та релеївського шуму). Валідацію було проведено на 1000 анонімізованих клінічних DICOM-зображеннях зі змінними рівнями шуму. Запропонована модель забезпечила збільшення PSNR на 8–10 дБ та збільшення SSIM з 0,72 до 0,97. Індекс збереження країв (EPI), який досяг значень 8,0 на шумних зображеннях через артефакти, стабілізувався на рівні 1,0 після обробки, що свідчить про ефективне видалення псевдоконтурів без розмиття справжніх анатомічних меж. Крім того, на реальних зображеннях спостерігалося середнє покращення SNR на 7% та зниження CV на 4–7%, що підтверджує стабільність методу. Поєднання фізично обґрунтованого моделювання шуму в частотній області та сучасних архітектур глибокого навчання дозволяє ефективно видаляти шум, зберігаючи при цьому критичні анатомічні межі. Метод має високий потенціал для клінічного впровадження в процедурах планування променевої терапії, зокрема для підвищення точності об'єднання МРТ/КТ.

Ключові слова: *шумозаглушення МРТ, моделювання шуму в k-просторі, глибоке навчання, адаптивне масштабування шуму, моделювання в області Фур'є, реконструкція медичних зображень, CNN*